

# Exploring the Reactivity of Bacterial Multicomponent Monooxygenases

by

Christine Elaine Tinberg  
B.A. Chemistry  
Northwestern University, 2005

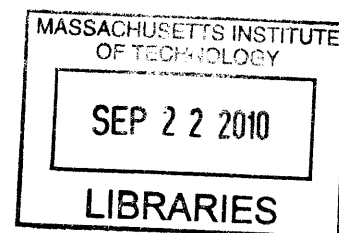
SUBMITTED TO THE DEPARTMENT OF CHEMISTRY IN PARTIAL  
FULLFILLMENT OF THE REQUIREMENTS FOR THE DEGREE OF

DOCTOR OF PHILOSOPHY OF BIOLOGICAL CHEMISTRY  
AT THE  
MASSACHUSETTS INSTITUTE OF TECHNOLOGY

JULY 2010

[September 2010]

© Massachusetts Institute of Technology, 2010  
All rights reserved



ARCHIVES

Signature of Author:

\_\_\_\_\_

Department of Chemistry  
July 15, 2010

Certified by:

\_\_\_\_\_

Stephen J. Lippard  
Arthur Amos Noyes Professor of Chemistry  
Thesis Supervisor

Accepted by:

\_\_\_\_\_

Robert W. Field  
Haslem and Dewey Professor of Chemistry  
Chairman, Departmental Committee on Graduate Studies

This doctoral thesis has been examined by a Committee of the Department of Chemistry as follows:

---

Alice Y. Ting  
Committee Chairman  
Associate Professor of Chemistry

---

Stephen J. Lippard  
Arthur Amos Noyes Professor of Chemistry  
Thesis Supervisor

---

JoAnne Stubbe  
Novartis Professor of Chemistry and Professor of Biology

# Exploring the Reactivity of Bacterial Multicomponent Monooxygenases

by

Christine Elaine Tinberg

Submitted to the Department of Chemistry on July 15, 2010, in partial fulfillment of the requirements for the Degree of Doctor of Philosophy

## ABSTRACT

### Chapter 1. Introduction: The Reactivity of Bacterial Multicomponent Monooxygenases

Bacterial multicomponent monooxygenases constitute a remarkable family of enzymes that oxidize small, inert hydrocarbon substrates using molecular oxygen. Three or more protein components are required for the timely reactions of electrons, protons, O<sub>2</sub>, and hydrocarbon at an active site carboxylate-bridged diiron center. This overview describes structural and biochemical studies of the BMM protein components, presents the proposed mechanisms of O<sub>2</sub> activation by BMMs and related carboxylate-bridged diiron proteins, and discusses substrate reactivity of the oxygenated diiron units responsible for BMM catalysis.

### Chapter 2. Revisiting the Mechanism of Dioxygen Activation in Soluble Methane Monooxygenase from *M. capsulatus* (Bath): Evidence for a Multi-Step, Proton-Dependent Reaction Pathway

Stopped-flow kinetic investigations of soluble methane monooxygenase (sMMO) from *M. capsulatus* (Bath) have clarified discrepancies that exist in the literature regarding several aspects of catalysis by this enzyme. The development of thorough kinetic analytical techniques has led to the discovery of two novel oxygenated iron species that accumulate in addition to the well-established intermediates H<sub>peroxo</sub> and Q. The first intermediate, P\*, is a precursor to H<sub>peroxo</sub> and was identified when the reaction of reduced MMOH and MMOB with O<sub>2</sub> was carried out in the presence of ≥540 mM methane to suppress the dominating absorbance signal due to Q. The optical properties of P\* are similar to those of H<sub>peroxo</sub>, with  $\epsilon_{420} = 3500 \text{ M}^{-1} \text{ cm}^{-1}$  and  $\epsilon_{720} = 1250 \text{ M}^{-1} \text{ cm}^{-1}$ . These values are suggestive of a peroxo-to-iron(III) charge-transfer transition and resemble those of peroxodiiron(III) intermediates characterized in other carboxylate-bridged diiron proteins and synthetic model complexes. The second identified intermediate, Q\*, forms on the pathway of Q decay when reactions are performed in the absence of hydrocarbon substrate. Q\* does not react with methane, forms independently of buffer composition, and displays a unique shoulder at 455 nm in its optical spectrum. Studies conducted at different pH values reveal that rate constants corresponding to P\* decay/H<sub>peroxo</sub> formation and H<sub>peroxo</sub> decay/Q formation are both significantly retarded at high pH and indicate that both events require proton transfer. The processes exhibit normal kinetic solvent isotope effects (KSIEs) of 2.0 and 1.8, respectively, when the reactions are performed in D<sub>2</sub>O.

Mechanisms are proposed to account for the observations of these novel intermediates and the proton dependencies of P\* to H<sub>peroxo</sub> and H<sub>peroxo</sub> to Q conversion.

### **Chapter 3. Oxidation Reactions Performed by Soluble Methane Monooxygenase Hydroxylase Intermediates H<sub>peroxo</sub> and Q Proceed by Distinct Mechanisms**

Soluble methane monooxygenase is a bacterial enzyme that converts methane to methanol at a carboxylate-bridged diiron center with exquisite control. Because the oxidizing power required for this transformation is demanding, it is not surprising that the enzyme is also capable of hydroxylating and epoxidizing a broad range of hydrocarbon substrates in addition to methane. In this work we take advantage of this promiscuity of the enzyme to gain insight into the mechanisms of action of H<sub>peroxo</sub> and Q, two oxidants that are generated sequentially during the reaction of reduced protein with O<sub>2</sub>. Using double-mixing stopped flow spectroscopy, we investigate the reactions of the two intermediate species with a panel of substrates of varying C–H bond strength. Three classes of substrates are identified according to the rate-determining step in the reaction. We show for the first time that an inverse trend exists between the rate constant of reaction with H<sub>peroxo</sub> and the C–H bond strength of the hydrocarbon examined for those substrates in which C–H bond activation is rate-limiting. Deuterium kinetic isotope effects reveal that reactions performed by Q, but not H<sub>peroxo</sub>, involve extensive quantum mechanical tunneling. This difference sheds light on the observation that H<sub>peroxo</sub> is not a potent enough oxidant to hydroxylate methane, whereas Q can perform this reaction in a facile manner. In addition, the reaction of H<sub>peroxo</sub> with acetonitrile appears to proceed by a distinct mechanism in which a cyanomethide anionic intermediate is generated, bolstering the argument that H<sub>peroxo</sub> is an electrophilic oxidant and operates via two-electron transfer chemistry.

### **Chapter 4. Dioxygen Activation and the Multiple Roles of Component Proteins in Phenol Hydroxylase from *Pseudomonas* sp. OX1**

O<sub>2</sub> activation was also investigated in PH, a BMM that oxidizes phenol to catechol. Rapid freeze-quench Mössbauer and stopped-flow optical spectroscopy were employed to study the reaction of the reduced, diiron(II) form of *Pseudomonas* sp. OX1 PH hydroxylase (PHH) with O<sub>2</sub> in the presence of the regulatory protein PHM. A single long-lived diiron(III) intermediate with  $\delta = 0.59$  mm/s and  $\Delta E_Q = 0.63$  mm/s and no discernable optical bands accumulates along the reaction pathway. The spectroscopic parameters of this intermediate are similar to those reported recently for a diiron(III) transient generated in toluene/*o*-xylene monooxygenase hydroxylase but are quite different from those of peroxodiiron(III) species formed in other diiron enzymes despite the fact that the active sites of these proteins have identical first-shell coordination environments. In contrast to reactions of MMOH, there is no evidence for accumulation of a high-valent diiron(IV) intermediate in PHH. Under steady state conditions in the absence of hydrocarbon substrate, electrons are consumed and PHH generates H<sub>2</sub>O<sub>2</sub> catalytically, suggesting that the observed diiron(III) intermediate is a peroxodiiron(III) species. Steady state biochemical studies were conducted to ascertain the functions of the PH reductase and regulatory protein. Single turnover experiments revealed that, unlike sMMO, *only* the complete system containing all three protein components is capable of oxidizing phenol. The yield of catechol produced under ideal conditions maximized at

~50% per diiron active site in single turnover experiments, suggesting that the enzyme operates by a half-sites reactivity mechanism. Results from single turnover studies in which the oxidized form of the reductase, PHP, was added to a mixture of reduced hydroxylase and regulatory protein revealed that PHP exerts an additional regulatory effect on PHH, most likely by an allosteric mechanism. The rate of H<sub>2</sub>O<sub>2</sub> formation by PHH in the absence of a hydrocarbon substrate was retarded when PHM was omitted from the reaction mixture, indicating that the regulatory protein controls the kinetics of O<sub>2</sub> activation and/or blocks unproductive quenching of the oxygenated intermediate by untimely electron transfer.

### **Chapter 5. Characterization of Iron Dinitrosyl Species Formed in the Reaction of Nitric Oxide with a Biological Rieske Center**

Reactions of nitric oxide with cysteine-ligated iron-sulfur cluster proteins typically result in disassembly of the iron-sulfur core and formation of dinitrosyl iron complexes (DNICs). Here we report the first evidence that these species can also form at Rieske-type [2Fe-2S] clusters. Upon treatment of a Rieske protein, component C of toluene/*o*-xylene monooxygenase (ToMOC) from *Pseudomonas* sp. OX1, with NO (g) or the NO-generators *S*-nitroso-*N*-acetyl-D,L-pencillamine (SNAP) and diethylamine NONOate (DEANO), the absorbance features of the [2Fe-2S] cluster bleach and a new band slowly appears at 367 nm. Characterization of the reaction products by EPR, Mössbauer, and NRVS spectroscopy reveals that the primary product observed in the reaction is the dinuclear iron dinitrosyl Roussin's red ester (RRE), [Fe<sub>2</sub>(μ-SCys)<sub>2</sub>(NO)<sub>4</sub>], and that mononuclear DNICs only account for a minor fraction of the nitrosylated iron. The RRE reaction product can be reduced by sodium dithionite to produce the one-electron reduced Roussin's red ester (rRRE) having absorption bands at 640 and 960 nm. These results show that NO reacts readily with protein-based Rieske centers and suggest that dinuclear RRE species, not mononuclear DNICs, may be the primary iron dinitrosyl species responsible for the pathological and physiological effects of nitric oxide in the presence of iron-sulfur clusters.

### **Appendix A. Preliminary Characterization of <sup>57</sup>Fe-enriched MMOH<sub>ox</sub> and MMOH<sub>Q</sub> by Nuclear Vibrational Resonance Spectroscopy**

Synchrotron-based <sup>57</sup>Fe Nuclear Resonance Vibrational Spectroscopy (NRVS) is a powerful technique that allows for identification of the full set of vibrational modes of a given <sup>57</sup>Fe center. In this work we present preliminary NRVS studies of <sup>57</sup>Fe-enriched oxidized soluble methane monooxygenase hydroxylase in complex with 2 equiv of its regulatory protein (MMOH<sub>ox</sub>:2B) and intermediate Q, the species responsible for methane oxidation in this enzyme. Although maximal protein concentrations were employed, very few vibrational peaks were resolved. Our data suggest that the sMMO protein system is not amenable to this method using the technologies that are currently available.

Thesis Supervisor: Stephen J. Lippard  
Title: Arthur Amos Noyes Professor of Chemistry

Dedicated to my parents

## ACKNOWLEDGEMENTS

I am extremely grateful for the support of my colleagues, friends, and family, without whom this thesis would not have been possible. First and foremost I thank my thesis advisor, Steve Lippard, for supporting my scientific growth during my time at MIT. Steve fostered a professional environment in which I learned not only how to think like a scientist but also how to behave with the utmost integrity while doing so. He set a bar of excellence for his students and expected nothing less than the most rigorous science and scholarly behavior. I greatly appreciate these high standards that allowed me to grow scientifically and personally. I am lucky to have been trained by the best!

I also thank my professors and mentors at MIT, who opened my eyes to the world of biological chemistry. In particular, my thesis chair Alice Ting supported me throughout my time at MIT and provided important feedback on my projects. JoAnne Stubbe fostered my love of biochemistry and taught me to think rigorously about science during and beyond my courses with her. JoAnne's enzymology class was the best course that I have ever taken! I also thank the other professors with whom I had the chance to work and learn from during my time at MIT.

The completion of this thesis would not have been possible without the numerous students and postdocs that I had the opportunity to interact with in the Lippard Lab. In particular, I thank members of the BMM subgroup, including Laurance Beauvais, Viviana Izzo, Leslie Murray, Mike McCormick, Erik Dill, Woon Ju Song, and Rachel Behan, who taught me the skills that I needed to complete my work. I enjoyed discussing science and developing friendships with them, and can only hope that I will be so lucky to have great co-workers in the future. I thank Loi Do for his friendship, scientific discussions, and help with experiments. I'll never forget eating Pocky and green tea ice cream with him in Japan during our Spring-8 trip! I also thank Fan Liu, an undergraduate student whom I mentored during the summer of 2007, for helping me with several projects and opening my eyes to the world of teaching. Finally, I recognize all of the Lippard Lab members that I have had a chance to work with over the years - I have learned so much from you all and I hope that I can continue to do so in the future!

During my last two years I had the opportunity to work on a project with an enthusiastic postdoc in the lab, Zach Tonzetich. I couldn't have asked for a better collaborator: Zach's enthusiasm, professionalism, and love of science helped drive the project and ultimately led to interesting and unforeseen conclusions. Presented in Chapter 5, the work that Zach and I performed together resulted from the marriage of the perspectives and skill sets of a synthetic inorganic chemist and a biochemist. I greatly enjoyed learning with Zach and would not trade this experience for any other.

Prior to my arrival at MIT I spent two years as an undergraduate research assistant in the lab of Amy Rosenzweig, an excellent mentor and female role model. Amy encouraged me to develop my scientific skills and provided a great environment in which to begin my training. Throughout my years at MIT Amy has been extremely supportive and I cannot thank her enough for her guidance and enthusiasm. My mentor in the Rosenzweig lab, Amanda Hakemian, was a great teacher and I greatly appreciate her help and introduction to bench work.

On a personal level, I could not have made it through this time without the support of my beloved friend Sarah Slavoff, a graduate student in the Ting lab and my fellow

classmate and TA. Sarah and I, who were known to be always together by most of the MIT staff, became great friends and advocates of each other. I thank Sarah for letting me bounce ideas off her and chatting over coffee almost every day, but most of all for giving me great support and enthusiasm when things in lab or in my personal life were not going well. Sarah, I couldn't have done it without you! I also thank John Wilde, who gave me a constant source of happiness during my latter two years at MIT. When things were tough in lab John was there with a smiling face and was always ready to do something fun to get my mind off of work.

Last, and most importantly, I thank my loving parents, Rich and Elaine Tinberg, and my brother, Richie, for their constant and unyielding support during this time. My parents taught me to always behave in the most ethical manner and showed me the value of hard work. They are my greatest mentors and best friends, and I could not have done this without their support and love. Thank you, mom and dad – I love you!

Christy Tinberg  
July 15, 2010



## TABLE OF CONTENTS

<b>ABSTRACT</b>	...3
<b>DEDICATION</b>	...6
<b>ACKNOWLEDGEMENTS</b>	...7
<b>TABLE OF CONTENTS</b>	...9
<b>LIST OF TABLES</b>	...15
<b>LIST OF SCHEMES</b>	...17
<b>LIST OF FIGURES</b>	...18
<b>LIST OF EQUATIONS</b>	...24
<b>ABBREVIATIONS</b>	...25

### **CHAPTER 1. Introduction: The Reactivity of Bacterial Multicomponent Monooxygenases**

Introduction	...30
A. BMM Structures and Component Interactions	...32
Hydroxylases	...32
Hydroxylase Diiron Centers	...33
Substrate Ingress and Product Egress	...36
Regulatory Proteins	...37
Reductase/Rieske Proteins and Electron Transfer	...43
A Fourth BMM Component in sMMO and PH	...44
Outlook and Future Directions	...46
B. Dioxygen Activation in BMMs and Related Carboxylate-Bridged Diiron Proteins	...46
Peroxydiiron(III) Species Formed at Carboxylate-Bridged Diiron Centers	...47
MMOH Intermediate Q	...51
RNR-R2 Intermediate X	...53
Outlook and Future Directions	...54

C. Substrate Reactivity of BMMs	...55
Peroxide Shunt Reactions	...56
Mechanistic Substrate Probes	...57
The NIH Shift and Hammett Plots	...60
Transient Kinetic Studies	...62
Computational Studies	...65
Outlook and Future Directions	...66
Organization and Scope of Thesis	...67
References	...67

**CHAPTER 2. Revisiting the Mechanism of Dioxygen Activation in Soluble Methane Monooxygenase from *M. capsulatus* (Bath): Evidence for a Multi-Step, Proton Dependent Reaction Pathway**

Introduction	...84
Materials and Methods	...88
General Considerations	...88
Stopped-Flow Optical Spectroscopy	...89
KSIE Measurements	...90
Data Analysis	...91
Results	...91
$\text{MMOH}_{\text{red}}:2\text{B} + \text{O}_2$ : Reactions in the Presence of Methane	...91
Kinetic Characterization of P*	...97
$\text{MMOH}_{\text{red}}:2\text{B} + \text{O}_2$ : Reactions in the Absence of Methane	...99
Temperature Dependencies of $\text{MMOH}_{\text{red}}:2\text{B} + \text{O}_2$ Reactions	...105
Double-Mixing Stopped-Flow Optical Spectroscopy: $\text{Q}/\text{Q}^* + \text{CH}_4$	...107
Effect of Buffer on Q Decay	...110
Proton Requirements of $\text{MMOH}_{\text{red}}:2\text{B} + \text{O}_2$ Reactions	...113
Discussion	...120
Origin of Proton Requirement	...120

Implications for Proton Transfer Reactions	...122
Identity of P*	...125
Nature of P* to H <sub>peroxo</sub> Conversion	...128
Nature of H <sub>peroxo</sub> to Q Conversion	...129
Mechanism of Q Decay	...131
Concluding Remarks	...133
References	...134
Appendix 2.1: Derivation of eq 2.2 Describing Model ii of Scheme 2.2	...140
Appendix 2.2: Derivation of eq 2.3 Describing Model iii of Scheme 2.3	...143
Appendix 2.3: Derivation of eq 2.4 Describing Model iv of Scheme 2.3	...147

**CHAPTER 3. Oxidation Reactions Performed by Soluble Methane Monooxygenase  
Hydroxylase Intermediates H<sub>peroxo</sub> and Q Proceed by Distinct Mechanisms**

Introduction	...151
Materials and Methods	...155
General Considerations	...155
Stopped-Flow Optical Spectroscopy	...155
Data Analysis	...156
Results and Discussion	...159
Single-Mixing Stopped-Flow Studies – Proof that H <sub>peroxo</sub> is a Hydrocarbon Oxidant	...160
Double-Mixing Stopped-Flow Studies – Delineating the Reactivities of Diiron(III) Peroxo vs. Diiron(IV) Oxo Intermediates	...162
Class I Reactions	...164
Class II Reactions	...168
Class III Reactions	...170
Implications for Reaction Mechanisms of H <sub>peroxo</sub> and Q	...177
Reactions of H <sub>peroxo</sub> with CH <sub>3</sub> CN	...180
Implications for Other Systems with Multiple Oxidizing Species	...182

Concluding Remarks	...183
References	...184

**CHAPTER 4. Dioxygen Activation and the Multiple Roles of Component Proteins  
in Phenol Hydroxylase from *Pseudomonas* sp. OX1**

Introduction	...191
Materials and Methods	...195
General Considerations	...195
Protein Expression and Purification	...196
Characterization of PHM	...201
Stopped-Flow Optical Spectroscopy	...201
Mössbauer Spectroscopy	...202
Single Turnover Assays	...203
Peroxide Shunt Assays	...204
H <sub>2</sub> O <sub>2</sub> Production Assays	...204
H <sub>2</sub> O <sub>2</sub> and NH <sub>2</sub> OH Inactivation Assays	...206
H <sub>2</sub> O <sub>2</sub> Consumption Assays	...207
NADH Consumption Assays	...207
Results	...207
Expression, Purification, and Characterization of PHH	...208
Characterization of PHM	...214
Mössbauer Spectra of Reduced and Oxidized PHH	...218
Stopped-Flow Optical Spectroscopy: PHH <sub>red</sub> :2M + O <sub>2</sub>	...221
RFQ-Mössbauer Spectroscopy: PHH <sub>red</sub> :2M + O <sub>2</sub>	...222
Attempt to Activate PHH <sub>ox</sub> for Hydrocarbon Oxidation with a Peroxide Shunt	...226
H <sub>2</sub> O <sub>2</sub> is Generated when PHH <sub>ox</sub> is Activated with Electrons and O <sub>2</sub> in the Absence of Phenol	...227

Single Turnover Assays: Evidence for Half-Sites Reactivity and the Allosteric Influence of PHP	...234
H <sub>2</sub> O <sub>2</sub> Production in the Absence of the Regulatory Protein	...237
NADH Consumption by PH	...238
Discussion	...239
The Hydroxylase Component of Recombinant Phenol Hydroxylase	...239
Studies of PHK, A Novel Zinc(II) Chaperone in the PH Operon?	...240
Dioxygen Activation in PH in the Absence of Hydrocarbon Substrate	...244
H <sub>2</sub> O <sub>2</sub> Generation by PH	...247
Evidence for Half-Sites Reactivity in PH	...249
PHP Regulates PHH Chemistry	...249
Roles of PHM	...251
Concluding Remarks	...252
Acknowledgements	...253
References	...254

## **CHAPTER 5. Characterization of Dinitrosyl Iron Species in the Reaction of Nitric Oxide with a Biological Rieske Center**

Introduction	...261
Materials and Methods	...265
General Considerations	...265
Preparation of <sup>57</sup> Fe-ToMOC	...266
ToMOC Reduction	...266
General Spectroscopic Measurements	...266
NRVS Measurements	...267
Stopped-Flow Optical Spectroscopy	...268
Results	...269
Reactions of ToMOC with NO and NO Donors	...269

Reduction of Iron Dinitrosyl Species Formed in Reaction of ToMOC with NO	...280
Kinetics of ToMOC Iron Dinitrosyl Formation	...284
Discussion	...286
Characterization of RRE as the Primary Product in the Reaction of the Rieske Protein ToMOC with NO	...286
Nature of DNIC Species Formed in the Reaction of ToMOC with NO	...287
Mechanism of Formation of Iron Dinitrosyl Species	...288
Implications for Other Iron-Sulfur Systems	...289
Concluding Remarks	...290
Acknowledgements	...290
References	...291

**APPENDIX A: Preliminary Characterization of  $^{57}\text{Fe}$ -enriched  $\text{MMOH}_{\text{ox}}$  and  $\text{MMOH}_{\text{Q}}$  by Nuclear Vibrational Resonance Spectroscopy**

Introduction	...298
Materials and Methods	...299
Sample Preparation	...299
NRVS Measurements	...300
Results and Discussion	...301
Concluding Remarks and Future Directions	...303
Acknowledgements	...303
References	...304

**BIOGRAPHICAL NOTE** ...307

**CURRICULUM VITAE** ...308

## LIST OF TABLES

Table 1.1	Spectroscopic Parameters of Peroxodiiron(III) Intermediates in Non-Heme Diiron Enzymes and Select Synthetic Model Systems	...50
Table 1.2	Spectroscopic Parameters of High-Valent Iron (IV) Intermediates in Non-Heme Diiron Enzymes and Synthetic Model Systems	...51
Table 2.1	Temperature Dependence of MMOH O <sub>2</sub> Activation Rate Constants	...105
Table 2.2	Activation Parameters of MMOH O <sub>2</sub> Activation Processes	...107
Table 2.3	pH Dependence of MMOH O <sub>2</sub> Activation Rate Constants	...115
Table 3.1	Classification of H <sub>peroxo</sub> and Q Substrates	...163
Table 3.2	Rate Constants for Class I Substrates of Q	...164
Table 3.3	Rate Constants for Class II Substrates of H <sub>peroxo</sub>	...168
Table 3.4	Class II Substrates of H <sub>peroxo</sub> : Correlation Between <i>k</i> <sub>obs</sub> and BDE	...170
Table 3.5	Class III Substrates of H <sub>peroxo</sub> and Q	...173
Table 3.6	Class III Substrates of H <sub>peroxo</sub> : Correlation Between <i>k</i> <sub>obs</sub> and BDE	...175
Table 3.7	Apparent KIEs and Correlation of <i>k</i> <sub>sat</sub> with Thermodynamic Parameters for Class III Substrates of Q at 4 °C and °20 C	...176
Table 3.8	Comparison of Second-Order Rate Constants for Reactions of H <sub>peroxo</sub> and Q with Substrates	...178
Table 4.1	PHH Expression Plasmids	...196
Table 4.2	Specific Activity and Iron Content of Purified PHH	...208
Table 4.3	Optimization of Fe <sup>2+</sup> and Zn <sup>2+</sup> Concentrations for <sup>57</sup> Fe PHH Expression	...213
Table 4.4	Mössbauer Parameters of PHH Species	...220

Table 4.5	Percent Mössbauer Absorption of Species Detected in the Reaction of $\text{PHH}_{\text{red}}:2\text{M}$ with $\text{O}_2$	...224
Table 4.6	PH Single Turnover Yields	...235
Table 4.7	PH NADH Consumption Rates	...239
Table 5.1	Comparison of Mössbauer Parameters for ToMOC-Derived and Synthetic Iron Dinitrosyl Species	...277
Table 5.2	Dependence of Rate Constants $k_{\text{obs}1}$ , $k_{\text{obs}2}$ , and $k_{\text{obs}3}$ for the Reaction of $\text{ToMOC}_{\text{ox}}$ with DEANO on $[\text{DEANO}]$	...286



## LIST OF SCHEMES

Scheme 2.1	Two Possible Mechanisms of O—O Bond Cleavage in MMOH	...87
Scheme 2.2	Models for the Reaction of $\text{MMOH}_{\text{red}}$ and Two Equiv of MMOB with $\text{O}_2$ in the Presence of 540 $\mu\text{M}$ Methane	...95
Scheme 2.3	Models for the Reaction of $\text{MMOH}_{\text{red}}$ and Two Equiv of MMOB with $\text{O}_2$	...102
Scheme 2.4	Mechanism of Q Decay in the Presence of $\text{CH}_4$	...110
Scheme 2.5	Models for the pH Dependencies of $\text{P}^*$ to $\text{H}_{\text{peroxo}}$ and $\text{H}_{\text{peroxo}}$ to Q Conversion	...116
Scheme 2.6	Postulated Mechanism of $\text{P}^*$ to $\text{H}_{\text{peroxo}}$ Conversion	...129
Scheme 2.7	Postulated Mechanism of $\text{H}_{\text{peroxo}}$ to Q Conversion	...131
Scheme 2.8	Possible Mechanisms of Q Decay in the Absence of Hydrocarbon Substrates	...132
Scheme 3.1	Current Working Model of Catalysis by the MMOH Diiron Center	...152
Scheme 3.2	Proposed Mechanisms of Methane Hydroxylation by Q and Diethyl Ether Oxidation by $\text{H}_{\text{peroxo}}$	...153
Scheme 3.3	Proposed Mechanism of $\text{CH}_3\text{CN}$ Hydroxylation by $\text{H}_{\text{peroxo}}$	...181
Scheme 4.1	Three Parallel Processes Model used to Fit PH Mössbauer Kinetic Data from Reaction of $\text{PHH}_{\text{red}}:2\text{M}$ with $\text{O}_2$	...224
Scheme 4.2	Inability of PH to Access a Peroxide Shunt	...226
Scheme 4.3	Steady State Product Evolution by PH	...229
Scheme 4.4	Cartoon Representation of Catalysis by PHH	...246
Scheme 5.1	Iron Dinitrosyl Species Observed in Biological and Biomimetic Synthetic Systems	...262

## LIST OF FIGURES

Figure 1.1	BMM Phylogenetic Tree	...31
Figure 1.2	Representative BMM Structures	...33
Figure 1.3	BMM Active Site Structures	...34
Figure 1.4	Surface Renderings of the T4moH <sub>ox</sub> :2D, T4moH <sub>red</sub> :2D, and PHH:PHM Complexes	...41
Figure 1.5	Proposed Structure of Intermediate Q	...52
Figure 1.6	Representative Examples of Carbocation-Derived Products Detected in the Reactions of sMMO with Mechanistic Substrate Probes	...59
Figure 1.7	Possible Mechanisms of Phenol and 4- <sup>2</sup> H <sub>1</sub> -Toluene Oxidation by Aromatic Hydroxylases	...61
Figure 1.8	Proposed Two-Electron Oxidation Mechanisms for Reactions of H <sub>peroxo</sub> with Diethyl Ether and Ethyl Vinyl Ether	...65
Figure 2.1	Representative 420 nm Absorbance Profiles for Reactions of MMOH <sub>red</sub> and MMOB with a Mixture of O <sub>2</sub> and CH <sub>4</sub> at 4 °C and pH 7.0	...92
Figure 2.2	Exponential Fits of Data Monitoring the Reaction of MMOH <sub>red</sub> and MMOB with a Mixture of O <sub>2</sub> and CH <sub>4</sub> at 4 °C and pH 7.0	...94
Figure 2.3	Representative Fits of Data Monitoring the Reaction of MMOH <sub>red</sub> and MMOB with a Mixture of O <sub>2</sub> and CH <sub>4</sub> at 4 °C and pH 7.0 to eq 2.1	...96
Figure 2.4	Representative Fits of Data Monitoring the Reaction of MMOH <sub>red</sub> and MMOB with a Mixture of O <sub>2</sub> and CH <sub>4</sub> at 4 °C and pH 7.0 to eq 2.2	...97
Figure 2.5	Optical Spectra of P* and H <sub>peroxo</sub>	...98
Figure 2.6	O <sub>2</sub> Dependence of P* Formation, P* to H <sub>peroxo</sub> Conversion, and H <sub>peroxo</sub> to Q Conversion at 4 °C and pH 7.0	...99

Figure 2.7	Representative Fits of Data Monitoring the Reaction of $\text{MMOH}_{\text{red}}$ and $\text{MMOB}$ with $\text{O}_2$ at 4 °C and pH 7.0 to a $\text{P}^* \rightarrow \text{H}_{\text{peroxo}} \rightarrow \text{Q} \rightarrow \text{H}_{\text{ox}}$ Model	...100
Figure 2.8	Exponential Fits of Data Monitoring the Reaction of $\text{MMOH}_{\text{red}}$ and $\text{MMOB}$ with $\text{O}_2$ at 4 °C and pH 7.0	...101
Figure 2.9	Representative Fits of Data Monitoring the Reaction of $\text{MMOH}_{\text{red}}$ and $\text{MMOB}$ with $\text{O}_2$ at 4 °C and pH 7.0 to eq. 2.3	...103
Figure 2.10	Representative Fits of Data Monitoring the Reaction of $\text{MMOH}_{\text{red}}$ and $\text{MMOB}$ with $\text{O}_2$ at 4 °C and pH 7.0 to eq. 2.4	...103
Figure 2.11	Optical spectra of Q and $\text{Q}^*$	...104
Figure 2.12	Eyring Plots for $\text{P}^*$ to $\text{H}_{\text{peroxo}}$ , $\text{H}_{\text{peroxo}}$ to Q, Q to $\text{Q}^*$ , and $\text{Q}^*$ to $\text{H}_{\text{ox}}$ Conversion at pH 7.0	...106
Figure 2.13	Speciation Plot Depicting the Time-Dependent Behavior of Transients Formed During the Reaction of $\text{MMOH}_{\text{red}}$ and $\text{MMOB}$ with $\text{O}_2$ at 4 °C and pH 7.0	...108
Figure 2.14	Representative Fits of Double-Mixing Stopped Flow Data Monitoring the Reactions of Q and $\text{Q}^*$ with $\text{CH}_4$ at 4 °C and pH 7.0	...109
Figure 2.15	Representative Fits of Data Monitoring the Reaction of $\text{MMOH}_{\text{red}}$ and $\text{MMOB}$ with $\text{O}_2$ in Cacodylate Buffer at 4 °C and pH 7.0	...111
Figure 2.16	Plot of $k_{\text{obs}}$ vs. [MOPS] for Decay of Q at 4 °C and pH 7.0	...112
Figure 2.17	Representative 420 nm Absorbance Profile for Reactions of $\text{MMOH}_{\text{red}}$ and $\text{MMOB}$ with $\text{O}_2$ at 4 °C and Varying pH Values	...113
Figure 2.18	pH Dependence of $\text{P}^*$ to $\text{H}_{\text{peroxo}}$ and $\text{H}_{\text{peroxo}}$ to Q Conversion	...114
Figure 2.19	pH Dependence of $\text{P}^*$ Formation, Q to $\text{Q}^*$ Conversion, and $\text{Q}^*$ Decay	...115
Figure 2.20	Poor Fit of the pH Dependence of $\text{H}_{\text{peroxo}}$ to Q Conversion to Model i of Scheme 2.5	...117
Figure 2.21	Representative Fits of Data Monitoring the Reaction of $\text{MMOH}_{\text{red}}$ and $\text{MMOB}$ with $\text{O}_2$ at 5 °C in Phosphate Buffer Prepared in $\text{D}_2\text{O}$ , pD 7.0	...118

Figure 2.22	MMOH <sub>ox</sub> Active Site	...122
Figure 2.23	Speciation Plots Depicting the Time-Dependent Behavior of Transients that Form During the Reaction of MMOH <sub>red</sub> and MMOB with a Mixture of O <sub>2</sub> and CH <sub>4</sub> at 4 °C and pH 7.0 According to Models i and ii of Scheme 2.2	...125
Figure 3.1	Representative Fits of Stopped-Flow Data Probing the Reactions of Q and H <sub>peroxo</sub> with 96 mM CH <sub>3</sub> NO <sub>2</sub>	...158
Figure 3.2	Representative Fit of Stopped-Flow Data Probing the Reaction of H <sub>peroxo</sub> with 272 mM CD <sub>3</sub> NO <sub>2</sub>	...158
Figure 3.3	Representative 420 nm Absorbance Profiles for the Reaction of MMOH <sub>red</sub> with a Mixture of Excess O <sub>2</sub> and CH <sub>3</sub> CH <sub>2</sub> CHO in the Presence of 2 equiv MMOB and Representative Fit of Data Collected in the Presence of 214.9 mM CH <sub>3</sub> CH <sub>2</sub> CHO to a Single Exponential Decay Process	...161
Figure 3.4	Representative 720 nm Absorbance Profiles for the Reaction of MMOH <sub>red</sub> with a Mixture of Excess O <sub>2</sub> and CH <sub>3</sub> CH <sub>2</sub> CHO in the Presence of 2 equiv MMOB and Representative Fit of Data Collected in the Presence of 214.9 mM CH <sub>3</sub> CH <sub>2</sub> CHO to a Single Exponential Decay Process	...161
Figure 3.5	Plot of $k_{obs}$ versus [CH <sub>3</sub> OH] or [CD <sub>3</sub> OH] for Reaction with Q at 4 °C and pH 7.0	...165
Figure 3.6	Plot of $k_{obs}$ versus [CH <sub>3</sub> CH <sub>2</sub> OH] or [CD <sub>3</sub> CD <sub>2</sub> OH] for Reaction with Q at 4 °C and pH 7.0	...165
Figure 3.7	Plot of $k_{obs}$ versus [CH <sub>3</sub> OH] or [CD <sub>3</sub> OH] for Reaction with H <sub>peroxo</sub> at 4 °C and pH 7.0	...169
Figure 3.8	Plot of $k_{obs}$ versus [CH <sub>3</sub> CH <sub>2</sub> OH] or [CD <sub>3</sub> CD <sub>2</sub> OH] for Reaction with H <sub>peroxo</sub> at 4 °C and pH 7.0	...169
Figure 3.9	Plot of $k_{obs}$ versus [CH <sub>3</sub> CH <sub>2</sub> CHO] for Reaction with H <sub>peroxo</sub> at 4 °C and pH 7.0	...171
Figure 3.10	Plot of $k_{obs}$ versus [CH <sub>3</sub> CHO] for Reaction with H <sub>peroxo</sub> at 4 °C and pH 7.0	...171
Figure 3.11	Plot of $k_{obs}$ versus [CH <sub>3</sub> NO <sub>2</sub> ] or [CD <sub>3</sub> NO <sub>2</sub> ] for Reactions with H <sub>peroxo</sub> and Q at 4 °C and pH 7.0	...172

Figure 3.12	Plot of $k_{\text{obs}}$ versus [HCOONa] for Reaction with $\text{H}_{\text{peroxo}}$ at 4 °C and pH 7.0	...172
Figure 3.13	Plot of $k_{\text{obs}}$ versus [CH <sub>3</sub> CN] or [CD <sub>3</sub> CN] for Reactions with $\text{H}_{\text{peroxo}}$ and Q at 4 °C and pH 7.0	...173
Figure 3.14	Linear Inverse Correlation Between $k_{\text{sat}}$ and C–H BDE for Class III Substrates of $\text{H}_{\text{peroxo}}$	...175
Figure 4.1	Schematic Representation of Phenol Metabolism by <i>Pseudomonas sp.</i> CF600	...193
Figure 4.2	<i>E. coli</i> Strain JM109 Transformed with pGEM3Z/PHLMNOP and pGEM/PHKLMNOP	...209
Figure 4.3	Q Sepharose FF Anion Exchange Trace for Purification of PHH Expressed from pGEM3Z/PHKLMNOP	...210
Figure 4.4	Q Sepharose FF Anion Exchange Trace for Purification of PHM	...215
Figure 4.5	Representative Native Gel Depicting Two Forms of PHM	...216
Figure 4.6	Dependence of Steady State PH Activity on Equiv of PHM Added at 25 °C	...217
Figure 4.7	4.2 K Mössbauer Spectrum of <sup>57</sup> Fe-Enriched PHH <sub>red</sub> :2M Generated by Reduction of PHH <sub>ox</sub> :2M with Excess Na <sub>2</sub> S <sub>2</sub> O <sub>4</sub> or with Excess NADH in the Presence of PHP	...218
Figure 4.8	4.2 K Mössbauer Spectrum of <sup>57</sup> Fe-Enriched PHH <sub>ox</sub> :2M Expressed from pGEM3Z/PHLMNOP and pGEM3Z/PHΔMΔP	...219
Figure 4.9	Overlay of 4.2 K Mössbauer Spectrum of <sup>57</sup> Fe-Enriched PHH <sub>ox</sub> :2M in 25 mM MOPS, pH 7.0, and 25 mM HEPES, pH 8.0	...221
Figure 4.10	4.2 K Mössbauer Spectra of Selected RFQ Samples Quenched During the 4 °C Reaction of PHH <sub>red</sub> :2M with O <sub>2</sub>	...223
Figure 4.11	Speciation Plot for the 4 °C Reaction of PHH <sub>red</sub> :2M with O <sub>2</sub>	...225
Figure 4.12	H <sub>2</sub> O <sub>2</sub> Assay Standard Curves	...227
Figure 4.13	H <sub>2</sub> O <sub>2</sub> Generation by PH in the Absence and Presence of Phenol	...228
Figure 4.14	Percent PH Activity Remaining as a Function of Time	...231

Figure 4.15	H <sub>2</sub> O <sub>2</sub> Consumption by PH in the Absence and Presence of PHM	...231
Figure 4.16	H <sub>2</sub> O <sub>2</sub> Generation by 2PHP and by PHH:6M:0.1P in the Absence of Phenol	...233
Figure 4.17	H <sub>2</sub> O <sub>2</sub> Consumption by 2PHP	...233
Figure 4.18	Overlay of 4.2 K Mössbauer Spectrum of <sup>57</sup> Fe-Enriched PHH <sub>ox</sub> :2M in the Absence and Presence of PHP	...236
Figure 4.19	H <sub>2</sub> O <sub>2</sub> Generation by PHH:2PHM and by PHH:0.1P in the Absence of Phenol	...237
Figure 4.20	Sequence Alignment of PHK and Related Gene Products	...241
Figure 4.21	Sequence Alignment of BMM Hydroxylase α-Subunits	...242
Figure 5.1	Solution NMR Structure of T4moC	...264
Figure 5.2	UV-visible Spectrum Monitoring Reaction of ToMOC <sub>ox</sub> with 20 Equiv DEANO	...269
Figure 5.3	Reductive Titration of ToMOC <sub>ox</sub> with Na <sub>2</sub> S <sub>2</sub> O <sub>4</sub>	...270
Figure 5.4	UV-visible Spectrum Monitoring Reaction of ToMOC <sub>ox</sub> with SNAP	...270
Figure 5.5	UV-visible Spectrum Monitoring Reaction of ToMOC <sub>ox</sub> with NO (g)	...271
Figure 5.6	UV-visible Spectrum Monitoring Reaction of ToMOC <sub>red</sub> with DEANO	...271
Figure 5.7	77 K EPR Spectrum of ToMOC <sub>red</sub>	...273
Figure 5.8	77 K EPR Spectra of Iron Dinitrosyl Species Formed in Reaction of ToMOC <sub>ox</sub> with DEANO, SNAP, and NO (g)	...273
Figure 5.9	77 K EPR Spectra of Iron Dinitrosyl Species Formation in Reaction of ToMOC <sub>red</sub> with DEANO	...274
Figure 5.10	77 K Mössbauer Spectrum of <sup>57</sup> Fe-enriched ToMOC <sub>ox</sub> and 230 K Mössbauer Spectrum of <sup>57</sup> Fe-enriched ToMOC <sub>red</sub>	...275
Figure 5.11	77 K Mössbauer Spectrum of Iron Dinitrosyl Species Formed from Reaction of <sup>57</sup> Fe-enriched ToMOC <sub>ox</sub> with DEANO	...276

Figure 5.12	$^{57}\text{Fe}$ partial vibrational density of states (PVDOS) NRVS spectra of $^{57}\text{Fe}$ -enriched $\text{ToMOC}_{\text{ox}}$ and $^{57}\text{Fe}$ -enriched $\text{ToMOC}_{\text{ox}}$ treated with DEANO	...278
Figure 5.13	Comparison of $^{57}\text{Fe}$ partial vibrational density of states (PVDOS) NRVS spectra of $^{57}\text{Fe}$ -enriched $\text{ToMOC}_{\text{ox}}$ treated with DEANO to Synthetic Iron Dinitrosyl Complexes	...279
Figure 5.14	UV-visible Spectrum of the Reaction of $\text{ToMO}_{\text{NO}}$ with $\text{Na}_2\text{S}_2\text{O}_4$	...280
Figure 5.15	Decay Kinetics of Reaction of $\text{ToMOC}_{\text{NO}}$ with $\text{Na}_2\text{S}_2\text{O}_4$	...281
Figure 5.16	77 K EPR Spectra of the Products of Reaction of $\text{ToMO}_{\text{NO}}$ with DEANO	...283
Figure 5.17	77 K Mössbauer spectrum of $\text{ToMOC}_{\text{NO}}$ Treated with $\text{Na}_2\text{S}_2\text{O}_4$	...283
Figure 5.18	Stopped-flow Absorbance Profiles for the Reaction of $\text{ToMOC}_{\text{ox}}$ with DEANO	...285
Figure 5.19	Plots of $k_{\text{obs}}$ versus $[\text{DEANO}]$ for the Reaction of $\text{ToMO}_{\text{ox}}$ with DEANO at 25 °C and pH 7.0	...285
Figure A.1	Designed NRVS RFQ Sample Cell Specifications	...300
Figure A.2	$^{57}\text{Fe}$ partial vibrational density of states (PVDOS) NRVS spectra of $^{57}\text{Fe}$ -enriched $\text{MMOH}_{\text{ox}}:2\text{B}$ and Intermediate Q	...302

## LIST OF EQUATIONS

Equation 2.1	Differential Solution to Model i of Scheme 2.2	...95
Equation 2.2	Differential Solution to Model ii of Scheme 2.2	...96
Equation 2.3	Differential Solution to Model iii of Scheme 2.3	...102
Equation 2.4	Differential Solution to Model iv of Scheme 2.3	...102
Equation 2.5	Eyring Equation	...105
Equation 2.6	Solution to Model i of Scheme 2.5	...116
Equation 2.7	Solution to Model ii of Scheme 2.5	...117
Equation 3.1	Mathematical Description of Class I and II Substrate Dependence Behavior	...164
Equation 3.2	Model of Class III Substrate Dependence Behavior	...170
Equation 3.3	Mathematical Description of Class III Substrate Dependence Behavior	...174



## Abbreviations

ACP	acyl carrier protein
AMO	alkene monooxygenase
AurF	amine oxidase
BDE	bond dissociation energy
BMM	bacterial multicomponent monooxygenase
DEANO	diethylamine NONOate
DFT	density functional theory
DmpH	<i>Pseudomonas sp.</i> CF600 phenol hydroxylase hydroxylase component
DmpK	<i>Pseudomonas sp.</i> CF600 phenol hydroxylase fourth component
DmpM	<i>Pseudomonas sp.</i> CF600 phenol hydroxylase regulatory component
DNIC	dinitrosyl iron complex
<i>E. coli</i>	<i>Escherichia coli</i>
ENDOR	electron nuclear double resonance
EPR	electron paramagnetic resonance
ESEEM	electron spin echo envelope modulation
ESI	electrospray ionization
EXAFS	extended x-ray absorption fine structure
hDOHH	human deoxyhypusine hydroxylase
HEPES	4-(2-hydroxyethyl)-1-piperazineethanesulfonic acid
Fd	ferredoxin
H <sub>peroxo</sub>	peroxodiiron(III) intermediate species of MMOH

HPLC	high-performance liquid chromatography
IP	ionization potential
IR	infrared
IPTG	isopropylthiogalactopyranoside
KSIE	kinetic solvent isotope effect
LB	Luria-Bertini
LUMO	lowest unoccupied molecular orbital
MCD	magnetic circular dichroism
MOPS	3-(N-morpholino)propanesulfonic acid
MMO	methane monooxygenase
MMOB	regulatory component of sMMO
MMOH	hydroxylase component of sMMO
MMOH <sub>ox</sub>	soluble methane monooxygenase hydroxylase component, oxidized diiron(III) form
MMOH <sub>red</sub>	soluble methane monooxygenase hydroxylase component, reduced diiron(II) form
MMOH <sub>mv</sub>	soluble methane monooxygenase hydroxylase component, mixed valent diiron(II/III) form
MMOR	reductase protein of sMMO
MMOR <sub>red</sub>	reductase protein of sMMO, reduced diiron(II/III) form
NADH	nicotinamide adenine dinucleotide, reduced form
NMR	nuclear magnetic resonance
NRVS	nuclear resonance vibrational spectroscopy

ORF	open reading frame
P*	transient H <sub>peroxo</sub> precursor
PAGE	polyacrylamide gel electrophoresis
PH	phenol hydroxylase
PHH	phenol hydroxylase hydroxylase component
PHH <sub>ox</sub>	phenol hydroxylase hydroxylase component, oxidized diiron(III) form
PHH <sub>red</sub>	phenol hydroxylase hydroxylase component, reduced diiron(II) form
PHK	phenol hydroxylase fourth component
PHM	phenol hydroxylase regulatory component
PHP	phenol hydroxylase reductase component
PVDOS	partial vibrational density of states
Q	di( $\mu$ -oxo)diiron(IV) intermediate species of MMOH
Q*	decay product of Q
QCR	ubiquinol-cytochrome <i>c</i> reductase
QM/MM	quantum mechanics/molecular mechanics
RBS	Roussin's black salt
RFQ	rapid freeze quench
RNR-R2	ribonucleotide reductase R2 subunit
RRE	Roussin's red ester
rRRE	reduced Roussin's red ester
SDS	sodium dodecyl sulfate
sMMO	soluble methane monooxygenase
SNAP	<i>S</i> -nitroso- <i>N</i> -acetyl-D,L-penicillamine

TCA	trichloroacetic acid
TCEP	<i>tris</i> (2-carboxyethyl)phosphine
T2MO	toluene 2-monooxygenase
T4mo	toluene 4-monooxygenase
T4moC	toluene 4-monooxygenase monooxygenase component C
T4moD	regulatory component of toluene 4-monooxygenase
TMO	four component alkene/arene monooxygenase
ToMO	toluene/ <i>o</i> -xylene monooxygenase
ToMOC	toluene/ <i>o</i> -xylene monooxygenase component C
ToMOD	toluene/ <i>o</i> -xylene monooxygenase regulatory component
ToMOH	toluene/ <i>o</i> -xylene monooxygenase hydroxylase component
ToMOH <sub>peroxo</sub>	peroxodiiron(III) intermediate species of ToMOH
ToMOH <sub>red</sub>	toluene/ <i>o</i> -xylene hydroxylase component, reduced diiron(II) form
X	mixed valent Fe(III)/Fe(IV) intermediate species of RNR-R2

## **Chapter 1**

### **Introduction: The Reactivity of Bacterial Multicomponent Monooxygenases**

## INTRODUCTION

Carboxylate-bridged diiron proteins play diverse roles in biology, including O<sub>2</sub> transport in hemerythrin, iron storage in ferritin, peroxide scavenging in rubrerythrin, fatty acid desaturation in stearyl-acyl carrier protein (ACP)  $\Delta^9$ -desaturase, radical generation in ribonucleotide reductase R2 subunit (RNR-R2), and hydrocarbon oxidation in bacterial multicomponent monooxygenases (BMMs) (1-5). In these proteins, the diiron center is housed within a four-helix bundle, a preferred biological scaffold for O<sub>2</sub> binding and reductive activation. BMMs constitute a subfamily of carboxylate-bridged diiron centers that enable their host organisms to utilize small hydrocarbons as a sole source of carbon and energy. Proteins belonging to the BMM family are subdivided into soluble methane monooxygenases (sMMOs), phenol hydroxylases (PHs), alkene monooxygenases (AMOs), and four-component alkene/arene monooxygenases (TMOs) based on catalytic abilities and phylogenetic analyses (Figure 1.1) (6, 7).

BMMs are remarkable enzymes that orchestrate a series of electron transfer and substrate activation events to insert an oxygen atom into a C–H bond. The ability of these protein systems to generate potent oxidizing species without damaging their active sites or consuming electrons in a futile manner depends on the dynamic involvement of three or more protein components: a hydroxylase that houses the catalytic diiron center at the site of hydrocarbon oxidation, a reductase that accepts electrons from NADH and shuttles them through its flavin (FAD) and [2Fe-2S] cluster cofactors to the diiron site of the hydroxylase, and a regulatory protein that couples electron consumption to hydrocarbon oxidation (3, 4, 8). In the four component alkene/arene monooxygenases, an additional

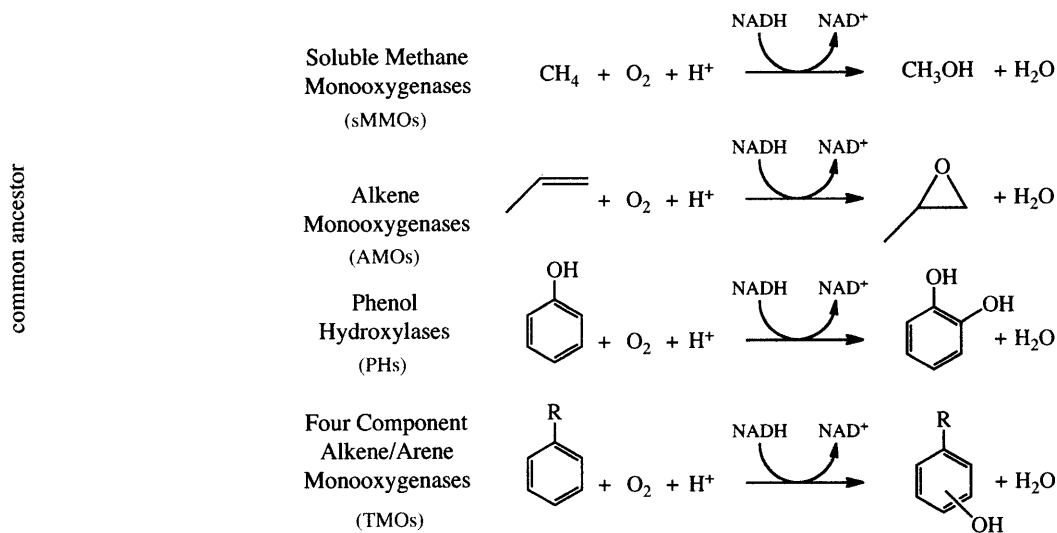


**Figure 1.1.** BMM Phylogenetic tree. The soluble methane monooxygenase, alkene monooxygenase, phenol hydroxylase, and four component alkene/arene monooxygenase subfamilies and their catalytic reactions are depicted.

Rieske protein is required for electron transfer (3). Careful regulation of protein interactions allows for the timely entry of four substrates into the hydroxylase active sites: hydrocarbons,  $\text{O}_2$ , electrons, and protons. Although the functions of the three protein components have been studied in detail for sMMO, the dynamics of component interactions during the reductive and oxidative phases of the catalytic cycle are not well understood.

In this chapter we review the structural features of BMMs to provide a framework by which to understand catalysis. Component interactions and functions are also detailed. A discussion of reactivity at the hydroxylase diiron centers follows. The reductive activation of  $\text{O}_2$  and the mechanisms of hydrocarbon oxidation by the oxygenated iron species that form during this process are discussed in detail.

## A. BMM Structures and Component Interactions

Structural characterization of BMM proteins, particularly the hydroxylases, by crystallographic and spectroscopic methods has enriched our understanding of catalysis by these systems. These studies have provided a framework for interpreting the nature of transient intermediates that form at the dinuclear iron center during O<sub>2</sub> activation, provided insight into mechanisms by which substrates and products access and exit the catalytic active site, and helped to calibrate theoretical studies of these proteins. In the past four years, two structures of hydroxylase-regulatory protein complexes have become available, providing insight into the nature of component interactions in these systems. With this knowledge in hand, we have begun to move beyond static snapshots of the catalytic cycle and to an understanding of the protein dynamics that facilitate hydrocarbon oxidation. The structural and functional aspects of the individual protein components are considered in the discussion that follows.

*Hydroxylases.* X-ray crystal structures of several BMM hydroxylases, including oxidized (9-11), reduced (12), mixed-valent (12), apo- (13), and manganese-reconstituted (13) methane monooxygenase hydroxylase (MMOH), oxidized (14) and manganese-reconstituted (15) toluene/*o*-xylene monooxygenase hydroxylase (ToMOH), and oxidized toluene 4-monooxygenase hydroxylase (T4moH) (16) have been reported. All BMM hydroxylase proteins are characterized by an  $\alpha_2\beta_2\gamma_2$  dimer architecture that does not exhibit global redox- or metal-dependent conformational changes. The subunits are arranged as a dimer of  $\alpha\beta\gamma$  protomers related by a virtual or crystallographic two-fold



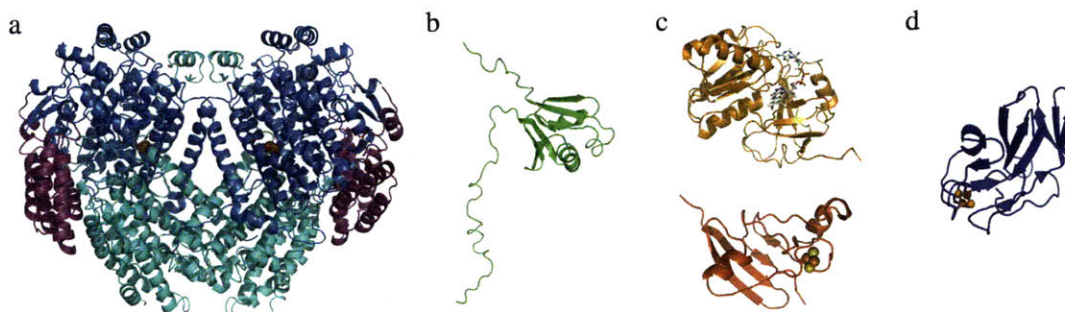


**Figure 1.2.** Representative BMM structures. (a) Hydroxylase component of sMMO, MMOH, showing the  $\alpha$ -,  $\beta$ -, and  $\gamma$ - subunits in blue, cyan, and purple, respectively (PDB ID 1MTY); (b) Regulatory component of sMMO, MMOB (PDB ID 1CKV); (c) FAD (orange) and ferredoxin (red) domains of the reductase component of sMMO, MMOR (PDB ID 1TVC and 1JQ4, respectively); (d) Rieske component of toluene 4-monooxygenase, T4moC (PDB 1SJG). Images were generated in PyMOL (DeLano Scientific LLC).

symmetry axis (Figure 1.2a). Contacts between the two  $\alpha$ - and two  $\beta$ -subunits form the dimer interface and create a large canyon in the middle of the protein. This canyon is the docking site for the regulatory protein (16, 17) and possibly the reductase/Rieske component (4). The catalytic diiron site is housed within a four-helix bundle composed of helices B, C, E, and F of the  $\alpha$ -subunit. Two of these helices, E and F, are located on the surface of the protein and form a ridge on the canyon  $\sim 12$  Å above the active site (4). With the exception of *Pseudomonas* sp. OX1 phenol hydroxylase hydroxylase (PHH), which contains a tetrahedrally coordinated Zn(II) ion in the  $\alpha$ -subunit (17), the active site iron atoms are the only metals in the BMM hydroxylases.

*Hydroxylase Diiron Centers.* The BMM active site diiron center is coordinated by two histidine and four glutamate ligands (Figure 1.3). Helices B and E each contribute a glutamate to the diiron center and helices C and E each donate a glutamate and a histidine

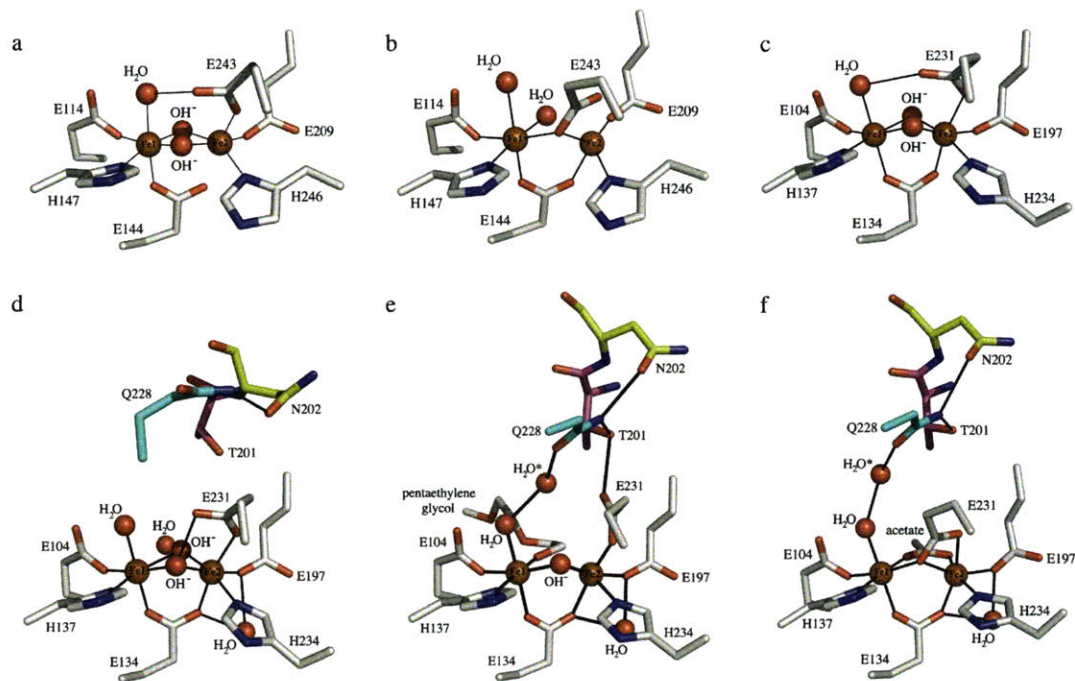


**Figure 1.3.** BMM active site structures. (a) Oxidized hydroxylase component of sMMO, MMOH<sub>ox</sub> (PDB ID 1MTY); (b) Reduced hydroxylase component of sMMO, MMOH<sub>red</sub> (PDB ID 1FYZ); (c) Oxidized hydroxylase component of ToMO, ToMOH<sub>ox</sub> (PDB ID 2INC); (d) Oxidized hydroxylase component of T4MO, T4moH<sub>ox</sub> (PDB ID 3DHG). (e) Oxidized hydroxylase-regulatory protein complex of T4MO, T4moH<sub>ox</sub>:2D (PDB ID 3DHH); (f) Reduced hydroxylase-regulatory protein complex of T4MO, T4moH<sub>red</sub>:2D (PDB ID 3DHI). Relevant atoms or side chains are depicted in stick format or as spheres and are colored by atom type (carbon, gray; oxygen, red; nitrogen, blue; iron, orange). Carbon atoms of T4mo residues Q228, T210, and N202 are shown in cyan, purple, and yellow, respectively. The ordered active site water molecule in T4moH that binds as a consequence of ToMOD association is starred in e and f. Images were generated in PyMOL (DeLano Scientific LLC).

residue from an EXXH motif. Solvent-derived water and hydroxide ligands complete the pseudo-octahedral iron coordination spheres (Figure 1.3). In the enzyme resting state, two hydroxide or oxide ligands bridge the diiron center and the iron atoms are separated by 3.0–3.4 Å (4). A terminal water molecule is coordinated to Fe1. Upon reduction of the diiron center, the two bridging solvent molecules are extruded and E243/E231 (sMMO/ToMO and T4mo), which is bound only to Fe1 in the oxidized hydroxylase,

assumes a bridging position while remaining chelated to Fe2 (Figure 1.3b). As a consequence, an open coordination site that faces the active site pocket is formed on Fe2 and the iron-iron distance is increased to  $\sim 3.4 \text{ \AA}$  (4).

In addition to crystallographic characterization of the active sites, the structural features of the oxidized diiron(III), reduced diiron(II), and mixed-valent diiron(II/III) centers of MMOH, ToMOH, T4moH, PHH, and toluene 2-monooxygenase hydroxylase (T2MOH) have been investigated by spectroscopic methods including EXAFS (18-22), EPR (18, 23-30), ENDOR/ESEEM (25, 31-39), MCD (40-43), and Mössbauer (18, 25, 27, 44, 45) spectroscopy. The high-spin Fe(III) ions of the oxidized hydroxylases are antiferromagnetically coupled to form EPR-silent,  $S = 0$  ground states (18, 25, 27, 30, 44, 46-48). Two hydroxide bridges mediate the antiferromagnetic spin-exchange between the Fe(III) ions in  $\text{MMOH}_{\text{ox}}$ ,  $\text{ToMOH}_{\text{ox}}$ , and  $\text{T4moH}_{\text{ox}}$  (18). In the reduced diiron(II) state, the high-spin Fe(II) atoms are weakly ferromagnetically coupled and the resulting  $S = 2$  integer spin system has a low energy Kramer's doublet that is split in zero applied field to give rise to a characteristic EPR signal at  $g = 16$  (18, 25, 27, 29, 35, 41, 46, 48-50). MCD spectra are consistent with both Fe(II) ions having five-coordinate square pyramidal geometries (41-43).

Crystallographic (12) and spectroscopic studies of the mixed-valent diiron(II/III) form of MMOH,  $\text{MMOH}_{\text{mv}}$ , have also been performed. Antiferromagnetic coupling between the high spin Fe(II) and Fe(III) sites results in a  $S = \frac{1}{2}$  ground state that gives rise to an rhombic EPR signal with  $g < 2$  (23-25, 27, 30, 44). A similar spectrum occurs in the mixed-valent form of T2moH (50). In contrast, samples of ToMOH (49) or T4moH (48)

treated with a half an equivalent of electrons resulted in a mixture of oxidized and reduced protein rather than a mixed-valent species.

*Substrate Ingress and Product Egress.* Substrate delivery to and product egress from the active site diiron center have also been probed using structural and spectroscopic techniques. Crystallographic investigations of MMOH, ToMOH, PHH, and T4moH all revealed the presence of several adjacent hydrophobic cavities in the  $\alpha$ -subunit that delineate a pathway from the exterior of the protein to the active site (11, 12, 14, 16, 17). Crystals of MMOH (51) and PHH (52) pressurized with xenon gas, an electron-rich O<sub>2</sub> and CH<sub>4</sub> surrogate, contained ordered Xe atoms almost exclusively in these cavities, revealing a route by which O<sub>2</sub> and CH<sub>4</sub> access the active site. Crystal structures of MMOH and ToMOH containing bound product and substrate analogues also support the notion that these cavities provide a pathway for small molecule ingress and egress (14, 51, 53). Protein breathing motions could allow gaseous and small molecule substrates to traverse the cavities, which are gated by hydrophobic residues.

The structures of ToMOH and T4moH also revealed a large solvent-filled channel of ~30–35 Å in length and ~6–10 Å in diameter extending from the diiron center to the protein exterior (14, 16). Several ordered water molecules (14) or buffer components such as hexaethylene glycol (15) line this channel, which is composed of both hydrophilic and hydrophobic residues. Crystals of ToMOH soaked with the product analogue 4-bromophenol revealed that aromatic small molecules also bind in this region, suggesting that this channel might be a major route of small molecule transport. Binding of T4moD to T4moH blocks this route (16), however, indicating that the channel might

not function in the natural context of the enzyme or that substrate accesses the active site prior to association of the regulatory protein.

An alternative entrance to the diiron center is a pore formed between helices E and F of the four-helix bundle that ligates the diiron center (12, 17, 52, 53). This pore represents the shortest and most direct route to the active site. Only a single residue, N214/N202/N204 (sMMO/ToMO/PH) blocks access to the diiron center, as opposed to several residues that link the hydrophobic cavities. The pore diameter is  $\sim 6$  Å, just large enough to accommodate aromatic substrates, but constricts to  $\sim 2.8$  Å upon binding of the regulatory protein (17). Hydrophilic residues line the pore, which has been proposed as a pathway of  $\text{H}_3\text{O}^+$  translocation (52).

The effects of substrate and product binding to the diiron centers of MMOH have been directly investigated by EPR (24), ENDOR (32, 36, 39), and MCD (42) spectroscopy in the reduced, oxidized, and mixed-valent oxidation states. Substrate binding perturbs only the geometry of Fe1. Product alcohols such as methanol and phenol bind to the diiron center of  $\text{MMOH}_{\text{ox}}$  and  $\text{MMOH}_{\text{mv}}$  (24, 36) but do not seem to interact directly with  $\text{MMOH}_{\text{red}}$  (42). These observations suggest that product is released from the active site upon reduction of the diiron center, facilitating substrate binding in the next round of catalysis. Addition of  $\text{CH}_4$  does not alter the spectroscopic parameters of  $\text{MMOH}_{\text{ox}}$  (24).

*Regulatory Proteins.* Every BMM requires a small 10–16 kDa regulatory protein for efficient catalysis (3, 4). These cofactorless proteins accelerate hydroxylase-mediated oxidation reactions by 30–150 fold in a complex manner that is not yet fully understood (4). Insights into the mechanism(s) by which these small proteins control catalysis have

been provided by a number of biochemical and structural investigations. Most of these studies have focused on the regulatory component of sMMO, MMOB.

The structures of the regulatory proteins of sMMO (54, 55), T4mo (56, 57), and *Pseudomonas* sp. CF600 phenol hydroxylase (Dmp) (58) have been probed by NMR spectroscopy and/or X-ray crystallography. Despite low sequence homology, they have a similar fold with three  $\alpha$ -helices flanked by two nearly perpendicular  $\beta$ -sheets (Figure 1.2b). The protein structures are relatively compact except for that of MMOB, which has a long, disordered N-terminal tail consisting of 35 amino acids (54, 55). Truncation or mutation of this tail completely inactivates the enzyme (59-61).

Mutagenesis and spectroscopic studies indicate that MMOB affects the O<sub>2</sub> activation and hydrocarbon reaction pathways of the hydroxylases (62-66). EPR spectroscopic experiments probing the decay rate of the characteristic  $g = 16$  MMOH<sub>red</sub> signal upon reaction with O<sub>2</sub> revealed that the reaction is 1000-fold slower in the absence of the regulatory protein (64). As a consequence, the oxygenated iron intermediates that form during reaction with the complete system do not accumulate (45, 64). Similar effects occur in ToMO (47).

Mutation of one, two, or four surface residues of MMOB predicted to interact with the hydroxylase caused dramatic changes in the kinetic rate constants (65, 67) and Eyring parameters (66) associated with formation and decay of the oxygenated iron species H<sub>peroxo</sub> and Q. These mutations also affected the rate at which methane-oxidizing intermediate Q oxidizes substrates (65) and suppressed the hydrogen quantum mechanical tunneling component of the methane hydroxylation reaction (63, 66, 68). The

kinetic isotope effect (KIE) for oxidation of methane was decreased from ~50 to 6 for a quadruple MMOB mutant, suggesting complete loss of tunneling (63).

MMOB has also been implicated in controlling substrate access to the MMOH active site by forming a size-selective “molecule sieve” that gates substrate and solvent ingress (62, 65, 68). Mutation of two or four MMOB residues led to enhanced reactivity of intermediate Q with larger substrates such as nitrobenzene and furan (62, 65). KIEs for several large substrates were also unmasked by the mutations (62, 65). The regiospecificity of hydroxylase-catalyzed reactions is also affected by MMOB (28). Similar effects on product type occur for the T4mo regulatory protein, T4moD (69).

MMOB regulates electron transfer between the hydroxylase and reductase proteins. Early studies demonstrated that MMOB reduces the redox potential of  $\text{MMOH}_{\text{ox}}$  (26, 70, 71). Stopped-flow kinetic studies showed that the presence of MMOB altered the reaction pathway of intermolecular electron transfer from reduced reductase ( $\text{MMOR}_{\text{red}}$ ) to oxidized hydroxylase when the former was mixed rapidly with a pre-equilibrated solution of  $\text{MMOH}_{\text{ox}}$  and MMOB (72). As a consequence, the electron transfer rates were severely retarded by the presence of the regulatory protein. In a separate study, MMOB was found to *enhance* the rate of electron transfer in reactions of the preformed MMOH-MMOR complex with NADH (73, 74). These two seemingly contradictory effects might be a consequence of a slow isomerization of the initial MMOH-MMOB-MMOR ternary complex that is required for rapid electron transfer (72). In the former study, these hysteresis effects were rate-determining. In the latter, the pre-formed ternary complex promoted rapid and rate-determining intermolecular electron transfer.

An additional role of the regulatory protein might be to prevent untimely electron injection into the hydroxylase to quench oxygenated intermediates in the catalytic cycle prior to substrate oxidation (16, 17, 72, 75). Recent X-ray crystal structures of T4mo and PH hydroxylase-regulatory protein complexes revealed that the regulatory protein binds to the hydroxylase at a region predicted to be the docking site of the component that delivers electrons to the diiron center (16, 17). MMOB and MMOR bind to MMOH noncompetitively at distinct interaction sites, however, suggesting a more complicated mechanism of inhibition (73, 74).

Insights into the MMOB-MMOH structure have been provided by NMR spectroscopy (55). Line broadening of several conserved MMOB residues in the presence of the paramagnetic MMOH enzyme suggested that the one face of this small protein forms the docking interface. Residues within the N-terminal tail also shifted and broadened upon addition of MMOH. A docking model based on results from these NMR studies predicted that MMOB binds the hydroxylase  $\alpha$ -subunits in the canyon region at the MMOH dimer interface (55). Chemical crosslinking studies provided further evidence that MMOB binds to the hydroxylase  $\alpha$ -subunit (26). Stopped-flow kinetic experiments monitoring intensity changes in intrinsic tryptophan (73) or surface-appended chemical probe (67) fluorescence upon rapid mixing of MMOB and MMOH indicated that the interaction kinetics involve rapid association followed by a slow conformational change.

The effects of regulatory binding to the hydroxylase at the diiron center have also been probed directly by spectroscopic methods in the sMMO, ToMO, and T4mo systems. An EXAFS analysis showed that binding of the ToMO regulatory protein, ToMOD, to



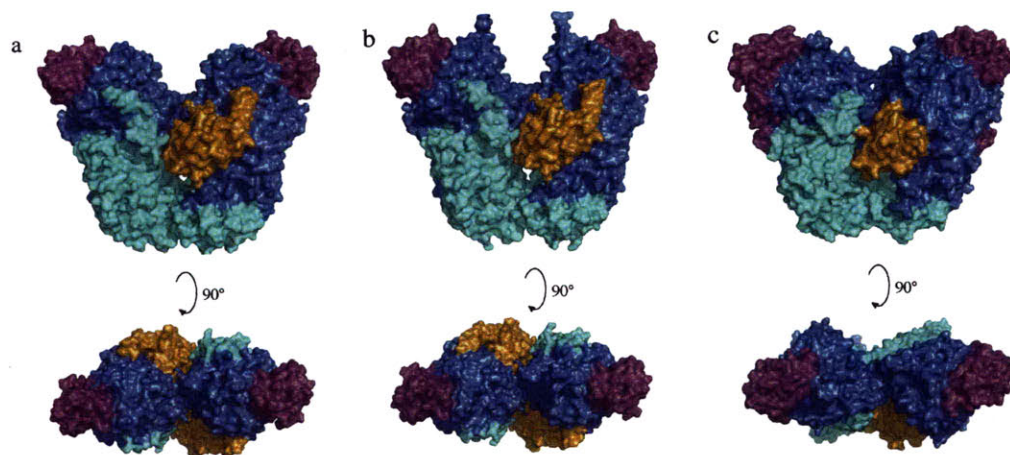


**Figure 1.4.** Surface renderings of the T4moH<sub>ox</sub>:2D (a), T4moH<sub>red</sub>:2D (b), and PHH:M (c) complexes. Hydroxylase  $\alpha$ -,  $\beta$ -, and  $\gamma$ -subunits are depicted in blue, cyan, and purple, respectively. Regulatory proteins are shown in orange. Images were generated in PyMOL (DeLano Scientific LLC) using PDB ID codes 3DHH (T4moH<sub>ox</sub>:2D), 3DHI (T4moH<sub>red</sub>:2D), and 2INP (PHH:M).

ToMOH<sub>red</sub> affects the first coordination shell of the diiron center and slightly decreases the Fe–Fe distance (20). MCD studies of T4mo indicated that association of T4moD with T4moH alters the geometry of Fe2, reorienting a redox active orbital of this atom. As a consequence, O<sub>2</sub> binds in a bridged structure and efficient two-electron inner sphere electron transfer occurs to form a peroxodiiron(III) intermediate (43). MMOB also affects the geometry of Fe2 in a similar manner (40, 41).

The X-ray crystal structures of PH hydroxylase (PHH) in complex with its associated regulatory protein PHM (17)<sup>1</sup> and oxidized and reduced T4moH bound to T4moD (16)

<sup>1</sup>Crystals of the PHH:PHM complex were prepared in the oxidized diiron(III) state; however, the structural features of the diiron center best resemble those of mixed valent MMOH, suggesting an Fe(II)/Fe(III) oxidation state. Photoreduction in the X-ray beam may have produced these effects. In these structures, PHM was only present at 40-50% occupancy. As a result, the diiron center is largely disordered and there is no evidence for bridging ligands.

have recently been determined. In both systems, the regulatory protein binds in the canyon region formed at the hydroxylase dimer interface. Although two molecules of T4moD interact with the  $(\alpha\beta\gamma)_2$  T4moH dimer in both the oxidized and reduced states, only one PHM unit binds to the PHH dimer (Figure 1.4). The reason for this difference is unknown.

Upon binding to the hydroxylase, the overall topology of the regulatory protein is maintained (16, 17). The global fold of the hydroxylase is also preserved. Only local structural changes occur in helix E and at the diiron center. As a consequence of regulatory protein binding, side chains of several residues from helix E including N202/204 (T4mo/PH) and T201/203 (T4mo/PH), are significantly repositioned (Figure 1.3d and Figure 1.3e). The side chain of helix F amino acid Q228/230 (T4mo/PH) swings inward toward the diiron site and engages in a hydrogen bonding network that extends from the diiron center to the protein surface where the regulatory protein binds. This network includes the newly positioned N202/204 (T4mo/PH) and T201/203 (T4mo/PH) residues (Figure 1.3e and Figure 1.3f). At the diiron center, the shifting carboxylate of the Fe2 ligand E231/E233/E243 (T4mo/PH/sMMO) rotates away from the diiron center and hydrogen bonds to T201 (Figure 1.3e). A water molecule present in the active site participates in the hydrogen-bonding network (16) might play an important role in proton translocation during the reductive and/or O<sub>2</sub> activation phases of catalysis (Figures 1.2e and 1.2f). Upon reduction of the T4moH:2B complex, the carboxyl group of E231 rotates inward to occupy the bridging position between the diiron atoms, as occurs in the absence of the regulatory protein for MMOH<sub>red</sub> (12) and Mn(II)-ToMOH (15). This shift does not disrupt the hydrogen-bonding network.

*Reductases/Rieske Proteins and Electron Transfer.* Transfer of two electrons to the hydroxylase diiron center is necessary to initiate catalysis in all BMMs. These electrons, provided by NADH,<sup>2</sup> are shuttled through a reductase protein containing redox-active FAD and [2Fe-2S] cofactors (44, 48, 76, 77). In the four-component alkene/arene monooxygenases, an additional [2Fe-2S] Rieske protein is involved in the electron transfer process, acting as a conduit between the reductase and the hydroxylase (48, 76, 78).

No structure of a full-length BMM reductase protein is available to date. The truncated FAD (79) and ferredoxin (Fd) (80) domains of MMOR have been structurally characterized by NMR spectroscopy, however. The FAD domain has two subsections: a FAD-binding portion consisting of a six-stranded  $\beta$ -barrel and one  $\alpha$ -helix, and a NAD-binding region formed by a five-stranded parallel  $\beta$ -sheet and four  $\alpha$ -helices. The FAD cofactor interacts with the protein at the interface of these two domains and adopts an extended conformation (79). The MMOR Fd domain has six  $\beta$ -strands arranged as two sheets and three  $\alpha$ -helices. The tetracysteine-coordinated [2Fe-2S] cluster at the surface of the domain is largely solvent-exposed (80).

Reduction potentials of the FAD and [2Fe-2S] cofactors of MMOR have been determined by EPR titrations in the presence of indicator dyes to be -176 mV ( $\text{FAD}_{\text{ox/sq}}$ ); -266 mV ( $\text{FAD}_{\text{sq/hq}}$ ); and -209 mV ([2Fe-2S]), where  $\text{FAD}_{\text{ox}}$ ,  $\text{FAD}_{\text{sq}}$ , and  $\text{FAD}_{\text{hq}}$  are the oxidized, one-electron reduced semiquinone, and two-electron reduced hydroquinone forms of FAD (81). The presence of MMOH and/or MMOB do not alter these values

---

<sup>2</sup>Some BMM systems can also use NADPH as a reductant. Reactions with NADPH are typically slower and binding constants for association with the reductases are generally weaker, however. Colby, J., Stirling, D. I., and Dalton, H. (1977) *Biochem. J.* 165, 395-402; Newman, L. M., and Wackett, L. P. (1995) *Biochemistry* 34, 14066-14076.

(81). MMOR increases the reduction potential for transfer of the second electron into the MMOH diiron center, providing a driving force for electron transfer and favoring transfer of two rather than one electron (75). Stopped-flow kinetic studies monitoring the reaction of  $\text{MMOR}_{\text{red}}$  with  $\text{MMOH}_{\text{ox}}$  revealed that intermolecular electron transfer proceeds by four distinct kinetic phases corresponding to electron transfer to the two dinuclear centers. Several intermediates have been characterized along this pathway (72, 73, 81).

In addition to providing a source of electrons for catalysis, MMOR affects the  $\text{O}_2$  activation and substrate reactivity phases of catalysis by sMMO. EPR experiments probing the decay rate of the characteristic  $g = 16$   $\text{MMOH}_{\text{red}}$  signal upon exposure to  $\text{O}_2$  in the presence of the regulatory protein revealed that the reaction is 20-fold slower in the presence of the reductase (75). This effect may be caused by MMOR-induced conformational changes in MMOH (72, 82). Such conformational changes are expected to occur far from the active site, because MMOR does not seem to affect the electronic or geometric structures of the hydroxylase diiron centers (24).

In the four component alkene/arene monooxygenase systems a Rieske protein delivers electrons to the hydroxylase. The structure of the Rieske protein of the T4mo system, T4moC, has been determined by NMR spectroscopy (83). The structure has ten  $\beta$ -strands arranged in a three antiparallel  $\beta$ -sheet topology. The Rieske center is housed on a solvent-exposed loop extending from one of these sheets. The  $[\text{2Fe-2S}]$  cluster is coordinated by two cysteine and two histidine residues and has a reduction potential of -173 mV, a value consistent with those measured for other Rieske proteins (78).

*A Fourth BMM Component in sMMO and PH.* In addition to the hydroxylase, regulatory protein, and reductase, the sMMO operon features an additional open reading

frame termed *orfY* that is located between the *mmoZ* and *mmoC* genes encoding the MMOH  $\gamma$ -subunit and MMOR (84). Northern blot analysis of total RNA from *M. capsulatus* (Bath) revealed a 5.5-kb fragment containing all six ORFs encoded in the sMMO operon, suggesting that the gene product of *orfY*, hereafter referred to as MMOD, may be expressed in vivo (85, 86). Sequence comparisons of putative MMOD-like proteins from different methanotrophs demonstrated low sequence homology (19.4%), although a central conserved region with 44.4% identity was located (84). Expression and characterization of MMOD revealed that the 12 kDa protein does not bind any cofactors, associates with MMOH, and inhibits steady-state activity but does not interact with MMOR or MMOB (84). Features indicative of oxo-bridged diiron(III) complexes appeared in the optical spectrum of  $\text{MMOH}_{\text{ox}}$  when MMOD was titrated into a solution of the hydroxylase. MMOD may function as a chaperone to assist or ameliorate damaged active sites (84). Fe K-edge and EXAFS analysis revealed negligible changes in the electronic and geometric structures of the diiron sites of  $\text{MMOH}_{\text{ox}}$  upon addition of MMOD, however (21). The true function of MMOD remains to be established.

As in sMMO, an additional ORF was identified at the 5' end of the BMM locus in the three-component phenol hydroxylases (87) encoding a protein having low sequence similarity to MMOD. A *Pseudomonas* strain transformed with a plasmid encoding the BMM operon from *Pseudomonas* sp. CF600, *dmp*, and the genes of the enzymes necessary to catabolize catechol could grow on phenol only if this identified ORF, *dmpK*, was also present (88). The gene product of *dmpK*, DmpK, is not essential for hydroxylase activity in vitro, although protein expressed recombinantly from a plasmid harboring *dmpK* in addition to the genes encoding the hydroxylase polypeptides yielded material

that was thirty times more active than that expressed from a vector lacking *dmpK* (89). Purified DmpK inhibits DmpH, its associated hydroxylase and was suggested to play a role in assembly of the diiron center because addition of Fe(II) to inactive DmpH yielded active protein only in its presence (89). Recent studies of the analogue of DmpK from *Pseudomonas* sp. OX1 phenol hydroxylase, PHK, suggest that it may assist in loading zinc into its associated hydroxylase, however (see Chapter 4).

*Outlook and Future Directions.* Structural and biochemical studies have provided insight into the functions of the BMM hydroxylases, regulatory proteins, reductases/Rieske proteins. The identification of a fourth component in the sMMO and three-component phenol hydroxylase systems has added an additional level of complexity. In the last ten years, a basic understanding of BMM protein dynamics has been developed from static structural information. Further studies monitoring the protein complexation states as a function of catalysis will help to delineate these roles.

## **B. Dioxygen Activation in BMMs and Related Carboxylate-Bridged Diiron Proteins**

An important step in the catalytic cycle of BMMs and structurally related carboxylate-bridged diiron proteins is reductive activation of O<sub>2</sub> by the hydroxylase diiron(II) center. Because transient intermediates that result from these reactions are responsible for substrate oxidation, much effort has expended to discern the mechanisms by which O<sub>2</sub> is activated in these enzymes. Kinetic and spectroscopic studies of the BMMs and comparisons to parallel work on synthetic diiron model complexes have enhanced our understanding of how Nature activates kinetically inert molecular oxygen to oxidize difficult substrates such as methane.

The reaction of BMM diiron(II) clusters with O<sub>2</sub> is typically rapid (45, 47, 90). Studies probing the O<sub>2</sub>-promoted decay of *M. trichosporium* OB3b MMOH<sub>red</sub> by EPR spectroscopy demonstrated a process independent of pH and O<sub>2</sub> concentration between 0.3 and 0.7 mM. The latter observation suggests that a discrete, irreversible O<sub>2</sub> binding event precedes the bimolecular reaction (90).<sup>3</sup> Oxygen kinetic isotope effect studies of the *M. capsulatus* (Bath) system do not support the notion that an enzyme-dioxygen Michaelis complex forms irreversibly, however (91). These seemingly contradictory studies can be reconciled if O<sub>2</sub> binding involves a reversible pre-equilibrium followed by an irreversible chemical reaction and if the binding constant ( $K_d$ ) is much lower than the concentrations of O<sub>2</sub> employed in the EPR experiments (91). For comparison, the covalent binding of O<sub>2</sub> to the diiron center of deoxyhemerythrin has a  $K_d$  of 15-30 μM (92).

*Peroxodiiron(III) Species Formed at Carboxylate-Bridged Diiron Centers.* Computational studies of MMO suggest that the first intermediate resulting from reaction of MMOH<sub>red</sub> with O<sub>2</sub> is a mixed-valent diiron(II/III) superoxide species (93, 94). An oxygen kinetic isotope effect (KIE) study of sMMO oxidation of CH<sub>3</sub>CN returned a KIE of 1.016, a value consistent with one-electron reduction of O<sub>2</sub> to superoxide as the first irreversible step in the reaction pathway, although other possibilities could not be definitively ruled out (91). An Fe(II)/Fe(III) superoxide unit has never been directly

---

<sup>3</sup>Studies in progress in our laboratory show that the formation rate constants describing a peroxodiiron(III) intermediate generated during reaction of the T201S ToMOH<sub>red</sub> variant with O<sub>2</sub> depends on [O<sub>2</sub>]. These results provide the first evidence that O<sub>2</sub> can affect H<sub>red</sub> decay and the events that follow. Song, W. J., and Lippard, S. J. *Manuscript in Preparation.*

observed in a carboxylate-bridged diiron protein in which the O<sub>2</sub>-activating species is diiron(II), however.<sup>4</sup>

The first spectroscopically-observed intermediate in reactions of the diiron(II) forms of BMMs with O<sub>2</sub> is an antiferromagnetically-coupled peroxodiiron(III) species. This unit is common to most carboxylate-bridged diiron proteins and has been characterized in sMMO (45, 95, 96), ToMOH (47, 97), a mutant form of ToMOH (98), RNR-R2 (99, 100), a variant of RNR-R2 (101-104), stearyl ACP  $\Delta^9$  desaturase (105, 106), frog M ferritin (107-109), human deoxyhypusine hydroxylase (hDOHH) (110), and amine oxidase (AurF) (111). Many of these peroxo intermediates display a peroxo-to-Fe(III) charge transfer band between 650 to 750 nm having  $\epsilon < 3000 \text{ M}^{-1} \text{ cm}^{-1}$ . Mössbauer parameters of these species typically range between 0.62 and 0.66 mm/s for the isomer shift and the quadrupole splitting parameters are larger than 1.00 mm/s (Table 1.1). The peroxo intermediates from a mutant form of RNR-R2 (103, 104), ferritin (108),  $\Delta^9$ -desaturase (106), and hDOHH (110) have also been probed by resonance Raman spectroscopy, which indicates a  $\mu$ -1,2 peroxide binding mode. A  $\mu$ -1,2-peroxide coordination geometry was also suggested from the X-ray crystal structure of the T4moH:2D complex soaked with H<sub>2</sub>O<sub>2</sub> (112).<sup>5</sup>

---

<sup>4</sup>Recent biochemical studies revealed that *myo*-inositol oxygenase, which activates O<sub>2</sub> at a mixed-valent diiron(II/III) center, utilizes a superoxodiiron(III) unit to oxidize *myo*-inositol. Xang, G., Diao, Y., Hoffart, L. M., Barr, E. W., Prabhu, K. S., Arner, R. J., Reddy, C. C., Krebs, C., and Bollinger Jr., J. M. (2006) *Proc. Natl. Acad. Sci. USA* 103, 6130-6135. Studies of a dendrimer-appended carboxylate-rich diiron model complex showed that a mixed-valent diiron(II/III) superoxide formed during reaction of the analogous diiron(II) complex with O<sub>2</sub> is responsible for oxidation of several external substrates. Zhao, M., Helms, B., Slonkina, E., Friedle, S., Lee, D., DuBois, J., Hedman, B., Hodgson, K. O., Fréchet, J. M. J., and Lippard, S. J. (2008) *J. Am. Chem. Soc.* 130, 4352-4363.

<sup>5</sup>These conclusions were based on modeling the active site  $2F_o - F_c$  difference density as H<sub>2</sub>O<sub>2</sub> by employing an O–O bond distance restraint of 1.5 Å; using this approach, the Fe–O bond distances were 2.2 and 2.4 Å, which are too long to assign the unit as a peroxodiiron(III) species. Attempts to release the restraint and refine the structure resulted in an increased O–O bond distance of 1.8 Å and decreased Fe–O bond distances of ~2.1 Å, neither of which support the peroxide formulation. Furthermore, the putative



Two peroxodiiron(III) intermediates are sequentially generated in MMOH, P\* and H<sub>peroxo</sub> (113). These clusters both have optical bands centered around 420 nm and 720 nm (96, 113). Their structures have been largely elusive due to the inability to obtain resonance Raman spectra, however. Comparison to a structurally characterized model complex that displays almost identical Mössbauer parameters to P\*, [Fe<sub>2</sub>(μ-1,2-O<sub>2</sub>)(μ-O<sub>2</sub>CCH<sub>2</sub>Ph)<sub>2</sub>{HB(pz')<sub>3</sub>}<sub>2</sub>], where pz' is 3,5-bis(isopropyl)-pyrazolyl, suggests that the peroxide unit of this intermediate is bound in a μ-1,2 configuration (114). High-level theoretical calculations also favor a gauche μ-1,2-peroxo structure for H<sub>peroxo</sub> (115). Although a nonplanar μ-η<sup>2</sup>:η<sup>2</sup> geometry has also been suggested (93, 94, 123), it is no longer favored (124). P\* to H<sub>peroxo</sub> conversion is promoted by transfer of a single proton most likely from within the enzyme active site (113, 116).

In contrast to the μ-1,2-peroxodiiron(III) units characterized in many carboxylate-bridged diiron enzymes, similar transients generated in ToMOH and PHH display Mössbauer quadrupole doublets < 1.0 mm/s and lack discernable optical bands (Table 1.1) (47, 97, 118). These observations suggest geometries that are distinct from those of the other diiron proteins (47, 97). The protonation states could differ as well (47). Recent high-level theoretical calculations of the peroxodiiron(III) center of ToMOH, ToMOH<sub>peroxo</sub>, suggest that it is a μ-1,1-hydroperoxide (124). The distal oxygen atom engages in a hydrogen-bonding network consisting of a water molecule and the hydroxyl group of the strictly conserved T201 residue (vide supra). Further analyses of these

---

peroxodiiron(III) species generated was not characterized spectroscopically and the H<sub>2</sub>O<sub>2</sub>-catalyzed reaction was 600-fold slower than O<sub>2</sub>-mediated catalysis, questioning the biological relevance of the results.

**Table 1.1.** Spectroscopic Parameters of Peroxodiiron(III) Intermediates in Non-Heme Diiron Enzymes and Select Synthetic Model Systems

	optical		Mössbauer	
	$\lambda_{\max}$ (nm)	$\epsilon$ ( $M^{-1} \text{ cm}^{-1}$ )	$\delta$ (mm/s)	$\Delta E_Q$ (mm/s)
sMMOH ( <i>M. capsulatus</i> (Bath))	420; 720	3880; 1350 <sup>a</sup>	0.66	1.51 <sup>b</sup>
sMMOH ( <i>M. trichosporium</i> OB3b)	725	2500 <sup>c</sup>	0.67	1.51 <sup>d</sup>
ToMOH ( <i>Pseudomonas</i> sp. OX1) <sup>e</sup>	no <sup>f</sup>		0.54	0.66
ToMOH T201S ( <i>Pseudomonas</i> sp. OX1) <sup>g</sup>	675	1500	0.67	1.51
PH ( <i>Pseudomonas</i> sp. OX1) <sup>h</sup>	no <sup>f</sup>		0.59	0.63
RNR-R2 D84E <sup>i</sup>	700	1500	0.63	1.58
RNR-R2 W48F/Y122F <sup>j</sup>	no <sup>f</sup>		0.52 and 0.45	0.55 and 1.53
$\Delta^9$ -desaturase <sup>k</sup>	700	1200	0.68; 0.64	1.90; 1.06
frog M ferritin <sup>l</sup>	650	-	0.62	1.08
AurF <sup>m</sup>	500	500	0.54; 0.61	0.66; 0.35
hDOHH <sup>n</sup>	630	2800	0.55; 0.58	1.16; 0.088
Fe <sub>2</sub> ( $\mu$ -1,2-O <sub>2</sub> )( $\mu$ -O <sub>2</sub> CCH <sub>2</sub> Ph) <sub>2</sub> {HB(pz') <sub>3</sub> } <sub>2</sub> <sup>o</sup>	694	2650	0.66	1.40
Fe <sub>2</sub> ( $\mu$ -OH)( $\mu$ -1,2-O <sub>2</sub> )(6-Me <sub>2</sub> -BPP) <sub>2</sub> <sup>+p</sup>	644	3000	0.50	1.31
Fe <sub>2</sub> ( $\mu$ -O)( $\mu$ -1,2-O <sub>2</sub> )(6-Me <sub>3</sub> -TPA) <sub>2</sub> <sup>2+q</sup>	494; 648	1100; 1200	0.54	1.68
Fe <sub>2</sub> ( $\mu$ -O)( $\mu$ -O <sub>2</sub> )( $\mu$ -OAc)(hexpy) <sub>2</sub> <sup>+r</sup>	510; 605	1300; 1310	0.53	1.67

<sup>a</sup>Data from (113). <sup>b</sup>Data from (45). <sup>c</sup>Data from (116). <sup>d</sup>Data from (117). <sup>e</sup>Data from (47). <sup>f</sup>Not observed. <sup>g</sup>Data from (98). <sup>h</sup>Data from (118). <sup>i</sup>Data from (102). <sup>j</sup>Data from (119). The two noted quadrupole doublets represent two distinct peroxodiiron(III) units formed simultaneously in this variant and not two inequivalent iron sites. <sup>k</sup>Data from (105). <sup>l</sup>Data from (109). <sup>m</sup>Data from (111). <sup>n</sup>Data from (110). <sup>o</sup>Data from (114). pz' = 3,5-bis(isopropyl)-pyrazolyl. <sup>p</sup>Data from (120). BPP = *N,N*-bis(2-pyridylmethyl)-3-aminopropionate. <sup>q</sup>Data from (121). TPA = *tris*(2-pyridylmethyl)amine. <sup>r</sup>Data from (122). hexpy = hexapyridine.

intermediates are necessary to determine their structures. Spectroscopic studies are complicated because ToMOH and PHH operate via half-sites reactivity mechanisms, however (47, 118). At best, 50% of the diiron centers accumulate the peroxodiiron(III) intermediate, and the resulting samples are heterogeneous.

The peroxodiiron(III) intermediates are responsible for most carboxylate-bridged diiron protein oxidations and convert directly to the diiron(III) enzyme resting state following such reactions. By contrast, the peroxodiiron(III) intermediates of MMOH and RNR-R2

evolve to higher valent states with rearrangement at the diiron center and scission of the O–O bond (Table 1.2). These two special cases are discussed in detail below.

*MMOH Intermediate Q.* Intramolecular transfer of one or two protons and heterolytic cleavage of the O–O bond (113, 116), results in the rapid conversion of  $\text{MMOH}_{\text{peroxo}}$  to intermediate Q, an antiferromagnetically coupled diiron(IV) unit with a strong absorption band centered at 420 nm that trails into the near IR (45, 90, 95, 117). The single quadrupole doublet of *M. trichosporium* OB3b Q suggested similar ligand environments for both Fe(IV) atoms, whereas two slightly different isomer shifts were detected in the *M. capsulatus* (Bath) enzyme spectrum. An EXAFS spectrum of *M. trichosporium* OB3b Q was interpreted in terms of a di( $\mu$ -oxo)diiron(IV) ‘diamond core’ structure with an Fe–Fe distance of 2.46 Å and Fe–O bond lengths of 1.77 Å and 2.05 Å at each iron atom (125). Based on these parameters the authors proposed a head-to-tail dimer of  $\text{Fe}^{\text{IV}}=\text{O}$

**Table 1.2.** Spectroscopic Parameters of High-Valent Iron (IV) Intermediates in Non-Heme Diiron Enzymes and Synthetic Model Systems

	optical		Mössbauer		Fe-Fe (Å)
	$\lambda_{\text{max}}$ (nm)	$\epsilon$ ( $\text{M}^{-1} \text{cm}^{-1}$ )	$\delta$ (mm/s)	$\Delta E_{\text{Q}}$ (mm/s)	
sMMOH Q ( <i>M. capsulatus</i> (Bath))	420	8415 <sup>a</sup>	0.21; 0.14	0.68; 0.55 <sup>b</sup>	-
sMMOH Q ( <i>M. trichosporium</i> OB3b)	330; 430	7500; 7500 <sup>c</sup>	0.17	0.53 <sup>d</sup>	2.46 <sup>e</sup>
RNR-R2 X	360 <sup>f</sup>	-	0.56, 0.26	-0.90; -0.60 <sup>g</sup>	2.5 <sup>h</sup>
MMOH Q <sub>x</sub> ( <i>M. capsulatus</i> (Bath)) <sup>i</sup>	-	-	0.48; 0.14	-0.90; -0.60	-
ToMOH I100W diiron(III/IV)-W <sup>j</sup>	-	-	0.47; 0.22	-0.7; -0.64	-
$[\text{Fe}_2(\mu\text{-O})_2(\text{L})_2]^{3+}$	366; 616	7900; 5200 <sup>k</sup>	0.48; 0.08	1.6; 0.5 <sup>l</sup>	2.683 <sup>m</sup>
$[\text{Fe}_2(\mu\text{-O})_2(\text{L})_2]^{4+ n}$	485; 875	9800; 2200	-0.04	2.09	2.73

<sup>a</sup>Data from (113). <sup>b</sup>Data from (45). <sup>c</sup>Data from (90). <sup>d</sup>Data from (117). <sup>e</sup>Data from (125). <sup>f</sup>Data from (126). <sup>g</sup>Data from (127). <sup>h</sup>Data from (128). <sup>i</sup>Data from (129). <sup>j</sup>Data from (130). <sup>k</sup>Data from (131). L = 5-Me<sub>3</sub>-TPA; TPA = tris(2-pyridylmethyl)amine. <sup>l</sup>Data from (132). L = 6-Me<sub>3</sub>-TPA. <sup>m</sup>Data from (133). L = 5-Et<sub>3</sub>-TPA. <sup>n</sup>Data from (134). L = tris((4-methoxy-3,5-dimethylpyrid-2-yl)d<sub>2</sub>-methyl)amine.

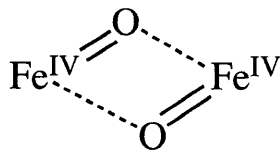


**Figure 1.5.** Proposed structure of intermediate Q, showing only the  $\{\text{Fe}_2\text{O}_2\}^{4+}$  core

units (Figure 1.5) having an additional carboxylate bridge to reconcile the unusually short Fe–Fe bond distance compared to synthetic model complexes with  $\{\text{Fe}_2\text{O}_2\}^{n+}$  core structures. The inability of the sole di( $\mu$ -oxo)diiron(IV) model complex (134) (Table 1.2) and various high-level density functional theory (DFT) calculations (93, 94, 123, 135) to reproduce the short Fe–Fe bond distance measured by EXAFS underscores the need for additional structural characterization of this intermediate.

The reactivity patterns of several model complexes also suggest that the proposed structure of Q be reconsidered. Reaction of the diiron(II) complex  $[\text{Fe}_2(\text{H}_4\text{HBamb})_2(\text{N-melIm})_2]$ , where  $\text{H}_4\text{HBamb}$  is 2,3-bis(2-hydroxybenzamido)-dimethylbutane and  $\text{melIm}$  is *N*-methylimidazole, with oxygen atom donors resulted in formation of a mixed-valent diiron(II/IV) complex featuring a terminal  $\text{Fe}^{\text{IV}}=\text{O}$  unit capable of oxidizing cyclohexane to cyclohexanol (136). In this example, the oxidative power of the system was achieved by concentrating the oxidizing capability at the Fe(IV) center, and the authors proposed that an analogous diiron(III/V) center might be responsible for methane oxidation in MMOH. A separate set of studies conducted in a different laboratory similarly claimed that the valence-localized  $[\text{OH}-\text{Fe}^{\text{III}}-\text{O}-\text{Fe}^{\text{IV}}=\text{O}]^{2+}$  form of a synthetic complex supported

by the *tris*((4-methoxy-3,5-dimethyl-pyridin-2-yl)methyl)amine ligand system can cleave strong C–H bonds a million-fold more rapidly than its valence-delocalized  $[\text{Fe}^{3.5}(\mu\text{-O})_2\text{Fe}^{3.5}]^{3+}$  ‘diamond core’ analogue (137). A third study revealed that the rate of 9,10-dihydroanthrocene oxidation by the diamond core species  $[\text{Fe}^{\text{IV}}_2(\mu\text{-O})_2\text{L}_2]^{4+}$ , where L = *tris*((4-methoxy-3,5-dimethylpyrid-2-yl)*d*<sub>2</sub>-methyl)amine, was two to three orders of magnitude slower for than that for  $[\text{Fe}^{\text{IV}}(\text{O})(\text{L})(\text{NCMe})]^{2+}$ , the corresponding mononuclear  $\text{Fe}^{\text{IV}}=\text{O}$  complex supported by the same ligand (134). Together, these data suggest that an oxidant with a terminal Fe=O unit may be more effective for C–H bond cleavage than an oxidant featuring a Fe–O–Fe structure and suggest that further structural characterization of Q is necessary to understand better how this intermediate can achieve the oxidizing power necessary to hydroxylate methane.

*RNR-R2 Intermediate X.* In RNR-R2, O–O bond cleavage of the peroxodiiron(III) unit is coupled to a one-electron reduction event that generates a mixed-valent diiron(III/IV) species termed X (99, 127, 138-140). The oxidant in this process is tryptophan 48,<sup>6</sup> which resides near the active site and donates a single electron to generate a W radical cation (138, 141, 142). Because X is directly responsible for initiating catalysis in the system through the one-electron oxidation of Y122 near the diiron center, many spectroscopic tools have been employed in order to elucidate its structure.

EPR spectroscopy revealed that X has a nearly isotropic  $S = \frac{1}{2}$  signal at  $g = 2$ , which is broadened upon reconstitution of the protein with <sup>57</sup>Fe (99, 143). Mössbauer spectroscopy indicated that the diiron unit has two inequivalent iron sites (139). The isomer shift of one iron site suggested high-spin Fe(III) whereas that of the other was consistent with either

---

<sup>6</sup>R2 residue numbers reported in this chapter follow the *E. coli* nomenclature.

high-spin Fe(III) or Fe(IV). The smaller isotope shift and the significant hyperfine anisotropy of the latter site established by ENDOR spectroscopy led to assignment of X as an Fe(III)/Fe(IV) unit with significant spin delocalization onto the oxygen ligands (127). The structure was formulated as having a terminal aqua or hydroxo ligand bound to the Fe(III) ion and one or two oxo bridges (140). The presence of an additional hydroxo bridge has also been proposed (144). Resonance Raman spectroscopy revealed that  $^{18}\text{O}$  is incorporated into the oxo bridge upon reaction of diiron(II) R2 with  $^{18}\text{O}_2$  (145). Similarly, ENDOR studies using  $^{17}\text{O}_2$  and  $\text{H}_2^{17}\text{O}$  labeled protein showed that one oxygen atom deriving from  $\text{O}_2$  is incorporated into an oxo bridge and the other forms the exchangeable terminal aqua ligand bound to Fe(III) (146, 147). As for studies of Q, EXAFS analysis characterized X as having a short Fe–Fe distance of 2.5 Å (128) that could not be reproduced by the sole existing valence-delocalized  $\{\text{Fe}_2(\mu\text{-O})_2\}^{3+}$  model complex (131, 133) or by theory (144, 148).

*Outlook and Future Directions.* One important question that arises from these collective studies of  $\text{O}_2$  activation by carboxylate-bridged diiron proteins is why the peroxodiiron(III) units of some enzymes evolve to stable high valent iron(IV) states whereas others do not. Rational mutagenesis employed to answer this question has provided few insights. Reaction of the T201 variant of  $\text{ToMOH}_{\text{red}}$  with  $\text{O}_2$  led to formation of a peroxodiiron(III) species with identical spectroscopic parameters to those of  $\text{H}_{\text{peroxo}}$  (Table 1.1); however, this intermediate does not convert to a high valent Q-like unit and instead decays directly to form the di( $\mu$ -hydroxo)diiron(III) resting state enzyme (98). On the other hand, reaction of the I100W variant of  $\text{ToMOH}_{\text{red}}$  with  $\text{O}_2$  generated a peroxodiiron(III) with the same spectroscopic parameters as wild type  $\text{ToMOH}_{\text{peroxo}}$ ,

which rapidly oxidized the installed tryptophan to form a diiron(III/IV) unit coupled to a neutral tryptophan radical (Table 1.2) (97, 130). These results provided the first evidence that high valent iron species can exist in ToMOH; however, the question of why a stable mixed-valent Fe(III)/Fe(IV), but not a diiron(IV), species can be accessed in this system is still not yet understood. Similarly, attempts to generate a Q-like diiron(IV) intermediate in RNR-R2 by blocking electron transfer to the diiron center in a W48F/Y122F double mutant resulted in accumulation of two peroxodiiron(III) species (Table 1.1), neither of which evolved to a Q-like state (119). Only upon addition of the external reductant 3-methylindole did these species convert to a high-valent state; however, the products of these reactions contained X and not the desired one-electron oxidized product Q.

Recent quantum mechanics/molecular mechanics (QM/MM) studies of MMOH indicated that compression of the Fe–Fe vector during O<sub>2</sub> activation might provide the necessary driving force to generate Q (94). Given the short Fe–Fe distances reported for Q (125) and X (128), relative to those in model complexes and proposed from theory, it is possible that mechanical strain imposed by the protein scaffolds that act upon the diiron centers of MMOH and RNR R2, selectively allow them to accumulate high valent intermediates. Further mutagenesis studies on the proteins are necessary to enhance our understanding of the surprisingly disparate pathways of O<sub>2</sub> activation in BMMs and related carboxylate-bridged diiron enzymes.

### **C. Substrate Reactivity of BMMs**

The mechanisms of BMM substrate oxidation have been investigated by steady state and transient kinetic methods. Steady state studies use mechanistic substrate probes to

delineate pathways of reactivity under catalytic conditions. Although providing information about the mechanisms of metalloenzymes including sMMO, they sometimes lead to contradictory results, particularly when multiple oxidants can operate in one system. Transient kinetic studies provide a more direct approach by employing rapid methods, such as stopped-flow or freeze-quench optical/IR or Mössbauer spectroscopy to monitor the reaction of a given substrate with the intermediate of interest. In contrast to steady state analyses, these studies fail to work on the complete BMM system of interest. Although neither the steady state nor the transient approach is perfect, but both have provided important mechanism insight. In this section, results from some of these studies are discussed.

*Peroxide Shunt Reactions.* One strategy that has been employed to define the nature of the oxidant(s) in BMM systems has been to use H<sub>2</sub>O<sub>2</sub> to activate the resting diiron(III) hydroxylase instead of adding O<sub>2</sub> to the reduced, diiron(II) form (47, 112, 149, 150). H<sub>2</sub>O<sub>2</sub>-mediated enzymatic oxidation of substrates including methane by *M. trichosporium* OB3b and *M. capsulatus* (Bath) MMOH was reported in the early 1990s (149, 150). Product distributions of such “peroxide shunt” reactions varied significantly from those of the natural system, providing the first evidence that the enzyme could operate by two different oxidative pathways (149, 150). Because MMOB and MMOR were not necessary for these reactions (149), and in certain cases the presence of MMOB completely inhibited the reactions (150), the biological relevance of the results is questionable.

In T4mo, the observation of oxidized toluene products in a peroxide shunt reaction was interpreted to mean that a peroxodiiron(III) intermediate, or high-valent species derived



therefrom, is responsible for catalysis (112). However, in this system, H<sub>2</sub>O<sub>2</sub>-catalyzed aromatic hydroxylation was 600-fold slower than that employing the natural oxidant. The reactions were independent of the regulatory protein, and the hydroxylated products were not proved conclusively to derive from enzymatic rather than nonenzymatic processes. These observations question the biological relevance of the results. Indeed, no peroxide shunt has yet been observed for ToMO (47) or PH (118) in the presence or absence of regulatory protein.

*Mechanistic Substrate Probes.* A second strategy for delineating the reaction mechanism(s) of substrate oxidation is to use substrate probes that rearrange to form different products depending on the mechanism of oxidation. This approach has been employed mainly for sMMO but has also but has also recently been applied to the ToMO and PH (151, 152) and T4mo (153) systems.

One strategy employed to study the oxidation mechanism of sMMO is to use chiral alkane substrates. Concerted oxidation mechanisms result in complete retention or inversion of stereochemical configuration at the hydroxylated carbon atom, whereas formation of a transient radical- or cation-based intermediate with a lifetime that is longer than the time needed for rotation around the C–C bond affords full racemization. Studies probing the hydroxylation of (*R*) and (*S*)-[1-<sup>2</sup>H,1-<sup>3</sup>H]ethane by *M. capsulatus* (Bath) (154) and *M. trichosporium* OB3b (155) sMMO revealed that these reactions occur predominantly (> 70%) with retention of configuration. Similar product yields were observed with (*R*) and (*S*)-[1-<sup>2</sup>H,1-<sup>3</sup>H]butane (154). Several mechanisms were proposed to explain these results: (i) a nonsynchronous concerted mechanism, (ii) multiple operative reaction pathways, (iii) generation of an extremely short-lived ‘radical’ that

rebounds with OH• faster than rotation around the C–C bond. A comparison of the measured lifetime of the ethyl radical (156) to the expected rate of C–C bond rotation is inconsistent with the latter interpretation, however.

To further delineate the reaction mechanism(s) of sMMO, steady state studies have been performed employing substrates that undergo differential carbon skeletal rearrangements to form characteristic products depending on the reaction mechanism (151, 152, 157-165). Radical clock probes, a subclass of these mechanistic substrates, have been used to approximate the lifetime of potential transient radicals formed along the reaction pathway (157, 159, 161-163, 165, 166). Because the rate constants for rearrangement of radical species derived from these probes have been measured, lifetimes can be estimated by comparing the yields of unrearranged and rearranged products. For several probes, oxidization of substrate occurred without formation of rearranged products and upper limits of the lifetimes of radical intermediates potentially formed in the reactions were computed to be 0.1–40 ps (161, 162, 165, 166). Studies employing certain radical clock substrate probes provided evidence for radical-based intermediates, although the yields of radical pathway products are typically very small (1-3% of total products formed), suggesting that the results be interpreted with caution (157, 159, 161-163). Collectively, these studies measured radical lifetimes ranging from to 0.1 to 34 ps (159, 161, 162, 165), an exception being the probe norcarane, for which longer lifetimes of 50-150 ps were claimed (157, 163).

Mechanistic substrate probes can differentiate between concerted, radical-, and carbocation-based mechanisms. Application of these probes to sMMO has provided

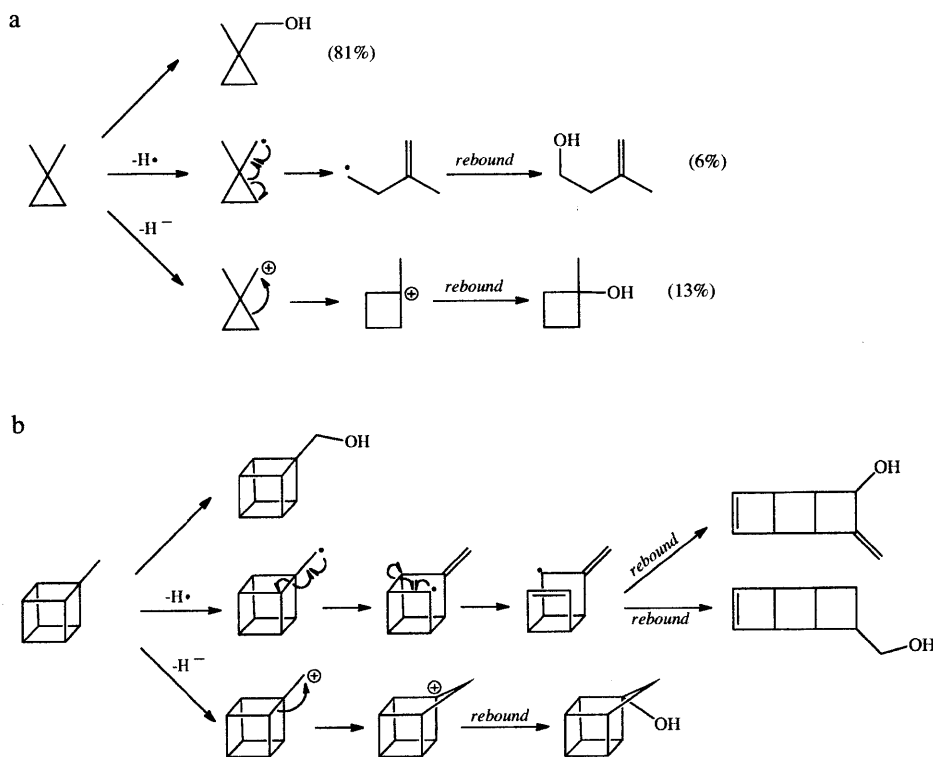


**Figure 1.6.** Representative examples of carbocation-derived products detected in reactions of sMMO with mechanistic substrate probes. (a) Reactions of sMMO with 1,1-dimethylcyclopropane gave the unrearranged alcohol (1-methylcyclopropyl)methanol, the radical-based product 3-methyl-3-buten-1-ol, and the carbocation-based product 1-methylcyclobutanol in 81%, 6%, and 13% yield. Product distributions are from Ruzicka, F., Huang, D.-S., Donnelly, M. R., and Frey, P. A. (1990) *Biochemistry* 29, 1696-1700. (b) Reactions of *M. capsulatus* (Bath) sMMO with methylcubane gave mostly the carbocation-based ring expansion product 1-homocubanol and some concerted unrearranged cubylmethanol and methylcubanol products. No radical-based ring-opened products were observed. Adapted from Merckx, M., Kopp, D. A., Sazinsky, M. H., Blazyk, J. L., Müller, J., and Lippard, S. J. (2001) *Angew. Chem. Int. Ed.* 40, 2782-2807 with permission. Copyright ©2001 John Wiley & Sons Inc.

evidence for carbocation-derived products in addition to unrearranged (concerted) and radical-based species (158-161, 164). Two representative examples are shown in Figure 1.6. An early study using 1,1-dimethylcyclopropane gave mostly unrearranged product, but small amounts of cation- and radical-derived species were also identified (Figure

1.6a) (164). Notably, studies with  $^{18}\text{O}_2$  demonstrated that  $^{18}\text{O}$  was partially incorporated into the cation-derived product, suggesting that it formed in the enzyme-catalyzed reaction. A small yield of cation-derived product was also obtained with (*trans, trans*-2-methoxy-3-phenylcyclopropyl)methane (159). Reactions of sMMO with methylcubane yielded the cation-derived species as the major product, and no radical-derived species (158-160). When these results were reported, their implications were not fully understood. Recent transient kinetic studies probing the chemistry of  $\text{H}_{\text{peroxo}}$  suggest that this intermediate reacts with substrates having weak C–H bonds by a reaction pathway that involves a substrate-derived cation (*vide infra*). In light of these results, the presence of multiple products in mechanistic substrate probe studies might result from two oxidants operating in the system, with the cation-derived products arising from  $\text{H}_{\text{peroxo}}$  reactivity. Reactions of the aromatic monooxygenases ToMO, PH, and T4mo with mechanistic substrate probes also provided evidence for both radical- and cation-derived products, the mechanistic implications of which are not yet understood (151-153).

*The NIH Shift and Hammett Plots.* The aromatic hydroxylation mechanisms of ToMO and T4mo have been probed using derivatized benzyl and phenolic substrates (47, 167). Several mechanisms have been proposed for these enzymes, including: (i) concerted oxygen insertion into a C–H bond; (ii) electrophilic attack of the oxidizing intermediate on the substrate; and (iii) formation of a transient substrate-derived epoxide (Figure 1.7). For reactions of T4MO, for which *para* hydroxylation dominates, these mechanisms can be distinguished by the using selectively isotopically labeled substrates. Reactions of 4- $^2\text{H}_1$ -toluene via mechanism (i) are expected to occur with complete label washout. Due to

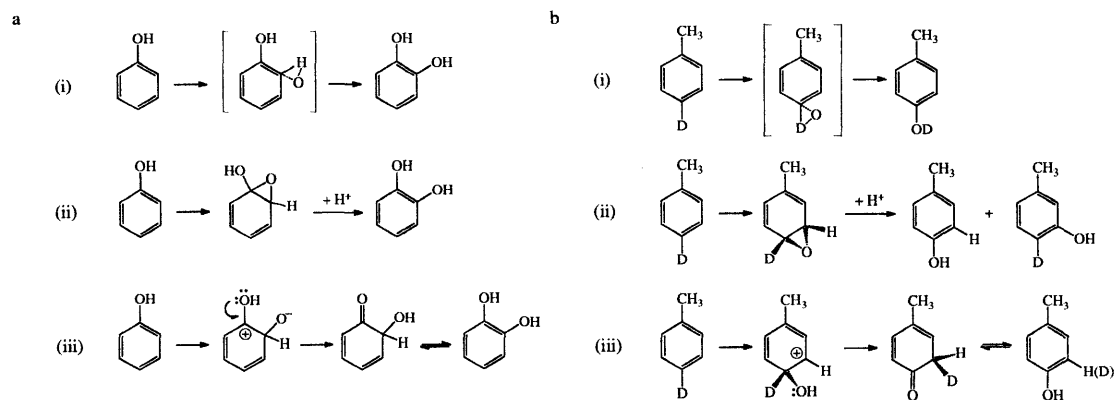


**Figure 1.7.** Possible mechanisms phenol (a) and 4-<sup>2</sup>H<sub>1</sub>-toluene (b) oxidation by aromatic hydroxylases: (i) direct oxygen insertion into a C-H bond; (ii) epoxidation; (iii) electrophilic addition. B was adapted from Mitchell, K. H., Rogge, C. E., Gierahn, T., and Fox, B. G. (2003). *Proc. Natl. Acad. Sci. USA* 100, 3784-3789 with permission. Copyright ©2003 by the National Academy of Sciences.

intermolecular deuterium migration, the label is expected to be fully or partially retained if mechanisms (ii) or (iii) are operative, however (Figure 1.7b) (168). Early investigations monitoring the reactions of partially-purified T4mo with 4-<sup>2</sup>H<sub>1</sub>-toluene reported 68% retention of <sup>2</sup>H in the oxidized *p*-cresol product, indicating that direct insertion into the C-H bond and H-atom abstraction are unlikely (169). A later set of experiments using this same substrate found nearly quantitative retention of <sup>2</sup>H in the oxidized *m*-cresol product and partial retention of deuterium atoms in all phenolic products of 3,5-<sup>2</sup>H<sub>2</sub>-toluene (167). Hydroxylation of *p*-xylene by T4MO proceeds with an inverse KIE, suggesting a change in hybridization from sp<sup>2</sup> to sp<sup>3</sup> for hydroxylation at the carbon atom bearing the deuterium (167). The authors of these studies argued that their results provide evidence for epoxide-based mechanism (iii), although the electrophilic addition mechanism (ii) could not be ruled out. In ToMO, Hammett plots relating the reaction

rates and equilibrium constants for reactions with para-substituted phenols had negative slopes, providing evidence for mechanism (ii) (47). It is important to note, however, that the proposed mechanism in this system could differ for reactions with less activated arenes such as toluene and benzene.

*Transient Kinetic Studies.* Although steady state investigations provide insight into the mechanisms of substrate oxidation in sMMO, ToMOH, PH, and T4moH, they are not a direct measure of reactivity of the oxygenated intermediate of interest, particularly for sMMO in which the reactions of multiple oxidants under catalytic conditions have led to results that are difficult to interpret (vide supra). Transient kinetic studies employ rapid detection methods such as stopped-flow optical spectroscopy or rapid freeze/chemical quench to monitor reaction progress during a single enzyme turnover. Both single-mixing, in which reduced hydroxylase is mixed with a solution containing O<sub>2</sub> and substrate, and double-mixing, in which the intermediate of interest is first generated by reaction of reduced hydroxylase with O<sub>2</sub> and then rapidly mixed with substrate in a second step, techniques have been applied. Because the sMMO intermediates display characteristic visible absorption bands, stopped-flow optical spectroscopy has been the method of choice for studies of this system. The lack of a discernable optical bands associated with the peroxodiiron(III) intermediates of ToMOH and PHH have prevented similar studies in these systems, and transient kinetic methods have relied on Mössbauer spectroscopy, which is not practical for extensive studies because it requires much protein.

Early transient kinetic studies focused on the use of stopped-flow optical spectroscopy to probe the rate constant for decay of intermediate Q in the presence of various

substrates (96, 170). Acceleration of the intermediate decay rate in the presence of substrate was interpreted as an indication of reactivity. Although important conclusions were drawn from these studies, there was no direct evidence that the kinetics of substrate-promoted intermediate decay was representative of product formation. The approach of using the intermediate decay rate constant as a measure of reactivity was validated in an elegant double-mixing stopped-flow Fourier transform infrared study monitoring the reaction of intermediate Q with  $\text{CD}_3\text{NO}_2$ , which demonstrated that the rate constant for decay of Q corresponded exactly to that of formation of the hydroxylated product (171). Similar conclusions were reached in stopped-flow optical spectroscopic experiments employing the substrate nitrobenzene, the product of which has a strong UV absorbance band, although the presence of multiple overlapping signals in this region complicated the data analysis (90).

Using stopped-flow optical spectroscopy, reactions of Q with methane and substituted methanes have been investigated. Non-linear Eyring plots were observed for reaction of  $\text{CH}_4$  with Q (96, 170). The interpretation of these results is still controversial, and it has been proposed that the behavior results from a temperature-dependent difference in rate-determining step (96) or that two methane molecules are involved in the decay process (170). Surprisingly, linear Eyring plots were observed for reaction with  $\text{CD}_4$ , a result that suggests that the reaction mechanism depends on substrate deuteration (96, 170). At 23 °C, a large kinetic isotope effect (KIE) of 50-100 on Q decay for reaction of methane was reported for the *M. trichosporium* OB3b MMOH (172), although similar studies of the *M. capsulatus* (Bath) (96, 173) enzyme provided a smaller value of 21–28. Hydrogen tunneling at the transition state was proposed to explain the large isotope effects.

Reactions of Q with several other alkanes have been probed. Surprisingly, the rate constants for reaction of these substrates do not correlate with the C–H bond strengths (96, 170). KIEs of unity were observed for ethane and larger alkane substrates, indicating that C–H bond activation is not rate-determining for these molecules (96, 170). Significant KIEs around ~3.5 for ethane were unmasked when MMOB mutants were employed, however, highlighting the effect of the regulatory protein on the mechanism of substrate hydroxylation (62, 63, 66).

The KIEs of unity noted for ethane and other alkanes were attributed to rate-determining substrate binding events (96, 170). Similarly, reactions of Q with substituted methanes  $\text{CH}_3\text{X}$ , where  $\text{X} = \text{CH}_3, \text{OH}, \text{CN}, \text{NO}_2$ , fit into two classes depending on whether C–H bond activation or substrate binding was rate-determining (173, 174). Like methane, acetonitrile exhibited a KIE of 46, which is larger than the semiclassical limit for reaction with Q, implying that the reaction mechanism proceeds with hydrogen atom quantum tunneling through the transition state barrier (173, 174). A large KIE of 8.1 was also observed for nitromethane (173).

Reactions of  $\text{MMOH}_{\text{peroxo}}$  have also been probed using single- and double-mixing stopped-flow optical spectroscopy (96, 175). Early studies in which  $\text{H}_{\text{peroxo}}$  was mixed with propylene revealed that this substrate accelerates the rate of decay of the intermediate in a concentration-dependent manner, providing the first evidence that  $\text{H}_{\text{peroxo}}$  reacts directly with substrates (96). Further studies showed that diethyl ether and ethyl vinyl ether react more rapidly with  $\text{H}_{\text{peroxo}}$  than Q (175). Based on the low heterolytic C–H bond dissociation energies of these substrates, the reactions were proposed to take place by two-electron transfer mechanisms, as shown in Figure 1.8.



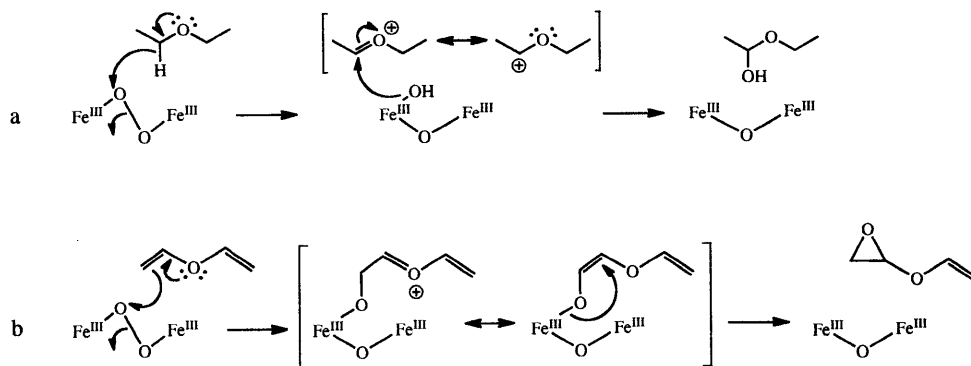


**Figure 1.8.** Proposed two-electron oxidation mechanisms for reactions of  $H_{\text{peroxo}}$  with diethyl ether (a) and ethyl vinyl ether (b). Adapted from Beauvais, L. G., and Lippard, S. J. (2005) *J. Am. Chem. Soc.* 127, 7370-7378 with permission. Copyright ©2005 by the American Chemical Society.

Because the peroxodiiron(III) transient of ToMOH lacks an optical band, stopped-flow optical spectroscopy cannot be employed in this system to follow reactions of the intermediate. However, double-mixing freeze-quench Mössbauer studies revealed that decay of the intermediate is accelerated in the presence of phenol, suggesting that this species is responsible for substrate oxidation (47). Single-mixing stopped-flow spectroscopy was also used to probe the rate of peroxodiiron(III)-mediated one-electron oxidation of an internal tryptophan substrate placed strategically near the active site via an I100W mutant, the product of which has a strong absorption around 500 nm (130).

*Computational Studies.* The substrate oxidation mechanisms of MMOH have also been probed by high-level quantum mechanics and/or molecular mechanics methods (123, 176-179). Many of these studies predict formation of a transient substrate-derived radical intermediate. Molecular orbital analysis of the reaction of Q with methane suggested that

the first step in the hydroxylation mechanism involves a proton-coupled outer-sphere electron transfer. An  $\alpha$ -spin from a C–H  $\sigma$  bond of methane is transferred to Fe2, resulting in a bound  $\text{CH}_3\cdot$  species with an unpaired  $\beta$ -spin and an O–H bond (176). The lowest unoccupied molecular orbital (LUMO) on Fe1 then accepts a  $\beta$ -spin, because Fe1 and Fe2 are antiferromagnetically coupled, from the lone pair on the bridging O–H oxygen atom, leaving an  $\alpha$ -spin in the oxygen  $p_z$  orbital that then pairs with the  $\beta$  spin on the radical to form a C–O bond. This second electron transfer event is promoted by upward rotation of the O–H moiety, which positions the  $p_z$  orbital for bond formation (176).

Reactions of Q with substituted methanes of general formula  $\text{CH}_3\text{X}$ , where  $\text{X} = \text{CH}_3$ , OH, CN,  $\text{NO}_2$ , and F, have also been investigated computationally (178). These substrates belong to one of two classes depending on whether C–H bond activation or substrate binding at the active site is rate-determining. For ethane and methanol, the barrier height for substrate binding is higher than that for C–H bond activation, results that agree with the experimental KIEs of unity for these substrates.

*Outlook and Future Directions.* Many different methods have been applied to study the mechanism(s) by which BMMs oxidize substrates, some of which have produced results that are difficult to interpret. Moving forward, it is necessary to deconvolute the simultaneous reactions of multiple enzymatic oxidants. Double-mixing chemical quench experiments probing the products of mechanistic substrate probes directly with the oxidant of interest could be informative but will require high concentrations of protein and well designed experimental controls. While performing such experiments it is important to remember that various substrates may react by different mechanisms,

particularly if the rate constants are considerably lower than with the natural substrate. As better computational algorithms are developed, these methods will help ascertain the substrate oxidation mechanisms of BMMs.

## ORGANIZATION AND SCOPE OF THESIS

The studies in this thesis address three aspects of BMM reactivity, namely, O<sub>2</sub> activation, hydrocarbon oxidation, and component interactions. In a fourth and separate study we examined the Rieske component of ToMO as a model system to investigate reactions of [2Fe-2S] centers with the biological signaling agent nitric oxide (NO). Studies of O<sub>2</sub> activation in MMOH are presented in chapter 2. Investigations of the reactions of MMOH intermediates H<sub>peroxo</sub> and Q are discussed in chapter 3. Dioxygen activation and component interactions in PH are addressed in chapter 4. Chapter 5 presents the reactions of the Rieske center of ToMOC with NO. Preliminary investigations of the structures of MMOH<sub>ox</sub> and MMOH<sub>Q</sub> by <sup>57</sup>Fe nuclear resonance vibrational spectroscopy are discussed in Appendix A. Together these studies help to provide a unified picture of catalysis by BMMs, allowing us to understand better how these remarkable proteins can selectively oxidize hydrocarbon substrates.

## REFERENCES

1. Feig, A. L., and Lippard, S. J. (1994) *Chem. Rev.* *94*, 759-805.
2. Kurtz, D. M. J. (1997) *J. Biol. Inorg. Chem.* *2*, 159-167.
3. Murray, L. J., and Lippard, S. J. (2007) *Acc. Chem. Res.* *40*, 466-474.

4. Sazinsky, M. H., and Lippard, S. J. (2006) *Acc. Chem. Res.* 39, 558-566.
5. Wallar, B. J., and Lipscomb, J. D. (1996) *Chem. Rev.* 96, 2625-2657.
6. Leahy, J. G., Batchelor, P. J., and Morcomb, S. M. (2003) *FEMS Microbiology Reviews* 27, 449-479.
7. Notomista, E., Lahm, A., Di Donato, A., and Tramontano, A. (2003) *J. Mol. Evol.* 56, 435-445.
8. Merx, M., Kopp, D. A., Sazinsky, M. H., Blazyk, J. L., Müller, J., and Lippard, S. J. (2001) *Angew. Chem. Int. Ed.* 40, 2782-2807.
9. Elango, N., Radhakrishnan, R., Froland, W. A., Wallar, B. J., Earhart, C. A., Lipscomb, J. D., and Ohlendorf, D. H. (1997) *Prot. Sci.* 6, 556-568.
10. Rosenzweig, A. C., Brandstetter, H., Whittington, D. A., Nordlund, P., Lippard, S. J., and Frederick, C. A. (1997) *Proteins* 29, 141-152.
11. Rosenzweig, A. C., Frederick, C. A., Lippard, S. J., and Nordlund, P. (1993) *Nature* 366, 537-543.
12. Whittington, D. A., and Lippard, S. J. (2001) *J. Am. Chem. Soc.* 123, 827-838.
13. Sazinsky, M. H., Merx, M., Cadieux, E., Tang, S., and Lippard, S. J. (2004) *Biochemistry* 43, 16263-16276.
14. Sazinsky, M. H., Bard, J., Di Donato, A., and Lippard, S. J. (2004) *J. Biol. Chem.* 279, 30600-30610.
15. McCormick, M. S., Sazinsky, M. H., Condon, K. L., and Lippard, S. J. (2006) *J. Am. Chem. Soc.* 128, 15108-15110.
16. Bailey, L. J., McCoy, J. G., Phillips Jr., G. N., and Fox, B. G. (2008) *Proc. Natl. Acad. Sci. USA* 105, 19194-19198.

17. Sazinsky, M. H., Dunten, P. W., McCormick, M. S., Di Donato, A., and Lippard, S. J. (2006) *Biochemistry* 45, 15392-15404.
18. DeWitt, J. G., Bentsen, J. G., Rosenzweig, A. C., Hedman, B., Green, J., Pilkington, S., Papaefthymiou, G. C., Dalton, H., Hodgson, K. O., and Lippard, S. J. (1991) *J. Am. Chem. Soc.* 113, 9219-9235.
19. DeWitt, J. G., Rosenzweig, A. C., Salifoglou, A., Hedman, B., Lippard, S. J., and Hodgson, K. O. (1995) *Inorg. Chem.* 34, 2505-2515.
20. Rudd, D. J., Sazinsky, M. H., Lippard, S. J., Hedman, B., and Hodgson, K. O. (2005) *Inorg. Chem.* 44, 4546-4554.
21. Rudd, D. J., Sazinsky, M. H., Merckx, M., Lippard, S. J., Hedman, B., and Hodgson, K. O. (2004) *J. Inorg. Chem* 43, 4579-4589.
22. Shu, L., Liu, Y., Lipscomb, J. D., and Que Jr., L. (1996) *J. Biol. Inorg. Chem.* 1, 297-304.
23. Davydov, R., Davydov, A., Gräslund, A., and Lipscomb, J. D. (1997) *J. Biol. Chem.* 272, 7022-7026.
24. Davydov, R., Valentine, A. M., Komar-Panicucci, S., Hoffman, B. M., and Lippard, S. J. (1999) *Biochemistry* 38, 4188.
25. Fox, B. G., Hendrich, M. P., Surerus, K. K., Andersson, K. K., Froland, W. A., Lipscomb, J. D., and Münck, E. (1993) *J. Am. Chem. Soc.* 115, 3688-3701.
26. Fox, B. G., Liu, Y., Dege, J. E., and Lipscomb, J. D. (1991) *J. Biol. Chem.* 266, 540-550.
27. Fox, B. G., Surerus, K. K., Münck, E., and Lipscomb, J. D. (1988) *J. Biol. Chem.* 263, 10553-10556.

28. Froland, W. A., Anersson, K. K., Lee, S.-K., Liu, Y., and Lipscomb, J. D. (1992) *J. Biol. Chem.* 257, 17588-17597.
29. Hendrich, M. P., Münck, E., Fox, B. G., and Lipscomb, J. D. (1990) *J. Am. Chem. Soc.* 112, 5861-5865.
30. Woodland, M. P., Patil, D. S., Cammack, R., and Dalton, H. (1986) *Biochim. Biophys. Acta* 873, 237-242.
31. Bender, C. J., Rosenzweig, A. C., Lippard, S. J., and Peisach, J. (1994) *J. Biol. Chem.* 269, 15993-15998.
32. DeRose, V. J., Liu, K. E., Kurtz, D. M. J., Hoffman, B. M., and Lippard, S. J. (1993) *J. Am. Chem. Soc.* 115, 6440-6441.
33. DeRose, V. J., Liu, K. E., Lippard, S. J., and Hoffman, B. M. (1996) *J. Am. Chem. Soc.* 118, 121-134.
34. Hendrich, M. P., Fox, B. G., Andersson, K. K., Debrunner, P. G., and Lipscomb, J. D. (1992) *J. Biol. Chem.* 267, 261-269.
35. Hoffman, B. M., Sturgeon, B., Doan, P. E., DeRose, V. J., Liu, K. E., and Lippard, S. J. (1994) *J. Am. Chem. Soc.* 116, 6023-6024.
36. Smoukov, S. K., Kopp, D. A., Valentine, A. M., Davydov, R., Lippard, S. J., and Hoffman, B. M. (2002) *J. Am. Chem. Soc.* 124, 1657-2663.
37. Sturgeon, B. E., Doan, P. E., Liu, K. E., Burdi, D., Tong, W. H., Nocek, J. M., Gupta, N., Stubbe, J., Kurtz, D. M. J., Lippard, S. J., and Hoffman, B. M. (1997) *J. Am. Chem. Soc.* 119, 375-386.
38. Thomann, H., Bernardo, M., McCormick, J. M., Pulver, S., Andersson, K. K., Lipscomb, J. D., and Solomon, E. I. (1993) *J. Am. Chem. Soc.* 115, 8881-8882.

39. Willems, J.-P., Valentine, A. M., Gurbiel, R., Lippard, S. J., and Hoffman, B. M. (1998) *J. Am. Chem. Soc.* *120*, 9410-9416.
40. Mitić, N., Schwartz, J. K., Brazeau, B. J., Lipscomb, J. D., and Solomon, E. I. (2008) *Biochemistry* *47*, 8386-8397.
41. Pulver, S., Froland, W. A., Fox, B. G., Lipscomb, J. D., and Solomon, E. I. (1993) *J. Am. Chem. Soc.* *115*, 12409-12422.
42. Pulver, S. C., Froland, W. A., Lipscomb, J. D., and Solomon, E. I. (1997) *J. Am. Chem. Soc.* *119*, 387-395.
43. Schwartz, J. K., Wei, P. P., Mitchell, K. H., Fox, B. G., and Solomon, E. I. (2008) *J. Am. Chem. Soc.* *130*, 7098-7109.
44. Fox, B. G., Froland, W. A., Dege, J. E., and Lipscomb, J. D. (1989) *J. Biol. Chem.* *264*, 10023-10033.
45. Liu, K. E., Valentine, A. M., Wang, D., Huynh, B. H., Edmondson, D. E., Salifoglou, A., and Lippard, S. J. (1995) *J. Am. Chem. Soc.* *117*, 10174-10185.
46. Cadieux, E., Vrajmasu, V., Achim, C., Powlowski, J., and Münck, E. (2002) *Biochemistry* *41*, 10680-10691.
47. Murray, L. J., Naik, S. G., Ortillo, D. O., García-Serres, R., Lee, J. K., Huynh, B. H., and Lippard, S. J. (2007) *J. Am. Chem. Soc.* *129*, 14500-14510.
48. Pikus, J. D., Studts, J. M., Achim, C., Kauffmann, K. E., Münck, E., Steffan, R. J., McClay, K., and Fox, B. G. (1996) *Biochemistry* *35*, 9106-9119.
49. Murray, L. J. (2007) Dioxygen Activation and Substrate Hydroxylation by the Hydroxylase Component of Toluene/*o*-Xylene Monooxygenase from

- Pseudomonas sporium* OX1, Ph.D. Thesis (Massachusetts Institute of Technology, Cambridge, MA).
50. Newman, L. M., and Wackett, L. P. (1995) *Biochemistry* 34, 14066-14076.
  51. Whittington, D. A., Rosenzweig, A. C., Frederick, C. A., and Lippard, S. J. (2001) *Biochemistry* 40, 3476-3482.
  52. McCormick, M. S. (2008) Structural Investigations of Hydroxylase Proteins and Complexes in Bacterial Multicomponent Monooxygenase Systems, Ph.D. Thesis (Massachusetts Institute of Technology, Cambridge, MA).
  53. Sazinsky, M. H., and Lippard, S. J. (2005) *J. Am. Chem. Soc.* 127, 5814-5825.
  54. Chang, S.-L., Wallar, B. J., Lipscomb, J. D., and Mayo, K. H. (1999) *Biochemistry* 38, 5799-5812.
  55. Walters, K. J., Gassner, G. T., Lippard, S. J., and Wagner, G. (1999) *Proc. Natl. Acad. Sci. USA* 96, 7877-7882.
  56. Hemmi, H., Studts, J. M., Chae, Y. K., Song, J., Markley, J. L., and Fox, B. G. (2001) *Biochemistry* 40, 3512-3524.
  57. Lountos, G. T., Mitchell, K. H., Studts, J. M., Fox, B. G., and Orville, A. M. (2005) *Biochemistry* 44, 7131-7142.
  58. Qian, H., Edlund, U., Powlowski, J., Shingler, V., and Sethson, I. (1997) *Biochemistry* 36, 495-504.
  59. Brandstetter, H., Whittington, D. A., Lippard, S. J., and Frederick, C. A. (1999) *Chem. Biol.* 6, 441-449.
  60. Lloyd, J. S., Bhambra, A., Murrell, J. C., and Dalton, H. (1997) *Eur. J. Biochem.* 248, 72-79.



61. Shinohara, Y., Uchiyama, H., Yagi, O., and Kusakabe, I. (1998) *J. Ferment. Bioeng.* 85, 37-42.
62. Brazeau, B. J., and Lipscomb, J. D. (2003) *Biochemistry* 42, 5618-5631.
63. Brazeau, B. J., Wallar, B. J., and Lipscomb, J. D. (2001) *J. Am. Chem. Soc.* 123, 10421-10422.
64. Liu, Y., Nesheim, J. C., Lee, S.-K., and Lipscomb, J. D. (1995) *J. Biol. Chem.* 270, 24662-24665.
65. Wallar, B. J., and Lipscomb, J. D. (2001) *Biochemistry* 40, 2220-2233.
66. Zheng, H., and Lipscomb, J. D. (2005) *Biochemistry* 45, 1685-1692.
67. Zhang, J., Wallar, B. J., Popescu, C. V., Renner, D. B., Thomas, D. D., and Lipscomb, J. D. (2006) *Biochemistry* 45, 2913-2926.
68. Zhang, J., and Lipscomb, J. D. (2006) *Biochemistry* 45, 1459-1469.
69. Mitchell, K. H., Studts, J. M., and Fox, B. G. (2002) *Biochemistry* 41, 3176-3188.
70. Liu, K. E., and Lippard, S. J. (1991) *J. Biol. Chem.* 266, 12836-12839.
71. Paulsen, K. E., Liu, Y., Fox, B. G., Lipscomb, J. D., Münck, E., and Stankovich, M. T. (1994) *Biochemistry* 33, 713-722.
72. Blazyk, J. L., Gassner, G. T., and Lippard, S. J. (2005) *J. Am. Chem. Soc.* 127, 17364-17376.
73. Gassner, G. T., and Lippard, S. J. (1999) *Biochemistry* 38, 12768-12785.
74. Green, J., and Dalton, H. (1985) *J. Biol. Chem.* 260, 15795-15801.
75. Liu, Y., Nesheim, J. C., Paulsen, K. E., Stankovich, M. T., and Lipscomb, J. D. (1997) *Biochemistry* 36, 5223-5233.

76. Cafaro, V., Scognamiglio, R., Viggiani, A., Izzo, V., Passaro, I., Notomista, E., Dal Paiz, F., Amoresano, A., Casbarra, A., Pucci, P., and Di Donato, A. (2002) *Eur. J. Biochem.* 269, 5689-5699.
77. Lund, J., Woodland, M. P., and Dalton, H. (1985) *Eur. J. Biochem.* 147, 297-305.
78. Elsen, N. L., Moe, L. A., McMartin, L. A., and Fox, B. G. (2007) *Biochemistry* 46, 976-986.
79. Chatwood, L. L., Müller, J., Gross, J. D., Wagner, G., and Lippard, S. J. (2004) *Biochemistry* 43, 11983-11991.
80. Müller, J., Lugovskoy, A. A., Wagner, G., and Lippard, S. J. (2002) *Biochemistry* 41, 42-51.
81. Kopp, D. A., Gassner, G. T., Blazyk, J. L., and Lippard, S. J. (2001) *Biochemistry* 40, 14932-14941.
82. Gallagher, S. C., Callaghan, A. J., Zhao, J., Dalton, H., and Trehwella, J. (1999) *Biochemistry* 38, 6752-6760.
83. Skjeldal, L., Peterson, F. C., Doreleijers, J. F., Moe, L. A., Pikus, J. D., Westler, W. M., Markley, J. L., Volkman, B. F., and Fox, B. G. (2004) *J. Biol. Inorg. Chem.* 9, 945-953.
84. Merx, M., and Lippard, S. J. (2002) *J. Biol. Chem.* 277, 5858-5865.
85. Nielsen, A. K., Gerdes, K., Degn, H., and Murrell, J. C. (1996) *Microbiol.* 142, 1289-1296.
86. Nielsen, A. K., Gerdes, K., and Murrell, J. C. (1997) *Mol. Microbiol.* 25, 399-409.
87. Arengi, F. L., Berlanda, D., Galli, E., Sello, G., and Barbieri, P. (2001) *Appl. Environ. Microbiol.* 67, 3304-3308.

88. Nordlund, I., Powlowski, J., and Shingler, V. (1990) *J. Bacteriology* 172, 6826-6833.
89. Powlowski, J., Sealy, J., Shingler, V., and Cadieux, E. (1997) *J. Biol. Chem.* 272, 945-951.
90. Lee, S.-K., Nesheim, J. C., and Lipscomb, J. D. (1993) *J. Biol. Chem.* 268, 21569-21577.
91. Stahl, S. S., Francisco, W. A., Merkx, M., Klinman, J. P., and Lippard, S. J. (2001) *J. Biol. Chem.* 276, 4549-4553.
92. Stenkamp, R. E. (1994) *Chem. Rev.* 94, 715-726.
93. Gherman, B. F., Baik, M.-H., Lippard, S. J., and Friesner, R. A. (2004) *J. Am. Chem. Soc.* 126, 2978-2990.
94. Rinaldo, D., Philipp, D. M., Lippard, S. J., and Friesner, R. A. (2007) *J. Am. Chem. Soc.* 129, 3135-3147.
95. Liu, K. E., Wang, D., Huynh, B. H., Edmondson, D. E., Salifoglou, A., and Lippard, S. J. (1994) *J. Am. Chem. Soc.* 116, 7465-7466.
96. Valentine, A. M., Stahl, S. S., and Lippard, S. J. (1999) *J. Am. Chem. Soc.* 121, 3876-3887.
97. Murray, L. J., García-Serres, R., Naik, S., Huynh, B. H., and Lippard, S. J. (2006) *J. Am. Chem. Soc.* 128, 7459-7460.
98. Song, W. J., Behan, R. K., Naik, S., Huynh, B. H., and Lippard, S. J. (2009) *J. Am. Chem. Soc.* 131, 6074-6075.
99. Bollinger, J. M. J., Edmondson, D. E., Huynh, B. H., Filley, J., Norton, J. R., and Stubbe, J. (1991) *Science* 253, 292-298.

100. Yun, D., García-Serres, R., Chicalese, B. M., An, Y. H., Huynh, B. H., and Bollinger, J. M. J. (2007) *Biochemistry* 46, 1925-1932.
101. Baldwin, J., Voegtli, W. C., Khidekel, N., Moënné-Loccoz, P., Krebs, C., Pereira, A. S., Ley, B. A., Huynh, B. H., Loehr, T. M., Riggs-Gelasco, P. J., Rosenzweig, A. C., and Bollinger, J. M. J. (2001) *J. Am. Chem. Soc.* 123, 7017-7030.
102. Bollinger, J. M. J., Krebs, C., Vicol, A., Chen, S., Ley, B. A., Edmondson, D. E., and Huynh, B. H. (1998) *J. Am. Chem. Soc.* 120, 1094-1095.
103. Moënné-Loccoz, P., Baldwin, J., Ley, B. A., Loehr, T. M., and Bollinger, J. M. J. (1998) *Biochemistry* 37, 14659-14663.
104. Skulan, A. J., Brunold, T. C., Baldwin, J., Saleh, L., Bollinger Jr., J. M., and Solomon, E. I. (2004) *J. Am. Chem. Soc.* 126, 8842-8855.
105. Broadwater, J. A., Achim, C., Münck, E., and Fox, B. G. (1999) *Biochemistry* 38, 12197-12204.
106. Broadwater, J. A., Ai, J., Loehr, T. M., Sanders-Loehr, J., and Fox, B. G. (1998) *Biochemistry* 37, 14664-14671.
107. Hwang, J., Krebs, C., Huynh, B. H., Edmondson, D. E., Theil, E. C., and Penner-Hahn, J. E. (2000) *Science* 287, 122-125.
108. Moënné-Loccoz, P., Krebs, C., Herlihy, K., Edmondson, D. E., Theil, E. C., Huynh, B. H., and Loehr, T. M. (1999) *Biochemistry* 38, 5290-5295.
109. Pereira, A. S., Small, W., Krebs, C., Tavares, P., Edmondson, D. E., Theil, E. C., and Huynh, B. H. (1998) *Biochemistry* 37, 9871-9876.
110. Vu, V. V., Emerson, J. P., Martinho, M., Kim, Y. S., Münck, E., Park, M. H., and Que Jr., L. (2009) *Proc. Natl. Acad. Sci. USA* 106, 14814-14819.

111. Korboukh, V. K., Li, N., Barr, E. W., Bollinger, J. M. J., and Krebs, C. (2009) *J. Am. Chem. Soc.* *131*, 13608-13609.
112. Bailey, L. J., and Fox, B. G. (2009) *Biochemistry* *48*, 8932-8939.
113. Tinberg, C., and Lippard, S. J. (2009) *Biochemistry* *48*, 12145-12158.
114. Kim, K., and Lippard, S. J. (1996) *J. Am. Chem. Soc.* *118*, 4914-4915.
115. Han, W.-G., and Noodleman, L. (2008) *Inorg. Chem.* *47*, 2975-2986.
116. Lee, S.-K., and Lipscomb, J. D. (1999) *Biochemistry* *38*, 4423-4432.
117. Lee, S.-K., Fox, B. G., Froland, W. A., Lipscomb, J. D., and Münck, E. (1993) *J. Am. Chem. Soc.* *115*, 6450-6451.
118. Tinberg, C. (2010) Exploring the Reactivity of Bacterial Multicomponent Monooxygenases, Ph.D. Thesis (Massachusetts Institute of Technology, Cambridge, MA).
119. Saleh, L., Krebs, C., Ley, B. A., Naik, S., Huynh, B. H., and Bollinger Jr., J. M. (2004) *Biochemistry* *43*, 5953-5964.
120. Zhang, X., Furutachi, H., Fujinami, S., Nagatomo, S., Maeda, Y., Watanabe, Y., Kitagawa, T., and Suzuki, M. (2005) *J. Am. Chem. Soc.* *127*, 826-827.
121. Dong, Y., Zang, Y., Shu, L., Wilkinson, E. C., Que Jr., L., Kauffmann, K., and Münck, E. (1997) *J. Am. Chem. Soc.* *119*, 12683-12684.
122. Kodera, M., Taniike, Y., Itoh, M., Tanahashi, Y., Shimakoshi, H., Kano, K., Hirota, S., Iijima, S., Ohba, M., and Okawa, H. (2001) *Inorg. Chem.* *40*, 4821-4822.
123. Siegbahn, P. E. M. (2001) *J. Biol. Inorg. Chem.* *6*, 27-45.

124. Bochevarov, A. D., Li, J., Song, W. J., Friesner, R. A., and Lippard, S. J. (2010) *Submitted to J. Am. Chem. Soc.*
125. Shu, L., Nesheim, J. C., Kauffmann, K., Münck, E., Lipscomb, J. D., and Que, L. J. (1997) *Science* 275, 515-518.
126. Bollinger, J. M. J., Tong, W. H., Ravi, N., Huynh, B. H., Edmondson, D. E., and Stubbe, J. (1994) *J. Am. Chem. Soc.* 116, 8015-8023.
127. Sturgeon, B., Burdi, D., Chen, S., Huynh, B. H., Edmondson, D. E., Stubbe, J., and Hoffman, B. M. (1996) *J. Am. Chem. Soc.* 118, 7551-7557.
128. Riggs-Gelasco, P. J., Shu, L., Chen, S., Burdi, D., Huynh, B. H., Que Jr., L., and Stubbe, J. (1998) *J. Am. Chem. Soc.* 120, 849-860.
129. Valentine, A. M., Tavares, P., Pereira, A. S., Davydov, R., Krebs, C., Hoffman, B. M., Edmondson, D. E., Huynh, B. H., and Lippard, S. J. (1998) *J. Am. Chem. Soc.* 120, 2190-2191.
130. Murray, L. J., García-Serres, R., McCormick, M. S., Davydov, R., Naik, S., Kim, S.-H., Hoffman, B. M., Huynh, B. H., and Lippard, S. J. (2007) *Biochemistry* 46, 14795-14809.
131. Dong, Y., Fujii, Hendrich, M. P., Leising, R. A., Pan, G., Randall, C. R., Wilkinson, E. C., Zang, Y., Que Jr., L., Fox, B. G., Kauffmann, K., and Münck, E. (1995) *J. Am. Chem. Soc.* 117, 2778-2792.
132. Dong, Y., and Que Jr., L. (1995) *J. Am. Chem. Soc.* 117, 11377-11378.
133. Hsu, H.-F., Dong, Y., Shu, L., Young Jr., V., and Que Jr., L. (1999) *J. Am. Chem. Soc.* 121, 5230-5237.

134. Xue, G., Wang, D., De Hont, R., Fiedler, A. T., Shan, X., Münck, E., and Que Jr., L. (2007) *Proc. Natl. Acad. Sci. USA* 104, 52.
135. Han, W.-G., and Noodleman, L. (2008) *Inorg. Chim. Acta* 361, 973-986.
136. Rowe, G. T., Rybak-Akimova, E. V., and Caradonna, J. P. (2007) *Inorg. Chem.* 46, 10594-10606.
137. Xue, G., De Hont, R., Münck, E., and Que Jr., L. (2010) *Nat. Chem.* 2, 400-405.
138. Bollinger, J. M. J., Tong, W. H., Ravi, N., Huynh, B. H., Edmondson, D. E., and Stubbe, J. (1994) *J. Am. Chem. Soc.* 116, 8024-8032.
139. Ravi, N., Bollinger, J. M. J., Huynh, B. H., Stubbe, J., and Edmondson, D. E. (1994) *J. Am. Chem. Soc.* 116, 8007-8014.
140. Shanmugam, M., Doan, P. E., Lees, N. S., Stubbe, J., and Hoffman, B. M. (2009) *J. Am. Chem. Soc.* 131, 3370-3376.
141. Baldwin, J., Krebs, C., Ley, B. A., Edmondson, D. E., Huynh, B. H., and Bollinger, J. M. J. (2000) *J. Am. Chem. Soc.* 122, 12195-12206.
142. Krebs, C., Chen, S., Baldwin, J., Ley, B. A., Patel, U., Edmondson, D. E., Huynh, B. H., and Bollinger Jr., J. M. (2000) *J. Am. Chem. Soc.* 122, 12207-12219.
143. Bollinger Jr., J. M., and Stubbe, J. (1991) *J. Am. Chem. Soc.* 113, 6291-6293.
144. Mitić, N., Clay, M. D., Saleh, L., Bollinger Jr., J. M., and Solomon, E. I. (2007) *J. Am. Chem. Soc.* 129, 9049-9065.
145. Ling, J., Sahlin, M., Sjöberg, B.-M., Loehr, T. M., and Sanders-Loehr, J. (1994) *J. Biol. Chem.* 269, 5595-5601.
146. Burdi, D., Sturgeon, B., Tong, W. H., Stubbe, J., and Hoffman, B. M. (1996) *J. Am. Chem. Soc.* 118, 281-282.

147. Burdi, D., Willems, J.-P., Riggs-Gelasco, P. J., Anthroline, W. E., Stubbe, J., and Hoffman, B. M. (1998) *J. Am. Chem. Soc.* *120*, 12910-12919.
148. Han, W.-G., and Noodleman, L. (2009) *Dalton Trans.*, 6045-6057.
149. Andersson, K. K., Froland, W. A., Lee, S.-K., and Lipscomb, J. D. (1991) *New J. Chem.* *15*, 411-415.
150. Jiang, Y., Wilkins, P. C., and Dalton, H. (1993) *Biochim. Biophys. Acta* *1163*, 105-112.
151. Newcomb, M., Chandrasena, R. E. P., Lansakara-P., D. S. P., Kim, H.-Y., Lippard, S. J., Beauvais, L. G., Murray, L. J., Izzo, V., Hollenberg, P. F., and Coon, M. J. (2007) *J. Org. Chem.* *72*, 1121-1127.
152. Newcomb, M., Lansakara-P., D. S. P., Kim, H.-Y., Chandrasena, R. E. P., Lippard, S. J., Beauvais, L. G., Murray, L. J., Izzo, V., Hollenberg, P. F., and Coon, M. J. (2007) *J. Org. Chem.* *72*, 1128-1133.
153. Moe, L. A., Hu, Z., Deng, D., Austin, R. N., Groves, J. T., and Fox, B. G. (2004) *Biochemistry* *43*, 15688-15701.
154. Valentine, A. M., Wilkinson, B., Liu, K. E., Komar-Panicucci, S., Priestley, N. D., Williams, P. G., Morimoto, H., Floss, H. G., and Lippard, S. J. (1997) *J. Am. Chem. Soc.* *119*, 1818-1827.
155. Priestley, N. D., Floss, H. G., Froland, W. A., Lipscomb, J. D., Williams, P. G., and Morimoto, H. (1992) *J. Am. Chem. Soc.* *114*, 7561-7562.
156. Sears, T. J., Johnson, P. M., Jin, P., and Oatis, S. (1996) *J. Chem. Phys.* *104*, 781-793.



157. Brazeau, B. J., Austin, R. N., Tarr, C., Groves, J. T., and Lipscomb, J. D. (2001) *J. Am. Chem. Soc.* *123*, 11831-11837.
158. Choi, S.-Y., Eaton, P. E., Hollenberg, P. F., Liu, K. E., Lippard, S. J., Newcomb, M., Putt, D., A., Upadhyaya, S. P., and Xiong, Y. (1996) *J. Am. Chem. Soc.* *118*, 6547-6555.
159. Choi, S.-Y., Eaton, P. E., Kopp, D. A., Lippard, S. J., Newcomb, M., and Shen, R. (1999) *J. Am. Chem. Soc.* *121*, 12198-12199.
160. Jin, Y., and Lipscomb, J. D. (1999) *Biochemistry* *38*, 6178-6186.
161. Jin, Y., and Lipscomb, J. D. (2000) *Biochim. Biophys. Acta* *1543*, 47-59.
162. Liu, K. E., Johnson, C. C., Newcomb, M., and Lippard, S. J. (1993) *J. Am. Chem. Soc.* *115*, 939-947.
163. Newcomb, M., Shen, R., Lu, Y., Coon, M. J., Hollenberg, P. F., Kopp, D. A., and Lippard, S. J. (2002) *J. Am. Chem. Soc.* *124*, 6879-6886.
164. Ruzicka, F., Huang, D.-S., Donnelly, M. I., and Frey, P. A. (1990) *Biochemistry* *29*, 1696-1700.
165. Valentine, A. M., LeTadic-Biadatti, M.-H., Toy, P. H., Newcomb, M., and Lippard, S. J. (1999) *J. Biol. Chem.* *274*, 10771-10776.
166. Dalton, H., Golding, B. T., and Waters, B. W. (1981) *J. Chem. Soc., Chem. Comm.*, 482-483.
167. Mitchell, K. H., Rogge, C. E., Gierahn, T., and Fox, B. G. (2003) *Proc. Natl. Acad. Sci. USA* *100*, 3784-3789.
168. Guroff, G., Daly, J. W., Jerina, D. M., Renson, J., Witkop, B., and Udenfriend, S. (1967) *Science* *157*, 1524-1530.

169. Whited, G. M., and Gibson, D. T. (1991) *J. Bacteriol.* *173*, 3010-3016.
170. Brazeau, B. J., and Lipscomb, J. D. (2000) *Biochemistry* *39*, 13503-13515.
171. Muthusamy, M., Ambundo, E. A., George, S. J., Lippard, S. J., and Thorneley, R. N. F. (2003) *J. Am. Chem. Soc.* *125*, 11150-11151.
172. Nesheim, J. C., and Lipscomb, J. D. (1996) *Biochemistry* *35*, 10240-10247.
173. Ambundo, E. A., Friesner, R. A., and Lippard, S. J. (2002) *J. Am. Chem. Soc.* *124*, 8770-8771.
174. Lippard, S. J. (2005) *Phil. Trans. R. Soc. A* *363*, 861-877.
175. Beauvais, L. G., and Lippard, S. J. (2005) *J. Am. Chem. Soc.* *127*, 7370-7378.
176. Baik, M.-H., Gherman, B. F., Friesner, R. A., and Lippard, S. J. (2002) *J. Am. Chem. Soc.* *124*, 14608-14615.
177. Gherman, B. F., Dunietz, B. D., Whittington, D. A., Lippard, S. J., and Friesner, R. A. (2001) *J. Am. Chem. Soc.* *123*, 3836-3837.
178. Gherman, B. F., Lippard, S. J., and Friesner, R. A. (2005) *J. Am. Chem. Soc.* *127*, 1025-1037.
179. Guallar, V., Gherman, B. F., Miller, W. H., Lippard, S. J., and Friesner, R. A. (2002) *J. Am. Chem. Soc.* *124*, 3377-3384.

## Chapter 2

### **Revisiting the Mechanism of Dioxygen Activation in Soluble Methane Monooxygenase from *M. capsulatus* (Bath): Evidence for a Multi-Step, Proton- Dependent Reaction Pathway\***

\*Reproduced in part with permission from *Biochemistry*

C. E. Tinberg and S. J. Lippard. *Biochemistry* **2009** 48, 12145-12158

© 2009 American Chemical Society

## INTRODUCTION

Methane monooxygenases (MMOs) from methanotrophic bacteria catalyze the remarkable oxidation of methane to methanol at ambient temperatures and pressures (1). One enzyme responsible for this process in the methanotroph *Methylococcus capsulatus* (Bath), hereafter *Mc*, is soluble methane monooxygenase (sMMO) (2). sMMO requires three protein components for efficient catalysis. A dimeric hydroxylase (MMOH) houses two copies of a carboxylate-bridged diiron active site, a reductase (MMOR) acquires electrons from NADH and transfers them to the hydroxylase, and a regulatory protein (MMOB) couples electron consumption to substrate oxidation. The resting state of the hydroxylase ( $H_{ox}$ ) active site is a di( $\mu$ -hydroxo)( $\mu$ -carboxylato)diiron(III) species. Upon two-electron reduction to the diiron(II) form ( $H_{red}$ ), the bridging hydroxide ligands dissociate and the diiron center reacts rapidly with  $O_2$  in the presence of MMOB. The events that occur as a result of this reaction have been characterized by multiple spectroscopic methods, and a series of oxygenated-iron intermediates accumulate prior to regeneration of the enzyme resting state (3-7).

Early studies relied on Mössbauer spectroscopy to probe the reaction of  $MMOH_{red}$  with  $O_2$  (6, 7). The first species observed by this method after addition of  $O_2$  is a peroxodiiron(III) unit comprising two antiferromagnetically coupled iron centers of indistinguishable Mössbauer parameters  $\delta = 0.66$  mm/s and  $\Delta E_Q = 1.51$  mm/s. UV-vis spectroscopy also supported the formation of a peroxodiiron(III) species displaying peroxo-to-iron charge transfer optical bands centered around 720 nm ( $\epsilon = 1800$  M<sup>-1</sup> cm<sup>-1</sup>) and 420 nm ( $\epsilon = 4000$  M<sup>-1</sup> cm<sup>-1</sup>) as the first observable intermediate (8, 9). The signals arising from Mössbauer and optical spectroscopy were attributed to the same

peroxodiiron(III) unit because the decay rates measured by these two methods were identical, and this species was termed  $H_{\text{peroxo}}$ .<sup>1</sup> The formation rates reported by these two methods differed by an order of magnitude, however. The presence of multiple peroxodiiron(III) species with similar Mössbauer parameters but distinct optical signatures was suggested to explain this disparity, although there was no direct evidence for this proposal. The presence of various peroxodiiron(III) species that accumulate on the reaction pathway was later addressed in a study of  $O_2$  activation in MMOH from *M. trichosporium* OB3b, hereafter referred to as *Mt*, which provided direct evidence for an optically distinct  $H_{\text{peroxo}}$  precursor,  $P^*$  (3). Experiments on the *Mc* enzyme provided no such evidence for this species.

Much effort has been devoted to understanding the nature of  $H_{\text{peroxo}}$ . Attempts to elucidate the binding mode of the peroxo moiety have been unsuccessful and there is no consensus on the structure of this intermediate. Analogy to peroxodiiron(III) species generated in other non-heme diiron enzymes, such as those formed in the W48F/D84E variant of ribonucleotide reductase (RNR) (10, 11), at the ferroxidase center of frog M ferritin (12), in  $\Delta^9$ -desaturase (13), and in human deoxyhypusine hydroxylase (14), supports a symmetric *cis*- $\mu$ -1,2 peroxide binding configuration. Some theoretical studies confirm this assignment (15), whereas others favor a nonplanar  $\mu$ - $\eta^2$ : $\eta^2$  geometry (16-18). The protonation state of the  $H_{\text{peroxo}}$  peroxo moiety also remains an unanswered question.

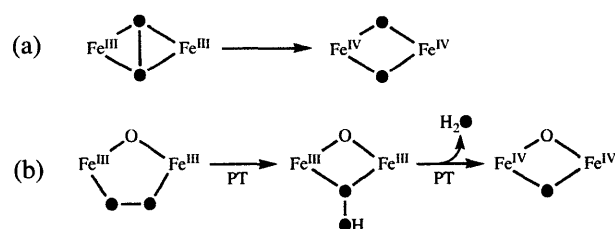
$H_{\text{peroxo}}$  oxidizes electron rich substrates such as propylene (9) and diethyl ether (8); however, in the absence of such substrates it rapidly decays to intermediate Q, an

---

<sup>1</sup>  $H_{\text{peroxo}}$  is denoted P in studies of sMMO from *M. trichosporium* OB3b.

antiferromagnetically coupled diiron(IV) unit responsible for methane oxidation. Structural characterization of Q by EXAFS spectroscopy revealed a short Fe–Fe distance of 2.46 Å from which a di( $\mu$ -oxo)diiron(IV) “diamond core” was postulated (19). The intense optical bands of Q centered at 350 nm ( $\epsilon = 3600 \text{ M}^{-1} \text{ cm}^{-1}$ ) and 420 nm ( $\epsilon = 7200 \text{ M}^{-1} \text{ cm}^{-1}$ ) that trail into the near infrared ( $\epsilon_{720} \approx 1000 \text{ M}^{-1} \text{ cm}^{-1}$ ) have been used as a handle for mechanistic studies (4-7). Q is thought to be responsible for oxidation of a variety of substrates (3, 5, 6, 9, 20), a process that might occur via two single-electron transfer events from substrate to Q in a manner that generates a transient bound radical species (21). In the absence of substrate, Q decays slowly to  $\text{H}_{\text{ox}}$  by an unknown pathway that requires the acquisition of two electrons and two protons at the diiron center. The mechanism by which this process occurs has not received much, if any, attention in the literature.

Another enigmatic aspect of MMOH catalysis is the mechanism of  $\text{H}_{\text{peroxo}}$  to Q conversion and concomitant O–O bond cleavage. Two distinct mechanisms have been proposed for this transformation based on existing inorganic chemistry (Scheme 2.1). The first involves homolytic O–O bond scission and concerted rearrangement of an  $\text{H}_{\text{peroxo}} \mu\text{-}\eta^2:\eta^2$  core to form intermediate Q in a manner similar to established peroxodicopper(II) transformations (22, 23). The second includes proton-promoted heterolytic O–O bond cleavage and rearrangement of the diiron center, a mechanism analogous to the generally accepted route of O–O bond scission in cytochrome P450 enzymes (24, 25). Key differences between these two proposed mechanisms are the origin of the two bridging oxygen atoms of Q and the proton requirement for the O–O bond-breaking process.



**Scheme 2.1.** Two Possible Mechanisms of O–O Bond Cleavage in MMOH, Depicting Oxygen Atoms Derived from O<sub>2</sub> as Filled Circles

Results from kinetic investigations of the proton requirement of H<sub>peroxo</sub> to Q conversion in the *Mc* and *Mt* enzymes are contradictory. The rate constants associated with H<sub>peroxo</sub> formation and H<sub>peroxo</sub> decay/Q formation in *Mt* MMOH are pH-dependent and display normal solvent kinetic isotope effects (KSIE) in proton inventory studies, results that implicate rate-limiting transfer of a single proton in both steps (26). The slopes of the proton inventory plots led the authors to conclude that H<sub>peroxo</sub> formation and its subsequent conversion to Q involve addition of two protons to an iron-bound peroxide oxygen atom followed by heterolytic O–O bond scission coupled to release of a water molecule. However, studies of MMO from *Mc* found that these processes were neither pH-dependent nor exhibited KSIEs greater than unity, consistent with proton transfer not being rate-limiting in either of these steps (6). A reconciliation of these results is important for understanding the H<sub>peroxo</sub> to Q pathway and the O–O bond cleavage mechanism in this enzyme, elucidating the protonation state and structure of H<sub>peroxo</sub>, and guiding experiments to devise synthetic models for the reaction chemistry.

Although these previous studies provide a framework for understanding O<sub>2</sub> activation for attack on the strong and kinetically difficult to access C–H bond of methane, many

aspects of MMOH catalysis remain vague. To clarify some of the ambiguities, we have in the present chapter employed stopped-flow optical spectroscopy to reexamine the mechanism of dioxygen activation in MMOH from *Mc*. Our findings provide direct evidence for a multi-step reaction pathway in which a minimum of four oxygenated-iron intermediates accumulate, including P\* previously identified in the *Mt* enzyme as well as a novel species termed Q\*. Q\* forms as a result of Q decay and is not reactive toward methane. Comparison of these results to previous work reveals that the H<sub>peroxo</sub> species formerly characterized by optical and Mössbauer spectroscopy are actually two distinct peroxodiiron(III) intermediates rather than one single entity. Additionally, in contrast with previous reports from the *Mc* enzyme, our data show that H<sub>peroxo</sub> formation and H<sub>peroxo</sub> decay/Q formation are both pH-dependent and exhibit normal KIEs, as found for the *Mt* MMOH. The results indicate that both processes involve rate-limiting proton transfer steps, and mechanisms to explain these results are discussed.

## MATERIALS AND METHODS

*General Considerations.* Hydroxylase protein (MMOH) was purified from *Methylococcus capsulatus* (Bath) as previously described, except that a Q Sepharose fast flow anion exchange column (4 x 50 cm) was used in place of the final MonoQ column (8). Protein obtained by this procedure typically exhibited specific activities of 400-500 mU/mg for propylene oxidation at 45 °C and iron contents of  $4.0 \pm 0.2$  iron atoms per protein dimer (8, 9). The regulatory (MMOB) and reductase (MMOR) proteins were expressed recombinantly in *E. coli* and purified by established methods (27, 28). The buffer system employed in all experiments was 25 mM potassium phosphate ( $6.6 \leq \text{pH} \leq$



8.6), prepared by adding the appropriate volumes of 1 M  $K_2HPO_4$  and 1 M  $KH_2PO_4$  to ddH<sub>2</sub>O and adjusting the pH using HCl or NaOH. Distilled water was deionized with a MilliQ filtering system. Methane (99.9%) was purchased from Airgas (Independence, OH). All other chemicals were obtained from Aldrich and used as received.

*Stopped-Flow Optical Spectroscopy.* Single turnover transient kinetic experiments were performed on a Hi-Tech Scientific (Salisbury, UK) SF-61 DX stopped-flow spectrophotometer made anaerobic by flushing the flow circuit extensively with ~10 mM  $Na_2S_2O_4$  and then  $N_2$ -purged buffer. A protein solution containing MMOH<sub>red</sub> and 2 equiv of MMOB was prepared by reduction with  $Na_2S_2O_4$  in the presence of methyl viologen, as described previously except that 25 mM potassium phosphate buffer was used instead of MOPS (9). Excess reducing agent was removed by dialyzing the mixture twice against 500 mL buffer for ~1 hr each. Following dialysis, the protein was transferred to the anaerobic stopped-flow instrument in a glass tonometer.

For stopped-flow experiments performed in the absence of substrate, reduced protein solution was mixed rapidly with an equal volume of O<sub>2</sub>-saturated buffer of the appropriate pH. For experiments performed in the presence of substrate, the reduced protein solution was mixed with an equal volume of buffer containing CH<sub>4</sub> and O<sub>2</sub>. Double-mixing stopped-flow (DX-SF) experiments were performed by introducing a solution of substrate-containing buffer at the time of maximization of the intermediate of interest. Substrate solutions were prepared by drawing the appropriate volumes of O<sub>2</sub>- and CH<sub>4</sub>-saturated buffers into a 10 mL gastight Hamilton syringe. Approximate methane and dioxygen concentrations were calculated using the solubility constants of gaseous

CH<sub>4</sub> and O<sub>2</sub> in water at 20 °C, the temperature at which the solutions were prepared (1.54 mM for CH<sub>4</sub> and 1.39 mM for O<sub>2</sub>) (29).

Q photodecomposes in response to the Xe lamp of the diode array apparatus (9); therefore, reactions investigating Q and events resulting from Q decay were all collected at single wavelengths using the photomultiplier tube, limiting the number of data points that could be obtained. Data were collected using Kinetic Studios (Hi-Tech Scientific) and fit with KaleidaGraph v 3.6 (Synergy Software) and Origin v 6.1 (OriginLab Corporation). Reactions were maintained at the appropriate temperature using a circulating water bath. The concentration of MMOH in the optical cell after mixing was 50 μM in all experiments unless otherwise noted. All experiments except for those included in Eyring analyses were carried out at least in triplicate using a minimum of three different batches of proteins.

*KSIE Measurements.* Deuterium oxide (99.9%) was purchased from Cambridge Isotope Laboratories (Andover, MA). Buffers containing 25 mM potassium phosphate (pD 7.0) were prepared by adding weighed mixtures of K<sub>2</sub>HPO<sub>4</sub> and KH<sub>2</sub>PO<sub>4</sub> to the appropriate amount of D<sub>2</sub>O. The pD of the buffer was adjusted with DCl, where pD = “pH meter reading” + 0.4. MMOH and MMOB were individually exchanged into D<sub>2</sub>O buffer by three repeated rounds of concentration and dilution in Amicon centrifugal concentrators (Millipore, Billerica, MA) over the course of 4 h, which was found to be sufficient for exchange. Protein solutions were prepared and reduced as noted above, except that dialyses were carried out in D<sub>2</sub>O buffer for ~1.5 h each. All KSIE experiments were performed at 5 °C. Adequate comparisons to data collected in H<sub>2</sub>O at 4 °C could be made because the one degree temperature difference had a negligible effect on the rate

constants. Approximate methane concentrations for these experiments were calculated using the solubility constant of gaseous CH<sub>4</sub> in D<sub>2</sub>O at 20 °C (1.64 mM) (29).

*Data Analysis.* Except where noted, all experiments were performed under first-order or pseudo-first order conditions and were analyzed accordingly. Multiple chemically reasonable kinetic models were considered when analyzing the results of stopped-flow studies probing the reactions of MMOH<sub>red</sub> and 2 equiv of MMOB with O<sub>2</sub> and O<sub>2</sub>/CH<sub>4</sub> mixtures. The kinetic solutions reported here are those that required the minimum number of variable parameters to adequately fit the data. Data fits were evaluated by examining the magnitude of the difference between the fit and the data at every data point collected (residual plots) and were accepted or rejected on the basis of these fit residuals, the reduced chi-squared value describing the goodness-of-fit ( $\chi^2_{\text{red}} = \chi^2/\text{degrees of freedom}$ ), and the parameter dependencies.

## RESULTS

*MMOH<sub>red</sub>:2B + O<sub>2</sub>: Reactions in the Presence of Methane.* Results of numerous studies provide compelling evidence that intermediate Q is the oxygenated iron species responsible for methane oxidation and it is generally accepted that H<sub>peroxo</sub> does not react with this substrate. To reinvestigate H<sub>peroxo</sub> formation and decay and to identify other optically significant events that occur prior to formation of Q, we reasoned that the dominant optical signal of Q will be suppressed if sufficiently high concentrations of this substrate are present such that the rate of Q decay exceeds that of its formation. Under these conditions, the weaker optical signatures of preceding intermediates can be

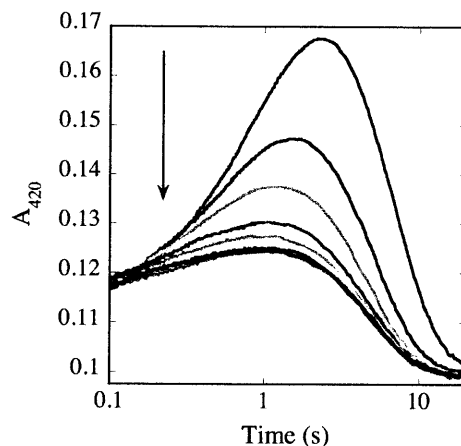


**Figure 2.1.** Representative 420 nm absorbance profiles for the reactions of 50  $\mu\text{M}$   $\text{MMOH}_{\text{red}}$  and 100  $\mu\text{M}$   $\text{MMOB}$  with a mixture of  $\text{O}_2$  and  $\text{CH}_4$  at pH 7.0 and 4  $^\circ\text{C}$ .  $[\text{CH}_4] = 77 \mu\text{M}$  (purple), 154  $\mu\text{M}$  (blue), 231  $\mu\text{M}$  (cyan), 308  $\mu\text{M}$  (aqua), 385  $\mu\text{M}$  (dark green), 462  $\mu\text{M}$  (light green), 500  $\mu\text{M}$  (yellow), 539  $\mu\text{M}$  (orange), 578  $\mu\text{M}$  (red), 616  $\mu\text{M}$  (maroon). Data collected on separate occasions with different batches of protein yielded similar results.

uncovered and evaluated by kinetic methods. Stopped-flow optical spectroscopy was therefore employed to monitor the optical changes that occur at 420 nm upon mixing  $\text{MMOH}_{\text{red}}$  and 2 equiv of  $\text{MMOB}$  with a solution containing  $\text{O}_2$  and  $\text{CH}_4$  (Figure 2.1). At low methane concentrations ( $< \sim 540 \mu\text{M}$ ), the optical signal changes with increasing substrate concentration, suggesting that Q accumulates under these conditions. However, at methane concentrations  $\geq \sim 540 \mu\text{M}$ , the optical signal no longer changes with increasing substrate concentration, indicating that Q does not build up, presumably because of rapid reaction with the substrate. Although the optical signal of Q is fully suppressed when  $[\text{CH}_4] \geq 540 \mu\text{M}$ , a time-dependent rise and decay in absorbance at 420 nm is observed, indicating the presence of at least one intermediate that is unaffected by methane and absorbs at this wavelength (Figure 1). Because  $\text{H}_{\text{peroxo}}$  absorbs at 420 nm (8,

9), it is reasonable to assume that this intermediate contributes to some of or all of the observed signal.

To investigate the processes associated with the rise and decay in absorbance observed at  $[\text{CH}_4] \geq 540 \mu\text{M}$  and to determine whether it is solely due to absorbance by  $\text{H}_{\text{peroxo}}$ , data collected under these conditions at 420 nm and 720 nm were fit using non-linear least squares methodology. Previous studies probing the reaction of  $\text{MMOH}_{\text{red}}$  and 2 equiv of  $\text{MMOB}$  with  $\text{O}_2$  have generally relied on fitting single-wavelength data to obtain kinetic information about the processes that occur as a result of this reaction. Here, we found that fitting single-wavelength data sets to sums of exponentials or to analytical kinetic models often resulted in solutions that appeared satisfactory for the data being analyzed but were poor descriptors of data collected under the same conditions at different wavelengths. By fitting data collected at only a single wavelength it was therefore easy to converge upon an incorrect solution. A more reliable method of fitting the kinetic traces was afforded by collecting data at a minimum of two wavelengths and simultaneously fitting these data sets using shared rate constant parameters (30). This approach reduces the number of parameters to be fit by adding constraints and therefore increases our confidence that the model used to fit the data is correct if a satisfactory result is obtained.

Using this method, we observed that the rise and decay in absorbance in the presence of high concentrations of methane did not fit well to a sum of two exponentials describing the process  $\text{H}_{\text{red}} \rightarrow \text{H}_{\text{peroxo}} \rightarrow \text{H}_{\text{ox}}$  described previously for *Mc* experiments conducted in the presence of methane (Figure 2.2a) (9). Instead, the data fit well to a sum of three exponentials representing a minimum of three processes, as reported for the *Mt* system (Figure 2.2b) (3). Two of those processes must arise from  $\text{H}_{\text{peroxo}}$  formation and from

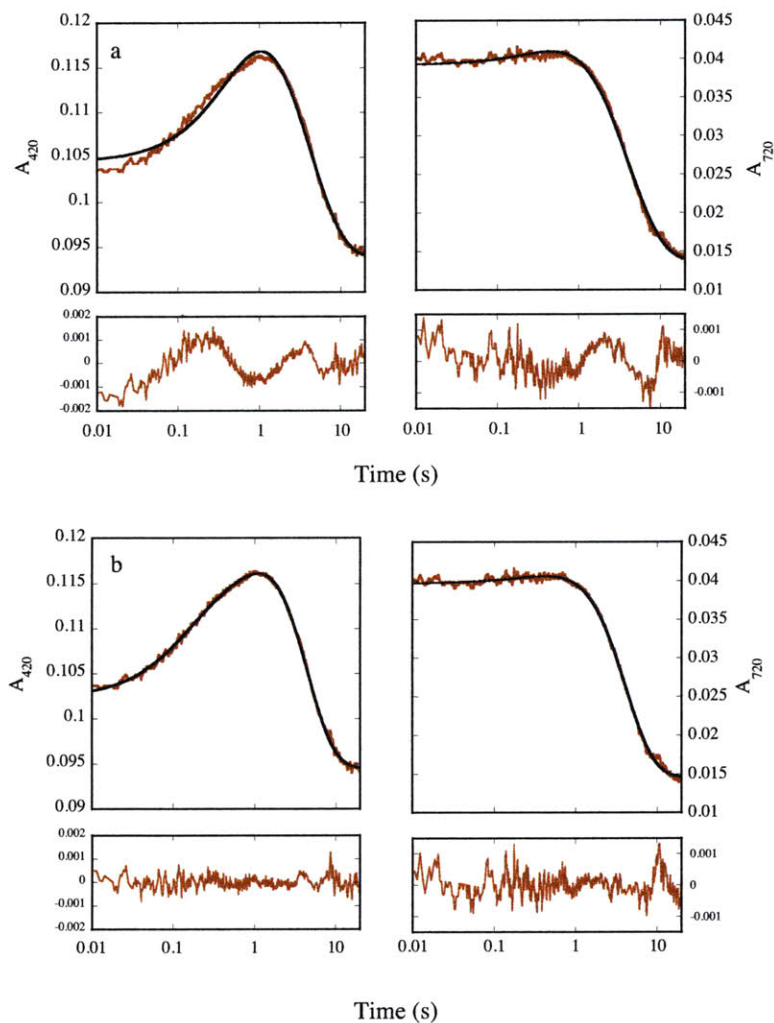
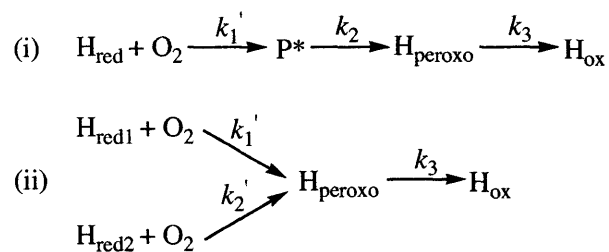


**Figure 2.2.** Exponential fits of data monitoring the reaction of 50  $\mu\text{M}$   $\text{MMOH}_{\text{red}}$  and 100  $\mu\text{M}$   $\text{MMOB}$  with  $\sim 210 \mu\text{M}$   $\text{O}_2$  in the presence of 540  $\mu\text{M}$   $\text{CH}_4$  at pH 7.0 and 4  $^\circ\text{C}$ . Data collected at 420 nm and 720 nm (red lines) were fit simultaneously (black lines) to a sum of two exponentials (a) or three exponentials (b). Residuals are depicted at the bottom of each plot.  $\chi^2_{\text{red}} = 3.52 \times 10^{-7}$  for the two exponential fit and  $1.01 \times 10^{-7}$  for the three exponential fit.

$\text{H}_{\text{peroxo}}$  decay. The additional feature observed in the data suggests one of the three following possibilities: (i) accumulation of an additional transient species on the reaction pathway, (ii) two productive populations of  $\text{H}_{\text{red}}$  that proceed with different rate constants



**Scheme 2.2.** Models for the Reaction of  $\text{MMOH}_{\text{red}}$  and Two Equiv of  $\text{MMOB}$  with  $\text{O}_2$  in the Presence of 540  $\mu\text{M}$  Methane

to  $\text{H}_{\text{peroxo}}$  upon reaction with  $\text{O}_2$ , or (iii) two pathways that lead to  $\text{H}_{\text{peroxo}}$  decomposition with different rate constants. Although process i seems most likely, processes ii and iii could arise from a heterogeneous population of  $\text{MMOH/MMOB}$  complexes (5) or via a half-sites reactivity mechanism in which the two diiron sites in the hydroxylase react with  $\text{O}_2$  on different timescales (31). Possibility iii was rejected because truncation of the data to include only points following the time of maximal absorbance fit well to a single exponential decay process (data not shown). Furthermore, the amplitude describing the additional phase is positive in the exponential fit, suggesting that it contributes to the rise phase of the absorbance profile.

Possibilities i and ii were assessed by fitting the data to differential equations 2.1 and 2.2 describing the analytical solutions to models i and ii of Scheme 2.2.  $\text{H}_{\text{peroxo}}$  presumably

$$\text{Abs}_\lambda(t) = [\text{H}_{\text{red}}]_0 \left\{ \begin{array}{l}
 \varepsilon_{\text{H}_{\text{ox}}} + (\varepsilon_{\text{H}_{\text{red}}} - \varepsilon_{\text{H}_{\text{ox}}})(e^{-k_1' t}) + \left( (\varepsilon_{\text{P}^*} - \varepsilon_{\text{H}_{\text{ox}}}) \left( \frac{k_1'}{k_2 - k_1'} \right) (e^{-k_1' t} - e^{-k_2 t}) \right) + \\
 \left( (\varepsilon_{\text{H}_{\text{peroxo}}} - \varepsilon_{\text{H}_{\text{ox}}}) \left( \frac{k_1' k_2}{k_2 - k_1'} \right) \left\{ \left( \frac{1}{k_3 - k_1'} \right) (e^{-k_1' t} - e^{-k_3 t}) - \left( \frac{1}{k_3 - k_2} \right) (e^{-k_2 t} - e^{-k_3 t}) \right\} \right) \right\} \quad (2.1)
 \end{array} \right.$$

$$\begin{aligned} \text{Abs}_\lambda(t) = & \varepsilon_{\text{H}_{\text{red1}}}([\text{H}_{\text{red1}}]_0 + [\text{H}_{\text{red2}}]_0) + (\varepsilon_{\text{H}_{\text{red}}} - \varepsilon_{\text{H}_{\text{ox}}})[\text{H}_{\text{red1}}]_0 e^{-k_1 t} + (\varepsilon_{\text{H}_{\text{red}}} - \varepsilon_{\text{H}_{\text{ox}}})[\text{H}_{\text{red2}}]_0 e^{-k_2 t} \\ & + (\varepsilon_{\text{H}_{\text{peroxo}}} - \varepsilon_{\text{H}_{\text{ox}}}) \left( k_1' [\text{H}_{\text{red1}}]_0 \left( \frac{1}{k_3 - k_1'} \right) (e^{-k_1' t} - e^{-k_3 t}) + k_2' [\text{H}_{\text{red2}}]_0 \left( \frac{1}{k_3 - k_2'} \right) (e^{-k_2' t} - e^{-k_3 t}) \right) \end{aligned} \quad (2.2)$$

decays to Q under these conditions; however, because Q is depleted faster than it forms it does not accumulate and therefore does not have to be accounted for in the kinetic model. Fitting the data to eq 2.1, which includes an additional intermediate that precedes  $\text{H}_{\text{peroxo}}$  formation,  $\text{P}^*$ , afforded excellent results with  $k_1' = 6.7 \pm 0.9 \text{ s}^{-1}$ ,  $k_2 = 0.75 \pm 0.04 \text{ s}^{-1}$ , and  $k_3 = 0.34 \pm 0.03 \text{ s}^{-1}$  (Figure 2.3). The values of  $k_2$  and  $k_3$  measured in this work are the same as those reported for  $\text{H}_{\text{peroxo}}$  formation and decay by optical spectroscopy in MOPS buffer (8, 9). We have therefore assigned the second species as  $\text{H}_{\text{peroxo}}$  and the precursor that forms in the faster phase governed by  $k_1'$  as the novel transient  $\text{P}^*$ . In contrast, fits to

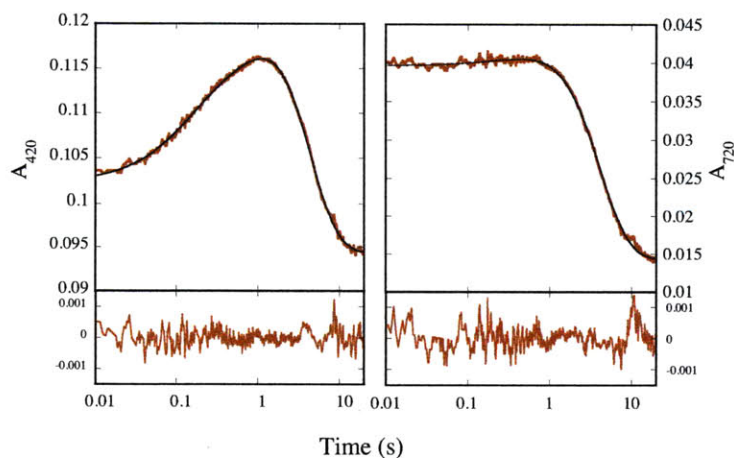


**Figure 2.3.** Representative fits of data monitoring the reaction of 50  $\mu\text{M}$   $\text{MMOH}_{\text{red}}$  and 100  $\mu\text{M}$   $\text{MMOB}$  with  $\sim 210 \mu\text{M}$   $\text{O}_2$  in the presence of 540  $\mu\text{M}$   $\text{CH}_4$  at pH 7.0 and 4  $^\circ\text{C}$ . Data collected at 420 nm (left, red lines) and 720 nm (right, red lines) were fit simultaneously to the  $\text{H}_{\text{red}} \rightarrow \text{P}^* \rightarrow \text{H}_{\text{peroxo}} \rightarrow \text{H}_{\text{ox}}$  model (eq 2.1). This method returned good fits (black lines) with acceptable residuals (bottom plots) and  $\chi^2_{\text{red}} < 1.07 \times 10^{-7}$ .



eq 2.2, which yielded similar rate constants, were not as satisfactory (Figure 2.4). The best fit from this model resulted when  $H_{\text{red}}$  comprised 20% of a rapidly reacting diiron population and 80% of a slowly reacting population, which is inconsistent with a half-sites reactivity mechanism. The fits obtained from this model demonstrated unacceptably large parameter error values and a worse  $\chi^2_{\text{red}}$  value than that obtained from fitting to process i. Also, the residual plots from these fits demonstrated sinusoidal behavior indicative of incorrect kinetic modeling. Therefore, both the goodness-of-fit parameters and fit residuals indicate that the  $H_{\text{red}} \rightarrow P^* \rightarrow H_{\text{peroxo}} \rightarrow H_{\text{ox}}$  model is more appropriate to describe the data.

*Kinetic Characterization of  $P^*$ .* Data collected at a variety of wavelengths in the presence of 540  $\mu\text{M}$   $\text{CH}_4$  were fit simultaneously to eq S1 by sharing rate constant

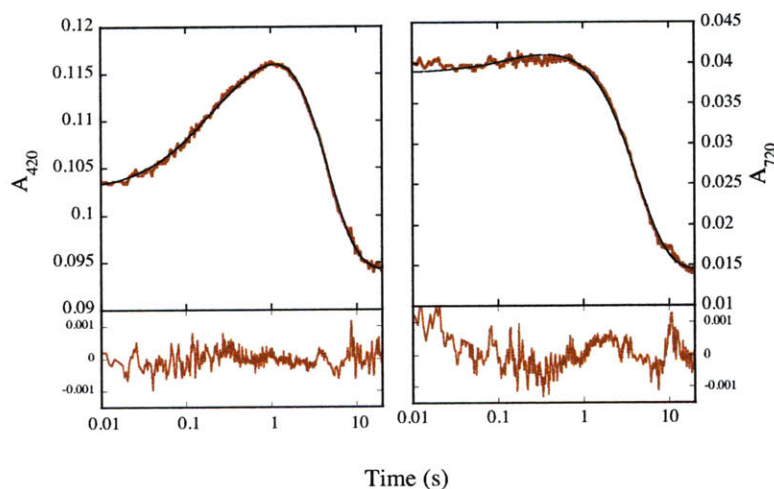


**Figure 2.4.** Fits of data monitoring the reaction of 50  $\mu\text{M}$   $\text{MMOH}_{\text{red}}$  and 100  $\mu\text{M}$   $\text{MMOB}$  with  $\sim 210 \mu\text{M}$   $\text{O}_2$  in the presence of 540  $\mu\text{M}$   $\text{CH}_4$  at pH 7.0 and 4  $^\circ\text{C}$ . Data collected at 420 nm (left, red lines) and 720 nm (right, red lines) were fit simultaneously to eq 2.2 describing Scheme 2.2ii. This best fit was obtained when  $[\text{H}_{\text{red}1}]$  and  $[\text{H}_{\text{red}2}]$  were let vary to yield  $[\text{H}_{\text{red}1}] = 20\%$  and  $[\text{H}_{\text{red}2}] = 80\%$ . This method yielded poor fits (black lines) with unacceptable parameter error, parameter dependence, residual plots (bottom), and  $\chi^2_{\text{red}} > 1.53 \times 10^{-7}$ .

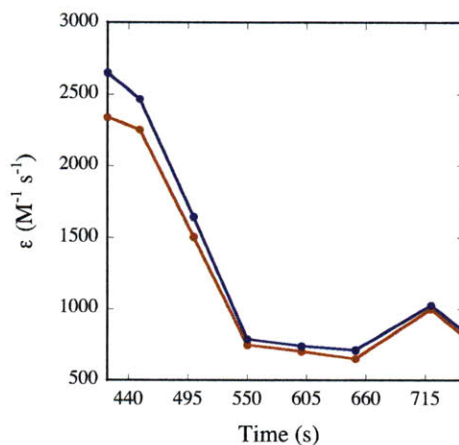


**Figure 2.5.** Approximate optical spectra of P\* (red line) and H<sub>peroxo</sub> (blue line) recorded at pH 7.0 and converted to molar extinction values. Spectra were obtained at 4 °C from data collected every 15 or 20 nm and analyzed by global fitting procedures described in the text.

parameters and setting  $[H_{red}]_0$  to 32  $\mu\text{M}$  to account for the observation that only 32% of the 100  $\mu\text{M}$  diiron sites in the sample proceed through a productive pathway (Figure 2.5) (6). The approximate extinction coefficients obtained were  $\epsilon_{420} \approx 3500 \text{ M}^{-1} \text{ cm}^{-1}$  and  $\epsilon_{720} \approx 1250 \text{ M}^{-1} \text{ cm}^{-1}$  for P\* and  $\epsilon_{420} \approx 3880 \text{ M}^{-1} \text{ cm}^{-1}$  and  $\epsilon_{720} \approx 1350 \text{ M}^{-1} \text{ cm}^{-1}$  for H<sub>peroxo</sub>, although these numbers are probably overestimated because the protein preparations used in these studies display significantly higher steady state activities than those previously employed to measure the percentage of active diiron sites (6). The similarities between the optical parameters of P\* and H<sub>peroxo</sub> reveal that the two intermediates are electronically identical. The dependence of  $k_1'$  on O<sub>2</sub> concentration was measured to probe the mechanism of P\* formation. No change was observed for  $k_1'$  or for the rate constants governing the subsequent steps when the concentration of O<sub>2</sub> was varied in the

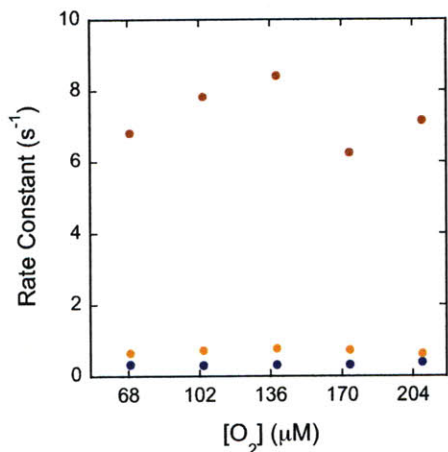


**Figure 2.6.** O<sub>2</sub>-dependence of P\* formation ( $k_1'$ , red), P\* decay/H<sub>peroxo</sub> formation ( $k_2$ , orange), and H<sub>peroxo</sub> decay ( $k_3$ , blue). Reactions of 50 μM MMOH<sub>red</sub> and 100 μM MMOB with O<sub>2</sub> were carried out in the presence of 540 μM CH<sub>4</sub> at pH 7.0 and 4 °C, and data were fit as noted in the text. All  $k_1'$  points are within the margin of error typically measured for this event.

experiments and the data were fit to eq 2.1, indicating that the first irreversible step in the reaction precedes P\* formation (Figure 2.6).<sup>2</sup>

*MMOH<sub>red</sub>:2B + O<sub>2</sub>: Reactions in the Absence of Methane.* Reactions of reduced MMOH and 2 equiv of MMOB with O<sub>2</sub> were monitored to study the events that occur when methane is not present. Previous experiments conducted in MOPS buffer indicated that the data should fit well to an analytical model describing the process H<sub>red</sub> → H<sub>peroxo</sub> → Q → H<sub>ox</sub> (8); however, data analyzed simultaneously at 20 different wavelengths spanning from 400 nm to 740 nm did not fit well to this solution (Figure 2.7) or to a sum of three exponentials describing the three processes involved in this model (Figure 2.8a).

<sup>2</sup>Because of limited solubility of O<sub>2</sub> in aqueous solutions and the need to use high CH<sub>4</sub> concentrations to monitor the rate of P\* formation, [O<sub>2</sub>] was not in sufficient excess over diiron sites at the lower O<sub>2</sub> concentrations employed to consider these experiments pseudo-first order. However, analysis of the data at low [O<sub>2</sub>] demonstrated identical absorbance profiles and rate constants for all steps, indicating that the first irreversible step occurs before the first event monitored and justifying the pseudo-first-order approximation implicit in the equation employed for data analysis.

Instead, the data fit well to a sum of four exponentials describing a minimum of four processes (Figure 2.8b). The values of the two fastest rate constants obtained from these fits are the same as those of the rate constants describing  $H_{\text{peroxo}}$  formation ( $k_2$ ) and decay ( $k_3$ ) measured in experiments performed in the presence of  $540 \mu\text{M CH}_4$  (vide supra), allowing us to unambiguously assign these events.<sup>3</sup>

To correlate the two slower observables with enzymatic events, two different chemically reasonable models were considered, and fits of the data to differential

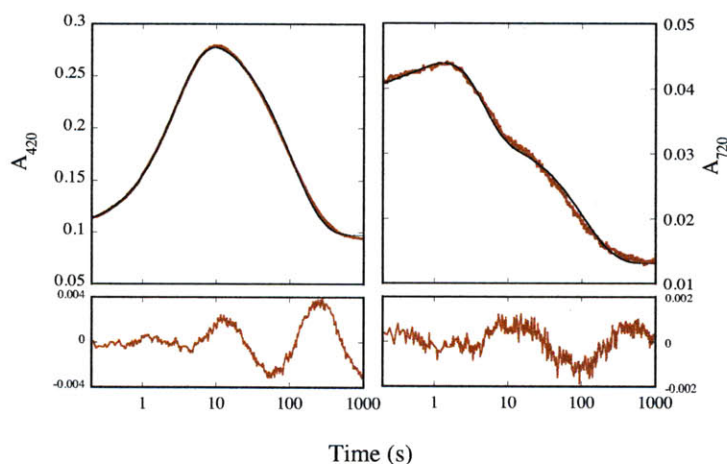


**Figure 2.7.** Fits of data monitoring the reaction of  $50 \mu\text{M MMOH}_{\text{red}}$  and  $100 \mu\text{M MMOB}$  with excess  $\text{O}_2$  at pH 7.0 and  $4 \text{ }^\circ\text{C}$ . Data collected at 420 nm (left, red lines) and 720 nm (right, red lines) were fit simultaneously to a  $\text{P}^* \rightarrow H_{\text{peroxo}} \rightarrow \text{Q} \rightarrow H_{\text{ox}}$  model differential equation with the form of eq 2.1. This method yielded poor fits (black lines) with unacceptable residuals (bottom plots) and  $\chi^2_{\text{red}} > 1.90 \times 10^{-6}$ .

<sup>3</sup>The first process  $H_{\text{red}} \rightarrow \text{P}^*$  does not have to be accounted for in these analyses because a significant portion of the rise in absorbance associated with this transformation occurs during the dead time of the stopped-flow instrument and because the process is characterized by only a very modest change in absorbance relative to events that follow. Including an additional term for the first process  $H_{\text{red}} \rightarrow \text{P}^*$  did not reduce the  $\chi^2_{\text{red}}$  of the fit, and the parameter dependency of the rate constant associated with that process was close to unity, suggesting that the inclusion of this step is unnecessary. One assumption implicit in these analyses is that  $[\text{P}^*] = 0$  at  $t = 0 \text{ s}$ . Such is not the case; however, the excellent fits obtained using this model and the fact that the fastest rate constant obtained from these fits matches that of  $k_2$  measured in experiments performed in the presence of  $540 \mu\text{M CH}_4$  justify this approximation.

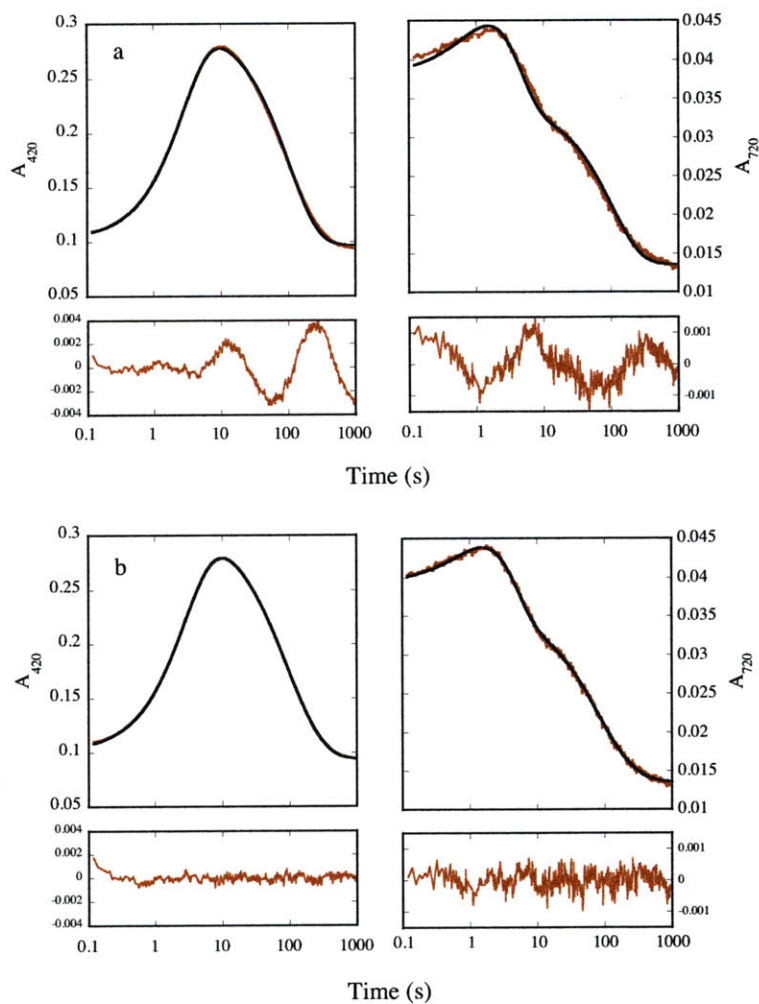
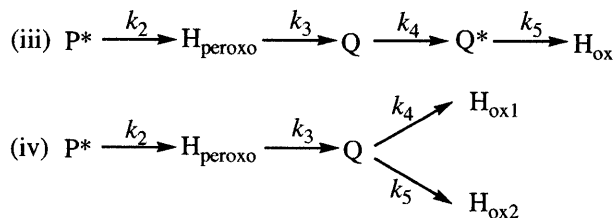


**Figure 2.8.** Exponential fits of data monitoring the reaction of 50  $\mu\text{M}$   $\text{MMOH}_{\text{red}}$  and 100  $\mu\text{M}$   $\text{MMOB}$  with excess  $\text{O}_2$  at pH 7.0 and 4  $^\circ\text{C}$ . Data collected at 420 nm and 720 nm (red lines) were fit simultaneously (black lines) to a sum of three exponentials (a) or four exponentials (b). Residuals are depicted at the bottom of each plot.  $\chi^2_{\text{red}} = 5.55 \times 10^{-6}$  for the three exponential fit and  $8.14 \times 10^{-8}$  for the four exponential fit.

equation solutions for these models were compared. The first model describes a process in which a chromophoric intermediate that follows Q decay (denoted  $\text{Q}^*$ ) contributes to

the observed optical events (iii, Scheme 2.3). The second model describes a situation in



**Scheme 2.3.** Models for the Reaction of  $\text{MMOH}_{\text{red}}$  and Two Equiv of  $\text{MMOB}$  with  $\text{O}_2$

which there are two populations of  $Q$  that decay on different timescales (iv, Scheme 2.3).

Fits of the data to eqs 2.3 and 2.4, the respective differential solutions to models iii and

$$\text{Abs}_\lambda(t) = \left\{ \begin{array}{l} \varepsilon_{H_{\text{ox}}} [P^*]_0 + (\varepsilon_{P^*} - \varepsilon_{H_{\text{ox}}}) ([P^*]_0 e^{-k_2 t}) + (\varepsilon_{H_{\text{peroxo}}} - \varepsilon_{H_{\text{ox}}}) \left( [P^*]_0 \left( \frac{k_2}{k_3 - k_2} \right) (e^{-k_2 t} - e^{-k_3 t}) \right) + \\ (\varepsilon_Q - \varepsilon_{H_{\text{ox}}}) \left( k_3 [P^*]_0 \left( \frac{k_2}{k_3 - k_2} \right) \left\{ \left( \frac{1}{k_4 - k_2} \right) (e^{-k_2 t} - e^{-k_4 t}) - \left( \frac{1}{k_4 - k_3} \right) (e^{-k_3 t} - e^{-k_4 t}) \right\} \right) + \\ (\varepsilon_{Q^*} - \varepsilon_{H_{\text{ox}}}) \left( k_4 k_3 [P^*]_0 \left( \frac{k_2}{k_3 - k_2} \right) \left\{ \left( \frac{1}{k_4 - k_2} \right) \left( \frac{1}{k_5 - k_2} \right) (e^{-k_2 t} - e^{-k_5 t}) - \left( \frac{1}{k_4 - k_2} \right) \left( \frac{1}{k_5 - k_4} \right) (e^{-k_4 t} - e^{-k_5 t}) \right\} - \right. \\ \left. \left( \frac{1}{k_4 - k_3} \right) \left( \frac{1}{k_5 - k_3} \right) (e^{-k_3 t} - e^{-k_5 t}) + \left( \frac{1}{k_4 - k_3} \right) \left( \frac{1}{k_5 - k_4} \right) (e^{-k_4 t} - e^{-k_5 t}) \right\} \right) \end{array} \right\} \quad (2.3)$$

$$\text{Abs}_\lambda(t) = [P^*]_0 \left( \begin{array}{l} \varepsilon_{P^*} + (\varepsilon_{P^*} - \varepsilon_{H_{\text{ox}}}) e^{-k_2 t} + (\varepsilon_{H_{\text{peroxo}}} - \varepsilon_{H_{\text{ox}}}) \left( \frac{k_2}{k_3 - k_2} \right) (e^{-k_2 t} - e^{-k_3 t}) + \\ (\varepsilon_Q - \varepsilon_{H_{\text{ox}}}) \left( \frac{k_3 k_2}{k_3 - k_2} \right) \left( \frac{1}{k_4 + k_5 - k_2} \right) (e^{-k_2 t} - e^{-(k_4 + k_5)t}) - \left( \frac{1}{k_4 + k_5 - k_3} \right) (e^{-k_3 t} - e^{-(k_4 + k_5)t}) \right) \end{array} \right) \quad (2.4)$$

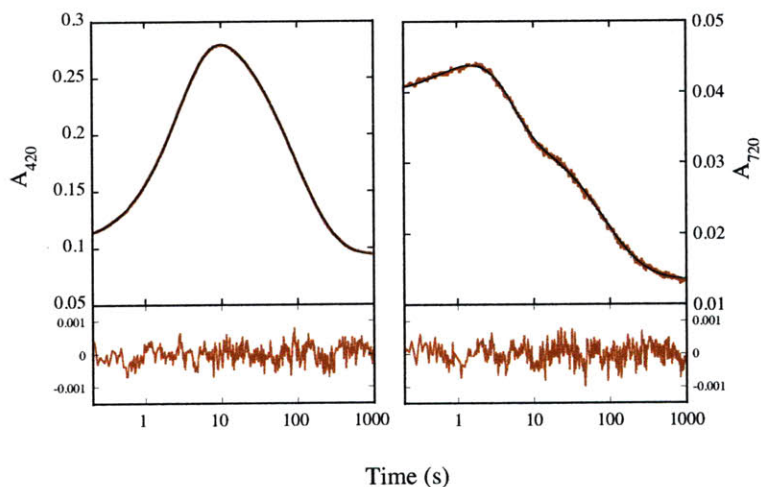


**Figure 2.9.** Representative fits of data monitoring the reaction of 50  $\mu\text{M}$   $\text{MMOH}_{\text{red}}$  and 100  $\mu\text{M}$   $\text{MMOB}$  with excess  $\text{O}_2$  at pH 7.0 and 4  $^\circ\text{C}$ . Data collected at 420 nm (left, red lines) and 720 nm (right, red lines) were fit simultaneously to the  $\text{P}^* \rightarrow \text{H}_{\text{peroxo}} \rightarrow \text{Q} \rightarrow \text{Q}^* \rightarrow \text{H}_{\text{ox}}$  model (eq 2.3). This method yielded good fits (black lines) with acceptable residuals (bottom plots) and  $\chi^2_{\text{red}} < 8.14 \times 10^{-8}$ .

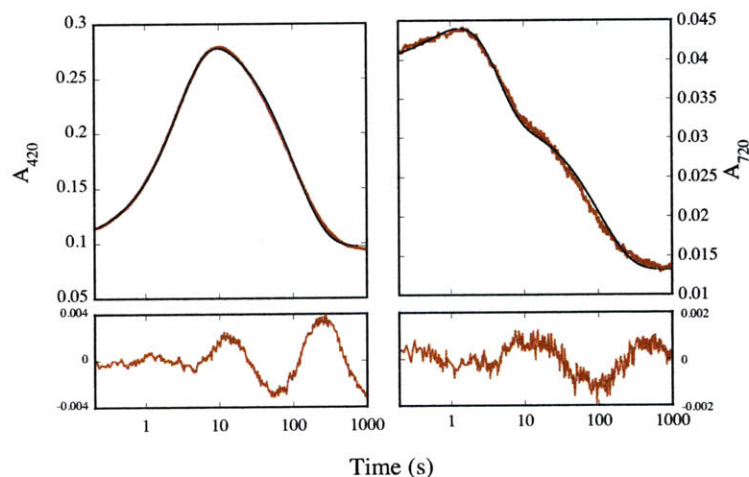


**Figure 2.10.** Fits of data monitoring the reaction of 50  $\mu\text{M}$   $\text{MMOH}_{\text{red}}$  and 100  $\mu\text{M}$   $\text{MMOB}$  with excess  $\text{O}_2$  at pH 7.0 and 4  $^\circ\text{C}$ . Data collected at 420 nm (left, red lines) and 720 nm (right, red lines) were fit simultaneously to eq 2.4 describing Scheme 2.3iv. This method yielded poor fits (black lines) with unacceptable residuals (bottom plots) and  $\chi^2_{\text{red}} > 1.90 \times 10^{-6}$ .

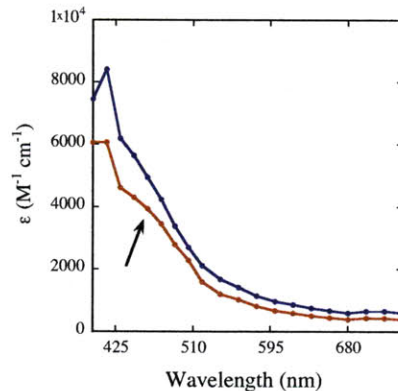


**Figure 2.11.** Optical spectra of Q (blue) and Q\* (red) recorded at pH 7.0 and converted to molar extinction values. Spectra were obtained at 4 °C from data collected every 15 or 20 nm and analyzed by global fitting procedures described in the text. The arrow points to the 455 nm shoulder of Q\*.

iv, are shown in Figures 2.9 and 2.10. Fits to model iii afforded excellent results, with  $k_2 = 0.75 \pm 0.05 \text{ s}^{-1}$ ,  $k_3 = 0.37 \pm 0.01 \text{ s}^{-1}$ ,  $k_4 = 0.011 \pm 0.002 \text{ s}^{-1}$ , and  $k_5 = 0.0026 \pm 0.0001 \text{ s}^{-1}$ , whereas those to iv yielded poor fits with sinusoidal residual plots and large parameter dependencies ( $\sim 1$ ).  $\chi^2_{\text{red}}$  values for fits to iii were over an order of magnitude better than those to iv, allowing us to unambiguously confirm iii as the process with the minimum number of steps necessary to describe the data. Global analysis of kinetic data collected at various wavelengths was employed to approximate the absorption spectrum of Q\* (Figure 2.11). Although spectral determination by this method can be biased by the absorbance of other species present during the reaction, it has been used widely to estimate the optical and fluorescent properties of individual components in complex mixtures (30). The optical spectrum of Q\* displays a band centered around 420 nm and a shoulder around 455 nm that is not present in the optical spectrum of Q.



*Temperature Dependences of  $\text{MMOH}_{\text{red}}:2\text{B} + \text{O}_2$  Reactions.* To characterize better the events occurring upon reaction of  $\text{MMOH}_{\text{red}}:2\text{B}$  with  $\text{O}_2$ , thermodynamic activation parameters for each step in the reaction pathway were obtained from fits of data collected at temperatures ranging from 4 °C to 34.5 °C to the Eyring equation (eq 2.5), where  $k$  is

$$\ln \frac{k}{T} = \frac{-\Delta H^\ddagger}{R} \cdot \frac{1}{T} + \ln \frac{k_B}{h} + \frac{\Delta S^\ddagger}{R} \quad (2.5)$$

the rate constant of interest,  $T$  is the absolute temperature,  $\Delta H^\ddagger$  and  $\Delta S^\ddagger$  are the enthalpy and entropy of activation, respectively,  $R$  is the gas constant,  $k_B$  is the Boltzmann constant, and  $h$  is Planck's constant. Primary data collected at 4 °C, 10 °C, and 15 °C were fit satisfactorily to eq 2.3 describing the model of Scheme 2.3iii. Data from experiments conducted at 20 °C, 25 °C, 30 °C, and 34.5 °C fit well to a sum of three exponentials instead of four describing the  $\text{P}^* \rightarrow \text{H}_{\text{peroxo}} \rightarrow \text{Q} \rightarrow \text{Q}^* \rightarrow \text{H}_{\text{ox}}$  process of scheme 2.3iii, however. At high temperatures,  $\text{P}^* \rightarrow \text{H}_{\text{peroxo}}$  conversion became faster than the limitation of the instrument and this process did not have to be included in the fits.

**Table 2.1.** Temperature Dependence of  $\text{O}_2$  Activation Rate Constants

Rate Constant	4 °C <sup>a</sup>	10 °C <sup>a</sup>	15 °C <sup>a</sup>	20 °C <sup>b</sup>	25 °C <sup>b</sup>	30 °C <sup>b</sup>	34.5 °C <sup>b</sup>
$k_2$ (s <sup>-1</sup> )	0.75	3.14	9.45	nd <sup>c</sup>	nd <sup>c</sup>	nd <sup>c</sup>	nd <sup>c</sup>
$k_3$ (s <sup>-1</sup> )	0.37	1.16	3.126	7.11	17.04	36.41	87.59
$k_4$ (s <sup>-1</sup> )	0.011	0.0214	0.051	0.082	0.140	0.203	0.362
$k_5$ (s <sup>-1</sup> )	0.0026	0.00560	0.00690	0.0101	0.0156	0.0215	0.0360

<sup>a</sup>Data collected at 4 °C, 10 °C, and 15 °C were fit to eq 2.3 describing scheme 2.3iii. <sup>b</sup>Data collected at 20 °C, 25 °C, 30 °C, and 34.5 °C were fit to an analytical solution to the  $\text{H}_{\text{peroxo}} \rightarrow \text{Q} \rightarrow \text{Q}^* \rightarrow \text{H}_{\text{ox}}$  model having the form of eq 2.1. <sup>c</sup>Not determined.

The data were therefore fit satisfactorily to the analytical solution to a  $H_{\text{peroxo}} \rightarrow Q \rightarrow Q^* \rightarrow H_{\text{ox}}$  model having the form of eq 2.1. Rate constants obtained from these fits are displayed in Table 2.1.

Activation parameters, shown in Table 2.2, were obtained by fitting the rate constants obtained from the primary fits to eq 2.5 (Figure 2.12). Notably, the activation parameters for  $H_{\text{peroxo}}$  to  $Q$  conversion are identical to those measured previously using exponential fitting procedures (3, 9). The positive entropy of activation measured for this step is

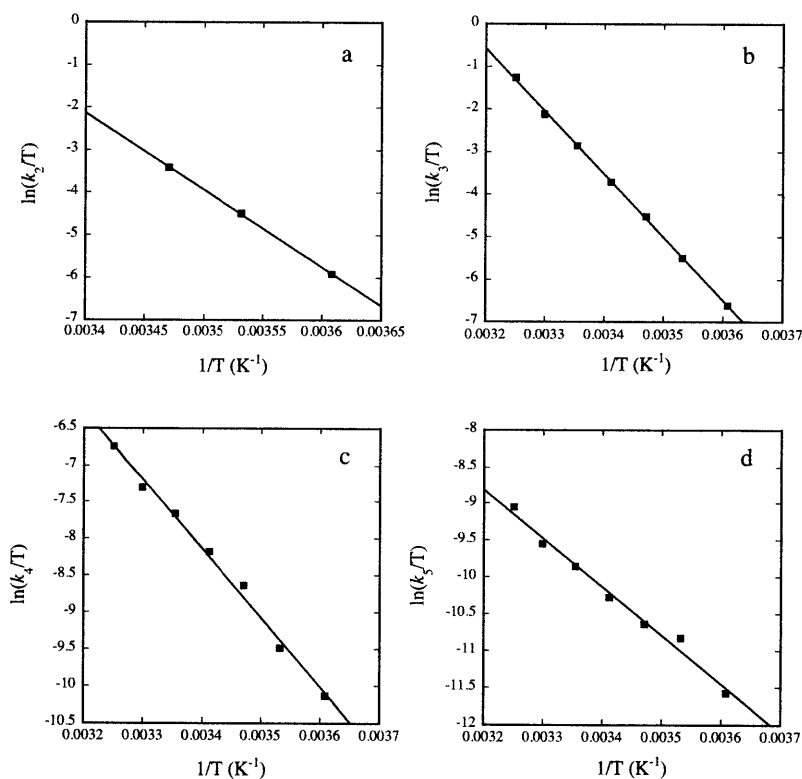


**Figure 2.12.** Eyring plots for  $P^*$  to  $H_{\text{peroxo}}$  (a),  $H_{\text{peroxo}}$  to  $Q$  (b),  $Q$  to  $Q^*$  (c), and  $Q^*$  to  $H_{\text{ox}}$  (d) conversion. Experiments were performed from 4 to 34.5 °C in 25 mM  $\text{KP}_i$ , pH 7.0. Primary data collected at 420 and 720 nm were fit simultaneously as discussed in the text. Eyring data were fit to eq 2.5 to obtain the enthalpy and entropy of activation for each catalytic step.

likely to arise from side chain movements that are expected to accommodate geometric changes occurring at the diiron center. The large magnitude of the positive enthalpy of activation is consistent with cleavage of the O—O bond to form a high valent intermediate. Q to Q\* conversion is characterized by small, positive enthalpy of

**Table 2.2.** Activation Parameters of MMOH O<sub>2</sub> Activation Processes

Rate Constant	$\Delta H^\ddagger$ (kcal/mol)	$\Delta S^\ddagger$ (cal/mol·K)
$k_2$	36.0	71.0
$k_3$	29.4	45.7
$k_4$	18.6	0.0
$k_5$	13.1	-22.9

activation and a negligible entropy of activation. The latter observation indicates that there is little to no structural rearrangement that accompanies this step or that several perturbations occur with individual entropic contributions that cancel one another. Q\* decay is characterized by a negative entropy of activation, as reported previously (3, 9). It is important to note that changes in the structure of the MMOH/MMOB complex that accompany these steps are also expected to affect the activation parameters. Interactions of MMOH with MMOB may also exhibit temperature-dependent changes.

*Double-Mixing Stopped-Flow Optical Spectroscopy: Q/Q\* + CH<sub>4</sub>:* To address the relative significance of Q and Q\* with respect to enzyme function, double mixing stopped-flow experiments were conducted in which either intermediate was generated and then mixed with a solution containing 770  $\mu$ M CH<sub>4</sub>. For each experiment, appropriate age times between the first and second push needed to monitor reactions of Q and Q\*

were determined by preparing a speciation plot using rate constants extracted from fits of the data to model iii (vide supra) and identifying the  $t_{\max}$  values of the two intermediates. From this method,  $t_{\max}$  values of Q and Q\* were 13 s and 186 s, respectively (Figure 2.13).

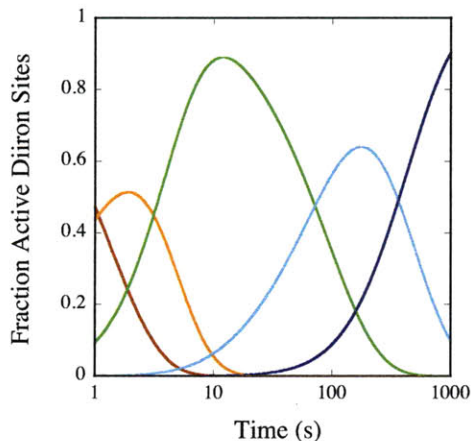


**Figure 2.13.** Speciation plot depicting the time-dependence of transients formed during the reaction of  $\text{MMOH}_{\text{red}}$  with  $\text{O}_2$  in the presence of two equiv of  $\text{MMOB}$  at pH 7.0 and 4 °C. The concentrations of  $\text{P}^*$  (red),  $\text{H}_{\text{peroxo}}$  (orange), Q (green),  $\text{Q}^*$  (cyan), and  $\text{H}_{\text{ox}}$  (blue) as a function of time were calculated from the  $\text{P}^* \rightarrow \text{H}_{\text{peroxo}} \rightarrow \text{Q} \rightarrow \text{Q}^* \rightarrow \text{H}_{\text{ox}}$  model using rate constants obtained from fits of data to eq 2.3.

Data investigating reactions of Q with  $\text{CH}_4$  at 420 nm were fit well by a single exponential decay process having  $k = 3.9 \pm 0.2 \text{ s}^{-1}$  (Figure 2.14). This rate constant is ~350 times larger than that for Q decay in the absence of substrate identified in single-mixing experiments (vide supra) and in double-mixing control experiments in which the intermediate was accumulated and mixed with buffer instead of  $\text{CH}_4$  ( $k_3 = 0.010 \text{ s}^{-1}$ ). The acceleration of Q decay in the presence of  $\text{CH}_4$  and the fact a term for  $\text{Q}^*$  is not necessary to fit the data indicate that Q is depleted by a different pathway in the presence of

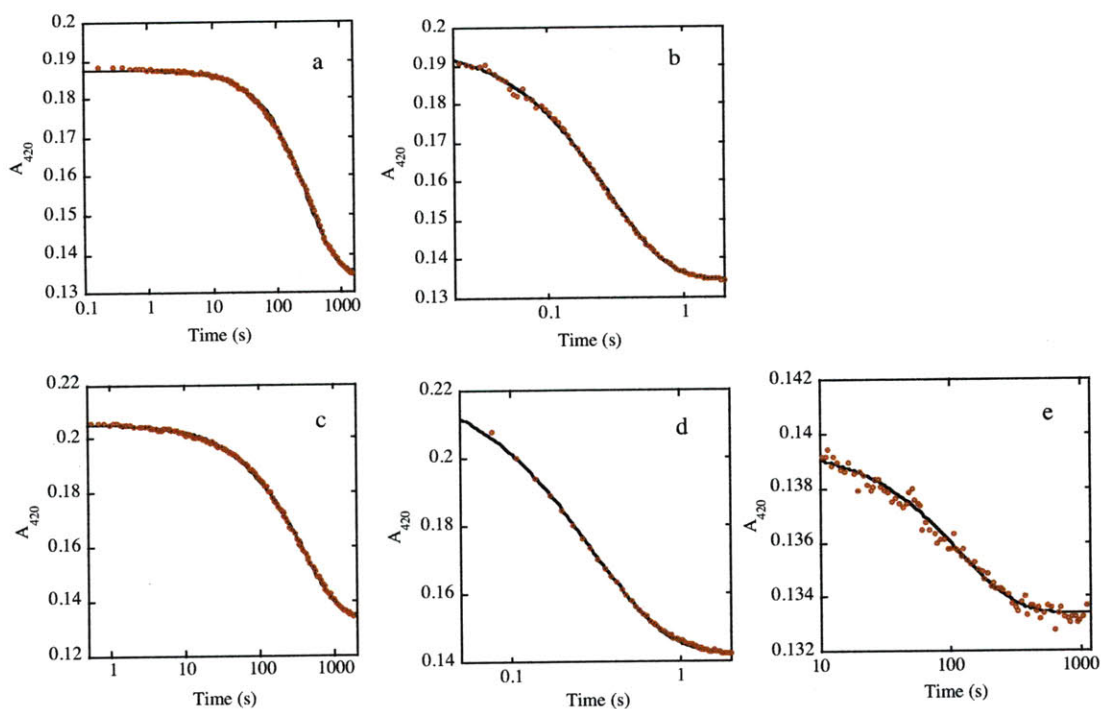


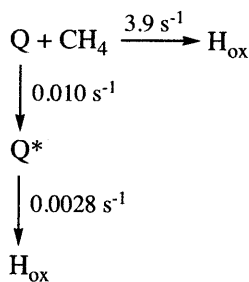
**Figure 2.14.** Representative fits (black lines) of double-mixing stopped-flow data (red circles) monitoring the reactions of Q (a-b) and Q\* (c-e) with 335  $\mu\text{M}$   $\text{CH}_4$ . Experiments were conducted by rapidly mixing 50  $\mu\text{M}$   $\text{MMOH}_{\text{red}}$  and 100  $\mu\text{M}$   $\text{MMOB}$  with  $\text{O}_2$ , waiting for maximal accumulation of Q (13 s) or Q\* (186 s), and then introducing a solution of  $\text{CH}_4$  or buffer in a second stopped flow push. Studies were performed at pH 7.0 and 4  $^\circ\text{C}$ . Data were analyzed as discussed in the text. For Q, experiments were performed by mixing the intermediate with buffer (a) or with  $\text{CH}_4$ -saturated buffer (b). For Q\*, studies were conducted by mixing the intermediate with buffer (c) or with  $\text{CH}_4$ -saturated buffer (d and e). Q\* data were fit by isolating the first (d) and second (e) exponential decay events and analyzing them individually, as noted in the text.

methane than in its absence. The mechanism of methane-promoted Q decay most likely arises from rapid reaction with this substrate (3, 9).

Experiments probing the reaction of Q\* with  $\text{CH}_4$  at 420 nm revealed the presence of two distinct decay processes (Figure 2.14). Because these two phases are separated by several orders of magnitude in rate constant and are independent of each other (vide infra), the data were fit well by separately analyzing each event. The rate constants for

the two phases obtained by this method are  $3.6 \pm 0.2 \text{ s}^{-1}$  and  $0.002 \pm 0.001 \text{ s}^{-1}$ . The observation that the faster rate constant agrees with that of methane-promoted Q decay (vide supra) allows us to unambiguously assign this process. Indeed, at the age time employed in these experiments (186 s), the protein sample is a complex mixture of 19% Q, 60% Q\*, and 21% H<sub>ox</sub> (Figure 2.13). It is therefore necessary to include a term for the substantial population of Q present, because this intermediate absorbs significantly at the wavelength employed ( $\epsilon_{420} = 8415 \text{ M}^{-1} \text{ cm}^{-1}$ ). The rate constant describing the slower event is identical to that of Q\* decay measured in single-mixing experiments (vide supra) and in double-mixing control experiments ( $k_3 = 0.0028 \text{ s}^{-1}$ ). These results indicate that this process represents Q\* decay and that it is not altered by the presence of methane. Although Q is competent for methane oxidation, Q\* does not appear to react with this substrate. These conclusions are summarized in Scheme 2.4.

*Effect of Buffer on Q Decay.* The data strongly suggest that a novel intermediate Q\* forms as Q decays in the absence of hydrocarbon substrate. To confirm that Q\* is on the reaction pathway and is not a physiologically irrelevant adduct of Q formed by



**Scheme 2.4.** Mechanism of Q Decay in the Presence of 335  $\mu\text{M}$  CH<sub>4</sub>

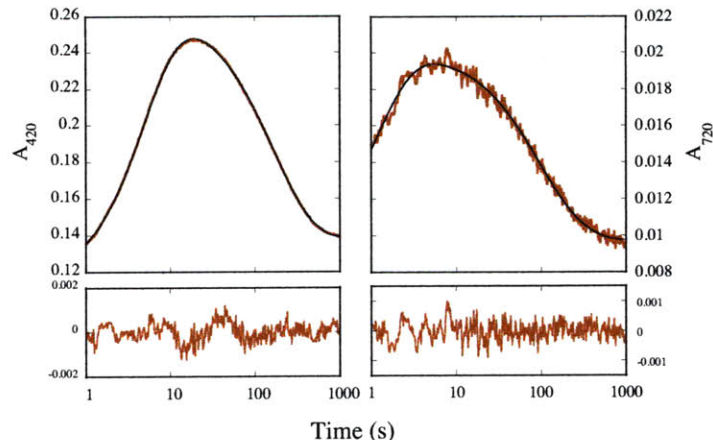


**Figure 2.15.** Fits of data monitoring the reaction of 50  $\mu\text{M}$   $\text{MMOH}_{\text{red}}$  and 100  $\mu\text{M}$   $\text{MMOB}$  with excess  $\text{O}_2$  at 4  $^\circ\text{C}$  in 25 mM sodium cacodylate buffer, pH 7.0. Data collected at 420 nm (left, red lines) and 720 nm (right, red lines) were fit simultaneously to the  $\text{P}^* \rightarrow \text{H}_{\text{peroxo}} \rightarrow \text{Q} \rightarrow \text{H}_{\text{ox}}$  model (eq 2.3). This method yielded acceptable fits (black lines) and residuals (bottom plots) with  $k_2 = 0.86 \text{ s}^{-1}$ ,  $k_3 = 0.21 \text{ s}^{-1}$ ,  $k_4 = 0.014 \text{ s}^{-1}$ , and  $k_5 = 0.0054 \text{ s}^{-1}$ .

reaction with buffer components, experiments monitoring the reaction of  $\text{MMOH}_{\text{red}}$  and 2 equiv of  $\text{MMOB}$  with  $\text{O}_2$  were performed in 25 mM sodium cacodylate, pH 7.0 (Figure 2.15), and in 25 mM MOPS, pH 7.0 (data not shown). As for experiments performed in phosphate buffer, data could only be fit well when a fourth term was included in the exponential fit. The data fit nicely to the  $\text{P}^* \rightarrow \text{H}_{\text{peroxo}} \rightarrow \text{Q} \rightarrow \text{Q}^* \rightarrow \text{H}_{\text{ox}}$  model (eq 2.3), and the rate constants obtained from the fits are within error of those measured in phosphate buffer. The exception is  $k_3$ , the value of which was reduced to  $0.21 \text{ s}^{-1}$  in cacodylate buffer. This effect might reflect a steric constraint imposed by the cacodylate molecules on this transformation, which involves geometric reorganization at the diiron center. The necessity of including a term for  $\text{Q}^*$  in all fits indicates that this phenomenon is a property of the protein rather than a result of unnatural buffer-diiron adducts.

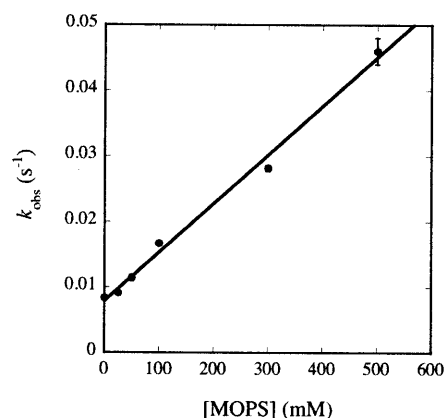


**Figure 2.16.** Plot of  $k_{\text{obs}}$  vs. [MOPS] for decay of Q at 4 °C in 25 mM phosphate buffer, pH 7.0. Data were collected by rapidly mixing a mixture of 50  $\mu\text{M}$  MMOH and 100  $\mu\text{M}$  MMOB with excess  $\text{O}_2$ , allowing the reaction mixture to age for 13 s, then introducing a solution of MOPS prepared in ddH<sub>2</sub>O in a second stopped-flow push. A linear fit of the data yielded a second order rate constant  $0.074 \text{ M}^{-1} \text{ s}^{-1}$  for the reaction. Data at 25 and 50 mM were fit to two exponentials, one of which corresponds to a summation of the rate constants describing substrate-promoted and natural Q decay and the other which represents Q\* decay and was fixed at  $0.00215 \text{ s}^{-1}$ , the value determined in the absence of substrate. Data collected at 100, 300, and 500 mM were fit to one exponential that corresponds to substrate-promoted Q decay. Samples of MOPS were prepared from a 1 M MOPS stock solution in ddH<sub>2</sub>O at pH 7.0. Error bars represent one standard deviation at the 95% confidence level. These experiments demonstrate that although Q reacts with MOPS, the reaction occurs with such a slow rate constant that Q\* still should accumulate to a significant amount when experiments are performed in 25 mM MOPS.

These results represent the first evidence for the existence of Q\*. Kinetic studies performed previously in MOPS buffer reported that Q decays with a rate constant of  $0.05 \text{ s}^{-1}$  (6, 9), which is considerably faster than that measured here ( $0.01 \text{ s}^{-1}$ ). The fact that Q decay was found to be faster in these earlier studies suggests reaction of this intermediate with a component not present in the current experiments, which would lead to a mechanism of Q decay that does not proceed through Q\*. Results of single- and double-mixing stopped-flow experiments with MOPS reveal that this phenomenon is not due to a difference in buffer composition between these and previous experiments, as we initially



suspected (Figure 2.16). The reason for the different Q decay mechanism found in this study therefore remains unknown.

*Proton Requirements of  $\text{MMOH}_{\text{red}}:2\text{B} + \text{O}_2$  Reactions.* Reactions of  $\text{MMOH}_{\text{red}}$  and 2 equiv of MMOB with  $\text{O}_2$  were monitored in the absence and presence of 540  $\mu\text{M}$  methane at different pH values in the range of 6.6 to 8.6. The enzyme system is stable over the duration of the experiments at all pH values employed. The data clearly demonstrate that buffer pH affects the kinetics of the oxygenated iron intermediates that accumulate (Figure 2.17). For example, data collected in the absence of methane display time-dependent rise and decay phases at 420 nm when  $\text{pH} < 8.6$ ; however, when the buffer pH is increased, the kinetics of the processes contributing to these features are altered such that the amplitude of the signal is reduced. At pH 8.6, rise and decay processes are no longer observed, indicating that chromophoric intermediates no longer

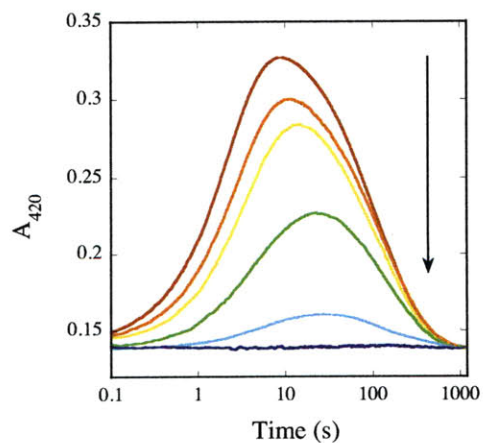


**Figure 2.17.** Representative 420 nm absorbance profiles monitoring the reactions of 50  $\mu\text{M}$   $\text{MMOH}_{\text{red}}$  with  $\text{O}_2$  in the presence of 2 equiv MMOB at 4 °C and pH 6.6 (red), pH 7.2 (orange), pH 7.4 (yellow), pH 7.8 (green), pH 8.2 (cyan), and pH 8.6 (blue).

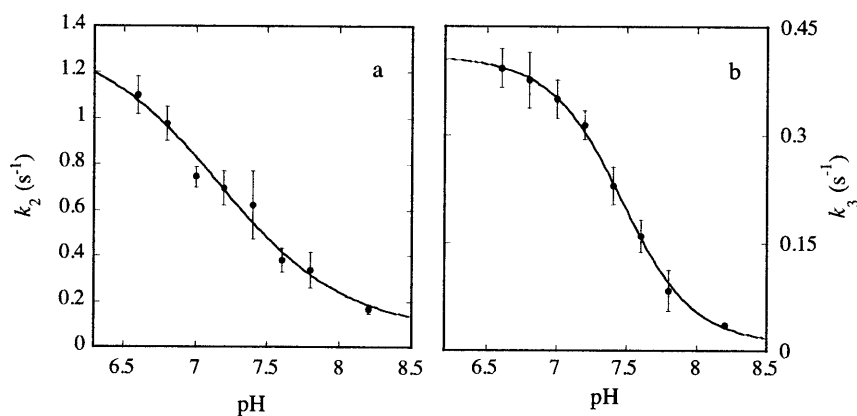


**Figure 2.18.** pH dependence of P\* decay/H<sub>peroxo</sub> formation,  $k_2$ , (a), and H<sub>peroxo</sub> decay/Q formation,  $k_3$ , (b) at 4 °C. Data were collected by mixing a solution of 50  $\mu\text{M}$  MMOH<sub>red</sub> and 100  $\mu\text{M}$  MMOB with excess O<sub>2</sub> at the appropriate pH and were analyzed as noted in the text. Each data point represents the average of 6 or more data sets collected in the presence (scheme 2.2i) or absence (scheme 2.3iii) of 578  $\mu\text{M}$  CH<sub>4</sub> with at least 3 different batches of protein. P\* decay/H<sub>peroxo</sub> formation,  $k_2$ , (a) fit well to eq 2.5 describing scheme 2.5i, whereas those of H<sub>peroxo</sub> decay/Q formation,  $k_3$ , (b) were fit to eq 2.6 describing scheme 2.5ii (red lines through points). Error bars depict one standard deviation at the 95% confidence level.

build up under these conditions, either because the kinetics are altered such that they no longer favor accumulation of these species or because the transients do not form under these conditions.

To determine which steps are affected, pH data collected at 420 nm and 720 nm were fit simultaneously at all pH values investigated (Table 2.3). Data probing the reactions of MMOH<sub>red</sub> and 2 equiv of MMOB with O<sub>2</sub> in the presence of methane fit well to eq 2.1 describing Scheme 2.2i at all pH values employed. Experiments conducted in the absence

**Table 2.3.** pH Dependence of O<sub>2</sub> Activation Rate Constants

pH	$k_1'$ (s <sup>-1</sup> ) <sup>a</sup>	$k_2$ (s <sup>-1</sup> ) <sup>b</sup>	$k_3$ (s <sup>-1</sup> ) <sup>b</sup>	$k_4$ (s <sup>-1</sup> ) <sup>b</sup>	$k_5$ (s <sup>-1</sup> ) <sup>c</sup>
6.6	7.1 ± 0.9	1.10 ± 0.08	0.39 ± 0.03	0.016 ± 0.005	0.005 ± 0.001
6.8	8.2 ± 3.4	0.98 ± 0.07	0.38 ± 0.04	0.014 ± 0.001	0.0039 ± 0.0003
7.0	6.7 ± 0.9	0.75 ± 0.04	0.35 ± 0.03	0.011 ± 0.002	0.0026 ± 0.0001
7.2	6.0 ± 1.3	0.67 ± 0.07	0.32 ± 0.02	0.011 ± 0.002	0.004 ± 0.001
7.4	7.5 ± 2.2	0.62 ± 0.15	0.23 ± 0.03	0.009 ± 0.003	0.003 ± 0.002
7.6	2.9 ± 1.3	0.38 ± 0.05	0.16 ± 0.02	0.011 ± 0.005	0.0031 ± 0.0004
7.8	4.0 ± 2.1	0.34 ± 0.08	0.08 ± 0.02	0.010 ± 0.005	0.004 ± 0.001
8.2	nd <sup>d</sup>	0.17 ± 0.02	0.037 ± 0.002	nd <sup>e</sup>	0.004 ± 0.001

<sup>a</sup> $k_1'$  values were determined from fits of data probing reactions of 50 μM MMOH and 100 μM MMOB with ~210 μM O<sub>2</sub> in the presence of 540 μM CH<sub>4</sub> to eq 2.1 describing a H<sub>red</sub> → P\* → H<sub>peroxo</sub> → H<sub>ox</sub> model. <sup>b</sup>For 6.6 ≤ pH ≤ 7.8,  $k_2$ ,  $k_3$ , and  $k_4$  values were determined from fits of data probing reactions of 50 μM MMOH and 100 μM MMOB with ~210 μM O<sub>2</sub> in the presence of 540 μM CH<sub>4</sub> to eq 2.1 describing a H<sub>red</sub> → P\* → H<sub>peroxo</sub> → H<sub>ox</sub> model and from fits of data probing reactions of 50 μM MMOH and 100 μM MMOB with excess O<sub>2</sub> to eq 2.3 describing a P\* → H<sub>peroxo</sub> → Q → Q\* → H<sub>ox</sub> model. For data collected at pH 8.2,  $k_2$ ,  $k_3$ , and  $k_4$  values were determined from fits of data probing reactions of 50 μM MMOH and 100 μM MMOB with excess O<sub>2</sub> to eq 2.3 describing a P\* → H<sub>peroxo</sub> → Q → Q\* → H<sub>ox</sub> model. <sup>c</sup> $k_5$  values were determined from fits of data probing reactions of 50 μM MMOH and 100 μM MMOB with excess O<sub>2</sub> to eq 2.3 describing a P\* → H<sub>peroxo</sub> → Q → Q\* → H<sub>ox</sub> model. <sup>d</sup>Not determined. Data could not be obtained because no optical change was observed when reactions of 50 μM MMOH and 100 μM MMOB with ~210 μM O<sub>2</sub> were carried out in the presence of 540 μM CH<sub>4</sub>. <sup>e</sup>Not determined. Because the value of  $k_3$  approaches that of  $k_4$  at pH 8.2, this process does not need to be accounted for to obtain satisfactory data fits. Data were therefore fit to eq 2.3 describing a P\* → H<sub>peroxo</sub> → Q → Q\* → H<sub>ox</sub> model by fixing  $k_4$  at 0.0114 s<sup>-1</sup>, the average value of this pH-independent rate constant across all pH values employed.

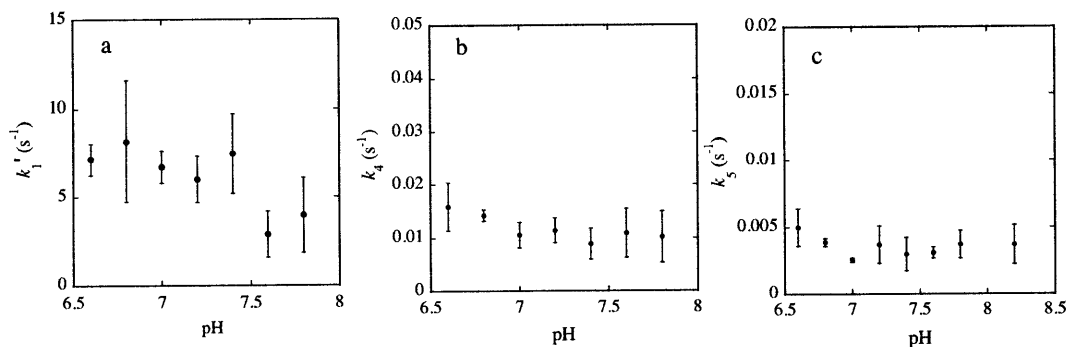
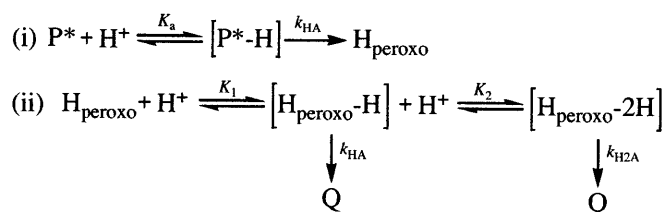


**Figure 2.19.** pH dependence of P\* formation ( $k_1'$ , a), Q decay/Q\* formation ( $k_4$ , b), and Q\* decay/H<sub>ox</sub> formation ( $k_5$ , c) at 4 °C. Data were collected by mixing a solution of 50 μM MMOH and 100 μM MMOB with excess O<sub>2</sub> at the appropriate pH and were analyzed as noted in the text. Each data point represents the average of 5 or more data sets collected with at least 3 different batches of protein.  $k_1'$  data were collected in the presence of 540 μM CH<sub>4</sub> (eq 2.1 describing scheme 2.2i), and  $k_4$  and  $k_5$  data were collected in the absence of CH<sub>4</sub> (eq 2.3 describing scheme 2.3iii). Error bars depict one standard deviation at the 95% confidence level.



**Scheme 2.5.** Models for the pH Dependencies of P\* to H<sub>peroxo</sub> and H<sub>peroxo</sub> to Q Conversion

of methane were analyzed satisfactorily with eq 2.3, the solution to Scheme 2.3iii.<sup>4</sup> Using these fitting procedures,  $k_2$  and  $k_3$  were found to vary with pH whereas  $k_1$ ,  $k_4$ , and  $k_5$  did not change (Figure 2.3, Figure 2.18, and Figure 2.19). The values of  $k_2$  and  $k_3$  both decrease with increasing pH, suggesting that the steps associated with these rate constants are facilitated by or dependent on a proton(s). The  $k_2$  and  $k_3$  values display sigmoidal dependencies on pH, although the experimentally accessible pH range hindered our ability to collect data points near the extrema of each curve where the rate constants flatten out with pH.

The pH titration data for P\* to H<sub>peroxo</sub> conversion ( $k_2$ ) fit well to eq 2.6, derived from Scheme 2.5i, which describes a single, reversible ionization event followed by irreversible conversion of the protonated species to H<sub>peroxo</sub> (Figure 2.18a), where  $k_{HA}$  and

$$k = \frac{k_{HA} 10^{(pK_a - \text{pH})}}{1 + 10^{(pK_a - \text{pH})}} + k_A \quad (2.6)$$

<sup>4</sup>Data collected in the absence of CH<sub>4</sub> at pH 8.2 fit well to a sum of three exponentials instead of the four describing the P\* → H<sub>peroxo</sub> → Q → Q\* → H<sub>ox</sub> process required to fit data collected at the other pH values studied. At pH 8.2, the value of  $k_3$  approaches that of  $k_4$  such that Q does not accumulate to a significant amount and the process does not need to be accounted for. For these fits, the P\* → H<sub>peroxo</sub> → Q → Q\* → H<sub>ox</sub> model was employed but  $k_4$  was fixed at 0.0114 s<sup>-1</sup>, the average value of this pH-independent rate constant across all pH values employed. Acceptable fits were obtained by this method.

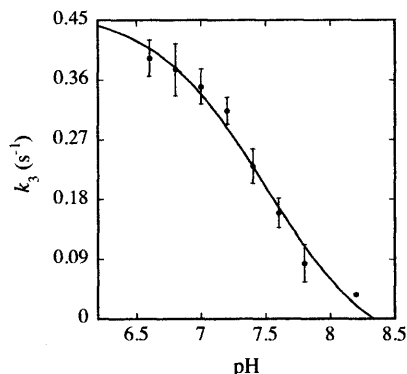


**Figure 2.20.** Poor fit of the pH dependence of  $H_{\text{peroxo}}$  decay/Q formation ( $k_3$ ) to eq 2.6 describing a system in which  $H_{\text{peroxo}}$  is reversibly protonated and the protonated species proceeds irreversibly to Q.  $\chi^2_{\text{red}} = 0.0021$ . Error bars depict one standard deviation at the 95% confidence level.

$k_A$  are the rate constants of conversion to  $H_{\text{peroxo}}$  for the protonated and deprotonated species, respectively (32). A fit of the data to this model afforded  $k_{\text{HA}} = 1.35 \text{ s}^{-1}$ ,  $k_A = 0.08 \text{ s}^{-1}$ , and  $\text{p}K_a = 7.2$ . The small magnitude of  $k_A$  and the fact that this number is probably overestimated by our inability to obtain data points at higher pH values strongly suggests that the system does not proceed to  $H_{\text{peroxo}}$  in the absence of this crucial rate-determining proton transfer step.

The pH titration data for  $H_{\text{peroxo}}$  to Q conversion ( $k_3$ ) fit poorly to eq 2.6 (Figure 2.20), with  $\chi^2_{\text{red}} = 0.0021$ , and were much better approximated by eq 2.7 derived from Scheme 2.5ii, which describes a doubly ionizing system (Figure 2.18b), where  $k_{\text{H}_2\text{A}}$ ,  $k_{\text{HA}}$ , and  $k_A$

$$k = \frac{k_{\text{H}_2\text{A}}[\text{H}^+]^2 + K_1 k_{\text{HA}}[\text{H}^+] + k_A K_1 K_2}{K_1 K_2 + K_1[\text{H}^+] + [\text{H}^+]^2} \quad (2.7)$$

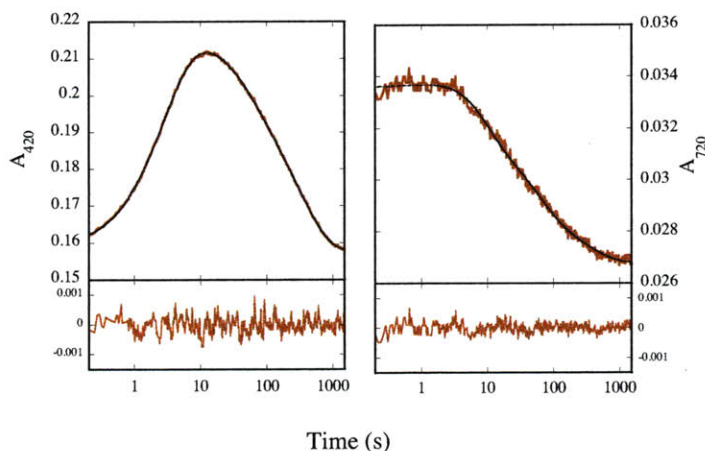


**Figure 2.21.** Representative fits of data monitoring the reaction of 50  $\mu\text{M}$   $\text{MMOH}_{\text{red}}$  and 100  $\mu\text{M}$   $\text{MMOB}$  with excess  $\text{O}_2$  at 5  $^\circ\text{C}$  in 25 mM phosphate buffer prepared in  $\text{D}_2\text{O}$ , pD 7.0. Data collected at 420 nm (left, red lines) and 720 nm (right, red lines) were fit simultaneously to the  $\text{P}^* \rightarrow \text{H}_{\text{peroxo}} \rightarrow \text{Q} \rightarrow \text{H}_{\text{ox}}$  model (eq 2.3) as discussed in the text. This method yielded acceptable fits (black lines) and residuals (bottom plots).

are rate constants for conversion of the doubly protonated, singly protonated, and unprotonated species, respectively,  $K_1$  and  $K_2$  are acid dissociation constants for the first and second protonation events, and  $\text{p}K_{\text{a}} = -\log(K_{\text{a}})$  and  $\text{pH} = -\log([\text{H}^+])$  (32). A fit of the data to this model afforded  $k_{\text{H}_2\text{A}} = 0.41 \text{ s}^{-1}$ ,  $k_{\text{HA}} = 0.19 \text{ s}^{-1}$ ,  $k_{\text{A}} = 0.008 \text{ s}^{-1}$ ,  $\text{p}K_1 = 7.9$ , and  $\text{p}K_2 = 7.0$ .  $\chi^2_{\text{red}}$  for the fit was 0.00028, which is an order of magnitude better than that of the fit to eq 2.6. These data demonstrate that both the monoprotonated and the diprotonated species are able to generate Q, but the unprotonated form cannot. The rate of conversion of the diprotonated species is approximately twice as fast as that of the monoprotonated species.

Reactions of  $\text{MMOH}_{\text{red}}$  and 2 equiv of  $\text{MMOB}$  with  $\text{O}_2$  in the absence and presence of  $\text{CH}_4$  were also conducted in buffer prepared in  $\text{D}_2\text{O}$  to discern the requirement of solvent-

derived protons during the processes monitored. Data fit well in the manner described for reactions of  $\text{MMOH}_{\text{red}}$  and 2 equiv of MMOB with  $\text{O}_2$  and  $\text{O}_2/\text{CH}_4$ , delivering  $k_1' = 6.5 \pm 2.2 \text{ s}^{-1}$ ,  $k_2 = 0.38 \pm 0.04 \text{ s}^{-1}$ ,  $k_3 = 0.20 \pm 0.03 \text{ s}^{-1}$ ,  $k_4 = 0.013 \pm 0.005 \text{ s}^{-1}$ , and  $k_5 = 0.0024 \pm 0.0007 \text{ s}^{-1}$  (Figure 2.21). The processes governed by  $k_2$  and  $k_3$  therefore display normal kinetic solvent isotope effects (KSIEs),  $k_{\text{H}}/k_{\text{D}}$ , of  $2.0 \pm 0.2$  and  $1.8 \pm 0.3$ , respectively, whereas those of  $k_1'$ ,  $k_4$ , and  $k_5$  are not affected by isotopic substitution within the error limits of the experiments. The KSIE magnitudes for  $k_2$  and  $k_3$  are typical for proton transfer reactions (33).

A concern in devising KSIE experiments is that  $\text{D}_2\text{O}$  is slightly more viscous than  $\text{H}_2\text{O}$ , which can lead to data misinterpretation if not properly accounted for. However, the changes of  $k_2$  and  $k_3$  in response to solvent content monitored here are not likely to arise from the increased viscosity effects. Glycerol affects the single turnover kinetics of this enzyme, but concentrations of this viscogen that mimic the viscosity change of  $\text{D}_2\text{O}$  are insufficient to reproduce the measured KSIE values (26, 34).

Previous kinetic experiments performed in our laboratory suggest that none of the transient events initiated by reaction of  $\text{MMOH}_{\text{red}}$  and 2 equiv of MMOB with  $\text{O}_2$  are pH-dependent nor do they exhibit significant KSIEs (6). For the pH-dependence studies, these experiments were performed via pH jump methods in which reduced protein in 10 mM MOPS pH 7.0 was mixed rapidly with  $\text{O}_2$ -saturated 100 mM MOPS of the desired pH. However, if reaction with  $\text{O}_2$  and subsequent steps are faster than exchange of relevant protons on the protein with bulk solvent, then these effects would not have been detected by using this method. For studies performed in  $\text{D}_2\text{O}$ , the values of the KSIEs are small ( $\leq 2$ ) and were most likely overlooked.

The data presented here support those reported for the *Mt* enzyme (26); however, there are some key differences between the results of the two studies. Both investigations found that the pH dependence of P\* to H<sub>peroxo</sub> conversion fit well to a model consisting of reversible protonation followed by an irreversible step (Scheme 2.5i). Studies from the *Mt* enzyme showed that the pH dependence of the H<sub>peroxo</sub> to Q conversion also fit nicely to this model, but the results reported here demonstrate that the model does not adequately represent the data. For the *Mc* enzyme, a model that describes two reversible stepwise protonation events fits the data much better. It seems unlikely that the same intermediate from two closely related sMMO systems requires separate mechanisms for proton transfer; however, the origin of the differences is unknown.

## DISCUSSION

The extraordinary ability of methane monooxygenases to catalyze the oxidation of methane selectively to methanol using atmospheric dioxygen has attracted much interest. While experiments probing the mechanism of this transformation have led to the identification of several oxygenated iron intermediate species that are capable of C–H bond abstraction, there are still many questions that remain about events that occur leading up to substrate oxidation and regeneration of the enzyme resting state. In this study, we employed stopped-flow optical spectroscopy to gain insight into the kinetics of the reactions of MMOH<sub>red</sub> with O<sub>2</sub> in the presence of regulatory protein MMOB.

*Origin of Proton Requirement.* The demonstration that P\* decay/H<sub>peroxo</sub> formation ( $k_2$ ) and H<sub>peroxo</sub> decay/Q formation ( $k_3$ ) are pH dependent and display normal KSIEs around 2 indicate that proton transfer is involved in the rate-determining steps of these processes.



The dependence of these data on pre-incubation of the protein solution at the pH of interest suggests that an exchangeable proton(s) on the protein in equilibrium with bulk solvent is associated with rate-limiting proton translocation events that give rise to the observed pH and D<sub>2</sub>O effects. Although these results verify the necessity of proton transfer for these steps, they cannot definitively describe the location or mechanism of the processes. Translocation of protons could occur at or near the active site or as a result of redox-dependent conformational changes and/or remodeling of protein-protein interactions that alter hydrogen-bonding patterns and accompany structural and electronic changes at the diiron center.

We favor mechanisms for both P\* decay/H<sub>peroxo</sub> formation and H<sub>peroxo</sub> decay/Q formation in which proton transfer occurs at or near the diiron active site or as a result of very minor structural perturbations instead of large ones. It is likely that large conformational changes or alterations in protein interactions would result in the formation and breakage of many hydrogen bonds rather than involve direct transfer of one or two protons, as the data indicate. Indeed, structural studies on the toluene 4-monooxygenase (T4mo) hydroxylase demonstrated that >20 new hydrogen bonds form as a result of conformational changes initiated by binding of its regulatory protein T4moD (35). Additionally, the observed KSIEs of ~ 2.0 are suggestive of direct proton transfer reactions rather than formation of hydrogen bonds, which usually display small, inverse KSIEs (36).

Given these observations, the pH dependencies of  $k_2$  and  $k_3$  are likely to result from proton transfer that occurs at or near the diiron center or from conformational changes restricted to single amino acid side chains that result in proton translocation. Because the

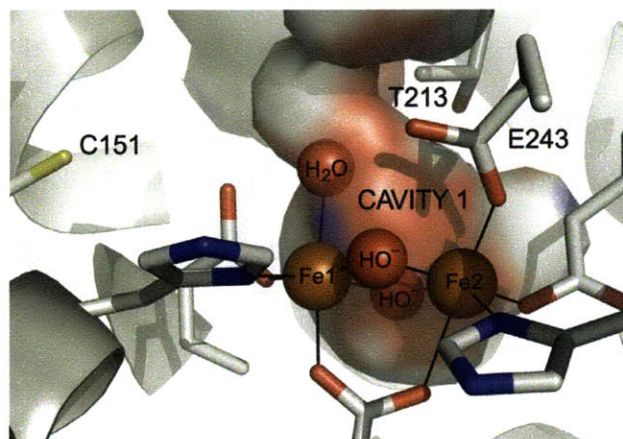


**Figure 2.22.** The  $\text{MMOH}_{\text{ox}}$  active site showing the diiron center, its ligands including the shifting carboxylate E243, and conserved active site hydrophobic residues C151 and T213. The thiol of C151 is located  $7.3 \text{ \AA}$  from Fe1 and the hydroxyl of T213 is positioned  $6.8 \text{ \AA}$  from Fe2. Hydrocarbons are expected to access the diiron site through hydrophobic cavity 1, which is shown as a surface rendering. Relevant atoms or side chains are depicted in ball-and-stick format or as spheres and are colored by atom type (carbon (gray), oxygen (red), nitrogen (blue), sulfur (yellow), iron (orange)). This image was generated in PyMOL (DeLano Scientific LLC) using PBD ID Code 1MTY.

MMOH active site cavity is mostly hydrophobic, a large thermodynamic driving force would be necessary to screen the charges that would be generated during the transfer of an active site proton (15, 18, 37). Therefore, any proton transfer event that occurs at or near the active site should maintain a charge neutral environment and diiron core.

*Implications for Proton Transfer Reactions.* Inspection of the MMOH active site cavity reveals very few non-coordinated amino acids typically thought to participate in general acid-base catalysis that are located within reasonable proton transfer distance to the iron center (Figure 2.22). Of those that can potentially participate in such reactions, the only candidates are T213, C151, Q140, D143, and D242. However, none of these amino acids are particularly attractive possibilities because they are all too far from the diiron center

to participate in direct proton transfer involving this unit and/or do not display  $pK_a$  values near the values measured for  $k_2$  and  $k_3$ . Additionally, proton transfer to or from these residues would result in an unlikely active site charge separation. Therefore, this type of mechanism is not anticipated.

A favorable alternative for a proton donor or acceptor is an active site water molecule. Although the  $pK_a$  of water is 15.7, this value is significantly reduced by coordination to iron (38, 39). Indeed, terminal Fe(III)-aqua complexes are acidic; for example, the  $pK_a$  for deprotonation of  $[\text{Fe}(\text{H}_2\text{O})_6]^{3+}$  is 2.74 and the species exists as  $[\text{Fe}(\text{OH})(\text{H}_2\text{O})_5]^{2+}$  at neutral pH (40). Possible candidates for iron-bound proton donors or acceptors with  $pK_a$  values in the range of those measured for  $k_2$  and  $k_3$  include terminal aqua or hydroxo groups and/or bridging hydroxide moieties. These possibilities are particularly attractive because proton transfer to/from an iron-bound water-derived molecule from/to another ligand coordinated to the diiron center would maintain a charge-neutral diiron core. Additionally, the proximity of a proton acceptor/donor pair in the case where both units are located at the diiron center is ideal for direct proton transfer. Of special interest to our system is the finding that  $\text{H}^+$  addition to a terminal hydroxo group drives the formation of a  $[\text{Fe}^{\text{IV}}_2(\mu\text{-O})_2]^{4+}$  Q-like species in a synthetic model system (41).

Protons could be transferred from a solvent-derived water ligand to a flexible iron ligand. Such an event would maintain a charge-neutral diiron core and might initiate electronic changes at the oxygen-iron unit that promote catalytic events during  $\text{O}_2$  activation. Of particular interest is the redox-dependent shifting carboxylate ligand E243, which coordinates in a bidentate fashion, binding to Fe2 and bridging the two irons atoms in the reduced form of the enzyme, but binds in a monodentate manner and only to Fe2

when the iron center is oxidized (42, 43). Departure of E243 from its bridging position may open a coordination site for O<sub>2</sub> to bind and/or accommodate active site structural changes associated with O–O bond cleavage and Q formation. Carboxylate shifts of this kind play an important role in controlling the reactivity of diiron proteins and synthetic model systems (42, 44, 45). It is therefore possible that protonation of E243 provides the driving force that promotes dissociation of this ligand from its bridging position and initiates structural and electronic changes during O<sub>2</sub> activation. Although carboxylate residues are acidic, the hydrophobic nature of the active site might raise the pK<sub>a</sub> of E243 to a neutral value. Other amino acid-based possibilities are the coordinating histidines H147 and H246, the protonation of which would most likely also cause these ligands to dissociate. Recent crystallographic studies of the diiron protein *Hedera helix* 18:0 Δ<sup>9</sup>-desaturase demonstrated that a histidine ligand undergoes redox-dependent decoordination of exactly this kind (46). The pK<sub>a</sub> values of histidine residues are within range of those measured for  $k_2$  and  $k_3$ .

One last possibility is that protons are transferred directly to the iron-bound peroxide moiety in these steps. This type of mechanism could result in a hydroperoxo intermediate and facilitate heterolytic O–O bond cleavage, as shown in Scheme 1b. It is invoked in electronically similar cytochrome P450 enzymes (24). Protonation of the peroxide could alternatively promote O–O bond cleavage directly. Recent theoretical studies investigating a similar peroxodiiron(III) species in RNR and a mutant form of RNR suggest that H<sup>+</sup> addition to the O–O unit does not result in a stable hydroperoxo species and instead causes O–O bond scission in this enzyme (47).

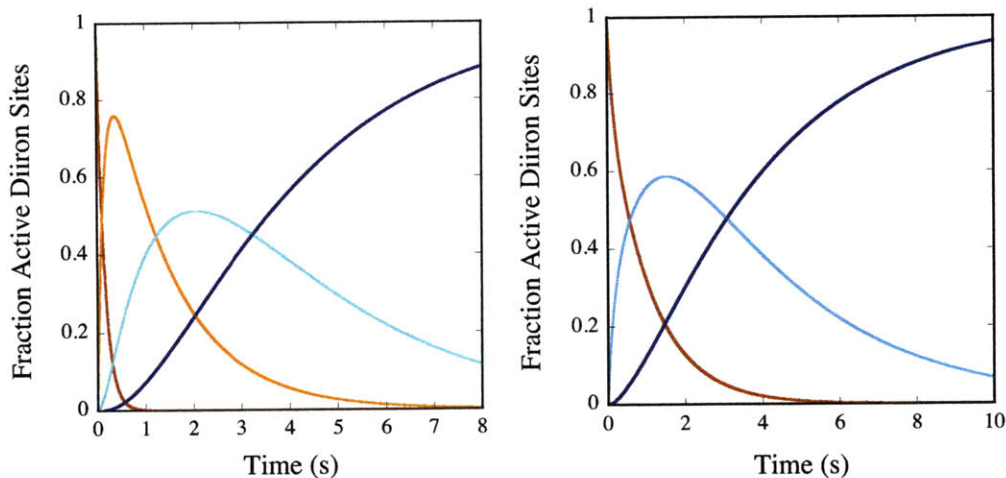


**Figure 2.23.** Speciation plots depicting the time-dependence of each species that forms during the reaction of 50  $\mu\text{M}$   $\text{MMOH}_{\text{red}}$  and 100  $\mu\text{M}$   $\text{MMOB}$  with  $\sim 210 \mu\text{M}$   $\text{O}_2$  in the presence of 540  $\mu\text{M}$   $\text{CH}_4$  at pH 7.0 and 4  $^\circ\text{C}$  according to models 2.2i (a) and 2.2ii (b). (a) The concentrations of  $[\text{H}_{\text{red}}]$  (red),  $[\text{P}^*]$  (orange),  $[\text{H}_{\text{peroxo}}]$  (cyan), and  $[\text{H}_{\text{ox}}]$  (blue) as a function of time were calculated from the  $\text{H}_{\text{red}} + \text{O}_2 \rightarrow \text{P}^* \rightarrow \text{H}_{\text{peroxo}} \rightarrow \text{H}_{\text{ox}}$  model i from scheme 2.2 using rate constants obtained from fits of data to eq 2.1. (b) The concentrations of  $[\text{H}_{\text{red}}]$  (red),  $[\text{H}_{\text{peroxo}}]$  (cyan), and  $[\text{H}_{\text{ox}}]$  (blue) as a function of time were calculated from scheme 2.2 model ii using rate constants obtained from fits of data to eq 2.2.

*Identity of P\**. Reactions of  $\text{MMOH}_{\text{red}}$  and 2 equiv of  $\text{MMOB}$  with  $\text{O}_2$  performed in the presence of high ( $\geq 540 \mu\text{M}$ ) concentrations of  $\text{CH}_4$  have provided for the first time in the *Mc* enzyme system direct kinetic evidence for two species that precede Q formation,  $\text{P}^*$  and  $\text{H}_{\text{peroxo}}$ . Comparisons of the data reported here to previous Mössbauer and optical spectroscopic studies are revealing. Mössbauer spectroscopy identified a single peroxodiiron(III) intermediate with  $k_{\text{form}} \approx 25 \text{ s}^{-1}$ ,  $k_{\text{decay}} = 0.45 \text{ s}^{-1}$ , and  $t_{\text{max}} = 156 \text{ ms}$  at 4  $^\circ\text{C}$  (6). Optical spectroscopic experiments also provided evidence for a single peroxodiiron(III) species, but this unit was characterized by quite different kinetic parameters:  $k_{\text{form}} \approx 1.6 \text{ s}^{-1}$ ,  $k_{\text{decay}} = 0.40 \text{ s}^{-1}$  and  $t_{\text{max}} = 1\text{-}2 \text{ s}$  at 4  $^\circ\text{C}$  (9). To reconcile the

dramatic difference in formation rate constants observed by these two methods, we proposed the presence of two peroxodiiron(III) species characterized by similar Mössbauer parameters, the first of which was not observable by optical spectroscopy (9). Data collected at high concentrations of CH<sub>4</sub> (≥540 μM) presented here unveil the spectrum of P\* and provide the first optical evidence for this H<sub>peroxo</sub> precursor in the *Mc* enzyme. Speciation plots derived from our data lead to the prediction that P\* has  $t_{\max} = 370$  ms and H<sub>peroxo</sub> is characterized by  $t_{\max} = 2.1$  s, which is reasonably consistent with the results obtained previously (Figure 2.23a). On the other hand, speciation plots derived from model ii are not consistent with these data, bolstering the argument that this model is not correct (Figure 2.23b).

Although this work helps to reconcile the differences observed between the two forms of spectroscopy, the rate constant for P\* formation measured here is still much lower than that obtained by Mössbauer spectroscopy. Due to limitations of our instrumentation, the value of  $k_1'$  measured here is almost certainly underestimated (and the  $t_{\max}$  of P\* overestimated) by the fact P\* accumulates considerably in the stopped-flow dead time, as evidenced by the fact that the starting absorbances at 420 nm and 720 nm are much greater than those expected for H<sub>red</sub> (Figure 2.2, Figure 2.3, and Figure 2.4). Therefore, P\* might evolve directly from H<sub>red</sub>, but these data do not rule out the possibility that there is an additional undetected intermediate that forms prior to P\*. Similar reasoning led to the proposal of intermediate O, a possible O<sub>2</sub>-bound diiron(II) species, in *Mt* MMOH (3, 48).

Because Mössbauer spectroscopy identified only one Q precursor, it is possible that P\* and H<sub>peroxo</sub> exhibit indistinguishable Mössbauer parameters. However, Mössbauer data were not reported in the 0.5-3 s time regime in which H<sub>peroxo</sub> maximally accumulates

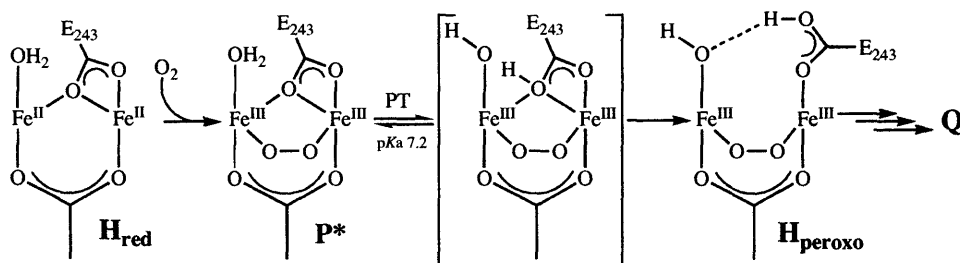
according to our optical data (6). Without further analysis we cannot rule out the possibility of distinct parameters for this intermediate. One certainty based on data collected before 0.5 s and the similar  $t_{\max}$  values of the species characterized by Mössbauer spectroscopy and P\* is that this intermediate is characterized by  $\delta = 0.66$  mm/s and  $\Delta E_Q = 1.51$  mm/s. Similar Mössbauer parameters have been assigned to a synthetic, structurally characterized model ( $\mu$ -1,2-peroxo)diiron(III) model complex supported by a tris(pyrazolyl)borate ligand scaffold (49) as well as the peroxodiiron(III) intermediate generated in the W48A/D84E variant of RNR-R2, both of which feature  $\mu$ -peroxide binding geometries (10, 50). The absorbance band of P\* at 720 nm ( $\epsilon = 1250$  M<sup>-1</sup> cm<sup>-1</sup>) is similar to those of well-characterized peroxodiiron(III) species in enzymes (13, 50-53) and model systems (49, 54) assigned as peroxo-to-Fe(III) charge transfer transitions. Because of its spectroscopic similarities to those of known enzyme intermediates and model complexes, P\* is likely to contain a peroxodiiron(III) unit. Another possibility is a mixed-valent Fe(II)Fe(III) superoxide complex, but this assignment is less likely because the Mössbauer spectrum of such a species should exhibit two distinct quadrupole doublets due to the expected valence localization of the unpaired electrons in this type of system.

The presence of two detectable intermediates that precede Q formation in *Mt* MMOH was previously reported (3). The first of these species, P\*, forms with a rate constant identical to that of O decay (26) and proceeds to intermediate P. The second, P, was reported to absorb minimally at 430 nm, the wavelength at which the data were collected, based on two observations. First, a phase corresponding to P\* to P conversion was not necessary to fit data monitored in the absence of substrate, which were modeled well by

three phases attributed to O to P\*, P to Q, and Q to H<sub>ox</sub> conversion. Secondly, formation of P contributed only a very small amount to the total amplitude of the absorbance rise phase when experiments were performed in the presence of high concentrations of furan to remove optical contributions from Q. The authors argued that the absorbance attributed to this intermediate (H<sub>peroxo</sub>) at 420 nm in previous reports from our group on the *Mc* system was an artifact from absorption of Q at this wavelength. However, the data presented here, collected in the presence of methane in which there is no possibility of interference from Q, now provide definitive evidence that H<sub>peroxo</sub> does indeed absorb strongly at this wavelength and disagree with the results from the *Mt* enzyme.

*Nature of P\* to H<sub>peroxo</sub> Conversion.* The similarities of the P\* optical extinction coefficients to those of H<sub>peroxo</sub> suggests that these intermediates are electronically and geometrically identical. Analysis of the pH dependence data indicates that a single proton is transferred during the rate-limiting step of P\* to H<sub>peroxo</sub> conversion and that this protonation event, with a pK<sub>a</sub> of 7.2, must occur for H<sub>peroxo</sub> to form. As discussed above, this process may involve direct protonation of the O–O moiety or of a coordinating diiron ligand. Formation of a hydroperoxo by protonation of the peroxide, however, would most likely alter the energy of the peroxo-to-iron(III) charge transfer band of P\* and the Mössbauer parameters of the species, and the spectroscopic properties of the protonated and unprotonated peroxodiiron(III) species are expected to be different (55, 56). Given this observation, it is most likely that P\* to H<sub>peroxo</sub> conversion occurs via proton transfer to a coordinating amino acid or water-based ligand and not the iron-bound peroxide moiety. For reasons stated above, we prefer E243 as the proton acceptor. Of relevance to this argument are recent theoretical studies of the peroxo intermediates of RNR and its





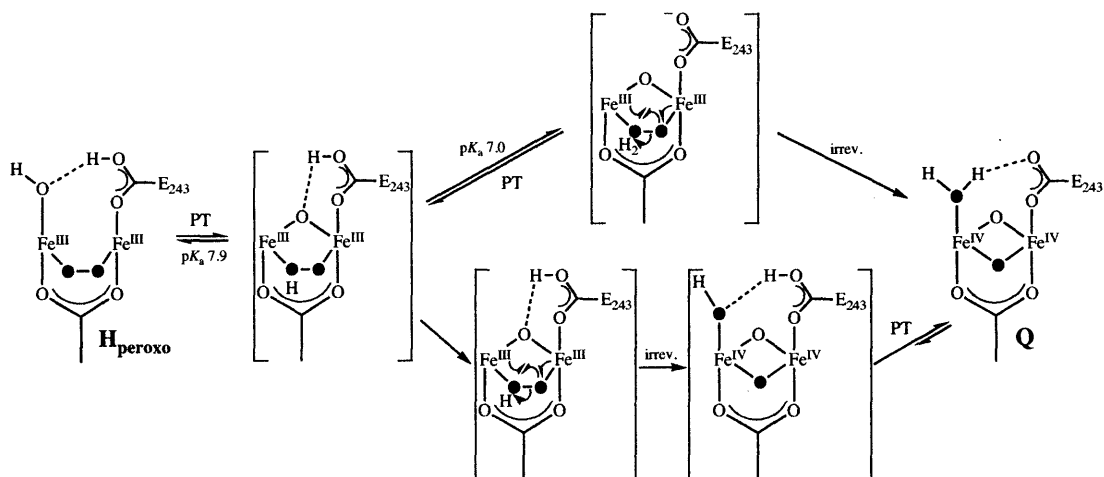
**Scheme 2.6.** Postulated Mechanism of P\* to H<sub>peroxo</sub>

W48A/Y122F variant (57), which find that proton transfer from an iron-bound water molecule or from a solvent-derived proton to a bridging carboxylate ligand are both energetically feasible and result in stable peroxodiiron(III) species (47). In the former mechanism, proton transfer occurs with concomitant opening of the bidentate carboxylate bridge. Furthermore, recent studies investigating the addition of a proton to the peroxodiiron(III) model complex  $[\text{Fe}_2(\mu\text{-O}_2)(N\text{-EtHPTB})(\mu\text{-PhCO}_2)]^{2+}$  resulted in protonation and dissociation of a bridging benzoate ligand instead of the peroxide unit (58). These findings, the necessity of E243 to dissociate from its bridging position to accommodate structural changes associated with H<sub>peroxo</sub> to Q conversion, and the potential of a hydrophobic active site to raise the  $pK_a$  of this carboxylate suggest the mechanism presented in Scheme 2.6. This mechanism is also consistent with the large, positive entropy of activation observed for this step.

*Nature of H<sub>peroxo</sub> to Q Conversion.* The ability of sMMO to provide a single oxygen atom from molecular oxygen for incorporation into hydrocarbon substrates depends on its ability to cleave the O–O bond and form a potent oxidant. O–O bond scission occurs concomitant with H<sub>peroxo</sub> to Q conversion; however, the mechanistic details of this step are

not well understood. Scheme 2.1 depicts two simplified mechanisms for this event in which O–O bond cleavage processes are either homolytic (2.1a) or heterolytic (2.1b). In principle, the products of steady state reaction of the enzyme with substrate using  $^{18}\text{O}_2$  might discriminate between these mechanisms. Product is expected to be completely labeled if both oxygen atoms of Q derive from  $\text{O}_2$ , but might contain a mixture of  $^{16}\text{O}$  and  $^{18}\text{O}$  labels if a solvent-derived oxygen atom were incorporated into Q. Such a study did reveal that 100% of label is incorporated into methanol (59), in support of a homolytic mechanism. However, this interpretation is not definitive because the second labeled oxygen atom might be retained in the active site. In this manner, 100% of the label could be incorporated into product, even when the O–O bond is cleaved heterolytically.

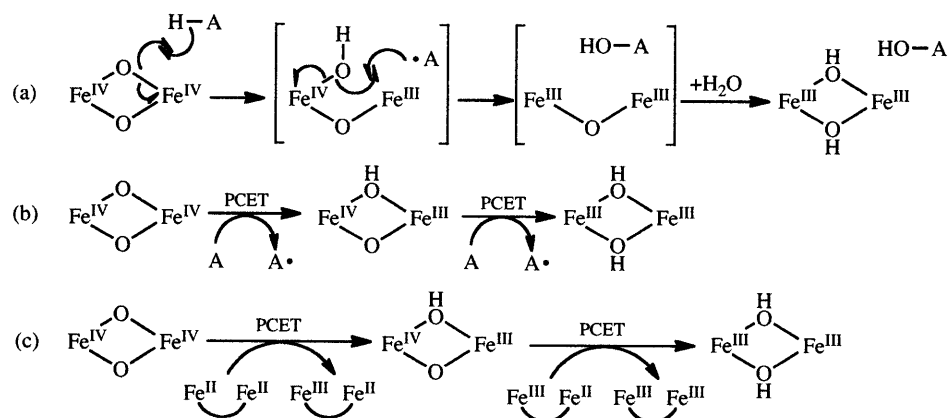
Analysis of the pH dependence data suggests that two protons can be transferred before the first irreversible step of  $\text{H}_{\text{peroxo}}$  to Q conversion. Whereas one protonation event, with a  $\text{p}K_{\text{a}}$  of 7.9, is crucial for Q formation, the second, with a  $\text{p}K_{\text{a}}$  of 7.0, accelerates the rate of conversion of the monoprotonated species but is not required. The absolute necessity of the first protonation step suggests that it occurs directly at the iron center and facilitates O–O bond cleavage. One possible mechanism of  $\text{H}_{\text{peroxo}}$  to Q conversion is depicted in Scheme 2.7. In this mechanism, a first and necessary proton transfer occurs from a terminal hydroxide, forming a hydroperoxide and an oxo bridge. The O–O bond of the hydroperoxide can then be cleaved heterolytically to form a transient  $\text{Fe}_2^{\text{IV}}$  species with a terminal hydroxide. Proton transfer from E243 after irreversible O–O bond cleavage could then generate Q. Whereas this single proton transfer pathway is sufficient for Q formation, a second protonation at the peroxide moiety, characterized by a  $\text{p}K_{\text{a}}$  of 7.0,



**Scheme 2.7.** Postulated Mechanism of  $H_{\text{peroxo}}$  to  $Q$  conversion, Depicting Only Key Iron Ligands and the Oxygen Atoms Derived from  $O_2$  as Filled Circles

might lead to more rapid O–O bond scission. The O–O bond breakage process is depicted to occur via a concerted heterolytic mechanism but might involve generation of a transient  $Fe^{III}Fe^V$  terminal oxo species (60).

*Mechanism of Q Decay.* The mechanism of  $Q$  decay in the absence of substrates has remained an enigma for many years. This reaction requires the acquisition of two protons and two electrons at the diiron active site, but the source of these substrates is unknown. Protons could derive from solvent; however, because there are no exogenous electron donors in the reaction mixture the electrons must come from the protein itself. Two possible protein-based reductants can be envisioned in this system: amino acid side chains, and/or a diiron(II) center in the neighboring MMOH protomer (Scheme 2.8). For



**Scheme 2.8.** Possible Mechanisms of Q Decay in the Absence of Hydrocarbon Substrates

the former, Q could abstract electrons and possibly protons from a nearby amino acid residue(s). This process could be achieved either by direct oxidative hydroxylation of a proximal amino acid residue (Scheme 2.8a) or by two stepwise electron transfer events, most likely proton-coupled (Scheme 2.8b). The latter option would generate a protein-based radical and a mixed valent  $\text{Fe}^{\text{III}}\text{Fe}^{\text{IV}}$  center. It is reminiscent of chemistry occurring in the R2 subunit of RNR, in which the nearby amino acids W48 and Y122 can donate electrons to the iron site during formation of the  $\text{Fe}^{\text{III}}\text{Fe}^{\text{IV}}$  intermediate X (Scheme 2.8c) (61, 62). For the second option, it is possible that electrons from a neighboring diiron(II) center could quench Q, as proposed to explain the formation of  $\text{Fe}^{\text{III}}\text{Fe}^{\text{IV}}$  and  $\text{Fe}^{\text{II}}\text{Fe}^{\text{III}}$  species in the reaction of a synthetic tetracarboxylate diiron(II) model system with  $\text{O}_2$  (63). If a diiron(II) center is present in the active site of one hydroxylase protomer when Q had formed in the other, intramolecular electron transfer between the diiron centers could lead to formation of two diiron(III)  $\text{H}_{\text{ox}}$  species. Indeed, a large population of  $\text{H}_{\text{red}}$

decays to  $H_{ox}$  by an unknown mechanism on a timescale that is much slower than the  $O_2$  activation phase (6) and therefore a significant portion diiron(II) is available to donate electrons to Q. However, this possibility seems less likely considering that the distance between the two iron centers is  $\sim 45 \text{ \AA}$  (64), an unprecedented distance for protein electron transfer.

The data reported here suggest for the first time an intermediate species,  $Q^*$ , which forms as a result of Q decay in the absence of hydrocarbon substrates. Two lines of evidence indicate that  $Q^*$  is an intermediate on the Q decay pathway rather than a functionally significant species. First,  $Q^*$  is not capable of methane oxidation, and second, Q reacts with methane and does so by a mechanism that does not proceed through  $Q^*$ . This intermediate could be composed of an  $Fe^{III}Fe^{IV}$  unit and a protein-based radical (Scheme 2.8b) or a combination of  $Fe^{III}Fe^{IV}$  and  $Fe^{II}Fe^{III}$  species (Scheme 2.8c), both of which are consistent with its optical spectrum. It is also possible that  $Q^*$  is a rearranged thermodynamically stable  $Fe^{IV}_2$  product of Q. Spectroscopic characterization of intermediate  $Q^*$  is currently in progress to investigate the nature of this species.

## CONCLUDING REMARKS

The data presented here provide conclusive kinetic evidence for the presence of multiple oxygenated diiron intermediates that accumulate during MMOH  $O_2$  activation and demonstrate that  $P^*$  to  $H_{peroxo}$  and  $H_{peroxo}$  to Q conversion are both pH dependent. These studies and recent investigations of other BMMs and model complexes highlight the complexity of the systems, particularly with respect to coordinating the steps of  $O_2$  activation, proton translocation, electron transfer, and hydrocarbon entry and egress.

Taken together, the present study and prior work on the *Mt* system have now begun to converge, providing a framework for understanding MMOH catalysis and a paradigm for interpreting kinetic data in this system. However, questions raised by these studies indicate the need for further kinetic and spectroscopic evaluation. For example, the nature of the proton transfer events during P\* to H<sub>peroxo</sub> and H<sub>peroxo</sub> to Q conversion and the electronic and geometric identities of the four intermediates are pressing, unsolved questions. Possible future experiments include reinvestigating the spectroscopic properties and protonation states of P\*, H<sub>peroxo</sub>, and Q and determining those of Q\*.

## REFERENCES

1. Merkx, M., Kopp, D. A., Sazinsky, M. H., Blazyk, J. L., Müller, J., and Lippard, S. J. (2001) *Angew. Chem. Int. Ed.* 40, 2782-2807.
2. Hakemian, A. S., and Rosenzweig, A. C. (2007) *Annu. Rev. Biochem.* 76, 223-241.
3. Brazeau, B. J., and Lipscomb, J. D. (2000) *Biochemistry* 39, 13503-13515.
4. Lee, S.-K., Fox, B. G., Froland, W. A., Lipscomb, J. D., and Münck, E. (1993) *J. Am. Chem. Soc.* 115, 6450-6451.
5. Lee, S.-K., Nesheim, J. C., and Lipscomb, J. D. (1993) *J. Biol. Chem.* 268, 21569-21577.
6. Liu, K. E., Valentine, A. M., Wang, D., Huynh, B. H., Edmondson, D. E., Salifoglou, A., and Lippard, S. J. (1995) *J. Am. Chem. Soc.* 117, 10174-10185.
7. Liu, K. E., Wang, D., Huynh, B. H., Edmondson, D. E., Salifoglou, A., and Lippard, S. J. (1994) *J. Am. Chem. Soc.* 116, 7465-7466.

8. Beauvais, L. G., and Lippard, S. J. (2005) *J. Am. Chem. Soc.* *127*, 7370-7378.
9. Valentine, A. M., Stahl, S. S., and Lippard, S. J. (1999) *J. Am. Chem. Soc.* *121*, 3876-3887.
10. Moënne-Loccoz, P., Baldwin, J., Ley, B. A., Loehr, T. M., and Bollinger Jr., J. M. (1998) *Biochemistry* *37*, 14659-14663.
11. Skulan, A. J., Brunold, T. C., Baldwin, J., Saleh, L., Bollinger Jr., J. M., and Solomon, E. I. (2004) *J. Am. Chem. Soc.* *126*, 8842-8855.
12. Moënne-Loccoz, P., Krebs, C., Herlihy, K., Edmondson, D. E., Theil, E. C., Huynh, B. H., and Loehr, T. M. (1999) *Biochemistry* *38*, 5290-5295.
13. Broadwater, J. A., Ai, J., Loehr, T. M., Sanders-Loehr, J., and Fox, B. G. (1998) *Biochemistry* *37*, 14664-14671.
14. Vu, V. V., Emerson, J. P., Martinho, M., Kim, Y. S., Münck, E., Park, M. H., and Que Jr., L. (2009) *Proc. Natl. Acad. Sci. USA* *106*, 14814-14819.
15. Han, W.-G., and Noodleman, L. (2008) *Inorg. Chem.* *47*, 2975-2986.
16. Gherman, B. F., Baik, M.-H., Lippard, S. J., and Friesner, R. A. (2004) *J. Am. Chem. Soc.* *126*, 2978-2990.
17. Rinaldo, D., Philipp, D. M., Lippard, S. J., and Friesner, R. A. (2007) *J. Am. Chem. Soc.* *129*, 3135-3147.
18. Siegbahn, P. E. M. (2001) *J. Biol. Inorg. Chem.* *6*, 27-45.
19. Shu, L., Nesheim, J. C., Kauffmann, K., Münck, E., Lipscomb, J. D., and Que Jr., L. (1997) *Science* *275*, 515-518.
20. Ambundo, E. A., Friesner, R. A., and Lippard, S. J. (2002) *J. Am. Chem. Soc.* *124*, 8770-8771.

21. Baik, M.-H., Gherman, B. F., Friesner, R. A., and Lippard, S. J. (2002) *J. Am. Chem. Soc.* *124*, 14608-14615.
22. Halfen, J. A., Mahapatra, S., Wilkinson, E. C., Kaderli, S., Young Jr., V. G., Que Jr., L., Zuberbühler, A. D., and Tolman, W. B. (1996) *Science* *271*, 1397-1400.
23. Lewis, E. A., and Tolman, W. B. (2004) *Chem. Rev.* *104*, 1047-1076.
24. Denisov, I. G., Makris, T. M., Sligar, S. G., and Schlichting, I. (2005) *Chem. Rev.* *105*, 2253-2277.
25. Nam, W. (2007) *Acc. Chem. Res.* *40*, 522-531.
26. Lee, S.-K., and Lipscomb, J. D. (1999) *Biochemistry* *38*, 4423-4432.
27. Coufal, D. E., Blazyk, J. L., Whittington, D. A., Wu, W. W., Rosenzweig, A. C., and Lippard, S. J. (2000) *Eur. J. Biochem.* *267*, 2174-2185.
28. Kopp, D. A., Gassner, G. T., Blazyk, J. L., and Lippard, S. J. (2001) *Biochemistry* *40*, 14932-14941.
29. Wilhelm, E., Battino, R., and Wilcock, R. J. (1977) *Chem. Rev.* *77*, 219-262.
30. Beechem, J. M. (1992) *Methods Enzymol.* *210*, 37-54.
31. Murray, L. J., and Lippard, S. J. (2007) *Acc. Chem. Res.* *40*, 466-474.
32. Fersht, A. (1977) *Enzyme Structure and Mechanism*, 2nd ed., W. H. Freeman and Co., New York, NY.
33. Quinn, D. M., and Sutton, L. D. (1991) Theoretical Basis and Mechanistic Utility of Solvent Isotope Effects, in *Enzyme Mechanism from Isotope Effects* (Cook, P. F., Ed.), CRC Press, Boca Raton.
34. Tinberg, C., and Lippard, S. J. (2009) Unpublished Results.



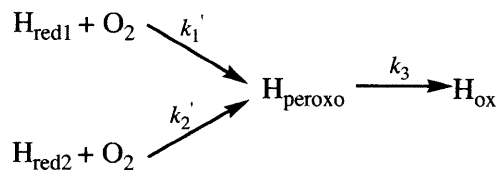
35. Bailey, L. J., McCoy, J. G., Phillips Jr., G. N., and Fox, B. G. (2008) *Proc. Natl. Acad. Sci. USA* 105, 19194-19198.
36. Schowen, K. B., and Schowen, R. L. (1982) *Methods Enzymol.* 87, 551-606.
37. Dunietz, B. D., Beachy, M. D., Cao, Y., Whittington, D. A., Lippard, S. J., and Friesner, R. A. (2000) *J. Am. Chem. Soc.* 122, 2828-2839.
38. Holm, R. H., Kennepohl, P., and Solomon, E. I. (1996) *Chem. Rev.* 96, 2239-2314.
39. Lippard, S. J., and Berg, J. M. (1994) *Principles of Bioinorganic Chemistry*, University Science Books, Mill Valley, CA.
40. Cotton, F. A., Wilkinson, G., Murillo, C. A., and Bochmann, M. (2003) *Advanced Inorganic Chemistry*, 6th ed., John Wiley & Sons, Inc, New York.
41. Xue, G., Fiedler, A. T., Martinho, M., Münck, E., and Que Jr., L. (2008) *Proc. Natl. Acad. Sci. USA* 105, 20615-20620.
42. Sazinsky, M. H., and Lippard, S. J. (2006) *Acc. Chem. Res.* 39, 558-566.
43. Whittington, D. A., and Lippard, S. J. (2001) *J. Am. Chem. Soc.* 123, 827-838.
44. Rardin, R. L., Tolman, W. B., and Lippard, S. J. (1991) *New J. Chem.* 15, 417-430.
45. Tshuva, E. Y., and Lippard, S. J. (2004) *Chem. Rev.* 104, 987-1012.
46. Shanklin, J., Guy, J. E., Mishra, G., and Lindqvist, Y. (2009) *J. Biol. Chem.* 284, 18559-18563.
47. Jensen, K. P., Bell, C. B. I., Clay, M. D., and Solomon, E. I. (2009) *J. Am. Chem. Soc.* 131, 12155-12171.

48. Liu, Y., Nesheim, J. C., Lee, S.-K., and Lipscomb, J. D. (1995) *J. Biol. Chem.* 270, 24662-24665.
49. Kim, K., and Lippard, S. J. (1996) *J. Am. Chem. Soc.* 118, 4914-4915.
50. Baldwin, J., Krebs, C., Saleh, L., Stelling, M., Huynh, B. H., Bollinger Jr., J. M., and Riggs-Gelasco, P. (2003) *Biochemistry* 42, 13269-13279.
51. Bollinger Jr., J. M., Krebs, C., Vicol, A., Chen, S., Ley, B. A., Edmondson, D. E., and Huynh, B. H. (1998) *J. Am. Chem. Soc.* 120, 1094-1095.
52. Pereira, A. S., Small, W., Krebs, C., Tavares, P., Edmondson, D. E., Theil, E. C., and Huynh, B. H. (1998) *Biochemistry* 37, 9871-9876.
53. Song, W. J., Behan, R. K., Naik, S. G., Huynh, B. H., and Lippard, S. J. (2009) *J. Am. Chem. Soc.* 131, 6074-6075.
54. Yamashita, M., Furutachi, H., Tosha, T., Fujinami, S., Saito, W., Maeda, Y., Takahashi, K., Tanaka, K., Kitagawa, T., and Suzuki, M. (2007) *J. Am. Chem. Soc.* 129, 2.
55. Liu, J.-G., Ohta, T., Yamaguchi, S., Ogura, T., Sakamoto, S., Maeda, Y., and Naruta, Y. (2009) *Angew. Chem. Int. Ed.* 48, 1-6.
56. Roelfes, G., Vrajmasu, V., Chen, K., Ho, R. Y. N., Rohde, J.-U., Zondervan, C., la Crois, R. M., Schudde, E. P., Lutz, M., Spek, A. L., Hage, R., Feringa, B. L., Münck, E., and Que Jr., L. (2003) *Inorg. Chem.* 42, 2639-2653.
57. Saleh, L., Krebs, C., Ley, B. A., Naik, S., Huynh, B. H., and Bollinger Jr., J. M. (2004) *Biochemistry* 43, 5953-5964.
58. Do, L. H., Hayashi, T., Moënne-Loccoz, P., and Lippard, S. J. (2010) *J. Am. Chem. Soc.* 132, 1273-1275.

59. Nesheim, J. C., and Lipscomb, J. D. (1996) *Biochemistry* 35, 10240-10247.
60. Rowe, G. T., Rybak-Akimova, E. V., and Caradonna, J. P. (2007) *Inorg. Chem.* 46, 10594-10606.
61. Krebs, C., Chen, S., Baldwin, J., Ley, B. A., Patel, U., Edmondson, D. E., Huynh, B. H., and Bollinger Jr., J. M. (2000) *J. Am. Chem. Soc.* 122, 12207-12219.
62. Stubbe, J., Nocera, D. G., Yee, C. S., and Chang, M. C. Y. (2003) *Chem. Rev.* 103, 2167-2201.
63. Lee, D., Du Bois, J., Petasis, D., Hendrich, M. P., Krebs, C., Huynh, B. H., and Lippard, S. J. (1999) *J. Am. Chem. Soc.* 121, 9893-9894.
64. Rosenzweig, A. C., Frederick, C. A., Lippard, S. J., and Nordlund, P. (1993) *Nature* 366, 537-543.

## APPENDIX 2.1

### Derivation of eq 2.2 Describing Model ii of Scheme 2.2:



We can derive an equation to fit the absorbance versus time ( $\text{Abs}_s(t)$ ) for any wavelength given the extinction coefficients for each species and assuming that all of the reactions are irreversible.

The change in concentration of  $\text{H}_{\text{red1}}$  is defined by (1). If  $[\text{O}_2] \gg \gg [\text{H}_{\text{red1}}]$ ,  $k_1$  becomes  $k_1'$ .

$$-\frac{d[\text{H}_{\text{red1}}]}{dt} = k_1[\text{H}_{\text{red1}}][\text{O}_2] = k_1'[\text{H}_{\text{red1}}]_t \quad (1)$$

Integrate (1).

$$[\text{H}_{\text{red1}}]_t = [\text{H}_{\text{red1}}]_0 e^{-k_1' t} \quad (2)$$

The change in concentration of  $\text{H}_{\text{red2}}$  is defined by (3). If  $[\text{O}_2] \gg \gg [\text{H}_{\text{red1}}]$ ,  $k_2$  becomes  $k_2'$ .

$$-\frac{d[\text{H}_{\text{red2}}]}{dt} = k_2[\text{H}_{\text{red2}}][\text{O}_2] = k_2'[\text{H}_{\text{red2}}]_t \quad (3)$$

Integrate (3).

$$[\text{H}_{\text{red2}}]_t = [\text{H}_{\text{red2}}]_0 e^{-k_2' t} \quad (4)$$

The change in concentration of  $\text{H}_{\text{peroxo}}$  is defined by (5).

$$-\frac{d[\text{H}_{\text{peroxo}}]}{dt} = k_1'[\text{H}_{\text{red1}}]_t + k_2'[\text{H}_{\text{red2}}]_t - k_3[\text{H}_{\text{peroxo}}]_t \quad (5)$$

Substitute (2) and (4) into (5).

$$-\frac{d[\text{H}_{\text{peroxo}}]}{dt} = k_1'[\text{H}_{\text{red1}}]_0 e^{-k_1' t} + k_2'[\text{H}_{\text{red2}}]_0 e^{-k_2' t} - k_3[\text{H}_{\text{peroxo}}]_t \quad (6)$$

Rearrange (6) to give a linear differential equation of the first order.

$$\frac{d[\text{H}_{\text{peroxo}}]}{dt} + k_3[\text{H}_{\text{peroxo}}]_t = k_1'[\text{H}_{\text{red1}}]_0 e^{-k_1' t} + k_2'[\text{H}_{\text{red2}}]_0 e^{-k_2' t} \quad (7)$$

Linear differential equations of the first order have the form shown in (8).

$$-\frac{dy}{dx} + P(x)y = Q(x) \quad (8)$$

The solution to (8) is obtained by letting S be an antiderivative of P, so that  $S'(x) = P(x)$ , and then multiplying both sides by  $\exp(S(x))$ .

$$e^{S(x)} \frac{dy}{dx} + e^{S(x)} P(x)y = e^{S(x)} Q(x) \quad (9)$$

The general solution to (9) is shown in (10).

$$y = e^{-S(x)} \int e^{S(x)} Q(x) dx \quad (10)$$

Multiply both sides of (7) by  $\exp(k_3 t)$ .

$$e^{k_3 t} \frac{d[\text{H}_{\text{peroxo}}]}{dt} + e^{k_3 t} k_3 [\text{H}_{\text{peroxo}}]_t = e^{k_3 t} (k_1'[\text{H}_{\text{red1}}]_0 e^{-k_1' t} + k_2'[\text{H}_{\text{red2}}]_0 e^{-k_2' t}) \quad (11)$$

Solve using (10).

$$[\text{H}_{\text{peroxo}}]_t = e^{-k_3 t} \int e^{k_3 t} (k_1'[\text{H}_{\text{red1}}]_0 e^{-k_1' t} + k_2'[\text{H}_{\text{red2}}]_0 e^{-k_2' t}) \quad (12)$$

Rearrange (12):

$$[\text{H}_{\text{peroxo}}]_t = e^{-k_3 t} \int k_1'[\text{H}_{\text{red1}}]_0 e^{(k_3 - k_1') t} + e^{-k_3 t} \int k_2'[\text{H}_{\text{red2}}]_0 e^{(k_3 - k_2') t} \quad (13)$$

Integrate (13):

$$[\text{H}_{\text{peroxo}}]_t = e^{-k_3 t} k_1' [\text{H}_{\text{red1}}]_0 \left( \frac{1}{k_3 - k_1'} \right) e^{(k_3 - k_1') t} + e^{-k_3 t} k_2' [\text{H}_{\text{red2}}]_0 \left( \frac{1}{k_3 - k_2'} \right) e^{(k_3 - k_2') t} + e^{-k_3 t} c \quad (14)$$

Simplify (14):

$$[\text{H}_{\text{peroxo}}]_t = k_1' [\text{H}_{\text{red1}}]_0 \left( \frac{1}{k_3 - k_1'} \right) e^{-k_1' t} + k_2' [\text{H}_{\text{red2}}]_0 \left( \frac{1}{k_3 - k_2'} \right) e^{-k_2' t} + e^{-k_3 t} c \quad (15)$$

At  $t = 0$ ,  $[\text{H}_{\text{peroxo}}] = 0$ . Solve for  $c$ .

$$c = -k_1' [\text{H}_{\text{red1}}]_0 \left( \frac{1}{k_3 - k_1'} \right) - k_2' [\text{H}_{\text{red2}}]_0 \left( \frac{1}{k_3 - k_2'} \right) \quad (16)$$

Substitute (16) into (14) and simplify to obtain the expression for  $[\text{H}_{\text{peroxo}}]_t$ .

$$[\text{H}_{\text{peroxo}}]_t = k_1' [\text{H}_{\text{red1}}]_0 \left( \frac{1}{k_3 - k_1'} \right) (e^{-k_1' t} - e^{-k_3 t}) + k_2' [\text{H}_{\text{red2}}]_0 \left( \frac{1}{k_3 - k_2'} \right) (e^{-k_2' t} - e^{-k_3 t}) \quad (17)$$

From mass balance, the concentration of  $\text{H}_{\text{ox}}$  is defined by (18):

$$[\text{H}_{\text{ox}}]_t = [\text{H}_{\text{red1}}]_0 + [\text{H}_{\text{red2}}]_0 - [\text{H}_{\text{red1}}]_t - [\text{H}_{\text{red2}}]_t - [\text{H}_{\text{peroxo}}]_t \quad (18)$$

The time-dependent absorbance at a given wavelength ( $\text{Abs}_\lambda(t)$ ) is defined by (19), where  $\epsilon_x$  is the extinction coefficient for species  $x$  at that wavelength.

$$\text{Abs}_\lambda(t) = \epsilon_{\text{H}_{\text{red1}}} [\text{H}_{\text{red1}}]_t + \epsilon_{\text{H}_{\text{red2}}} [\text{H}_{\text{red2}}]_t + \epsilon_{\text{H}_{\text{peroxo}}} [\text{H}_{\text{peroxo}}]_t + \epsilon_{\text{H}_{\text{ox}}} [\text{H}_{\text{ox}}]_t \quad (19)$$

Substitute (18) into (19).

$$\text{Abs}_\lambda(t) = \epsilon_{\text{H}_{\text{red1}}} [\text{H}_{\text{red1}}]_t + \epsilon_{\text{H}_{\text{red2}}} [\text{H}_{\text{red2}}]_t + \epsilon_{\text{H}_{\text{peroxo}}} [\text{H}_{\text{peroxo}}]_t + \epsilon_{\text{H}_{\text{ox}}} ([\text{H}_{\text{red1}}]_0 + [\text{H}_{\text{red2}}]_0 - [\text{H}_{\text{red1}}]_t - [\text{H}_{\text{red2}}]_t - [\text{H}_{\text{peroxo}}]_t) \quad (20)$$

Simplify:

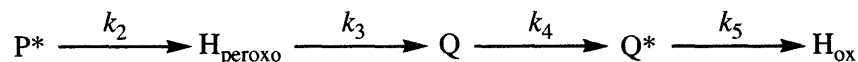
$$\text{Abs}_\lambda(t) = \epsilon_{\text{H}_{\text{ox}}} ([\text{H}_{\text{red1}}]_0 + [\text{H}_{\text{red2}}]_0) + (\epsilon_{\text{H}_{\text{red1}}} - \epsilon_{\text{H}_{\text{ox}}}) [\text{H}_{\text{red1}}]_t + (\epsilon_{\text{H}_{\text{red2}}} - \epsilon_{\text{H}_{\text{ox}}}) [\text{H}_{\text{red2}}]_t + (\epsilon_{\text{H}_{\text{peroxo}}} - \epsilon_{\text{H}_{\text{ox}}}) [\text{H}_{\text{peroxo}}]_t \quad (21)$$

Substitute (2), (4) and (17) into (21) to obtain the final equation for  $\text{Abs}_\lambda(t)$ .

$$\begin{aligned} \text{Abs}_\lambda(t) = & \epsilon_{\text{H}_{\text{ox}}} ([\text{H}_{\text{red1}}]_0 + [\text{H}_{\text{red2}}]_0) + (\epsilon_{\text{H}_{\text{red1}}} - \epsilon_{\text{H}_{\text{ox}}}) [\text{H}_{\text{red1}}]_0 e^{-k_1' t} + (\epsilon_{\text{H}_{\text{red2}}} - \epsilon_{\text{H}_{\text{ox}}}) [\text{H}_{\text{red2}}]_0 e^{-k_2' t} \\ & + (\epsilon_{\text{H}_{\text{peroxo}}} - \epsilon_{\text{H}_{\text{ox}}}) \left( k_1' [\text{H}_{\text{red1}}]_0 \left( \frac{1}{k_3 - k_1'} \right) (e^{-k_1' t} - e^{-k_3 t}) + k_2' [\text{H}_{\text{red2}}]_0 \left( \frac{1}{k_3 - k_2'} \right) (e^{-k_2' t} - e^{-k_3 t}) \right) \end{aligned} \quad (22)$$

## APPENDIX 2.2

### Derivation of eq 2.3 Describing Model iii of Scheme 2.3:



We can derive an equation to fit the absorbance versus time ( $Abs_s(t)$ ) for any wavelength given the extinction coefficients for each species and assuming that all of the reactions are irreversible.

The change in concentration of  $P^*$  is defined by (1).

$$[P^*]_t = [P^*]_0 e^{-k_2 t} \quad (1)$$

The change in concentration of  $H_{\text{peroxo}}$  is defined by (2).

$$[H_{\text{peroxo}}]_t = [P^*]_0 \left( \frac{k_2}{k_3 - k_2} \right) (e^{-k_2 t} - e^{-k_3 t}) \quad (2)$$

The change in concentration of  $Q$  is defined by (3).

$$[Q]_t = k_3 [P^*]_0 \left( \frac{k_2}{k_3 - k_2} \right) \left\{ \left( \frac{1}{k_4 - k_2} \right) (e^{-k_2 t} - e^{-k_4 t}) - \left( \frac{1}{k_4 - k_3} \right) (e^{-k_3 t} - e^{-k_4 t}) \right\} \quad (3)$$

The change in concentration of  $Q^*$  is defined by (4).

$$\frac{-d[Q^*]}{dt} = k_4 [Q]_t - k_5 [Q^*]_t \quad (4)$$

Substitute (3) into (4) and rearrange to give a linear differential equation of the first order.

$$\frac{-d[Q^*]}{dt} + k_5 [Q^*]_t = k_4 k_3 [P^*]_0 \left( \frac{k_2}{k_3 - k_2} \right) \left\{ \left( \frac{1}{k_4 - k_2} \right) (e^{-k_2 t} - e^{-k_4 t}) - \left( \frac{1}{k_4 - k_3} \right) (e^{-k_3 t} - e^{-k_4 t}) \right\} \quad (5)$$

Linear differential equations of the first order have the form shown in (6).

$$-\frac{dy}{dx} + P(x)y = Q(x) \quad (6)$$

The solution to (6) is obtained by letting  $S$  be an antiderivative of  $P$ , so that  $S'(x) = P(x)$ , and then multiplying both sides by  $\exp(S(x))$ .

$$e^{S(x)} \frac{dy}{dx} + e^{S(x)} P(x)y = e^{S(x)} Q(x) \quad (7)$$

The general solution to (7) is shown in (8).

$$y = e^{-S(x)} \int e^{S(x)} Q(x) dx \quad (8)$$

Multiply both sides of (5) by  $\exp(k_5 t)$ .

$$e^{k_5 t} \frac{d[Q^*]}{dt} + e^{k_5 t} k_5 [Q^*]_t = e^{k_5 t} \left( k_4 k_3 [P^*]_0 \left( \frac{k_2}{k_3 - k_2} \right) \left\{ \left( \frac{1}{k_2 - k_2} \right) (e^{-k_2 t} - e^{-k_4 t}) - \left( \frac{1}{k_4 - k_3} \right) (e^{-k_3 t} - e^{-k_4 t}) \right\} \right) \quad (9)$$

Solve using (8).

$$[Q^*]_t = e^{-k_5 t} \int e^{k_5 t} \left( k_4 k_3 [P^*]_0 \left( \frac{k_2}{k_3 - k_2} \right) \left\{ \left( \frac{1}{k_4 - k_2} \right) (e^{-k_2 t} - e^{-k_4 t}) - \left( \frac{1}{k_4 - k_3} \right) (e^{-k_3 t} - e^{-k_4 t}) \right\} \right) dt \quad (10)$$

Define the constant  $a = k_4 k_3 [P^*]_0 \left( \frac{k_2}{k_3 - k_2} \right)$  and rearrange (10):

$$[Q^*]_t = e^{-k_5 t} \left( a \int e^{k_5 t} \left( \left( \frac{1}{k_4 - k_2} \right) (e^{-k_2 t} - e^{-k_4 t}) - \left( \frac{1}{k_4 - k_3} \right) (e^{-k_3 t} - e^{-k_4 t}) \right) dt \right) \quad (11)$$

Rearrange (11):

$$[Q^*]_t = e^{-k_5 t} \left( a \int e^{k_5 t} \left( \frac{1}{k_4 - k_2} \right) (e^{-k_2 t} - e^{-k_4 t}) - a \int e^{k_5 t} \left( \frac{1}{k_4 - k_3} \right) (e^{-k_3 t} - e^{-k_4 t}) dt \right) \quad (12)$$

Define the constants  $b = \left( \frac{1}{k_4 - k_2} \right)$  and  $f = \left( \frac{1}{k_4 - k_3} \right)$  and rearrange (12):

$$[Q^*]_t = e^{-k_5 t} \left( ab \int e^{(k_5 - k_2)t} - ab \int e^{(k_5 - k_4)t} - af \int e^{(k_5 - k_3)t} + af \int e^{(k_5 - k_4)t} dt \right) \quad (13)$$

Integrate 13:

$$[Q^*]_t = e^{-k_5 t} \left( ab \left( \frac{1}{k_5 - k_2} \right) e^{(k_5 - k_2)t} - ab \left( \frac{1}{k_5 - k_4} \right) e^{(k_5 - k_4)t} - af \left( \frac{1}{k_5 - k_3} \right) e^{(k_5 - k_3)t} + af \left( \frac{1}{k_5 - k_4} \right) e^{(k_5 - k_4)t} + c \right) \quad (14)$$



Rearrange (14):

$$[Q^*]_t = ab \left( \frac{1}{k_5 - k_2} \right) e^{-k_2 t} - ab \left( \frac{1}{k_5 - k_4} \right) e^{-k_4 t} - af \left( \frac{1}{k_5 - k_3} \right) e^{-k_3 t} + af \left( \frac{1}{k_5 - k_4} \right) e^{-k_4 t} + e^{-k_3 t} c \quad (15)$$

At  $t = 0$ ,  $[Q^*] = 0$ . Solve for  $c$ .

$$c = -ab \left( \frac{1}{k_5 - k_2} \right) + ab \left( \frac{1}{k_5 - k_4} \right) + af \left( \frac{1}{k_5 - k_3} \right) - af \left( \frac{1}{k_5 - k_4} \right) \quad (16)$$

Substitute (16) into (15):

$$[Q^*]_t = ab \left( \frac{1}{k_5 - k_2} \right) e^{-k_2 t} - ab \left( \frac{1}{k_5 - k_4} \right) e^{-k_4 t} - af \left( \frac{1}{k_5 - k_3} \right) e^{-k_3 t} + af \left( \frac{1}{k_5 - k_4} \right) e^{-k_4 t} - ab \left( \frac{1}{k_5 - k_2} \right) e^{-k_2 t} + ab \left( \frac{1}{k_5 - k_4} \right) e^{-k_4 t} + af \left( \frac{1}{k_5 - k_3} \right) e^{-k_3 t} - af \left( \frac{1}{k_5 - k_4} \right) e^{-k_4 t} \quad (17)$$

Simplify (17).

$$[Q^*]_t = a \left\{ b \left( \frac{1}{k_5 - k_2} \right) (e^{-k_2 t} - e^{-k_3 t}) - b \left( \frac{1}{k_5 - k_4} \right) (e^{-k_4 t} - e^{-k_3 t}) - f \left( \frac{1}{k_5 - k_3} \right) (e^{-k_3 t} - e^{-k_4 t}) + f \left( \frac{1}{k_5 - k_4} \right) (e^{-k_4 t} - e^{-k_3 t}) \right\} \quad (18)$$

Replace a, b, and f for the final expression of  $[Q^*]_t$ :

$$[Q^*]_t = k_4 k_3 [P^*]_0 \left( \frac{k_2}{k_3 - k_2} \right) \left\{ \left( \frac{1}{k_4 - k_2} \right) \left( \frac{1}{k_3 - k_2} \right) (e^{-k_2 t} - e^{-k_3 t}) - \left( \frac{1}{k_4 - k_2} \right) \left( \frac{1}{k_3 - k_4} \right) (e^{-k_4 t} - e^{-k_3 t}) - \left( \frac{1}{k_4 - k_3} \right) \left( \frac{1}{k_5 - k_3} \right) (e^{-k_3 t} - e^{-k_4 t}) + \left( \frac{1}{k_4 - k_3} \right) \left( \frac{1}{k_5 - k_4} \right) (e^{-k_4 t} - e^{-k_3 t}) \right\} \quad (19)$$

From mass balance, the concentration of  $H_{ox}$  is defined by (20):

$$[H_{ox}]_t = [P^*]_0 - [P^*]_t - [H_{peroxo}]_t - [Q]_t - [Q^*]_t \quad (20)$$

The time-dependent absorbance at a given wavelength ( $Abs_\lambda(t)$ ) is defined by (21), where  $\epsilon_x$  is the extinction coefficient for species x at that wavelength.

$$Abs_\lambda(t) = \epsilon_{P^*} [P^*]_t + \epsilon_{H_{peroxo}} [H_{peroxo}]_t + \epsilon_Q [Q]_t + \epsilon_{Q^*} [Q^*]_t + \epsilon_{H_{ox}} [H_{ox}]_t \quad (21)$$

Substitute (20) into (21).

$$Abs_\lambda(t) = \epsilon_{P^*} [P^*]_t + \epsilon_{H_{peroxo}} [H_{peroxo}]_t + \epsilon_Q [Q]_t + \epsilon_{Q^*} [Q^*]_t + \epsilon_{H_{ox}} ([P^*]_0 - [P^*]_t - [H_{peroxo}]_t - [Q]_t - [Q^*]_t) \quad (22)$$

Simplify:

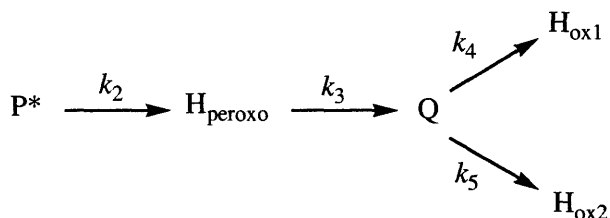
$$Abs_\lambda(t) = \epsilon_{H_{ox}} [P^*]_0 + (\epsilon_{P^*} - \epsilon_{H_{ox}}) [P^*]_t + (\epsilon_{H_{peroxo}} - \epsilon_{H_{ox}}) [H_{peroxo}]_t + (\epsilon_Q - \epsilon_{H_{ox}}) [Q]_t + (\epsilon_{Q^*} - \epsilon_{H_{ox}}) [Q^*]_t \quad (23)$$

Substitute (1), (2), (3), and (19) into (23) to obtain the final equation for Abs.(t).

$$\text{Abs}_\lambda(t) = \left\{ \begin{aligned} & \varepsilon_{H_{\text{ax}}} [\mathbf{P}^*]_0 + (\varepsilon_{P^*} - \varepsilon_{H_{\text{ax}}}) ([\mathbf{P}^*]_0 e^{-k_2 t}) + (\varepsilon_{H_{\text{peroxo}}} - \varepsilon_{H_{\text{ax}}}) \left( [\mathbf{P}^*]_0 \left( \frac{k_2}{k_3 - k_2} \right) (e^{-k_2 t} - e^{-k_3 t}) \right) + \\ & (\varepsilon_Q - \varepsilon_{H_{\text{ax}}}) \left( k_3 [\mathbf{P}^*]_0 \left( \frac{k_2}{k_3 - k_2} \right) \left\{ \left( \frac{1}{k_4 - k_2} \right) (e^{-k_2 t} - e^{-k_4 t}) - \left( \frac{1}{k_4 - k_3} \right) (e^{-k_3 t} - e^{-k_4 t}) \right\} \right) + \\ & (\varepsilon_{Q^*} - \varepsilon_{H_{\text{ax}}}) \left( k_4 k_3 [\mathbf{P}^*]_0 \left( \frac{k_2}{k_3 - k_2} \right) \left\{ \begin{aligned} & \left( \frac{1}{k_4 - k_2} \right) \left( \frac{1}{k_5 - k_2} \right) (e^{-k_2 t} - e^{-k_5 t}) - \left( \frac{1}{k_4 - k_2} \right) \left( \frac{1}{k_5 - k_4} \right) (e^{-k_4 t} - e^{-k_5 t}) - \\ & \left( \frac{1}{k_4 - k_3} \right) \left( \frac{1}{k_5 - k_3} \right) (e^{-k_3 t} - e^{-k_5 t}) + \left( \frac{1}{k_4 - k_3} \right) \left( \frac{1}{k_5 - k_4} \right) (e^{-k_4 t} - e^{-k_5 t}) - \end{aligned} \right\} \right) \end{aligned} \right\} \quad (24)$$

## APPENDIX 2.3

### Derivation of eq 2.4 Describing Model iv of Scheme 2.3:



We can derive an equation to fit the absorbance versus time ( $\text{Abs}_i(t)$ ) for any wavelength given the extinction coefficients for each species and assuming that all of the reactions are irreversible.

The change in concentration of  $\text{P}^*$  is defined by (1).

$$[\text{P}^*]_t = [\text{P}^*]_0 e^{-k_2 t} \quad (1)$$

The change in concentration of  $\text{H}_{\text{peroxo}}$  is defined by (2).

$$[\text{H}_{\text{peroxo}}]_t = [\text{P}^*]_0 \left( \frac{k_2}{k_3 - k_2} \right) (e^{-k_2 t} - e^{-k_3 t}) \quad (2)$$

The change in concentration of Q is defined by (3).

$$\frac{-d[\text{Q}]}{dt} = k_3 [\text{H}_{\text{peroxo}}]_t - k_4 [\text{Q}]_t - k_5 [\text{Q}]_t = k_3 [\text{H}_{\text{peroxo}}]_t - (k_4 + k_5) [\text{Q}]_t \quad (3)$$

Substitute (2) into (3) and rearrange to give a linear differential equation of the first order.

$$\frac{-d[\text{Q}]}{dt} + (k_4 + k_5) [\text{Q}]_t = k_3 [\text{P}^*]_0 \left( \frac{k_2}{k_3 - k_2} \right) (e^{-k_2 t} - e^{-k_3 t}) \quad (4)$$

Linear differential equations of the first order have the form shown in (5).

$$-\frac{dy}{dx} + P(x)y = Q(x) \quad (5)$$

The solution to (5) is obtained by letting  $S$  be an antiderivative of  $P$ , so that  $S'(x) = P(x)$ , and then multiplying both sides by  $\exp(S(x))$ .

$$e^{S(x)} \frac{dy}{dx} + e^{S(x)} P(x)y = e^{S(x)} Q(x) \quad (6)$$

The general solution to (6) is shown in (7).

$$y = e^{-S(x)} \int e^{S(x)} Q(x) dx \quad (7)$$

Multiply both sides of (4) by  $\exp((k_3+k_4)t)$ .

$$e^{(k_3+k_4)t} \frac{d[Q]}{dt} + e^{(k_3+k_4)t} (k_4 + k_5)[Q]_t = e^{(k_3+k_4)t} \left( k_3 [P^*]_0 \left( \frac{k_2}{k_3 - k_2} \right) (e^{-k_2 t} - e^{-k_3 t}) \right) \quad (8)$$

Solve using (7).

$$[Q]_t = e^{-(k_4+k_5)t} \int e^{(k_4+k_5)t} \left( k_3 [P^*]_0 \left( \frac{k_2}{k_3 - k_2} \right) (e^{-k_2 t} - e^{-k_3 t}) \right) \quad (9)$$

Rearrange (9):

$$[Q]_t = e^{-(k_4+k_5)t} \left( [P^*]_0 \left( \frac{k_3 k_2}{k_3 - k_2} \right) \int (e^{(k_4+k_5-k_2)t} - e^{(k_4+k_5-k_3)t}) \right) \quad (10)$$

Integrate (10):

$$[Q]_t = e^{-(k_4+k_5)t} \left( [P^*]_0 \left( \frac{k_3 k_2}{k_3 - k_2} \right) \left( \frac{1}{k_4 + k_5 - k_2} e^{(k_4+k_5-k_2)t} - \frac{1}{k_4 + k_5 - k_3} e^{(k_4+k_5-k_3)t} \right) + c \right) \quad (11)$$

Rearrange (11):

$$[Q]_t = [P^*]_0 \left( \frac{k_3 k_2}{k_3 - k_2} \right) \left( \frac{1}{k_4 + k_5 - k_2} e^{-k_2 t} - \frac{1}{k_4 + k_5 - k_3} e^{-k_3 t} \right) + e^{-(k_4+k_5)t} c \quad (12)$$

At  $t = 0$ ,  $[Q] = 0$ . Solve for  $c$ .

$$c = -[P^*]_0 \left( \frac{k_3 k_2}{k_3 - k_2} \right) \left( \frac{1}{k_4 + k_5 - k_2} - \frac{1}{k_4 + k_5 - k_3} \right) \quad (13)$$

Substitute (13) into (12):

$$[Q]_t = [P^*]_0 \left( \frac{k_3 k_2}{k_3 - k_2} \right) \left( \frac{1}{k_4 + k_5 - k_2} e^{-k_2 t} - \frac{1}{k_4 + k_5 - k_3} e^{-k_3 t} \right) - [P^*]_0 \left( \frac{k_3 k_2}{k_3 - k_2} \right) \left( \frac{1}{k_4 + k_5 - k_2} e^{-(k_4 + k_5) t} - \frac{1}{k_4 + k_5 - k_3} e^{-(k_4 + k_5) t} \right) \quad (14)$$

Simplify (14).

$$[Q]_t = [P^*]_0 \left( \frac{k_3 k_2}{k_3 - k_2} \right) \left( \frac{1}{k_4 + k_5 - k_2} (e^{-k_2 t} - e^{-(k_4 + k_5) t}) - \frac{1}{k_4 + k_5 - k_3} (e^{-k_3 t} - e^{-(k_4 + k_5) t}) \right) \quad (15)$$

From mass balance, the concentration of  $H_{ox}$  is defined by (16):

$$[H_{ox1}]_t + [H_{ox2}]_t = [P^*]_0 - [H_{red}]_t - [H_{peroxo}]_t - [Q]_t \quad (16)$$

The time-dependent absorbance at a given wavelength ( $Abs_\lambda(t)$ ) is defined by (17), where  $\epsilon_x$  is the extinction coefficient for species x at that wavelength.

$$Abs_\lambda(t) = \epsilon_{P^*} [P^*]_t + \epsilon_{H_{peroxo}} [H_{peroxo}]_t + \epsilon_Q [Q]_t + \epsilon_{H_{ox}} ([H_{ox1}]_t + [H_{ox2}]_t) \quad (17)$$

Substitute (16) into (17).

$$Abs_\lambda(t) = \epsilon_{P^*} [P^*]_t + \epsilon_{H_{peroxo}} [H_{peroxo}]_t + \epsilon_Q [Q]_t + \epsilon_{H_{ox}} ([P^*]_0 - [P^*]_t - [H_{peroxo}]_t - [Q]_t) \quad (18)$$

Simplify (18).

$$Abs_\lambda(t) = \epsilon_{P^*} [P^*]_0 + (\epsilon_{H_{red}} - \epsilon_{H_{ox}}) [H_{red}]_t + (\epsilon_{H_{peroxo}} - \epsilon_{H_{ox}}) [H_{peroxo}]_t + (\epsilon_Q - \epsilon_{H_{ox}}) [Q]_t \quad (19)$$

Substitute (1), (2), and (15) into (19) to obtain the final equation for  $Abs_\lambda(t)$ .

$$Abs_\lambda(t) = \left( \begin{aligned} &\epsilon_{H_{ox}} [P^*]_0 + (\epsilon_{P^*} - \epsilon_{H_{ox}}) [P^*]_0 e^{-k_2 t} + (\epsilon_{H_{peroxo}} - \epsilon_{H_{ox}}) [P^*]_0 \left( \frac{k_2}{k_3 - k_2} \right) (e^{-k_2 t} - e^{-k_3 t}) + \\ &(\epsilon_Q - \epsilon_{H_{ox}}) [P^*]_0 \left( \frac{k_3 k_2}{k_3 - k_2} \right) \left( \frac{1}{k_4 + k_5 - k_2} (e^{-k_2 t} - e^{-(k_4 + k_5) t}) - \frac{1}{k_4 + k_5 - k_3} (e^{-k_3 t} - e^{-(k_4 + k_5) t}) \right) \end{aligned} \right) \quad (24)$$

Simplify (24):

$$Abs_\lambda(t) = [P^*]_0 \left( \begin{aligned} &\epsilon_{P^*} + (\epsilon_{P^*} - \epsilon_{H_{ox}}) e^{-k_2 t} + (\epsilon_{H_{peroxo}} - \epsilon_{H_{ox}}) \left( \frac{k_2}{k_3 - k_2} \right) (e^{-k_2 t} - e^{-k_3 t}) + \\ &(\epsilon_Q - \epsilon_{H_{ox}}) \left( \frac{k_3 k_2}{k_3 - k_2} \right) \left( \frac{1}{k_4 + k_5 - k_2} (e^{-k_2 t} - e^{-(k_4 + k_5) t}) - \frac{1}{k_4 + k_5 - k_3} (e^{-k_3 t} - e^{-(k_4 + k_5) t}) \right) \end{aligned} \right) \quad (25)$$

## Chapter 3

### Oxidation Reactions Performed by Soluble Methane Monooxygenase Hydroxylase

#### Intermediates H<sub>peroxo</sub> and Q Proceed by Distinct Mechanisms

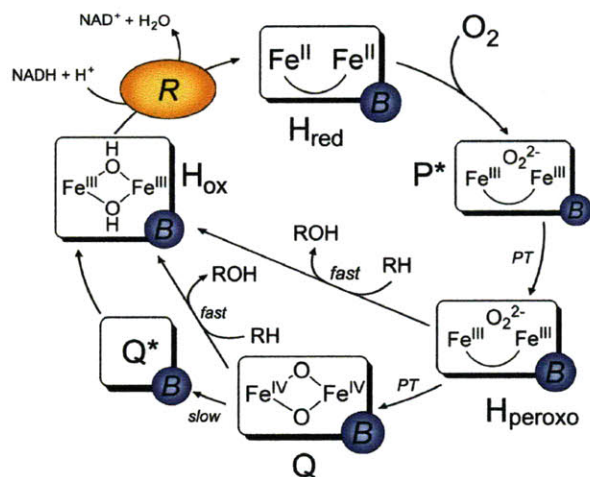
\*Reproduced in part with permission from *Biochemistry*, submitted for publication

Unpublished Work © 2010 American Chemical Society

## INTRODUCTION

Soluble methane monooxygenase (sMMO) isolated from *Methylococcus capsulatus* (Bath) catalyzes the selective conversion of methane to methanol at room temperature and atmospheric pressure (1). This difficult transformation requires the coordinated effort of three protein components: a dimeric hydroxylase (MMOH) that houses two copies of a diiron catalytic center, a reductase (MMOR) that accepts electrons from NADH and transfers them to the hydroxylase, and a regulatory protein (MMOB) that couples electron transfer to substrate oxidation in a complex manner. Although its physiologically relevant substrate is methane, sMMO can oxidize a wide variety of substrates including alkanes, alkenes, alkynes, aromatics, heterocycles, halogenated compounds, and small inorganic molecules such as carbon monoxide (2-4). Substrates range in size from methane to the relatively large radical clock probe 2,2-diphenylmethylcyclopropane (5). The oxidation reactions of MMOH proceed by multiple mechanisms including hydroxylation, epoxidation, and oxygen atom transfer depending on the substrate (4).

The catalytic cycle of MMOH in the presence of MMOB is well established (Scheme 3.1). In the first step, the diiron(III) resting state of  $H_{ox}$  is reduced to an  $O_2$ -reactive diiron(II) species,  $H_{red}$ , by two electrons originating from NADH. Following reaction of  $H_{red}$  with dioxygen, the first intermediate observed spectroscopically is  $P^*$ , a putative peroxodiiron(III) species (6, 7). The Mössbauer spectrum of  $P^*$  is consistent with two antiferromagnetically coupled high-spin iron(III) centers with similar coordination geometries (8).  $P^*$  rapidly converts to  $H_{peroxo}$ , a distinct peroxodiiron(III) species characterized by optical bands at 420 and 725 nm, in a proton-driven process (7, 9). Because of similarities in the spectroscopic parameters of  $P^*$  and  $H_{peroxo}$ , these two



**Scheme 3.1.** Current Working Model of Catalysis by the MMOH Diiron Center

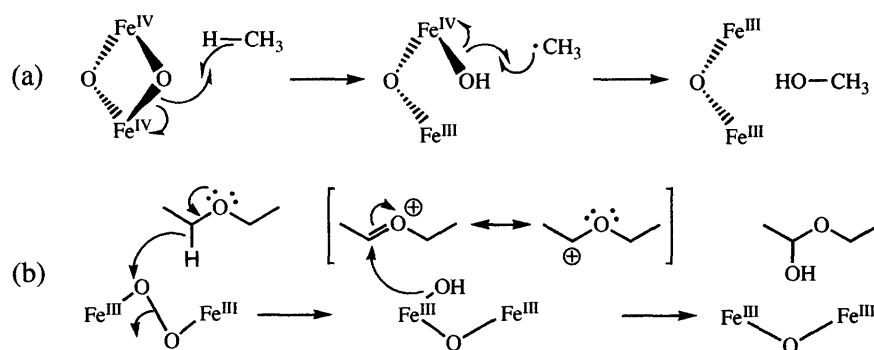
intermediates are expected to have similar iron-oxygen cores (7). Based on analogy to peroxy intermediates from other diiron proteins (10-14) and theoretical calculations (15),  $H_{\text{peroxy}}$  is most likely a gauche  $\mu$ -1,2-peroxy species; however, a nonplanar  $\mu$ - $\eta^2$ : $\eta^2$  peroxide diiron(III) binding mode has also been proposed (16-18).

In the absence of substrate,  $H_{\text{peroxy}}$  decays to intermediate Q in a second proton-driven process (7, 9). Q features a broad absorption band centered at 420 nm (8, 19, 20). Spectroscopic characterization of this intermediate revealed that it is a di( $\mu$ -oxo)diiron(IV) cluster with a diamagnetic ground state due to antiferromagnetic coupling between the iron atoms (8, 19, 21), and analysis by EXAFS spectroscopy revealed a short Fe-Fe distance of 2.46 Å (22). The reactivity of Q with various substrates has been extensively investigated and it is generally accepted that this species is responsible for methane oxidation (6, 23, 24). Studies employing high-level density functional theory suggested that the hydroxylation of methane by Q is initiated by a proton-coupled outer-sphere



electron transfer from a C–H  $\sigma$  bond in methane through the bridging oxygen atom to one of the iron atoms, generating a transiently bound, substrate-derived radical intermediate (Scheme 3.2a) (25). Although the rate-determining step in the reaction mechanism is thought to involve hydrogen atom transfer, multiple studies have revealed that there is no correlation between the rate constant for reaction of a given substrate with Q and the homolytic bond dissociation energy (BDE) of that substrate. These findings indicate that there are aspects of the reaction mechanisms that are still incompletely understood. In the absence of substrate, Q decays slowly to  $H_{ox}$  by a mechanism that proceeds through a recently identified intermediate  $Q^*$  of unknown composition (7).

Most of the literature on the hydroxylation mechanisms of MMOH has focused on reactions of Q because this species is responsible for methane oxidation, but evidence suggests that  $H_{peroxo}$  also reacts with hydrocarbon substrates (20, 26). Early clues that the  $H_{peroxo}$  and Q intermediate species of MMOH operate as distinct oxidants were provided by reports that different product distributions were obtained for certain substrates



**Scheme 3.2.** Proposed Mechanisms of Methane Hydroxylation by Q (a) and Diethyl Ether Oxidation by  $H_{peroxo}$  (b)

depending on whether the oxidized form of the enzyme was activated with NADH and O<sub>2</sub> or with hydrogen peroxide in the absence of MMOB (27, 28). More recently, double-mixing stopped-flow spectroscopy demonstrated that the rate constant for H<sub>peroxo</sub> decay is accelerated in the presence of the electron-rich substrates propylene, ethyl vinyl ether, and diethyl ether (20, 26). Both ethyl vinyl ether and diethyl ether react more rapidly with H<sub>peroxo</sub> than with Q under pre-steady-state conditions. A comparison of rate constants for these reactions indicates that H<sub>peroxo</sub> is a more electrophilic oxidant than Q. Based on these results, we suggested that the mechanism of oxidation by H<sub>peroxo</sub> involves an initial two-electron transfer event from substrate to form a transient, substrate-derived cationic species that rebounds with the two-electron reduced iron core to form H<sub>ox</sub> and an epoxide or hydroxylated product (Scheme 3.2b) (26). The proposed mechanism is also supported by the presence of cation-derived products observed in the steady state reactions of radical clock substrate probes with sMMO (29-32).

To elaborate on the mechanisms of substrate reactivity in MMOH, we conducted a systematic study investigating structure-activity relationships for hydroxylation reactions promoted by H<sub>peroxo</sub> and Q and describe the results in this report. Substrates that span a range of different C–H bond energies were chosen for these studies. These experiments, enabled by the promiscuity of the enzyme, demonstrate that H<sub>peroxo</sub> and Q interact and react with different substrates by distinct mechanisms in a manner that depends largely on the molecular dipole of the substrate. Three classes of substrates are defined: (i) those for which substrate binding is rate-determining at all substrate concentrations; (ii) those for which C–H bond cleavage is rate-determining at all substrate concentrations; and (iii) those for which the rate-determining step is dependent on substrate concentration. An

analysis of the substrates belonging to the three classes is presented and mechanistic findings regarding the reactions of the two intermediates are discussed.

## MATERIALS AND METHODS

*General Considerations.* The hydroxylase (MMOH) enzyme was purified from *Methylococcus capsulatus* (Bath) as described previously (26). Protein obtained had a specific activity at 45 °C in the range of 300-450 mU/mg, as measured for propylene oxidation at 45 °C (20). Iron content was determined using the ferrozine colorimetric iron assay and ranged from 3.4-4.0 iron atoms per protein dimer (20). The regulatory (MMOB) and reductase (MMOR) proteins were expressed recombinantly in *E. coli* and purified as described elsewhere (33, 34). The buffer system employed in all experiments was 25 mM potassium phosphate pH 7.0. Distilled water was deionized with a Milli-Q filtering system. Other reagents were purchased from Sigma Aldrich and were used as received.

*Stopped-Flow Optical Spectroscopy.* Kinetic experiments were performed on a Hi-Tech Scientific (Salisbury, UK) SF-61 DX2 stopped-flow spectrophotometer as described in detail elsewhere (20). Briefly, a solution of 200  $\mu$ M MMOH and 400  $\mu$ M MMOB was prepared in 25 mM potassium phosphate buffer, pH 7.0. The hydroxylase was reduced with excess sodium dithionite using stoichiometric methyl viologen as a redox mediator. Excess reducing agent was removed by dialysis.

Double-mixing stopped-flow experiments were performed by rapidly mixing the reduced protein solution with O<sub>2</sub>-saturated buffer. After a specified time delay corresponding to the maximal accumulation of H<sub>peroxo</sub> or Q, substrate-containing buffer

was introduced in a second push to initiate the reaction and trigger the start of data collection. The delay times between the first and second mixing events were determined by monitoring the reaction kinetics at 420 and 720 nm in the absence of substrate, 12 s for Q and 2 s for H<sub>peroxo</sub> (7). All experiments were performed at 4 °C using a circulating water bath. The concentration of MMOH:2B in the sample cell after mixing was 50 μM in all experiments. Data monitoring the reactions of Q and H<sub>peroxo</sub> were collected at 420 and 720 nm, respectively, using a photomultiplier tube. Data were collected in duplicate or triplicate, using different protein preparations for each experiment. Data were collected under control of the KinetAsyst 3 (Hi-Tech Scientific) and Kinetic Studio (Hi-Tech Scientific) software.

All substrates used in double-mixing stopped-flow experiments were purchased from Sigma Aldrich and used as received. Substrate purity was assessed by <sup>1</sup>H-NMR spectroscopy. Substrate solutions were prepared in volumetric flasks containing a weighed amount of material. For volatile liquid substrates, the volumetric flask was fitted with a rubber septum and the substrate was injected through the septum into buffer maintained at 4 °C. Protein stability was not compromised in the presence of any of the substrates at the concentrations employed in the experiments, as noted optically by the absence of protein precipitation over the course of 30 min incubation with substrate.

*Data Analysis.* Data analyses were performed with KinetAsyst 3 (Hi-Tech Scientific) and/or Kinetic Studio (Hi-Tech Scientific) and/or KaleidaGraph v 3.51 (Synergy Software) software, and the programs provided the same results in all cases. In fitting primary data, only results that displayed an R<sup>2</sup> value of 0.998 or greater were deemed

acceptable. Data were evaluated on the basis of this value, the fit residuals, and the parameter errors.

Data monitoring Q decay in the presence of substrate were fit well to a single exponential function, as described previously (Figure 3.1) (6, 20, 23, 26). This procedure is justified by the fact that Q represents most of the active diiron centers (89%) at the age time employed in these experiments (7). Additionally, Q reacts with all substrates employed, presumably to form  $H_{ox}$  and product; therefore, kinetic terms representing Q\* formation and decay did not have to be included in any fits.

Data monitoring  $H_{peroxo}$  decay in the presence of substrate were fit well by a two-exponential function, as described previously (Figure 3.1b) (26). At 2 s, the age time employed in the experiments, the active diiron sites comprise 22% P\*, 51%  $H_{peroxo}$ , and 26% Q (7); therefore, it is necessary to account for a significant population of Q that is present in the reaction mixture. For most substrates it was sufficient to fix the value of  $k_{obs2}$  at that measured independently in experiments monitoring substrate-promoted Q decay. However, for some substrates satisfactory fits were not obtained when  $k_{obs2}$  was fixed. These substrates include  $CH_3CHO$  and  $CH_3CH_2CHO$  at concentrations above ~10 mM. In both cases,  $k_{obs2}$  was smaller than the value of substrate-promoted Q decay observed independently in experiments probing reaction of Q. This finding is most likely due to optical contributions from  $H_{peroxo}$  to Q conversion, which are not explicitly accounted for in the exponential fitting model and can arise if a population of  $H_{peroxo}$  decays by conversion to Q rather than by reaction with substrate. These processes should have a more dominant effect on the rate constant measured for Q decay when reaction

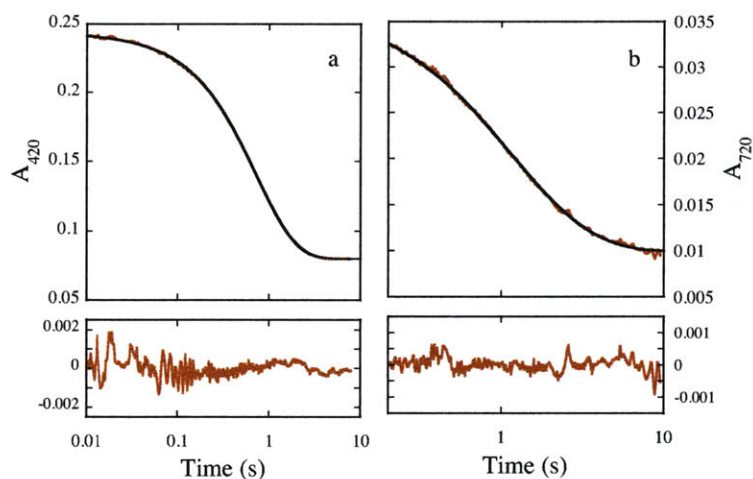


**Figure 3.1.** Representative fits (black lines) of data (red lines) probing the reactions of Q (a) and H<sub>peroxo</sub> (b) with 96 mM CH<sub>3</sub>NO<sub>2</sub> at 4 °C and pH 7.0. 200 μM MMOH<sub>red</sub> and 400 μM MMOB were mixed rapidly with excess O<sub>2</sub>, the reaction mixture was aged for 12 s (a) or 2 s (b), and then buffer containing 192 mM CH<sub>3</sub>NO<sub>2</sub> was introduced. Data probing the reaction with Q fit nicely to one exponential decay phase (a). Data monitoring the reaction with H<sub>peroxo</sub> fit nicely to two exponential decay phases, where the rate constant for the second process was fixed at the value monitored in experiments probing the reaction with Q (b). Fit residuals are shown in the bottom plots. These results and fitting procedures are typical for all substrates employed unless otherwise noted.

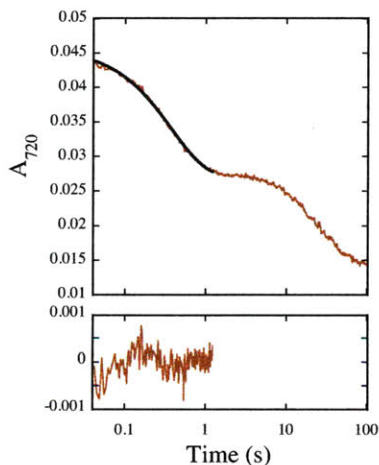


**Figure 3.2.** Representative fit (black lines) of data (red lines) probing the reaction of H<sub>peroxo</sub> with 272 mM CD<sub>3</sub>NO<sub>2</sub> at 4 °C and pH 7.0. 200 μM MMOH<sub>red</sub> and 400 μM MMOB were mixed rapidly with excess O<sub>2</sub>, the reaction mixture was aged for 2 s, and then buffer containing 544 mM CD<sub>3</sub>NO<sub>2</sub> was introduced. Because the exponential phases corresponding to H<sub>peroxo</sub> and Q decay are well separated at [CD<sub>3</sub>NO<sub>2</sub>] > 200 mM, the data were fit well by truncating and analyzing each phase separately using independent single exponential processes. Fit (top) and fit residuals (bottom) are shown here for the first, H<sub>peroxo</sub>, reaction phase.

with  $H_{\text{peroxo}}$  is rapid, because substrate-promoted  $H_{\text{peroxo}}$  decay separates in time from  $H_{\text{peroxo}}$  to Q conversion and substrate-promoted Q decay. This phenomenon causes Q formation to be incorporated into the exponential term for Q decay, thereby making  $k_{\text{obs}2}$  appear smaller than it is when the rate constant for reaction with substrate ( $k_{\text{obs}}$  in Q experiments) is larger than that of  $H_{\text{peroxo}}$  to Q conversion. For all other substrates, this problem did not arise because the rate constant for reaction with  $H_{\text{peroxo}}$  was not significantly faster than that for Q, except for  $\text{CD}_3\text{NO}_2$ . For this substrate, reactions with  $H_{\text{peroxo}}$  were least 100 times faster than those with Q at each substrate concentration when  $[\text{CD}_3\text{NO}_2] > 200 \text{ mM}$ . At these concentrations, the exponential phases corresponding to  $H_{\text{peroxo}}$  and Q decay were well separated when a 2 s age time was employed. These data were fit well by truncating and analyzing each phase separately using independent single exponential processes (Figure 3.2).

## RESULTS AND DISCUSSION

Soluble methane monooxygenase is a remarkable enzyme system that selectively oxidizes methane to methanol even in the presence of cellular metabolites and active site amino acid residues having much weaker C–H bonds. Studies from our lab suggest that *two* sequential oxidants in the system,  $H_{\text{peroxo}}$  and Q, are responsible for its broad reactivity with a variety of substrates. To characterize the reactive properties of this enzyme, we undertook a systematic study employing single- and double-mixing stopped-flow optical spectroscopy to demonstrate conclusively that  $H_{\text{peroxo}}$  is reactive and to monitor the reactions of the oxygenated-iron intermediates with substrates of varying C–H bond strength. Structure-reactivity correlations in enzyme systems are often hindered

by the substrate binding specificities; however, the broad substrate reactivity pattern of MMOH enabled us to perform such a study in this system.

*Single-Mixing Stopped Flow Studies – Proof that  $H_{\text{peroxo}}$  is a Hydrocarbon Oxidant.* The evidence that  $H_{\text{peroxo}}$  reacts with substrates is substantial (20, 26). However, to further evaluate this hypothesis we used the unique approach of investigating the reaction of  $\text{MMOH}_{\text{red}}$  with a mixture of  $\text{O}_2$  and a substrate known to react with  $H_{\text{peroxo}}$  in the presence of 2 equiv of MMOB by single-mixing stopped-flow spectroscopy. The substrate chosen for these studies was  $\text{CH}_3\text{CH}_2\text{CHO}$ , because this aldehyde was identified as a substrate that reacts rapidly with  $H_{\text{peroxo}}$  in double-mixing studies (vide infra). Similar studies performed in the presence of methane, which reacts with Q but not  $H_{\text{peroxo}}$ , demonstrated a rise and decay in absorbance at 420 nm and high substrate concentrations. Because Q does not accumulate under these conditions, the observed absorbance profile was attributed solely to accumulation of  $H_{\text{peroxo}}$  and its precursor,  $\text{P}^*$ , both of which absorb at this wavelength (7). We reasoned that if  $H_{\text{peroxo}}$  and/or  $\text{P}^*$ , which is believed to have a similar oxygen-iron core as  $H_{\text{peroxo}}$  and therefore might exhibit similar reactivity properties, react with  $\text{CH}_3\text{CH}_2\text{CHO}$  then we should observe no rise and decay in absorbance at 420 nm when the concentration of substrate is high enough to prevent accumulation of these species due to rapid reaction. If no reaction occurred, the results would be identical to those for the reaction with methane (7).

Reactions of  $\text{MMOH}_{\text{red}}$  with a mixture of  $\text{O}_2$  and  $\text{CH}_3\text{CH}_2\text{CHO}$  in the presence of 2 equiv of MMOB are shown in Figure 3.3 (420 nm) and Figure 3.4 (720 nm). In the absence of substrate, the time-dependent formation and decay of intermediates  $\text{P}^*$ ,  $H_{\text{peroxo}}$ ,



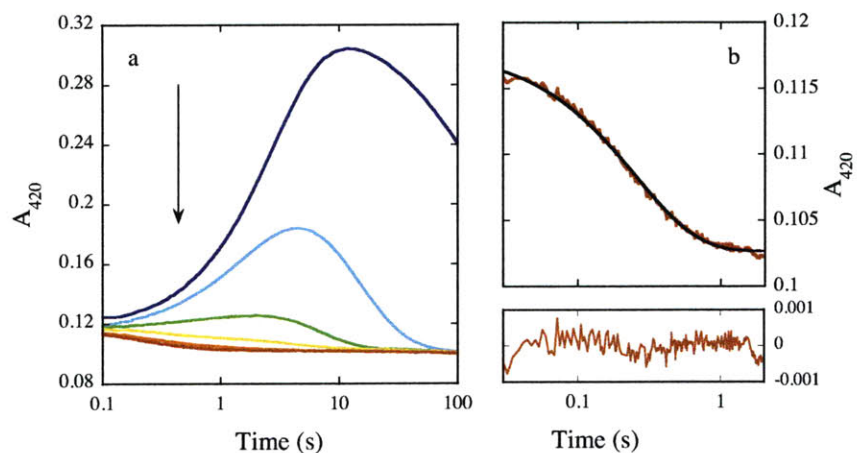


**Figure 3.3.** (a) Representative absorbance profile for the reaction of 50  $\mu\text{M}$  MMOH<sub>red</sub> with a mixture of excess O<sub>2</sub> and CH<sub>3</sub>CH<sub>2</sub>CHO in the presence of 2 equiv MMOB at 4 °C and 420 nm. [CH<sub>3</sub>CH<sub>2</sub>CHO] = 0 mM (blue), 5.8 mM (cyan), 24.9 mM (green), 69.7 mM (yellow), 122.3 mM (orange), and 214.9 mM (red). Data collected on separate occasions with different batches of protein yielded similar results. (b) Representative fit of data (red line) depicted in (a) collected in the presence of 214.9 mM CH<sub>3</sub>CH<sub>2</sub>CHO to a single exponential decay process (black line). Fit residuals are depicted below the plot.

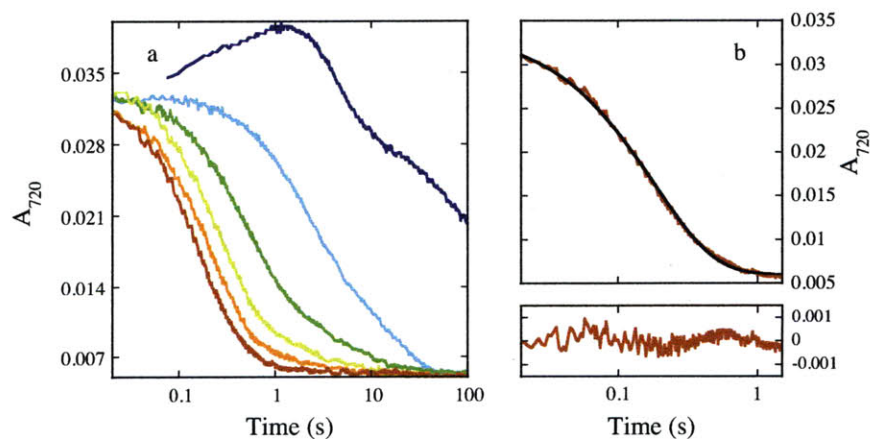


**Figure 3.4.** (a) Representative absorbance profile for the reaction of 50  $\mu\text{M}$  MMOH<sub>red</sub> with a mixture of excess O<sub>2</sub> and CH<sub>3</sub>CH<sub>2</sub>CHO in the presence of 2 equiv MMOB at 4 °C and 720 nm. [CH<sub>3</sub>CH<sub>2</sub>CHO] = 0 mM (blue), 5.8 mM (cyan), 24.9 mM (green), 69.7 mM (yellow), 122.3 mM (orange), and 214.9 mM (red). Data collected on separate occasions with different batches of protein yielded similar results. (b) Representative fit of data (red line) depicted in (a) collected in the presence of 214.9 mM CH<sub>3</sub>CH<sub>2</sub>CHO to a single exponential decay process (black line). Fit residuals are depicted below the plot.

and Q are responsible for a rise and decay in absorbance at 420 nm (Figure 3.3a). As the substrate concentration was increased, the amplitude of this signal diminished and the time of maximal accumulation decreased, indicating that components contributing to the signal are depleted faster than in the absence of substrate. At the highest substrate concentrations employed, this rise and decay in absorbance was not observed because the intermediates do not accumulate. At these concentrations the time-dependent profiles did not change significantly with increasing substrate concentration. Only a slight decay in absorbance was seen, presumably due to decay of  $H_{red}$  (Figure 3.3b). Data collected at 214.9 mM  $CH_3CH_2CHO$ , the highest substrate concentration employed, fit well to a single exponential decay with rate constant  $5.6 \pm 0.1 \text{ s}^{-1}$  at 420 nm and 720 nm (Figures 3.3b and Figure 3.4b). This value is within error of that measured previously for  $H_{red}$  decay/ $P^*$  formation (7), confirming conclusively that  $P^*$  and possibly  $H_{peroxo}$  do not accumulate under these conditions. These observations are distinct from those probing the reaction of the enzyme with methane, and reactivity with  $P^*$  and probably  $H_{peroxo}$  is the only plausible explanation for these results.

*Double-Mixing Stopped Flow Studies – Delineating the Reactivities of Diiron(III) Peroxo vs Diiron(IV) Oxo Intermediates.* To gain insight into the reaction mechanisms of  $H_{peroxo}/P^*$  and Q with substrates, we used double mixing stopped-flow spectroscopy to generate  $H_{peroxo}$  or Q and then we introduced a substrate of interest and followed the ensuing optical events. Previous reports have taken the rate constant for  $H_{peroxo}$  or Q decay in the presence of a given substrate as a measure of the rate at which the intermediate of

**Table 3.1.** Classification of H<sub>peroxo</sub> and Q Substrates

Substrate	Substrate Class (H <sub>peroxo</sub> )	Substrate Class (Q)	Dipole Moment (D) <sup>a</sup>
CH <sub>4</sub> <sup>b</sup>	nr <sup>c</sup>	II	0
C <sub>2</sub> H <sub>6</sub> <sup>d</sup>	nd <sup>e</sup>	I	0
Et <sub>2</sub> O <sup>f</sup>	II	II	1.10
HCOONa	III	nr <sup>c</sup>	1.41 <sup>g</sup>
CH <sub>3</sub> CH <sub>2</sub> OH	II	I	1.69
CH <sub>3</sub> OH	II	I	1.70
CH <sub>3</sub> CH <sub>2</sub> CHO	III	I or II <sup>h</sup>	2.52
CH <sub>3</sub> CHO	III	II	2.69
CH <sub>3</sub> NO <sub>2</sub>	III	III	3.46
CH <sub>3</sub> CN	III	III	3.92

<sup>a</sup>Data from (38). <sup>b</sup>Data from (23). <sup>c</sup>No reaction. <sup>d</sup>Data from (39). <sup>e</sup>Not determined. <sup>f</sup>Data from (26). <sup>g</sup>This value was determined for HCOOH but should approximate that of HCOONa. <sup>h</sup>For CH<sub>3</sub>CH<sub>2</sub>CHO, the KIE was not determined but a linear dependence on substrate concentration was observed, designating this substrate as Class I or Class II.

interest reacts with that substrate (6, 8, 19, 20, 23, 26, 35). A definitive study employing stopped-flow Fourier transform infrared spectroscopy confirmed that this method appropriately describes the rate of reaction with substrate; the rate constant for Q decay, measured by optical spectroscopy, in the presence of the alternative substrate CD<sub>3</sub>NO<sub>2</sub> stopped-flow Fourier transform infrared spectroscopy confirmed that this method was the same at that for substrate consumption, measured by FT-IR spectroscopy (36). A similar conclusion was reached in an early study employing nitrobenzene as a substrate (37). These findings allowed us to employ stopped-flow spectroscopy in order to measure the decay rate constants for H<sub>peroxo</sub> and Q in the presence of various substrates in order to gain information about the reactions of these intermediates.

Reactions of H<sub>peroxo</sub> and Q monitored at 4 °C and pH 7.0 in this manner fit into one of three categories based on the nature of the rate-determining step in the reaction, as

**Table 3.2.** Rate Constants for Class I Substrates of Q

Substrate	$k_{\text{obs}}$ ( $\text{M}^{-1} \text{s}^{-1}$ )	KIE <sub>app</sub> <sup>a</sup>
CH <sub>3</sub> CH <sub>2</sub> OH	35.7 ± 0.1	
CD <sub>3</sub> CD <sub>2</sub> OH	34 ± 3	1.05 ± 0.9
CH <sub>3</sub> OH	218 ± 8	
CD <sub>3</sub> OD	206 ± 16	1.06 ± 0.9

<sup>a</sup>Apparent kinetic isotope effect,  $k_{\text{H}}/k_{\text{D}}$ .

determined by the dependence of the rate constant for intermediate decay ( $k_{\text{obs}}$ ) on substrate concentration and by the effects of substrate deuteration (Table 3.1). Substrates were classified according to the following criteria: (i) linear dependence of  $k_{\text{obs}}$  on substrate concentration and a kinetic isotope effect (KIE),  $k_{\text{H}}/k_{\text{D}}$ , of unity; (ii) linear dependence of  $k_{\text{obs}}$  on substrate concentration and KIE > 1; and (iii) hyperbolic dependence of  $k_{\text{obs}}$  on substrate concentration (23, 40).

*Class I Reactions.* Reactions of Q with Class I substrates display a linear dependence of rate on substrate concentration and a KIE near unity, results suggesting that for these substrates C–H bond breaking is not rate-determining (Table 3.2). Rather, substrate access to the active site appears to determine the kinetics, even at high substrate concentrations. Second order rate constants for these reactions were determined by fitting the data to eq 3.1, where  $k_{\text{obs}}$  is the observed rate constant at a given substrate concentration,  $k_0$  is the rate constant of intermediate decay in the absence of substrate,

$$k_{\text{obs}} - k_0 = k[\text{S}] \quad (3.1)$$

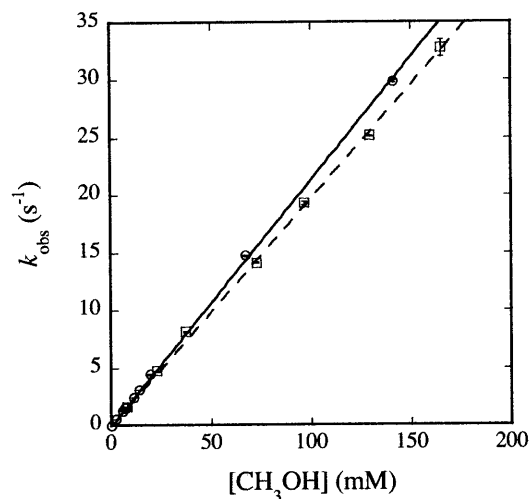


**Figure 3.5.** Plot of  $k_{\text{obs}}$  versus  $[\text{CH}_3\text{OH}]$  (circles, solid line) or  $[\text{CD}_3\text{OH}]$  (squares, dashed line) for reaction with Q at 4 °C and pH 7.0. 200  $\mu\text{M}$   $\text{MMOH}_{\text{red}}$  and 400  $\mu\text{M}$   $\text{MMOB}$  were mixed rapidly with excess  $\text{O}_2$ , the reaction mixture was aged for 12 s, and then buffer containing the appropriate concentration of methanol was introduced. Data were analyzed as noted in the text. Error bars represent one standard deviation at the 95% confidence level.

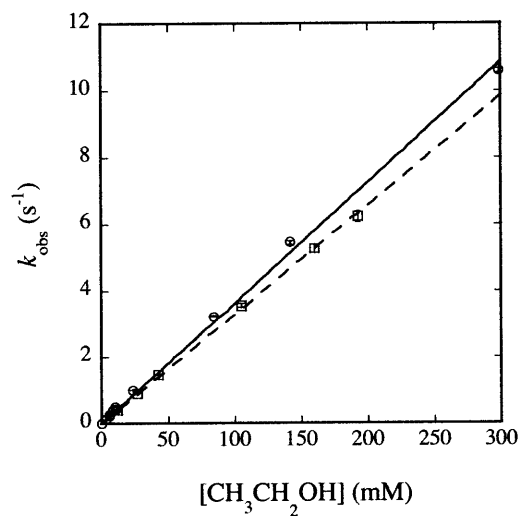


**Figure 3.6.** Plot of  $k_{\text{obs}}$  versus  $[\text{CH}_3\text{CH}_2\text{OH}]$  (circles, solid line) or  $[\text{CD}_3\text{CD}_2\text{OH}]$  (squares, dashed line) for reaction with Q at 4 °C and pH 7.0. 200  $\mu\text{M}$   $\text{MMOH}_{\text{red}}$  and 400  $\mu\text{M}$   $\text{MMOB}$  were mixed rapidly with excess  $\text{O}_2$ , the reaction mixture was aged for 12 s, and then buffer containing the appropriate concentration of ethanol was introduced. Data were analyzed as noted in the text. Error bars represent one standard deviation at the 95% confidence level.

and  $k$  is the second-order rate constant for the overall reaction. Class I substrates for Q include only the alcohols methanol (Figure 3.5) and ethanol (Figure 3.6), where the former reaction yields formaldehyde exclusively (23). An additional substrate that falls into this class for reaction with Q is ethane (39).

For Class I substrates, the approach to the active site, rather than C–H bond activation, might be rate-determining. In MMOH, hydrocarbon substrates are thought to access the active site diiron center via a series of five hydrophobic cavities that feature only a few polar amino acid side chains (41). Favorable hydrophobic interactions between nonpolar substrates such as ethane and the hydrophobic side chains of residues in the active site pocket and possibly those that line the protein cavities could prevent rapid access to the active site. High-level QM/MM density functional theory studies probing the reaction of Q with ethane support this mechanism (42). In the case of alcohols, *favorable* hydrogen-bonding or van der Waals interactions between the substrate hydroxyl group and polarizable residues in the active site and possibly the other cavities could lead to the observed effect by stabilizing the transition state for C–H bond activation relative to that for substrate binding. In this manner, such interactions could lower the barrier height for the former process and render the latter rate-determining at all substrate concentrations. Computational studies predict that this type of mechanism is operative during the reaction of methanol with Q (42). During this reaction, the active site cavity orients the substrate in such a way that a hydrogen bond forms between the alcohol group and the backbone carbonyl of an active site glycine residue, G113, stabilizing the transition state for C–H

bond activation relative to that of substrate binding (42). A similar interaction is expected to occur with ethanol.

Surprisingly, class I type behavior was not observed for  $H_{\text{peroxo}}$  among the substrates employed in the study. Even methanol and ethanol, class I substrates of Q, displayed KIEs greater than unity for reaction with  $H_{\text{peroxo}}$  (vide infra). These findings reveal that there is a disparity in the manner that the two intermediates react with these substrates, a conclusion derived from differences in the rate-determining steps of the reaction. For reactions of alcohols with  $H_{\text{peroxo}}$ , the rate-determining step is C–H bond activation instead of substrate binding. It is likely that structural changes occur at the diiron center during conversion of  $H_{\text{peroxo}}$  to Q, which might alter the manner by which substrates can approach the active site, thereby influencing the rate-determining step. Of relevance is the finding that significant KIEs were observed in pre-steady state reactions of ethane with Q when mutant forms of MMOB were employed, but not when wild-type MMOB was used (39, 43). Although these results do not specifically inform us about the differential reactivity of the two MMOH intermediates, they suggest that geometric differences at the active site in the MMOH/MMOB complex, in this case imparted by MMOB amino acid substitutions, can alter the relative thermodynamics of the substrate binding and C–H bond activation steps. Differential steric constraints imposed by the geometries of the iron-oxygen intermediate species could have a similar effect on the reactions. For the reaction of methanol with  $H_{\text{peroxo}}$ , a favorable interaction of the alcohol group with the carbonyl of G113 to lower the barrier height for reaction with Q (vide supra) might not provide the same stabilizing force for reaction with  $H_{\text{peroxo}}$  due to stereochemical differences, leading to the observed effects.

**Table 3.3.** Rate Constants for Class II Substrates of H<sub>peroxo</sub>

Substrate	$k_{\text{obs}}$ (M <sup>-1</sup> s <sup>-1</sup> )	KIE <sub>app</sub> <sup>a</sup>
(CH <sub>3</sub> CH <sub>2</sub> ) <sub>2</sub> O <sup>b</sup>	17 ± 1	
(CD <sub>3</sub> CD <sub>2</sub> ) <sub>2</sub> O <sup>b</sup>	8.7 ± 0.1	2.02 ± 0.2
CH <sub>3</sub> CH <sub>2</sub> OH	12.13 ± 0.01	
CD <sub>3</sub> CD <sub>2</sub> OH	3.93 ± 0.06	3.09 ± 0.05
CH <sub>3</sub> OH	2.4 ± 0.6	
CD <sub>3</sub> OD	1.54 ± 0.02	1.6 ± 0.4

<sup>a</sup>Apparent kinetic isotope effect,  $k_H/k_D$ . <sup>b</sup>Data from (26).

*Class II Reactions.* Reactions of H<sub>peroxo</sub> and Q with Class II substrates depend linearly on substrate concentration and have KIE > 1, suggesting that C–H activation is fully or partially rate-determining for these substrates, even at low substrate concentrations. For these substrates, there does not appear to be a discrete substrate-binding step, and the kinetics best resemble those for a small molecule catalyst rather than an enzyme, which requires a traditional Michaelis-Menten treatment. Diffusion to the active site is rapid and in all cases faster than the C–H bond activation chemistry. For H<sub>peroxo</sub>, these substrates include methanol (Figure 3.7), ethanol (Figure 3.8), and diethyl ether (26) (Table 3.3). For Q, only diethyl ether (26) and methane (6, 20, 23) exhibit such behavior.

The second-order rate constants for reaction of class II substrates with H<sub>peroxo</sub> correlate with the strength of the weakest C–H bond (Table 3.4). For diethyl ether, which has two types of C–H groups, the weakest C–H bond is the one that becomes hydroxylated during steady state assays (2, 26). Substrates with the lowest homolytic ( $D(\text{RH})$ ) and heterolytic ( $D(\text{R}^+\text{H}^-)$ ) bond dissociation energies display the fastest reaction rates. These results



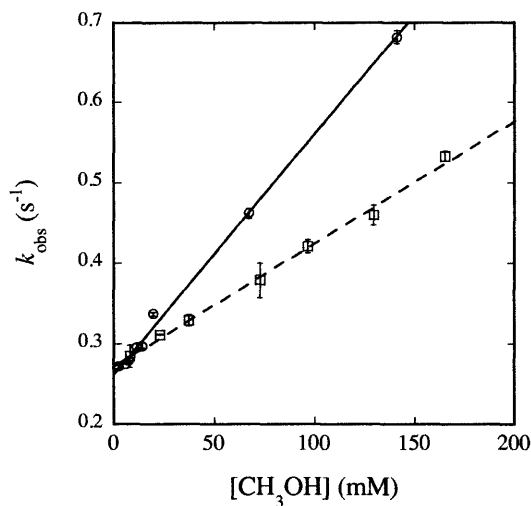


**Figure 3.7.** Plot of  $k_{\text{obs}}$  versus  $[\text{CH}_3\text{OH}]$  (circles, solid line) or  $[\text{CD}_3\text{OH}]$  (squares, dashed line) for reaction with  $\text{H}_{\text{peroxo}}$  at 4 °C and pH 7.0. 200  $\mu\text{M}$   $\text{MMOH}_{\text{red}}$  and 400  $\mu\text{M}$   $\text{MMOB}$  were mixed rapidly with excess  $\text{O}_2$ , the reaction mixture was aged for 2 s, and then buffer containing the appropriate concentration of methanol was introduced. Data were analyzed as noted in the text. Error bars represent one standard deviation at the 95% confidence level.

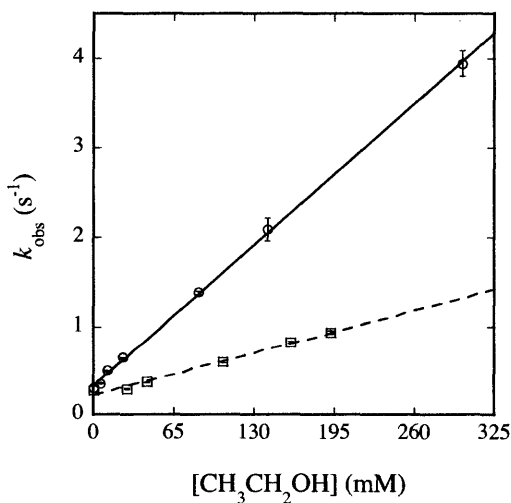


**Figure 3.8.** Plot of  $k_{\text{obs}}$  versus  $[\text{CH}_3\text{CH}_2\text{OH}]$  (circles, solid line) or  $[\text{CD}_3\text{CD}_2\text{OH}]$  (squares, dashed line) for reaction with  $\text{H}_{\text{peroxo}}$  at 4 °C and pH 7.0. 200  $\mu\text{M}$   $\text{MMOH}_{\text{red}}$  and 400  $\mu\text{M}$   $\text{MMOB}$  were mixed rapidly with excess  $\text{O}_2$ , the reaction mixture was aged for 2 s, and then buffer containing the appropriate concentration of ethanol was introduced. Data were analyzed as noted in the text. Error bars represent one standard deviation at the 95% confidence level.

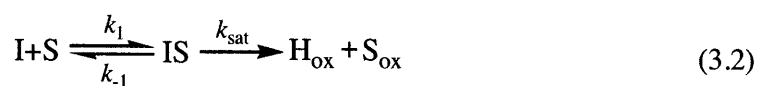
**Table 3.4.** Class II Substrates of  $H_{\text{peroxo}}$ : Correlation Between  $k_{\text{obs}}$  and BDE

Substrate <sup>a</sup>	$k_{\text{obs}}$ ( $M^{-1} s^{-1}$ )	$D(R^*H)$ (kcal/mol) <sup>b</sup>	$-\Delta G_{\text{hydride}}(R^*)_s$ (kcal/mol) <sup>c</sup>	$D(RH)$ (kcal/mol) <sup>d</sup>
$(CH_3CH_2)_2O^e$	$17 \pm 1$	214	94.8	93.0
$CH_3CH_2OH$	$12.13 \pm 0.01$	231.9	110.9	94.6
$CH_3OH$	$2.4 \pm 0.6$	255	131.8	96.06

<sup>a</sup> $D(R^*H)$  and  $D(RH)$  are given for the bolded C–H bond. For diethyl ether, this position is the sole C–H bond activated by sMMO in steady state assays (26). <sup>b</sup>Data from (44). <sup>c</sup>Calculated using  $-\Delta G_{\text{hydride}}(R^*)_s = 0.904D(R^*H) - 98.7$  kcal/mol from (45). This relationship was originally derived for aromatic molecules in acetonitrile and DMSO, but should provide a good approximation for non-aromatic systems in aqueous solution. <sup>d</sup>Data from (46). <sup>e</sup>Data from (26).

indicate that hydrogen abstraction from substrate, either in the form of hydride or hydrogen atom, is involved in the rate-determining step of reactions of  $H_{\text{peroxo}}$ .

*Class III Reactions.* Reactions of  $H_{\text{peroxo}}$  and Q with Class III substrates display a hyperbolic dependence on substrate concentration typical of classical enzyme kinetic mechanisms. For these substrates, binding is rate-determining at low substrate concentration but C–H activation chemistry is rate-determining at high substrate concentration. These substrates include propionaldehyde (Figure 3.9), acetaldehyde (Figure 3.10), nitromethane (Figure 3.11a), sodium formate (Figure 3.12), and acetonitrile (Figure 3.13a) for  $H_{\text{peroxo}}$ , and nitromethane (Figure 3.11b) and acetonitrile (Figure 3.13b) for Q (Table 3.5). Data belonging to this class follow the behavior



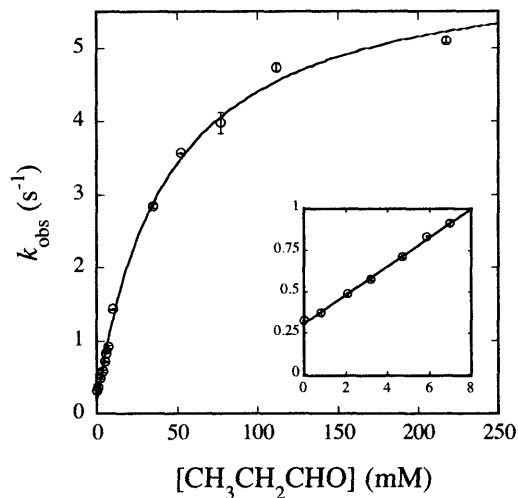


**Figure 3.9.** Plot of  $k_{\text{obs}}$  versus  $[\text{CH}_3\text{CH}_2\text{CHO}]$  for reaction with  $\text{H}_{\text{peroxo}}$  at 4 °C and pH 7.0. 200  $\mu\text{M}$   $\text{MMOH}_{\text{red}}$  and 400  $\mu\text{M}$   $\text{MMOB}$  were mixed rapidly with excess  $\text{O}_2$ , the reaction mixture was aged for 2 s, and then buffer containing the appropriate concentration of propionaldehyde was introduced. Data were analyzed as noted in the text. Data collected at low  $[\text{CH}_3\text{CH}_2\text{CHO}]$  ( $k_{\text{init}}$ ) is depicted in the inset. Error bars represent one standard deviation at the 95% confidence level.

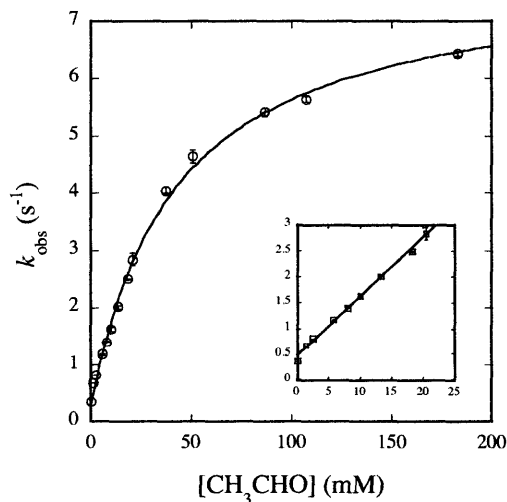


**Figure 3.10.** Plot of  $k_{\text{obs}}$  versus  $[\text{CH}_3\text{CHO}]$  for reaction with  $\text{H}_{\text{peroxo}}$  at 4 °C and pH 7.0. 200  $\mu\text{M}$   $\text{MMOH}_{\text{red}}$  and 400  $\mu\text{M}$   $\text{MMOB}$  were mixed rapidly with excess  $\text{O}_2$ , the reaction mixture was aged for 2 s, and then buffer containing the appropriate concentration of acetaldehyde was introduced. Data were analyzed as noted in the text. Data collected at low  $[\text{CH}_3\text{CHO}]$  ( $k_{\text{init}}$ ) is depicted in the inset. Error bars represent one standard deviation at the 95% confidence level.

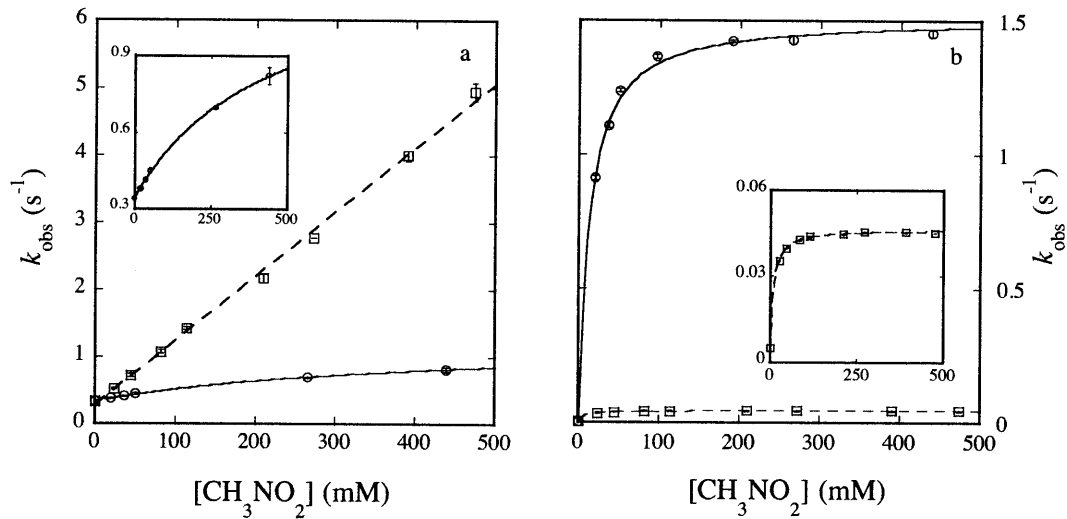


**Figure 3.11.** Plot of  $k_{\text{obs}}$  versus [CH<sub>3</sub>NO<sub>2</sub>] (circles, solid line) or [CD<sub>3</sub>NO<sub>2</sub>] (squares, dashed line) for reactions with H<sub>peroxo</sub> (a) and Q (b) at 4 °C and pH 7.0. 200 μM MMOH<sub>red</sub> and 400 μM MMOB were mixed rapidly with excess O<sub>2</sub>, the reaction mixture was aged for 2 s (H<sub>peroxo</sub>) or 12 s (Q), and then buffer containing the appropriate concentration of nitromethane was introduced. Data were analyzed as noted in the text. Insets show clearer plots of data displaying small rate constants. Error bars represent one standard deviation at the 95% confidence level.

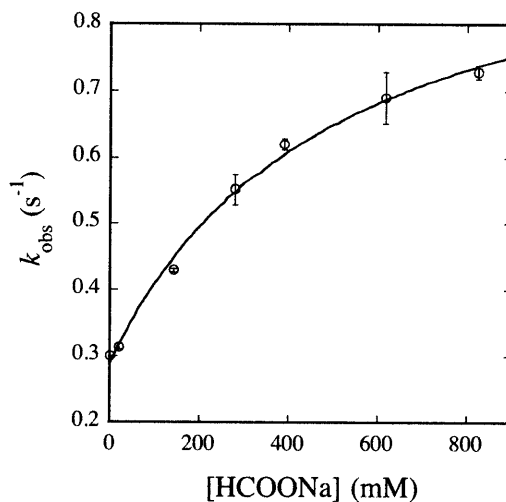


**Figure 3.12.** Plot of  $k_{\text{obs}}$  versus [HCOONa] for reaction with H<sub>peroxo</sub> at 4 °C and pH 7.0. 200 μM MMOH<sub>red</sub> and 400 μM MMOB were mixed rapidly with excess O<sub>2</sub>, the reaction mixture was aged for 2 s, and then buffer containing the appropriate concentration of sodium formate was introduced. Data were analyzed as noted in the text. Error bars represent one standard deviation at the 95% confidence level.

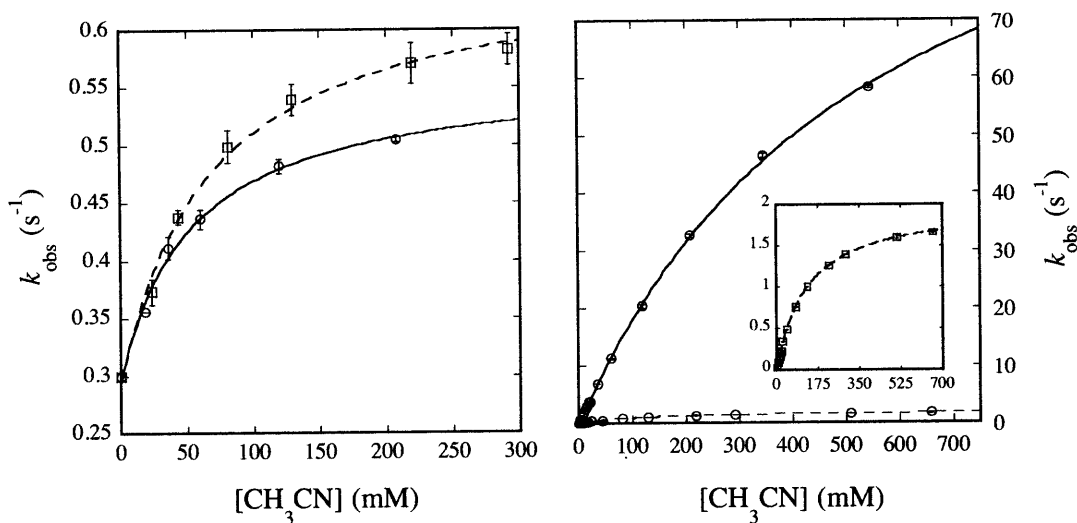


**Figure 3.13.** Plot of  $k_{\text{obs}}$  versus  $[\text{CH}_3\text{CN}]$  (circles, solid line) or  $[\text{CD}_3\text{CN}]$  (squares, dashed line) for reaction with  $\text{H}_{\text{peroxo}}$  (a) and Q (b) at 4 °C and pH 7.0. 200  $\mu\text{M}$   $\text{MMOH}_{\text{red}}$  and 400  $\mu\text{M}$   $\text{MMOB}$  were mixed rapidly with excess  $\text{O}_2$ , the reaction mixture was aged for 2 s ( $\text{H}_{\text{peroxo}}$ ) or 12 s (Q), and then buffer containing the appropriate concentration of acetonitrile was introduced. Data were analyzed as noted in the text. The inset of (b) shows a clearer plot of the  $[\text{CD}_3\text{CN}]$  data and fit for Q. Error bars represent one standard deviation at the 95% confidence level.

**Table 3.5.** Class III Substrates of  $\text{H}_{\text{peroxo}}$  and Q

Substrate	Species	$k_{\text{sat}}$ ( $\text{s}^{-1}$ )	$K_{\text{M}}$ (mM)	$k_{\text{init}}$ ( $\text{M}^{-1} \text{s}^{-1}$ ) <sup>a</sup>	$\text{KIE}_{\text{app}}$ <sup>b</sup>
$\text{CH}_3\text{CH}_2\text{CHO}$	$\text{H}_{\text{peroxo}}$	$6.0 \pm 0.2$	$44 \pm 4$	$85.5 \pm 0.1$	nd <sup>c</sup>
$\text{CH}_3\text{CHO}$	$\text{H}_{\text{peroxo}}$	$7.6 \pm 0.2$	$43 \pm 3$	$110.08 \pm 0.03$	nd <sup>c</sup>
$\text{HCOONa}$	$\text{H}_{\text{peroxo}}$	$0.71 \pm 0.01$	$458 \pm 65$	$0.91 \pm 0.01$	nd <sup>c</sup>
$\text{CH}_3\text{CN}$	$\text{H}_{\text{peroxo}}$	$0.2727 \pm 0.0003$	$39 \pm 6$	$2.93 \pm 0.01$	
$\text{CD}_3\text{CN}$	$\text{H}_{\text{peroxo}}$	$0.352 \pm 0.001$	$78 \pm 3$	2.02	$0.775 \pm 0.002$
$\text{CH}_3\text{NO}_2$	$\text{H}_{\text{peroxo}}$	$0.912 \pm 0.002$	$403 \pm 11$	nd <sup>c</sup>	na <sup>d</sup>
$\text{CH}_3\text{CN}$	Q	$126 \pm 8$	$617 \pm 71$	$180 \pm 1$	
$\text{CD}_3\text{CN}$	Q	$2.02 \pm 0.03$	$130 \pm 3$	12.4	$62 \pm 4$
$\text{CH}_3\text{NO}_2$	Q	$1.54 \pm 0.2$	$13 \pm 1$	nd <sup>c</sup>	
$\text{CD}_3\text{NO}_2$	Q	$0.005 \pm 0.0005$	$11 \pm 5$	nd <sup>c</sup>	$31 \pm 3$

<sup>a</sup> $k_{\text{init}}$  values were calculated by fitting the linear portion of the curve at low substrate concentration to eq 3.1.

<sup>b</sup>Apparent kinetic isotope effect,  $k_{\text{sat,H}}/k_{\text{sat,D}}$ . <sup>c</sup>Not determined. <sup>d</sup>Not applicable. For  $\text{CD}_3\text{NO}_2$ ,  $\text{KIE}_{\text{app}}$  could not be determined for the reaction of  $\text{H}_{\text{peroxo}}$  because  $k_{\text{obs}}$  displayed a linear dependence on substrate concentration.

$$k_{obs} - k_0 = \frac{k_{sat}[S]}{K_M + [S]} \quad (3.3)$$

approximated by eq 3.2 and can be fit to eq 3.3, where  $k_{obs}$  is the observed rate constant at a defined substrate concentration,  $k_0$  is the rate constant of intermediate conversion in the absence of substrate,  $k_{sat}$  is defined in eq 3.2, and  $K_M$  is the apparent Michaelis constant describing the intermediate-substrate complex, defined as  $(k_{-1} + k_{sat})/k_1$ .

For both  $H_{peroxo}$  and Q, all of the substrates that fit into Class III contain highly polarizable double bonds involving a heteroatom. The molecular dipole moments of these molecules are higher (>2.5 D) than those of Class I and Class II substrates (Table 3.1). This property provides a means by which these substrates can participate in dipole-induced interactions with protein amide bonds and polar side chains that line the hydrophobic cavities leading from the protein exterior to the active site. Whereas  $H_{peroxo}$  displays Class III behavior with substrates having  $D > \sim 2.5$ , Q displays only Class II behavior with the two substrates for which  $D > \sim 3.5$ . These findings reinforce the conclusion that the mechanisms by which  $H_{peroxo}$  and Q interact with substrates differ. The results also provide some guidance for predicting the behavior of a given substrate.

The values of  $k_{sat}$  provide a direct measure of the C–H bond activation step for the substrates employed and can therefore be used to obtain information about the details of the reaction mechanism for the intermediate species. In addition, a comparison of  $k_{sat}$  values for  $H_{peroxo}$  Class III substrates reveals a correlation between the rate constant and the heterolytic and homolytic C–H bond strengths of the substrate (Table 3.6 and Figure

**Table 3.6.** Class III Substrates of  $H_{\text{peroxo}}$ : Correlation Between  $k_{\text{obs}}$  and BDE

Substrate <sup>a</sup>	$k_{\text{sat}}$ ( $s^{-1}$ )	$D(R^*H)$ (kcal/mol) <sup>b</sup>	$-\Delta G_{\text{hydride}}(R^*)_s$ (kcal/mol) <sup>c</sup>	D(RH) (kcal/mol)
$CH_3CH_2CHO$	$6.0 \pm 0.2$	224	103.8	87.5 <sup>f</sup>
$CH_3CHO$	$7.6 \pm 0.2$	231.4	110.5	94.3 <sup>d</sup>
$CH_3NO_2$	$0.912 \pm 0.002$	-	-	96.3 <sup>d</sup>
HCOONa	$0.71 \pm 0.04$	267 <sup>e</sup>	142.7	96.6 <sup>d,e</sup>

<sup>a</sup> $D(R^*H)$  and D(RH) are given for the bolded C–H bond. <sup>b</sup>Data from (44). <sup>c</sup>Calculated using  $-\Delta G_{\text{hydride}}(R^*)_s = 0.904D(R^*H) - 98.7$  kcal/mol from (45). This relationship was originally derived for aromatic molecules in acetonitrile and DMSO, but should provide a good approximation for non-aromatic systems in aqueous solution. <sup>d</sup>Data from (46) <sup>e</sup>These values were originally determined for HCOOH but should approximate that of HCOONa. <sup>f</sup>Data from (47).

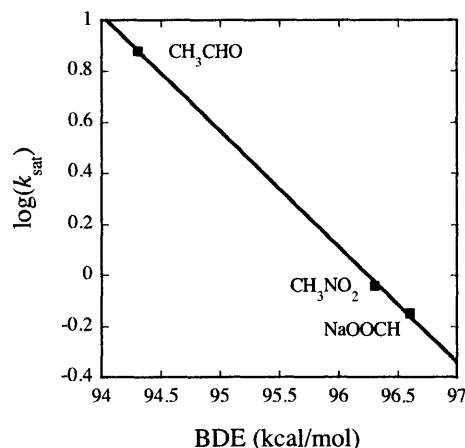


**Figure 3.14.** Linear inverse correlation between  $k_{\text{sat}}$  and C–H BDE for Class III substrates of  $H_{\text{peroxo}}$ . Reactions employed final concentrations of 50  $\mu\text{M}$  MMOH and 100  $\mu\text{M}$  MMOB and were performed at 4  $^{\circ}\text{C}$  and pH 7.0.

3.14).<sup>1</sup> Although the substrates analyzed fall into a relatively narrow range of C–H bond strengths, it is apparent that those with lower C–H bond strengths react more rapidly with

<sup>1</sup>According to this hypothesis, the value of  $k_{\text{sat}}$  for reaction of  $CH_3CH_2CHO$  with  $H_{\text{peroxo}}$  is expected to be larger than that of all other substrates examined, but was slightly smaller than that for  $CH_3CHO$ . This result does not necessarily negate the conclusion that a trend between reaction rate and C–H bond strength exists because propionaldehyde is expected to react at its methyl group in addition to its aldehydic position, for which the C–H bond strengths are compared. Reactivity at multiple sites having different C–H bond strengths partially invalidates the comparison for this substrate.

**Table 3.7.** Apparent KIEs and Correlation of  $k_{\text{sat}}$  with Thermodynamic Parameters for Class III Substrates of Q at 4 °C and 20 °C

Substrate	T (°C)	$k_{\text{sat}}$ (s <sup>-1</sup> )	KIE <sub>app</sub> <sup>a</sup>	D(RH) (kcal/mol) <sup>b</sup>	IP (eV)	pK <sub>a</sub> <sup>c</sup>
CH <sub>3</sub> CN	4	126 ± 8		97.0	12.20 <sup>d</sup>	25.0
	20 <sup>e</sup>	282 ± 10				
CD <sub>3</sub> CN	4	2.02 ± 0.03	62 ± 4			
	20 <sup>e</sup>	6.1 ± 0.1	46.4 ± 2.3			
CH <sub>3</sub> NO <sub>2</sub>	4	1.54 ± 0.02		96.3	11.28 <sup>f</sup>	10.2
	20 <sup>e</sup>	5.34 ± 0.02				
CD <sub>3</sub> NO <sub>2</sub>	4	0.050 ± 0.0005	31 ± 3			
	20 <sup>e</sup>	0.66 ± 0.2	8.1 ± 0.2			

<sup>a</sup>Apparent kinetic isotope effect,  $k_{\text{sat,H}}/k_{\text{sat,D}}$ . <sup>b</sup>Data from (46). <sup>c</sup>Data from (48). <sup>d</sup>Data from (49). <sup>e</sup>Data from (23). <sup>f</sup>Data from (50).

H<sub>peroxo</sub>, bolstering the argument that the rate-determining step in the reaction involves C–H bond cleavage.

Two substrates display Class III behavior for reaction with Q, acetonitrile and nitromethane (Table 3.5). The large, non-classical magnitudes of the isotope effects for reactions of Q with these substrates suggest that they proceed with extensive quantum mechanical tunneling through the transition state at both 4 °C and 20 °C (Table 3.7). Although the two substrates are expected to exhibit both primary and secondary isotope effects, secondary effects should lie within semi-classical limits (< ~7). The large effects observed are therefore likely to be dominated by primary effects arising from hydrogen atom tunneling (51). The significant temperature dependence of the observed KIEs, which are larger at lower temperatures, also necessitates involvement of H-atom tunneling as defined by semi-classical transition state theory. This model predicts that both zero point energy considerations and hydrogen tunneling effects lead to a smaller



free energy for hydrogen than for deuterium in a temperature-dependent manner (51, 52). Similar effects were previously observed for methane (23, 53).

For reactions with Q, there is no correlation of  $k_{\text{sat}}$  with the reported C–H bond activation energies; acetonitrile and nitromethane have similar homolytic and heterolytic BDEs but display a 62-fold difference in their reaction rates with Q at 4 °C, acetonitrile reacting much more rapidly than nitromethane. Similarly, the rate constants do not correlate with the  $pK_a$  values or ionization potentials (IPs) of the substrates (Table 3.7). These results suggest that classical hydrogen atom transfer or hydride transfer featuring no quantum tunneling effects, proton transfer, and/or electron transfer from the substrate to the oxygenated diiron core are not determinants in the rate-determining step in the reaction mechanism. However, the observation that extensive quantum mechanical tunneling is operative in the reaction mechanism of Q (vide supra) suggests that C–H bond activation could be rate-determining via a non-classical mechanism. Differential contributions of quantum tunneling to the overall reaction processes for the two substrates could therefore lead to the observed effects.

*Implications for the Reaction Mechanisms of  $H_{\text{peroxo}}$  and Q.* The data presented here suggest that the mechanisms by which  $H_{\text{peroxo}}$  and Q react with substrate differ in both the nature of the C–H bond breaking process and the physical interaction with the substrate. Although reactions of  $H_{\text{peroxo}}$  seem to proceed by a classical hydrogen atom or hydride transfer mechanism, those of Q involve extensive non-classical character. Substrates with lower C–H bond strengths react preferentially with  $H_{\text{peroxo}}$ , although there is no correlation between bond energy and Q reaction rates, most likely because of non-classical character

**Table 3.8.** Comparison of Second-Order Rate Constants for Reactions of H<sub>peroxo</sub> and Q with Substrates

Substrate <sup>a</sup>	Species	$k_{\text{obs}}$ (M <sup>-1</sup> s <sup>-1</sup> ) <sup>b</sup>	$k_{\text{peroxo}}/k_{\text{Q}}$	D(R <sup>+</sup> H) (kcal/mol) <sup>c</sup>	$-\Delta G_{\text{hydride}}(\text{R}^+)_{\text{s}}$ (kcal/mol) <sup>d</sup>	D(RH) (kcal/mol)
(CH <sub>3</sub> CH <sub>2</sub> ) <sub>2</sub> O <sup>e</sup>	H <sub>peroxo</sub>	17 ± 1	7.7	214	94.8	89.0 <sup>f</sup>
	Q	2.2 ± 1				
CH <sub>3</sub> CH <sub>2</sub> CHO	H <sub>peroxo</sub>	85.5 ± 0.1	6.06	224	103.8	87.5 <sup>g</sup>
	Q	14.10 ± 0.02				
CH <sub>3</sub> CHO	H <sub>peroxo</sub>	110.08 ± 0.03	1.35	231.4	110.5	94.3 <sup>f</sup>
	Q	81.7 ± 0.1				
CH <sub>3</sub> CH <sub>2</sub> OH	H <sub>peroxo</sub>	12.13 ± 0.01	0.34	231.9	110.9	94.6 <sup>f</sup>
	Q	35.7 ± 0.1				
CH <sub>3</sub> OH	H <sub>peroxo</sub>	2.4 ± 0.6	0.011	255	131.8	96.1 <sup>f</sup>
	Q	218 ± 8				

<sup>a</sup>D(R<sup>+</sup>H) and D(RH) are given for the bolded C–H bond. <sup>b</sup>Second-order rate constants for Class III substrates are given by the measured  $k_{\text{init}}$  values. Only Class III substrates for which  $k_{\text{init}}$  values were discretely measured by collecting >5 data points at low substrate concentration in the linear region of the curve are shown. <sup>c</sup>Data from (44). <sup>d</sup>Calculated using  $-\Delta G_{\text{hydride}}(\text{R}^+)_{\text{s}} = 0.904\text{D}(\text{R}^+\text{H}) - 98.7$  kcal/mol from (45). This relationship was originally derived for aromatic molecules in acetonitrile and DMSO, but should provide a good approximation for non-aromatic systems in aqueous solution. <sup>e</sup>Data from (26). <sup>f</sup>Data from (46). <sup>g</sup>Data from (47).

involving the latter. This conclusion is especially evident from inspection of Table 3.8, which compares the second-order rate constants for the *overall* reactions to substrate C–H bond strengths. For Class I and II substrates, the rate constants provided in Table 3.8 were determined by fitting the data to eq 3.1. For Class III substrate reactions, the rate constants were measured by fitting the linear portion of the curves at low substrate concentration to eq 3.1 to obtain a second-order value ( $k_{\text{init}}$  in Table 3.5).

The second-order rate constants provided in Table 3.8 account for all processes involved in the reactions, including substrate binding and C–H bond activation. Therefore, a direct comparison of rate constants to thermodynamic parameters is inappropriate given that the rate-determining steps of the reactions can differ among the substrates employed. A comparison of the *ratio* of the rate constants for reaction with

$H_{\text{peroxo}}$  and Q normalizes the substrate binding contributions in the limit that the binding affinities for the  $H_{\text{peroxo}}$  and Q protein complexes are the same for a given substrate. It is clear that, for some substrates, this situation does not obtain since these substrates belong to different classes of reactions with  $H_{\text{peroxo}}$  and Q. However, the presence of a correlation between the rate constant ratio and the C–H bond strength (vide infra) justifies the approximation.

A comparison of the ratio of the second-order rate constants for  $H_{\text{peroxo}}$  and Q reactions with the heterolytic and homolytic C–H bond strengths of the substrates clearly reveals an inverse trend between these parameters (Table 3.8). Substrates with weak C–H bonds are characterized by large rate constant ratios, consistent with substrates having weak C–H bonds preferentially reacting with  $H_{\text{peroxo}}$  vs. Q. Given this trend in reaction rate with C–H bond strength, it is understandable why methane, with high heterolytic and homolytic bond strengths of 312.2 kcal/mol (54) and 104.0 kcal/mol (46), respectively, reacts rapidly with Q but not at all with  $H_{\text{peroxo}}$ .

One major difference between the reactions of  $H_{\text{peroxo}}$  and Q with hydrocarbons is that large kinetic isotope effects, implicating hydrogen atom tunneling, are observed for Q but not  $H_{\text{peroxo}}$  for both Class II and Class III substrates.<sup>2</sup> In all cases the KIEs observed for reaction with  $H_{\text{peroxo}}$  were within the semiclassical limit ( $< \sim 7$ ), suggesting that quantum mechanical tunneling does not play a role in the reaction mechanism. This finding also sheds light on the lack of reactivity of  $H_{\text{peroxo}}$  with methane. Because methane is

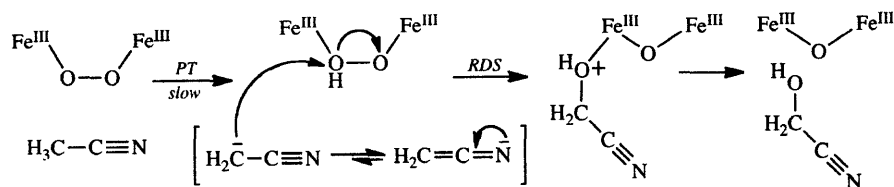
---

<sup>2</sup>The KIE value for reaction of  $H_{\text{peroxo}}$  with  $\text{CH}_3\text{NO}_2$  could not be determined, because reaction with  $\text{CD}_3\text{NO}_2$  depends linearly on substrate concentration but the protio analogue displays Class III saturation behavior. A similar phenomenon was observed for reaction of this substrate with Q at 20 °C and was attributed to a difference in the rate-determining step for the protio and deutero substrates in Baik, M.-H., Newcomb, M., Friesner, R. A., and Lippard, S. J. (2003). *Chem. Rev.* 103, 2385-2419.

kinetically stable, a large barrier height for its reaction is expected. For Q, tunneling across this barrier leads to progression along the reaction coordinate; for  $H_{\text{peroxo}}$ , no tunneling is involved, the barrier is too high to penetrate, and the reaction cannot proceed.

*Reactions of  $H_{\text{peroxo}}$  with  $CH_3CN$ .* The inverse isotope effect observed for reaction of  $CH_3CN$  with  $H_{\text{peroxo}}$  (Table 3.5 and Figure 3.13a) is unexpected and suggests a distinctive reaction mechanism for this substrate. Because the sole oxidation product is glycolonitrile (55), the mechanism necessarily involves C–H bond activation. This reaction could occur by hydrogen atom abstraction to form a radical that recombines with a hydroxyl radical to form the hydroxylated product, by hydride abstraction to form a carbocation that is attacked by hydroxide, or by proton abstraction to form a carbanion that undergoes electrophilic addition with an electron-deficient group. All three of these mechanisms could potentially provide sufficient driving force for peroxide O–O bond cleavage and hydrocarbon oxidation.

The magnitude of the observed isotope effect ( $k_H/k_D$ ) represents the product of primary and secondary contributions to the rate-determining step of the reaction. Primary contributions are expected to yield normal KIEs whereas secondary effects can be inverse or normal depending on the nature of the transition state. The inverse nature and relatively large magnitude of the KIE measured for the reaction of  $H_{\text{peroxo}}$  with  $CH_3CN$  indicates a significant involvement of secondary effects. Inverse secondary KIEs are caused by an increase in the out-of-plane bending force constant of the heavy isotope that may result from  $sp^2$  to  $sp^3$  rehybridization in the transition state (48). Secondary KIEs arising from this type of mechanism typically range from 0.8 to 0.9 (48), consistent with



**Scheme 3.3.** Proposed Mechanism of  $\text{CH}_3\text{CN}$  Hydroxylation by  $\text{H}_{\text{peroxo}}$ ; RDS, Rate-Determining Step

the observed value of 0.77. On the basis of these results we therefore suggest a reaction mechanism in which acetonitrile is first deprotonated to form the cyanomethide anion, the structure of which involves significant  $\text{sp}^2$  character at the  $\alpha$ -carbon atom (56). This species can then attack, in a nucleophilic manner, an electrophilic oxygen atom of the iron-bound (hydro)peroxide resulting in the  $\text{sp}^3$ -hybridized product and the O–O bond is cleaved to form the oxidized product, glycolonitrile (Scheme 3.3).

Formation of a radical intermediate is not expected, because such a mechanism would not involve significant rehybridization at carbon and would therefore lead to a small and normal secondary kinetic isotope effect (48, 51, 57). For the same reason, hydride abstraction is also expected to produce a small and normal KIE. We therefore favor the mechanism proposed in Scheme 3.3. Similar conclusions were reached in a related study probing the mechanism of  $[1,1\text{-}^2\text{H}_2]$ nitroethane anion oxidation by D-amino acid oxidase (58).

The proposed reaction mechanism necessarily involves deprotonation of the acetonitrile molecule and formation of the cyanomethide anion prior to the rate-determining step. Although the  $\text{pK}_a$  of acetonitrile is  $\sim 25$  (48), this value is most likely reduced by coordination to transition metals, which behave as Lewis acids. Additionally,

the cyanomethide anion can be readily generated via deprotonation of acetonitrile by a strong base (59). These results imply that  $H_{\text{peroxo}}$  is highly basic. Indeed, we recently provided evidence that this peroxide moiety acquires a proton during conversion to Q, an event that leads to O–O bond cleavage, a necessary step for reaction with substrate (7).

In light of the proposed carbocation-based mechanism for reaction of  $H_{\text{peroxo}}$  with diethyl ether (Scheme 3.2b), these results were surprising. A mechanism in which a diiron(III) peroxide moiety undergoes electrophilic attack on the substrate carbanion in the rate-determining step to account for the inverse secondary isotope effect seems to contradict the finding that C–H bond activation is rate-determining for diethyl ether and the other substrates employed in the study. Nevertheless, we favor such a mechanism and argue that, because  $k_{\text{sat}}$  for acetonitrile is very slow, the reaction pathway could differ significantly from that of diethyl ether and other much more rapidly reacting substrates. The large heterolytic C–H bond energy of acetonitrile disfavors formation of an intermediate carbocation via hydride abstraction. Presumably the favored mechanism is a consequence of the slow reactivity of this substrate.

When considered together, the two distinct two-electron mechanisms proposed for reaction of  $H_{\text{peroxo}}$  with diethyl ether vs acetonitrile are interesting. The results indicate (i) that  $H_{\text{peroxo}}$  prefers two-electron rather than one-electron transfer mechanisms and (ii) that  $H_{\text{peroxo}}$  is an electrophilic oxidant.

*Implications for Other Systems with Multiple Oxidizing Species.* The observation from this work and others (20, 26) that  $H_{\text{peroxo}}$  can oxidize organic substrates contributes to a growing body of evidence that two oxidants are operative in MMOH. Because the metabolic capabilities of methanotrophic organisms are restricted to the  $C_1$  growth

substrates methane and methanol, it is likely that the reactivity of  $H_{\text{peroxo}}$  is an adventitious result of being on the pathway of formation of Q, a potent methane oxidant. However, given the ability of  $H_{\text{peroxo}}$  to effect hydroxylation and epoxidation reaction chemistry, it is possible that some of the bioremediation applications of the sMMO system, such as removal of trichloroethylene from polluted groundwater (3), arise from its activity.

Similar evidence for two oxidizing species has been provided for the hydrocarbon reactive,  $O_2$ -activating cytochrome P450 enzymes, which contain heme-iron active sites. The results of numerous studies employing kinetic isotope measurements and product analyses of wild-type and mutant enzyme reactions indicate the presence of a second electrophilic oxidant in addition to CpdI, the well-established  $Fe(IV)=O$  porphyrin cation radical species (60-68). The observed behavior is thought to arise from reactivity of a peroxo- and/or hydroperoxo-iron(III) species, similar in electronic arrangement to  $H_{\text{peroxo}}$ , which form after reaction of ferrous enzyme with  $O_2$  and one electron. The mechanism proposed here for the reaction of  $H_{\text{peroxo}}$  with  $CH_3CN$  provides a benchmark for calibrating mechanisms imparted by iron peroxide species in the P450 as well as other enzyme systems.

## CONCLUDING REMARKS

The present study conclusively demonstrates that both  $H_{\text{peroxo}}$  and Q react with substrates in the soluble methane monooxygenase system. Although both species are capable of performing oxidation reactions, they do so by distinct mechanisms. Reactions with Q involve extensive H-atom tunneling and with significant radical character,

whereas reactions with electrophilic  $H_{\text{peroxo}}$  intermediate do not invoke tunneling and seem to occur by two-electron carbocation or carbanion-based mechanisms.

## REFERENCES

1. Merkx, M., Kopp, D. A., Sazinsky, M. H., Blazyk, J. L., Müller, J., and Lippard, S. J. (2001) *Angew. Chem. Int. Ed.* 40, 2782-2807.
2. Colby, J., Stirling, D. I., and Dalton, H. (1977) *Biochem. J.* 165, 395-402.
3. Fox, B. G., Borneman, J. G., Wackett, L. P., and Lipscomb, J. D. (1990) *Biochemistry* 29, 6419-6427.
4. Green, J., and Dalton, H. (1989) *J. Biol. Chem.* 264, 17698-17703.
5. Liu, K. E., Johnson, C. C., Newcomb, M., and Lippard, S. J. (1993) *J. Am. Chem. Soc.* 115, 939-947.
6. Brazeau, B. J., and Lipscomb, J. D. (2000) *Biochemistry* 39, 13503-13515.
7. Tinberg, C., and Lippard, S. J. (2009) *Biochemistry* 48, 12145-12158.
8. Liu, K. E., Valentine, A. M., Wang, D., Huynh, B. H., Edmondson, D. E., Salifoglou, A., and Lippard, S. J. (1995) *J. Am. Chem. Soc.* 117, 10174-10185.
9. Lee, S.-K., and Lipscomb, J. D. (1999) *Biochemistry* 38, 4423-4432.
10. Broadwater, J. A., Ai, J., Loehr, T. M., Sanders-Loehr, J., and Fox, B. G. (1998) *Biochemistry* 37, 14664-14671.
11. Moënné-Loccoz, P., Baldwin, J., Ley, B. A., Loehr, T. M., and Bollinger Jr., J. M. (1998) *Biochemistry* 37, 14659-14663.



12. Moënne-Loccoz, P., Krebs, C., Herlihy, K., Edmondson, D. E., Theil, E. C., Huynh, B. H., and Loehr, T. M. (1999) *Biochemistry* 38, 5290-5295.
13. Skulan, A. J., Brunold, T. C., Baldwin, J., Saleh, L., Bollinger Jr., J. M., and Solomon, E. I. (2004) *J. Am. Chem. Soc.* 126, 8842-8855.
14. Vu, V. V., Emerson, J. P., Martinho, M., Kim, Y. S., Münck, E., Park, M. H., and Que Jr., L. (2009) *Proc. Natl. Acad. Sci. USA* 106, 14814-14819.
15. Han, W.-G., and Noodleman, L. (2008) *Inorg. Chem.* 47, 2975-2986.
16. Gherman, B. F., Baik, M.-H., Lippard, S. J., and Friesner, R. A. (2004) *J. Am. Chem. Soc.* 126, 2978-2990.
17. Rinaldo, D., Philipp, D. M., Lippard, S. J., and Friesner, R. A. (2007) *J. Am. Chem. Soc.* 129, 3135-3147.
18. Siegbahn, P. E. M. (2001) *J. Biol. Inorg. Chem.* 6, 27-45.
19. Lee, S.-K., Nesheim, J. C., and Lipscomb, J. D. (1993) *J. Biol. Chem.* 268, 21569-21577.
20. Valentine, A. M., Stahl, S. S., and Lippard, S. J. (1999) *J. Am. Chem. Soc.* 121, 3876-3887.
21. Liu, K. E., Wang, D., Huynh, B. H., Edmondson, D. E., Salifoglou, A., and Lippard, S. J. (1994) *J. Am. Chem. Soc.* 116, 7465-7466.
22. Shu, L., Nesheim, J. C., Kauffmann, K., Münck, E., Lipscomb, J. D., and Que Jr., L. (1997) *Science* 275, 515-518.
23. Ambundo, E. A., Friesner, R. A., and Lippard, S. J. (2002) *J. Am. Chem. Soc.* 124, 8770-8771.

24. Lee, S.-K., Fox, B. G., Froland, W. A., Lipscomb, J. D., and Münck, E. (1993) *J. Am. Chem. Soc.* *115*, 6450-6451.
25. Baik, M.-H., Gherman, B. F., Friesner, R. A., and Lippard, S. J. (2002) *J. Am. Chem. Soc.* *124*, 14608-14615.
26. Beauvais, L. G., and Lippard, S. J. (2005) *J. Am. Chem. Soc.* *127*, 7370-7378.
27. Andersson, K. K., Froland, W. A., Lee, S.-K., and Lipscomb, J. D. (1991) *New J. Chem.* *15*, 411-415.
28. Jiang, Y., Wilkins, P. C., and Dalton, H. (1993) *Biochim. Biophys. Acta* *1163*, 105-112.
29. Brazeau, B. J., Austin, R. N., Tarr, C., Groves, J. T., and Lipscomb, J. D. (2001) *J. Am. Chem. Soc.* *123*, 11831-11837.
30. Choi, S.-Y., Eaton, P. E., Kopp, D. A., Lippard, S. J., Newcomb, M., and Shen, R. (1999) *J. Am. Chem. Soc.* *121*, 12198-12199.
31. Newcomb, M., Shen, R., Lu, Y., Coon, M. J., Hollenberg, P. F., Kopp, D. A., and Lippard, S. J. (2002) *J. Am. Chem. Soc.* *124*, 6879-6886.
32. Ruzicka, F., Huang, D.-S., Donnelly, M. I., and Frey, P. A. (1990) *Biochemistry* *29*, 1696-1700.
33. Coufal, D. E., Blazyk, J. L., Whittington, D. A., Wu, W. W., Rosenzweig, A. C., and Lippard, S. J. (2000) *Eur. J. Biochem.* *267*, 2174-2185.
34. Kopp, D. A., Gassner, G. T., Blazyk, J. L., and Lippard, S. J. (2001) *Biochemistry* *40*, 14932-14941.
35. Beauvais, L. G., and Lippard, S. J. (2005) *Biochem. Biophys. Res. Commun.* *338*, 262-266.

36. Muthusamy, M., Ambundo, E. A., George, S. J., Lippard, S. J., and Thorneley, R. N. F. (2003) *J. Am. Chem. Soc.* *125*, 11150-11151.
37. Lee, S.-K., Nesheim, J. C., and Lipscomb, J. D. (1993) *J. Biol. Chem.* *268*, 21569-21577.
38. (1987) *CRC Handbook of Chemistry and Physics*, 68 ed., CRC Press, Inc., Boca Raton, FL.
39. Brazeau, B. J., and Lipscomb, J. D. (2003) *Biochemistry* *42*, 5618-5631.
40. Lippard, S. J. (2005) *Phil. Trans. R. Soc. A* *363*, 861-877.
41. Rosenzweig, A. C., Frederick, C. A., Lippard, S. J., and Nordlund, P. (1993) *Nature* *366*, 537-543.
42. Gherman, B. F., Lippard, S. J., and Friesner, R. A. (2005) *J. Am. Chem. Soc.* *127*, 1025-1037.
43. Zheng, H., and Lipscomb, J. D. (2006) *Biochemistry* *45*, 1685-1692.
44. Halle, L. F., Klein, F. S., and Beauchamp, J. L. (1984) *J. Am. Chem. Soc.* *106*, 2543-2549.
45. Cheng, J.-P., Handoo, K. L., and Parker, V. D. (1993) *J. Am. Chem. Soc.* *115*, 2655-2660.
46. Luo, Y.-R. (2007) *Comprehensive Handbook of Chemical Bond Energies*, CRC Press, Boca Raton, FL.
47. Gligorovski, S., and Herrmann, H. (2004) *Phys. Chem. Chem. Phys.* *6*, 4118-4126.
48. Anslyn, E. V., and Dougherty, D. A. (2006) *Modern Physical Organic Chemistry*, University Science Books, Sausalito, CA.

49. Gochel-Dupuis, M., Delwiche, J., Hubin-Franskin, M.-J., and Collin, J. E. (1992) *Chem. Phys. Lett.* *193*, 41-48.
50. Allam, S. H., Migahed, M. D., and El Khodary, A. (1981) *Int. J. Mass Spectrom. Ion Phys.* *39*, 117-122.
51. Sühnel, J., and Schowen, R. L. (1991) Theoretical Basis for Primary and Secondary Hydrogen Isotope Effects, in *Enzyme Mechanism from Isotope Effects* (Cook, P. F., Ed.), pp 3-36, CRC Press, Boca Raton, FL.
52. Pu, J., Gao, J., and Truhlar, D. J. (2006) *Chem. Rev.* *106*, 3140-3169.
53. Nesheim, J. C., and Lipscomb, J. D. (1996) *Biochemistry* *35*, 10240-10247.
54. Screttas, C. G. (1980) *J. Org. Chem.* *45*, 333-336.
55. Stahl, S. S., Francisco, W. A., Merckx, M., Klinman, J. P., and Lippard, S. J. (2001) *J. Biol. Chem.* *276*, 4549-4553.
56. Moran, S., Ellis Jr., H. B., DeFrees, D. J., McLean, A. D., and Ellison, G. B. (1987) *J. Am. Chem. Soc.* *109*, 5996-6003.
57. Hanzlik, R. P., and Shearer, G. O. (1975) *J. Am. Chem. Soc.* *97*, 5231-5233.
58. Kurtz, K. A., and Fitzpatrick, P. F. (1997) *J. Am. Chem. Soc.* *119*, 1155-1156.
59. Rossi, L., Feroci, M., and Inesi, A. (2005) *Mini-Rev. Org. Chem.* *2*, 79-90.
60. Jin, S., Bryson, T. A., and Dawson, J. H. (2004) *J. Biol. Inorg. Chem.* *9*, 644-653.
61. Jin, S., Makris, T. M., Bryson, T. A., Sligar, S. G., and Dawson, J. H. (2003) *J. Am. Chem. Soc.* *125*, 3406-3407.
62. Newcomb, M., Aebischer, D., Shen, R., Chandrasena, R. E. P., Hollenberg, P. F., and Coon, M. J. (2003) *J. Am. Chem. Soc.* *125*, 6064-6065.

63. Newcomb, M., Hollenberg, P. F., and Coon, M. J. (2003) *Arch. Biochem. Biophys.* 409, 72-79.
64. Sheng, X., Zhang, H., Hollenberg, P. F., and Newcomb, M. (2009) *Biochemistry* 48, 1620-1627.
65. Vatsis, K. P., and Coon, M. J. (2002) *Arch. Biochem. Biophys.* 397, 119-129.
66. Vaz, A. D. N., McGinnity, D. F., and Coon, M. J. (1998) *Proc. Natl. Acad. Sci. USA* 95, 3555-3560.
67. Vaz, A. D. N., Pernecky, S. J., Raner, G. M., and Coon, M. J. (1996) *Proc. Natl. Acad. Sci. USA* 93, 4644-4648.
68. Volz, T. J., Rock, D. A., and Jones, J. P. (2002) *J. Am. Chem. Soc.* 124, 9724-9725.

## Chapter 4

### Dioxygen Activation and the Multiple Roles of Component Proteins in Phenol

#### Hydroxylase from *Pseudomonas* sp. OX1\*

\* Mössbauer studies presented in this chapter were performed in collaboration with Dr. Viviana Izzo (Lippard Lab, MIT) and Dr. Sunil G. Naik and Prof. Boi Hahn Huynh (Emory University, Atlanta, GA).

Dr. Viviana Izzo developed the PHH, PHM, and PHP purification protocols and the PHM thermal reconstitution procedure presented in this chapter. Dr. Ioannis Papayannopoulos at the MIT Biopolymers

Facility performed ESI-MS experiments.

## INTRODUCTION

Bacterial multicomponent monooxygenases (BMMs) are remarkable enzymes that orchestrate a series of electron transfer and substrate activation events in order to prime dioxygen for donation of a single oxygen atom into a C—H or across a C=C bond (1, 2). Proteins belonging this family are subdivided into classes, soluble methane monooxygenases (sMMOs), phenol hydroxylases (PHs), alkene monooxygenases (AMOs), and four-component alkene/arene monooxygenase (TMOs), based on substrate preferences and sequence homology (3, 4). The ability of BMMs to generate potent oxidizing species without damaging their active sites or consuming electrons in a futile manner depends on the dynamic involvement of three or more protein components: a 200-255 kDa dimeric hydroxylase that houses two copies of a carboxylate-bridged diiron catalytic center; a 38-45 kDa reductase that accepts electrons from NADH and shuttles them through its flavin and [2Fe-2S] cluster cofactors into the hydroxylase diiron sites; and a 10-16 kDa regulatory protein that couples electron consumption to hydrocarbon oxidation (1, 2). Careful and timely regulation of the interactions between these proteins assures efficient catalysis.

A key step in BMM catalysis is the reductive activation of O<sub>2</sub> for incorporation into substrate. The most extensively studied BMM O<sub>2</sub> activation pathways are those of soluble methane monooxygenase (sMMO) from *Methylococcus capsulatus* (Bath) and from *Methylosinus trichosporium* OB3B. In these systems, reaction of a reduced hydroxylase with O<sub>2</sub> leads to the sequential generation of two peroxodiiron(III) units, P\* (5, 6) and H<sub>peroxo</sub> in the presence of the regulatory protein (7-9). Subsequent transfer of one or two protons (6, 10) leads to rearrangement of the iron-oxygen core and formation of Q, a

di( $\mu$ -oxo)diiron(IV) species responsible for methane oxidation (8, 11-13). In the absence of methane and other substrates, Q decays slowly to  $H_{ox}$  via a pathway that is not fully understood (6).

The  $O_2$  activation pathway in toluene/*o*-xylene monooxygenase (ToMO) from *Pseudomonas* sp. OX1 was also recently delineated (14). Upon reaction of reduced ToMO hydroxylase (ToMOH) with  $O_2$  in the presence of the regulatory protein ToMOD, a diiron(III) intermediate with no obvious absorption features rapidly formed and subsequently decayed to the diiron(III) protein resting state without progressing through a stable, high-valent Q-like intermediate (14). The diiron(III) intermediate, having Mössbauer parameters  $\delta = 0.55 \pm 0.02$  mm/s and  $\Delta E_Q = 0.67 \pm 0.03$  mm/s, could be a peroxide or hydroperoxide unit (15). The spectroscopic characteristics of this species are unusual for a peroxodiiron(III) center, however, which typically exhibit  $\lambda_{max} > 650$  nm,  $\delta > 0.6$  mm/s and  $\Delta E_Q > 1.0$  mm/s. These notable differences suggest that the ToMO intermediate must deviate in geometry and/or protonation state from well characterized diiron(III) peroxide species, but its exact nature remains to be fully elucidated. This species is the active oxidant in the ToMO system, however, because rapid freeze quench (RFQ) double-mixing Mössbauer spectroscopic experiments revealed that its rate of decay is accelerated in the presence of the substrate phenol (15).

The function of the regulatory proteins of BMMs has been a source of ongoing investigation. These proteins have been implicated in the dioxygen activation, substrate entry, proton transfer, and electron transfer phases of the hydrocarbon oxidation catalytic cycles (16). A variety of studies have demonstrated that the regulatory proteins effect catalysis through many different processes. They increase the rates and electron coupling



efficiencies of the steady-state reactions (17-20), modulate the redox potentials of the hydroxylase diiron site (21, 22), accelerate the rates of electron transfer between the reductase and the hydroxylase (18, 19), perturb the spectroscopic features of the hydroxylase active site (17, 23-27), rearrange the hydroxylase iron ligands (26, 28, 29), promote conformational changes in the hydroxylase (19, 26, 28, 30, 31), gate substrate and solvent access to the hydroxylase diiron centers (28, 32), alter the substrate specificity and regioselectivity of hydroxylation reactions (25, 32-34), promote the binding of an active site water molecule invoked in proton transfer (28), modulate the kinetics of the reaction of reduced hydroxylase with O<sub>2</sub> (35), and prevent inopportune reduction of the oxygenated iron intermediates of the hydroxylase by untimely electron transfer (28-30, 36). At high concentrations, the regulatory proteins inhibit steady state activity (17, 18, 37). The ability of these proteins to influence so many distinct processes of catalysis clearly indicates that the mechanisms by which they impart their functions are complex. These mechanisms and the dynamics of the protein-protein interactions during the phases of catalysis are not well understood, however.

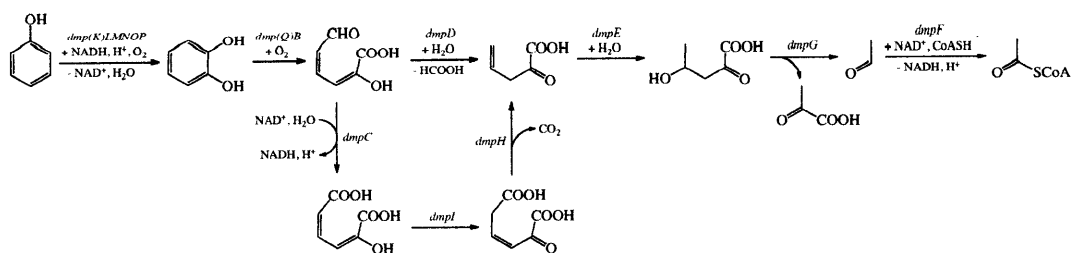


**Figure 4.1.** Schematic representation of phenol metabolism by *Pseudomonas* sp. CF600, an organism related to *Pseudomonas* sp. OX1. The hydrolytic (*dmpD*-encoded) and 4-oxalocrotonate (*dmpCIH*-encoded) pathways represent divergent branches of the *meta*-cleavage pathway beginning with the ring-cleavage reaction catalyzed by catechol 2,3-dioxygenase (encoded by *dmp(Q)B*). Phenol metabolism by *Pseudomonas* sp. OX1 is expected to occur via a similar pathway.

The reductases in BMM systems provide electrons to the hydroxylase diiron center (1, 29, 35). However, they also affect catalysis in a complicated, versatile manner, tuning the redox potentials of the hydroxylase diiron site (21, 36), altering the kinetics of the reaction with O<sub>2</sub> (36), promoting conformational changes in the hydroxylases (30, 31), and influencing how the hydroxylases interact with substrates (25). These observations suggest that the reductase proteins regulate catalysis in a complex fashion in addition to providing electrons for the reductive activation of dioxygen.

Phenol hydroxylase is the second enzyme in a pathway that allows *Pseudomonas* sp. OX1 to metabolize aromatics as its sole carbon source (Figure 4.1). Enzymes involved in the upstream segment of this pathway, ToMO and PH, destabilize aromatic molecules through oxidation reactions. Downstream ‘*meta*-cleavage’ enzymes then cleave the destabilized aromatic ring and process the resulting products for entry into major metabolic pathways (37, 38). PH is characterized by broad substrate specificity and oxidizes a variety of aromatic hydrocarbons in addition to its native substrate phenol, including *o*-, *m*-, and *p*-cresol, several dimethylphenols, and benzene (37, 39). The hydroxylase is believed to harbor a dinuclear iron center and can be expressed recombinantly in *E. coli* in the presence of iron to form active enzyme that catalyzes the oxidation of phenol to catechol (37, 39).

In this chapter, we explore O<sub>2</sub> activation and the functions of the auxiliary proteins in phenol hydroxylase from *Pseudomonas* sp. OX1. Methods of obtaining recombinant hydroxylase with optimal iron content of four irons per protein dimer and high specific activity relative to that of *Pseudomonas* sp. CF600 phenol hydroxylase expressed and purified from the native organism are presented. Mössbauer studies probing the dinuclear

iron units of recombinant hydroxylase show that this protein is composed of two distinct dinuclear iron cluster forms, similar to native *Pseudomonas sp.* CF600 phenol hydroxylase. The reaction of reduced PH hydroxylase (PHH) with O<sub>2</sub> in the presence of the regulatory protein PHM reveals a transient diiron(III) species with parameters similar to those of the intermediate characterized in ToMOH. Steady state experiments demonstrate that H<sub>2</sub>O<sub>2</sub> is formed by the complete enzyme system in the absence of hydrocarbon substrate. A series of studies employing different mixtures of protein components, performed in the presence of the *E. coli* catalase inhibitor NH<sub>2</sub>OH to eliminate trace catalase impurity activity, reveal that the H<sub>2</sub>O<sub>2</sub> generated derives from the reductase and the hydroxylase proteins. The latter results suggest that the hydroxylase intermediate identified in Mössbauer experiments is a peroxodiiron(III) unit. Single turnover assays indicate that the reductase protein, PHP, is important not only for electron transfer but also for hydrocarbon oxidation. Studies of H<sub>2</sub>O<sub>2</sub> generation by the enzyme in the absence of the regulatory protein, PHM, show that this protein promotes the accumulation of the oxygenated iron intermediates responsible for hydrocarbon oxidation.

## **MATERIALS AND METHODS**

*General Considerations.* Distilled water was deionized with a Milli-Q filtering system. 4-20% Tris-HCl gradient gels were purchased from Bio-Rad Laboratories. Phenol and catechol were purified by vacuum-sublimation prior to use. Other reagents were purchased from Sigma Aldrich and used as received unless otherwise noted.

**Table 4.1.** PHH Expression Plasmids<sup>a</sup>

Plasmid	<i>phk</i>	<i>phl</i>	<i>phm</i>	<i>phn</i>	<i>pho</i>	<i>php</i>
pGEM3Z/PHLMNOP		X	X	X	X	X
pGEM3Z/PHKLMNOP	X	X	X	X	X	X
pGEM3Z/PHΔP	X	X		X	X	X
pGEM3Z/PHΔMΔP	X	X		X	X	

<sup>a</sup>X denotes inclusion of the gene in the plasmid

*Protein Expression and Purification.* Constructs used to express PHH in *E. coli* varied among the experiments presented within this chapter and are therefore explained in detail in the paragraphs that follow and also summarized in Table 4.1. PHH used for RFQ Mössbauer kinetic experiments was expressed from a vector containing the *phl*, *phm*, *phn*, *pho* and *php* genes encoding the  $\alpha$  (*phn*)-,  $\beta$  (*phl*)-, and  $\gamma$  (*pho*)- subunits of PHH, PHM (*phm*), and PHP (*php*) (pGEM3Z/PHLMNOP). Protein used in all biochemical experiments was expressed from a vector containing the *phk*, *phl*, *phn*, and *pho* genes (pGEM3Z/PHΔMΔP), where *phk* encodes a small protein of unknown function located upstream of the PH operon. PHH used in certain activity assays was purified from the pGEM3Z/PHΔM vector encoding the *phk*, *phl*, *phn*, and *pho*, and *php* genes or the pGEM3Z/PHKLMNOP construct encoding the *phk*, *phl*, *phm*, *phn*, *pho* and *php* genes.

PHH employed in all experiments was overexpressed in *E. coli*. The same expression procedure was used for all four plasmid constructs. PHH starter cultures were grown in Luria-Bertini (LB) media supplemented with 100  $\mu$ g/mL of Ampicillin. Single colonies from freshly transformed *E. coli* st. JM109 cells (Stratagene) were inoculated into 100 mL of LB-Amp and grown for 14-16 hours at 37 °C. These cultures were used to inoculate 12 L of media and were then grown at 37 °C and 215 rpm until the  $OD_{600}$

reached 0.7. Expression of PHH was induced by the addition of isopropylthiogalactopyranoside (IPTG) to a final concentration of 200  $\mu\text{M}$ . To maximize iron incorporation in recombinant PHH,  $\text{Fe}(\text{NH}_4)_2(\text{SO}_4)_2 \cdot 6\text{H}_2\text{O}$  was added to a final concentration of 400  $\mu\text{M}$  at induction. Growth was continued for 6 h at 37 °C. Cells were collected by centrifugation at 4 °C and the cell paste was drop-frozen in liquid nitrogen and stored at -80 °C until further use.

PHH used in RFQ-Mössbauer experiments was overexpressed in *E. coli* from the pGEM3Z/PHLMNOP plasmid. Cells were grown in sterile minimal media containing 10 g/L Bactotryptone (BD Biosciences), 5 g/L NaCl, 0.1 g/L thiamine hydrochloride, 5 g/L glucose monohydrate, 1 g/L casamino acids, and 100  $\mu\text{g}/\text{mL}$  ampicillin.  $^{57}\text{Fe}$  metal foil (95%, Cambridge Isotope Laboratories) was dissolved in ultrapure, conc. (37%) HCl and the pH of the resulting orange  $^{57}\text{FeCl}_3$  solution was neutralized by adding a small volume of buffered media. This mixture was added to the media at a final concentration of 300-400  $\mu\text{M}$   $^{57}\text{Fe}$  before inoculation. Cells were grown using the method employed for natural abundance iron conditions (vide supra).

PHH used in all other Mössbauer experiments was overexpressed in *E. coli* from the pGEM3Z/PH $\Delta$ M $\Delta$ P plasmid. This construct did not express well under the conditions used to obtain  $^{57}\text{Fe}$ -enriched PHH from the pGEM3Z/PHLMNOP plasmid, and expression tests were therefore conducted in M9 minimal media. 10X Minimal M9 salts media was prepared by dissolving 60 g  $\text{Na}_2\text{HPO}_4$ , 30 g  $\text{KH}_2\text{PO}_4$ , 10 g  $\text{NH}_4\text{Cl}$ , and 5 g NaCl in 1L ddH<sub>2</sub>O. Following sterilization, M9 media was supplemented with 2 mM  $\text{MgSO}_4$ , 100  $\mu\text{M}$   $\text{CaCl}_2$ , 1 mM thiamine hydrochloride, 4 g/L glucose monohydrate, and 4 g/L casamino acids. Because protein did not express well in M9 media as prepared, five

different media additives were tested for expression enhancement: 300 mM NaCl, 10 g/L glucose, 1 % glycerol, 25, 50, or 200  $\mu\text{M}$   $\text{ZnSO}_4$ , and 500  $\mu\text{L}$  of a trace element solution containing 672  $\mu\text{M}$   $\text{Na}_2\text{EDTA}$ , 1.4 mM  $\text{ZnSO}_4 \cdot 7\text{H}_2\text{O}$ , 100  $\mu\text{M}$   $\text{MnCl}_2 \cdot 4\text{H}_2\text{O}$ , 160  $\mu\text{M}$   $\text{H}_3\text{BO}_3$ , 210  $\mu\text{M}$   $\text{CoCl}_2 \cdot 6\text{H}_2\text{O}$ , 800  $\mu\text{M}$   $\text{CuCl}_2 \cdot 2\text{H}_2\text{O}$ , 42  $\mu\text{M}$   $\text{NiCl}_2 \cdot 6\text{H}_2\text{O}$ , and 12.4  $\mu\text{M}$   $\text{Na}_2\text{MoO}_4 \cdot 2\text{H}_2\text{O}$  in 500  $\mu\text{L}$  ddH<sub>2</sub>O. Expression conditions were the same as those detailed for PHH grown with natural abundance iron (vide supra).

SDS-PAGE gel electrophoresis was used to analyze the contents of the supernatant and cell pellet from all expression trials. For comparative expression gels, a small amount of cell paste was thawed in 6 mL 25 mM MOPS pH 7.0. The  $OD_{600}$  values of the resuspended cell solutions were monitored using a Hewlett Packard Model 8453 diode array spectrophotometer, and all samples were diluted to the same  $OD_{600}$  (5 – 8 absorbance units) in 8 mL buffer. Cells were lysed by sonication in an ice-water bath using a Branson sonifier in 15 s pulses for 6 min at 40% output. Following cell lysis, 100  $\mu\text{L}$  of each sample was removed, placed in an Eppendorf tube, and centrifuged for 10 min at 13,500 rpm. The supernatant was extracted and the cell pellet was resuspended in buffer containing sodium dodecyl sulfate (SDS). Samples were loaded onto a 4-20% Tris-glycine (BioRad) gel.

PHH expressed from all plasmids under all conditions was purified using the same procedure. Cell paste (~24 g) was sonicated on ice using a Branson sonifier in 30 s pulses for 12 min at 40% output in ~100 mL of 25 mM MOPS, pH 7.0, 2 mM L-cysteine, and 10% glycerol (Buffer A) containing 100 U of DNaseI (New England Biolabs). Insoluble material was removed by ultracentrifugation at 183,000 x g for 60 min, and the supernatant was filtered through a 0.45  $\mu\text{m}$  membrane and loaded onto a Q Sepharose FF

column (100 mL) equilibrated in Buffer A. The column was washed with 200 mL of Buffer A, after which bound proteins were eluted in 1 L by running a linear gradient from 0.1 to 0.45 M NaCl at 1.25 mL/min. Fractions containing PHH were identified by SDS-PAGE analysis. These fractions were pooled and concentrated to ~7 mL using a 30K MWCO Amicon centrifugal concentrator (Millipore, Inc.). The resulting protein was loaded onto a Superdex S300 column equilibrated in Buffer A containing 0.2 M NaCl (Buffer B). Proteins were eluted by running Buffer B over the column at a flow rate of 1 mL/min.

Plasmids containing the genes for PHM (pET22b(+)/PHM) and PHP (pET22b(+)/PHP) were supplied by Prof. Alberto Di Donato (Università di Napoli Federico II, Naples, Italy). PHP was expressed as described previously, except that  $\text{Fe}(\text{NH}_4)_2(\text{SO}_4)_2$  and IPTG were added to final concentrations of 200  $\mu\text{M}$  and 75  $\mu\text{M}$ , respectively, at induction (37). The resulting cell paste (~20 g) was sonicated on ice using a Branson sonifier in 30 s pulses for 12 min at 40% output in ~100 mL of 20 mM sodium phosphate pH 7.0, 1 mM DTT, and 10% glycerol (Buffer A) containing 100 U of DNaseI (New England Biolabs). Insoluble material was removed by ultracentrifugation at 183,000  $\times g$  for 60 min, and the supernatant was filtered through a 0.45  $\mu\text{m}$  membrane and loaded onto a Q Sepharose FF column (100 mL) equilibrated in Buffer A. The column was washed with 200 mL of Buffer A, after which bound proteins were eluted in 1 L by running a linear gradient from 0.08 to 1.0 M NaCl at 1.5 mL/min. Fractions containing PHP eluted at ~350 mM NaCl and were identified by SDS-PAGE analysis and by absorbance at 271, 340, and 459 nm. These fractions were pooled and concentrated to ~7 mL using a 30K MWCO Amicon centrifugal concentrator (Millipore). The resulting

protein was loaded onto a Superdex S75 column equilibrated with Buffer A containing 0.2 M NaCl (Buffer B). Proteins were eluted by running Buffer B over the column at a flow rate of 1 mL/min. Fractions displaying an  $A_{271}:A_{459}$  ratio of 2.5 to 3 and an  $A_{340}:A_{459}$  ratio slightly lower than 1 and appearing pure by SDS-PAGE were pooled, concentrated, flash-frozen in liquid nitrogen, and stored at  $-80\text{ }^{\circ}\text{C}$  until further use.

PHM was expressed as described previously (37). The resulting cell paste (~30 g) was sonicated on ice using a Branson sonifier in 30 s pulses for 12 min at 40% output in ~100 mL of 25 mM MOPS pH 7.0, 10% glycerol (Buffer C) containing 100 U of DNaseI (New England Biolabs). Insoluble material was removed by ultracentrifugation at  $183,000 \times g$  for 60 min and the supernatant was filtered through a  $0.45\text{ }\mu\text{m}$  membrane and loaded onto a Q Sepharose FF column (100 mL) equilibrated in Buffer C. The column was washed with 200 mL of Buffer C, after which bound proteins were eluted in 1 L by running a linear gradient from 0 to 0.5 M NaCl at 1.5 mL/min. PHM eluted in two peaks centered around at ~340 and ~400 mM NaCl that were identified by monitoring the absorbance at 280 nm and by SDS-PAGE and native gel electrophoresis. The contents of fractions corresponding to the first, the second, or both peaks were pooled and concentrated to ~7 mL using a 3K MWCO Amicon centrifugal concentrator (Millipore). The resulting protein was loaded onto a Superdex S75 column equilibrated with Buffer C containing 0.2 M NaCl (Buffer D). Proteins were eluted by running Buffer D over the column at a flow rate of 1 mL/min. PHM eluted in one broad peak with a shoulder. Fractions appearing pure by SDS-PAGE were pooled and concentrated. Pure PHM was refolded by thermally denaturing the protein and then letting it refold by slow cooling to room temperature. PHM was diluted to  $75\text{ }\mu\text{M}$  in 25 mM MOPS, pH 7.0, containing 10%



glycerol. The protein was heated to 70 °C over 30 min in a water bath, then the bath was removed from the heating block and allowed to cool until it reached room temperature. The resulting protein was analyzed by native gel electrophoresis, flash-frozen in liquid nitrogen, and stored at -80 °C until further use.

Specific activity of PH was measured using a coupled assay employing catechol 2,3-dioxygenase and catechol as a substrate (40). Hydroxylase iron content was determined by the ferrozine colorimetric assay (41). Approximate extinction coefficients used to quantify the hydroxylase, regulatory protein, and reductase were calculated from primary amino acid sequences were 600,000 M<sup>-1</sup> cm<sup>-1</sup>, 12,000 M<sup>-1</sup> cm<sup>-1</sup>, and 21,000 M<sup>-1</sup> cm<sup>-1</sup> at 280 nm. The use of approximate extinction coefficients likely represents a source of error in all biochemical experiments.

*Characterization of PHM.* Electrospray ionization mass spectrometry (ESI-MS) analysis of PHM was conducted at the Proteomics Core Facility of the Koch Institute (MIT). Analytical gel filtration chromatography was carried out using a Shodex analytical sizing column. A 20 mL portion of 150 μM PHM prepared in 25 mM MOPS, pH 7.0 containing 0.2 M NaCl, was injected onto the column. The sample was run at 1 mL/min in 20 mM Tris, pH 7.5 containing 0.2 M NaCl, 0.25 mM TCEP (*tris*(2-carboxyethyl)phosphine), and 3 mM NaN<sub>3</sub>. Elution times were compared to those of a BioRad gel filtration standard mixture.

*Stopped-Flow Optical Spectroscopy.* Single-turnover kinetic experiments were performed on a Hi-Tech Scientific (Salisbury, UK) SF-61 DX2 spectrophotometer employing a photomultiplier tube (PMT) for single wavelength data collection or a diode array detector for multiwavelength detection. A solution of 225 μM PHH and 2 equiv

PHM was prepared in 25 mM MOPS, pH 7.0, in a glass vial. The vial was capped with a septum and the solution was made anaerobic by 12 cycles of evacuation/backfill with N<sub>2</sub> before it was brought into a Vacuum Atmospheres anaerobic chamber. In the chamber, hydroxylase was reduced with excess sodium dithionite using stoichiometric methyl viologen as a redox mediator. The solution was allowed to incubate for 45 min before dialyzing twice against buffer for 1 h each. Following dialysis, protein was removed from the glove box in a glass tonometer. Prior to use, the stopped-flow instrument was made anaerobic by flushing exhaustively with buffer containing ~5 mM sodium dithionite. The instrument temperature was maintained with a circulating water bath. Data collection and analysis were performed by using KinetAsyst 3 (Hi-Tech Scientific) and Kaleidagraph v 3.51 (Synergy Software) software.

*Mössbauer Spectroscopy.* 4.2 K Mössbauer spectroscopy and rapid freeze quench (RFQ) sample preparations were performed in the laboratory of Prof. Boi Hanh Huynh (Emory University, Atlanta, GA). A sample of <sup>57</sup>Fe-enriched PHH having a specific activity of 204 ± 11 mU/mg and an iron content of 3.6 ± 0.1 Fe/dimer was reduced and dialyzed as described for stopped-flow experiments. Single-mixing RFQ experiments were carried out by rapidly mixing a solution of 450 μM reduced PHH (PHH<sub>red</sub>) and 2 equiv PHM with an equal volume of O<sub>2</sub>-saturated 20 mM potassium phosphate buffer, pH 7.0, at 4 °C. After specified time delays, the reaction mixtures were quenched in isopentane at -150 °C. Samples were packed into Mössbauer cups and stored in liquid nitrogen. Mössbauer measurements were carried out at 4.2 K with an applied magnetic field parallel to the γ-irradiation source using spectrometers described previously (42). Analyses of the Mössbauer spectra were performed with WMOSS (WEB Research) (43).

The zero velocity refers to the centroid of a room-temperature spectrum of metallic Fe foil.

*Single Turnover Assays.* For all assays, the appropriate protein mixture prepared in 400  $\mu\text{L}$  of 0.1 M Tris-HCl, pH 7.5, was reduced in an anaerobic chamber by addition of a stoichiometric quantity of sodium dithionite or on the benchtop by addition of stoichiometric NADH. Accurate  $\text{Na}_2\text{S}_2\text{O}_4$  concentrations were determined by anaerobic titration into  $\text{K}_3[\text{Fe}(\text{CN})_6]$  (44). Reaction solutions contained 100  $\mu\text{M}$  PHH, 0 or 600  $\mu\text{M}$  PHM, 10 or 200  $\mu\text{M}$  PHP, 5 mM phenol, and 200  $\mu\text{M}$  NADH or  $\text{Na}_2\text{S}_2\text{O}_4$ . For studies investigating the influence of the appropriate electron transfer protein on  $\text{O}_2$  activation, a solution containing hydroxylase, phenol, and regulatory protein if employed was pre-reduced with stoichiometric  $\text{Na}_2\text{S}_2\text{O}_4$  for 20 min before the addition of oxidized PHP. Following protein reduction and removal from the glove box, 100  $\mu\text{L}$  of  $\text{O}_2$ -saturated buffer was added to each solution. Reaction mixtures were incubated for 20 min at 25  $^\circ\text{C}$ , after which they were quenched by addition of 100  $\mu\text{L}$  of 0.4 M TCA. Precipitated protein was removed by centrifugation at 17,110  $\times g$  for 10 min and the supernatant was assayed for catechol content by HPLC.

HPLC experiments were performed on a Vydac  $\text{C}_{18}$  reversed-phase protein and peptide column thermostatted at 25  $^\circ\text{C}$ . Absorbance of the eluent was monitored continuously at 280 and 274 nm. The separation program utilized a 1 mL/min flow rate with a step gradient of a two-solvent system consisting of 0.1% HCOOH in ddH<sub>2</sub>O (solvent A) and 0.1% HCOOH in methanol (solvent B). HPLC separations first employed an isocratic elution with 2% B for 10 min that was followed by a linear gradient from 2% to 98% B over 10 min. The column was then flushed with 98% B for 10 min followed by a linear

gradient from 98% to 2% B. Finally, 2% B was flushed over the column for 15 min to prime it for the next run. A 100  $\mu$ L aliquot of sample was injected on the column for each run. Under these conditions, phenol and catechol eluted at 18.5 and 10.1 min, respectively. Peaks corresponding to phenol or catechol were integrated and the phenol or catechol content was measured by comparison to a standard curve prepared in the same manner as the reaction solutions. For certain experiments, standards of vacuum-sublimed resorcinol and hydroquinone were also analyzed. These compounds eluted at 8.6 and 5.7 min, respectively. All experiments were run in triplicate using enzymes prepared from different batches of cell paste. Standard curves were run each time the assay was performed.

*Peroxide Shunt Assays.* The ability of hydrogen peroxide to activate oxidized PHH for catalysis was monitored by HPLC. In these experiments, reaction solutions contained 5  $\mu$ M PHH, 0 or 30  $\mu$ M PHM, 10  $\mu$ M PHP, and 1 mM phenol in 500  $\mu$ L of 0.1 M Tris-HCl, pH 7.5. Reactions were initiated by the addition of 5 mM  $H_2O_2$  and were incubated at  $25.0 \pm 0.1$  °C. Reactions were quenched after specified times by the addition of 100  $\mu$ L of 0.7 M TCA. Precipitated protein was removed by centrifugation at  $17110 \times g$  for 5 min. Following centrifugation, 500  $\mu$ L of supernatant was transferred to an HPLC vial and analyzed for catechol content as described above. A peak at 240 nm corresponding to  $H_2O_2$  was integrated and the  $H_2O_2$  content was measured by comparison to a standard curve prepared in the same manner as the reaction solutions.

*$H_2O_2$  Production Assays.*  $H_2O_2$  was detected using a modified version of a discontinuous colorimetric assay employing KSCN and  $Fe(NH_4)_2(SO_4)_2$  (45). This procedure had to be changed because NADH was found to interfere with the assay, and

therefore a step was added to inactivate the reducing agent prior to assaying the reaction mixtures. Reaction solutions contained 1  $\mu\text{M}$  PHH, 0 or 6  $\mu\text{M}$  PHM, 0.1 or 2  $\mu\text{M}$  PHP, and 200  $\mu\text{M}$  NADH in 500  $\mu\text{L}$  of 0.1 M Tris-HCl, pH 7.5. Reaction mixtures also contained 10  $\mu\text{M}$  of the *E. coli* catalase inhibitor  $\text{NH}_2\text{OH}$  (46) to eliminate trace catalase impurity activity, which has been shown to affect previous BMM  $\text{H}_2\text{O}_2$  assays performed with recombinant proteins (20). For reactions employing substrate, the concentration of phenol was 5 mM. All reactions were performed at  $25.0 \pm 0.1$   $^\circ\text{C}$  or  $4.0 \pm 0.5$   $^\circ\text{C}$ . Reactions were initiated by the addition NADH and were quenched after a specified reaction time by the addition of 100  $\mu\text{L}$  of 0.4 M TCA. To inactivate unconsumed NADH, acid-quenched reaction mixtures were placed in a water bath at 90  $^\circ\text{C}$  for 15 min, then removed and allowed to cool to room temperature for 45 min prior to separation of the protein precipitate by centrifugation at 17,110 x g for 5 min. Following centrifugation, 500  $\mu\text{L}$  of supernatant was transferred to a fresh Eppendorf tube. A 200  $\mu\text{L}$  portion of 10 mM  $\text{Fe}(\text{NH}_4)_2(\text{SO}_4)_2 \cdot 6\text{H}_2\text{O}$  prepared in dd $\text{H}_2\text{O}$  and 100  $\mu\text{L}$  of 2.5 M KSCN prepared in dd $\text{H}_2\text{O}$  was added to each Eppendorf tube. The reaction mixtures were stirred and allowed to stand for 5 min before their absorption at 480 nm was monitored. Solutions of  $\text{H}_2\text{O}_2$  in buffer were treated in the same manner as enzyme reactions in order to generate a standard curve. For the standards, the concentration of a freshly prepared  $\text{H}_2\text{O}_2$  stock solution was determined by measuring its absorbance at 240 nm ( $\epsilon_{240} = 43.6 \text{ M}^{-1} \text{ cm}^{-1}$ ) (47). Included in the preparation of standard curves were 10  $\mu\text{M}$   $\text{NH}_2\text{OH}$  and 200  $\mu\text{M}$  NADH. Data displaying hyperbolic  $\text{H}_2\text{O}_2$  generation kinetics were fit to the exponential growth model  $y = A \cdot \exp(-kt) + B$  to obtain the first-order rate constant for  $\text{H}_2\text{O}_2$  production.

*H<sub>2</sub>O<sub>2</sub> and NH<sub>2</sub>OH Inactivation Assays.* Two methods were used to monitor inactivation of PH by H<sub>2</sub>O<sub>2</sub>. In the first, reaction solutions containing 0.5 μM PHH, 3 μM PHM, and 1 μM PHP in 500 μL of 0.1 M Tris-HCl, pH 7.5 were incubated with 0 or 50 μM H<sub>2</sub>O<sub>2</sub> and 1 mM phenol for 20 min. Subsequently, 1 mM NADH was added to initiate the hydrocarbon oxidation reaction. These reactions were quenched after a specified time delay by the addition of 100 μL of 0.4 M TCA. In the second method, reaction solutions containing 1 μM PHH, 6 μM PHM, and 2 μM PHP in 500 μL of 0.1 M Tris-HCl, pH 7.5 were incubated with 5 mM NADH for a specified time period, after which phenol was added to a final concentration of 5 mM. Reactions were allowed to proceed for 20 min and then were quenched by the addition of 100 μL of 0.4 M TCA. For both methods, precipitated protein was removed by centrifugation at 17,110 x g for 10 min. Following centrifugation, 400 μL of supernatant was transferred to an HPLC vial and the samples were assayed for catechol content by HPLC as described above. For the first method, activity was assessed by plotting the amount of catechol formed versus time incubated with NADH and fitting the data to the linear equation  $y = kx + b$ . For the second method, data were plotted as the percentage of the amount of catechol formed in experiments in which NADH and phenol were added simultaneously (t = 0 min) versus the time that the reaction mixture was incubated with NADH before addition of phenol.

To determine whether addition of the *E. coli* catalase inhibitor NH<sub>2</sub>OH affects enzyme activity, HPLC-based activity assays were performed in its presence and absence. Reaction solutions contained 2 μM PHH, 12 μM PHM, 4 μM PHP, 1 mM phenol, and 0 or 20 μM NH<sub>2</sub>OH in 500 μL of 0.1 M Tris-HCl, pH 7.5. Aliquots of 350 μM NADH were added to initiate hydrocarbon oxidation. Reactions were quenched after 2 or 10 min

by addition of 100  $\mu\text{L}$  0.4 M TCA, and precipitated protein was removed by centrifugation at 17,110 x g for 10 min. Following centrifugation the samples were assayed for catechol content by HPLC as described above.

*H<sub>2</sub>O<sub>2</sub> Consumption Assays.* H<sub>2</sub>O<sub>2</sub> consumption was detected using the discontinuous colorimetric assay described above without the NADH inactivation step. Reaction mixtures contained 0 or 1  $\mu\text{M}$  PHH, 0 or 6  $\mu\text{M}$  PHM, 2  $\mu\text{M}$  PHP, 10  $\mu\text{M}$  of NH<sub>2</sub>OH and 1 mM phenol in 500  $\mu\text{L}$  of 0.1 M Tris-HCl, pH 7.5. Reactions were initiated by addition of 10 or 50  $\mu\text{M}$  H<sub>2</sub>O<sub>2</sub> and were quenched after specified reaction times with 100  $\mu\text{L}$  of 0.4 M TCA. Precipitated protein was removed by centrifugation at 17110 x g for 5 min. Following centrifugation, 500  $\mu\text{L}$  of supernatant was transferred to a fresh Eppendorf tube, and the reaction mixtures were assayed for H<sub>2</sub>O<sub>2</sub> content as described above.

*NADH Consumption Assays.* NADH consumption was monitored continuously by absorbance at 340 nm ( $\epsilon_{340} = 6220 \text{ M}^{-1} \text{ cm}^{-1}$ ). Reaction mixtures contained 0 or 1  $\mu\text{M}$  PHH, 0 or 6  $\mu\text{M}$  PHM, 0.1 or 2  $\mu\text{M}$  PHP, and 200  $\mu\text{M}$  NADH in 600  $\mu\text{L}$  of 0.1 M Tris-HCl, pH 7.5. For reactions containing substrate, the concentration of phenol was 5 mM. All reactions were initiated by addition of PHP. Reactions were thermostatted at  $25.0 \pm 0.1$  °C using a circulating water bath. Data were analyzed by fitting the initial time points to the linear function  $y = kx + b$ .

## RESULTS

Phenol hydroxylase from *Pseudomonas* sp. OX1 is a BMM responsible for catalyzing the first step in the metabolism of phenol and other aromatics that can serve as the sole

**Table 4.2.** Specific Activity and Iron Contents of Purified PHH

Expression Plasmid	Q Sepharose FF Peak	Specific Activity <sup>a</sup> (mU/mg)	Iron Content (Fe/dimer)
pGEM3Z/PHLMNOP	2	nd <sup>b</sup>	nd <sup>b</sup>
	3	204 ± 11	3.6 ± 0.1
pGEM3Z/PHKLMNOP	1	9 ± 1	0.44 ± 0.04
	2	54 ± 6	2.20 ± 0.02
	3	40 ± 3	2.95 ± 0.08
pGEM3Z/PHΔP	1	291 ± 18	2.28 ± 0.01
	2	695 ± 21	3.66 ± 0.03
	3	208 ± 4	3.92 ± 0.04
pGEM3Z/PHΔMΔP	1 (shoulder)	nd <sup>b</sup>	nd <sup>b</sup>
	2	1203-1590	4.0 – 4.5

<sup>a</sup>For all specific activity measurements, 2 equiv of recombinant PHM was added. <sup>b</sup>Not determined.

source of carbon and energy for the organism. To understand better the manner in which PH is able to utilize a carboxylate-bridged diiron center to hydroxylate phenol, we conducted a series of studies aimed at investigating O<sub>2</sub> activation and component interactions in this system.

*Expression, Purification, and Biochemical of PHH.* Initial studies of PH performed in our laboratory utilized hydroxylase expressed from a plasmid encoding the entire *Pseudomonas* sp. OX1 PH operon that includes genes for the hydroxylase, regulatory protein, and reductase. Protein obtained from this construct was characterized by low specific activity compared to that of native phenol hydroxylase purified from *Pseudomonas* sp. CF600 (56) and ToMOH when phenol was used as a substrate (48), however (Table 4.2). These findings led us to investigate whether there are additional components in the *Pseudomonas* sp. OX1 genome that might function to enhance the activity of phenol hydroxylase. A genetic analysis of the *ph* operon in *Pseudomonas* sp.



OX1 had previously revealed the presence of an open reading frame (ORF) located at the 5' end of the PH locus (39). The nucleotide sequence of this ORF shares high sequence identity (57%) with a gene located upstream of the phenol hydroxylase operon in *Pseudomonas* sp. CF600, *dmpK*. Although the gene product, DmpK, is not essential for in vitro hydroxylase activity (49), a *Pseudomonas* strain harboring the *dmp* operon together with the genes of those enzymes necessary to catabolize catechol grew on phenol only if the *dmpK* gene was also present (50). Phenol hydroxylase expressed recombinantly from a plasmid harboring *dmpK* in addition to the genes encoding the hydroxylase polypeptides yielded protein that was thirty times more active than that expressed from a vector in which *dmpK* was omitted (49).

To examine whether co-expression of *Pseudomonas* sp. OX1 phenol hydroxylase with the putative *phk* gene product yields higher activity protein, the gene was cloned upstream of the PH operon in a pGEM3Z vector and the resulting plasmid, pGEM3Z/PHKLMNOP, was transformed into *E. coli* JM109 cells. During protein

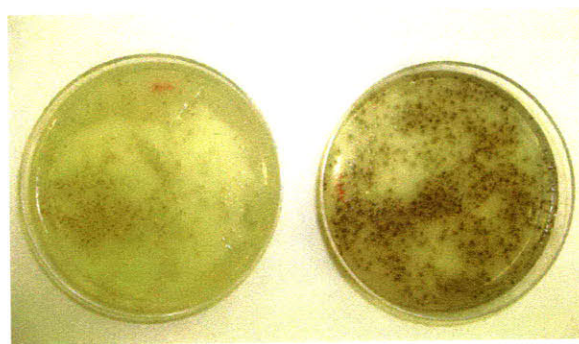


**Figure 4.2.** *E. coli* strain JM109 transformed with pGEM3Z/PHLMNOP (left) and pGEM3Z/PHKLMNOP (right).

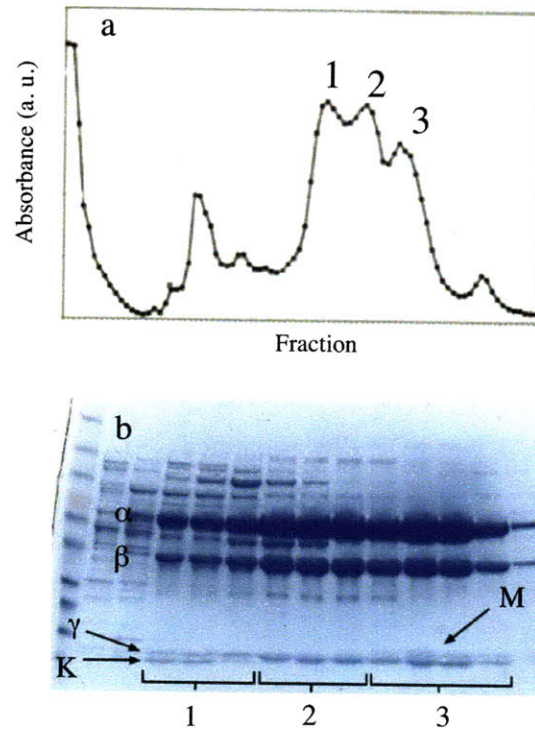


**Figure 4.3.** Representative Q Sepharose FF anion exchange trace for purification of PHH expressed from pGEM3Z/PHKLMNOP. (a) Trace of eluent monitored at 280 nm displays three overlapping peaks. (b) SDS-PAGE gel of the three peak contents shows that they all contain PHH. Peak 1 contains an additional band located below the  $\gamma$ -subunit (PHK), whereas peak 3 contains an additional band located above the  $\gamma$ -subunit (PHM).

expression, the growth media became dark brown, suggesting that simultaneous translation of all six polypeptide chains generated high-activity hydroxylase that was able to oxidize aromatics in the media. Similar results were obtained when the cells were grown on LB-agar plates even though protein expression had not been induced (Figure 4.2).

Purification of the pGEM3Z/PHKLMNOP cell lysate on a Q Sepharose FF anion exchange column yield three overlapping peaks that contained PHH (Figure 4.3). Peak 2 contained PHH and *E. coli* impurities, as assessed by SDS-PAGE gel electrophoresis. Similar analysis of peaks 1 and 3 revealed that these peaks contain PHH as well as additional proteins located below and above the  $\gamma$ -subunit of PHH on a denaturing gel, respectively. These bands are attributed to PHK and PHM, respectively, on the basis of expected molecular weights. These three peaks were purified separately over a S300 size exclusion column and assessed for specific activity and iron content (Table 4.2). Surprisingly, PHH purified from all three peaks displayed low activity despite the suggestion that aromatic compounds in the growth media were rapidly hydroxylated during protein expression. High catalytic turnover during protein expression may have damaged the enzyme by repeated cycles of oxidation and reduction. The iron content of the material in the three peaks was also lower than the optimal value of 4.0 irons per dimer, perhaps explaining the low activity.

To prevent protein inactivation by high turnover numbers during expression, a new plasmid was constructed in which the gene for the reductase component PHP was deleted (pGEM3Z/PHAP). *E. coli* strain JM109 cells expressing the vector were yellow in color, suggesting that the active complex is not formed in vivo. The cell lysate was purified on a

Q Sepharose column and the resulting trace revealed the presence of three peaks similar to those observed when PHH was expressed from the pGEM3Z/PHKLMNOP vector (data not shown). These three peaks, also containing the PHH/PHK complex, PHH, and the PHH/PHM complex, respectively, were purified separately over a S300 size exclusion column and then assayed for specific activity and iron content (Table 4.2). PHH obtained from peak 2 displayed a high specific activity relative to the analogous protein sample obtained from the pGEM3Z/PHKLMNOP plasmid, suggesting that the addition of the *phk* gene to the expression system enhances enzyme activity. Hydroxylase purified from peak 2 also displayed higher activity than those from peaks 1 and 3 in assays in which 2 equiv of recombinant PHM were added. The latter observation likely results from the inhibitory effect of the regulatory protein at high PHM to PHH ratios (vide infra).

To better ensure a PHH preparation of homogenous protein content, an additional plasmid was constructed in which the genes for the reductase component PHP and the regulatory protein PHM were both deleted, pGEM3Z/PH $\Delta$ M $\Delta$ P. PHH expressed from this vector eluted in one major peak with a small shoulder consisting of the PHH/PHK complex (data not shown). Protein purified from the major peak (peak 2) displayed relatively high specific activities ranging from 1203 to 1590 mU/mg and iron contents of 4.0 to 4.5 (Table 4.2). The enhancement in activity of PHH expressed from this construct relative to that obtained from the pGEM3Z/PH $\Delta$ P vector probably results from the improved sample homogeneity and therefore better control over the number of equivalents of PHM present in assays. For this reason, hydroxylase obtained from the

**Table 4.3.** Optimization of Fe<sup>2+</sup> and Zn<sup>2+</sup> Concentrations for <sup>57</sup>Fe PHH Expression

Growth Conditions			Purified Protein	
Media	[Fe] (μM) <sup>a</sup>	[Zn] (μM) <sup>b</sup>	Fe/dimer	Specific Activity (mU/mg)
LB	400	-	4.05 - 4.58	1435-1605
M9	200	200	1.18 ± 0.08	182 ± 5
M9	200	50	1.95 ± 0.04	500 ± 15
M9	300	50	2.34 ± 0.02	903 ± 64
M9	400	50	3.40 ± 0.04	913 ± 71
M9	400	25	3.40 ± 0.05	1335 ± 109

<sup>a</sup>Fe was added as Fe(NH<sub>4</sub>)<sub>2</sub>(SO<sub>4</sub>)<sub>2</sub>·6H<sub>2</sub>O. <sup>b</sup>Zn was added as ZnSO<sub>4</sub>.

pGEM3Z/PHΔMΔP expression system was used in all biochemical analyses presented here.

Initial PHH Mössbauer studies performed in our laboratory utilized hydroxylase expressed from pGEM3Z/PHLMNOP in a bactotryptone-based minimal media supplemented with an <sup>57</sup>Fe source. However, attempts to express PHH from pGEM3Z/PHΔMΔP in this media resulted in no soluble or insoluble hydroxylase, as determined by SDS-PAGE analysis. Cells grown in M9-based media yielded hydroxylase in the insoluble fraction, however. Further expression trials were therefore carried out using variations of the M9 media. Neither reducing the temperature from 37 °C to 25 °C nor lowering the IPTG concentration from 400 μM to 200 μM resulted in soluble protein. Similarly, incorporation of the solubilizing additives glycerol, NaCl, or lysine did not yield soluble hydroxylase. The only conditions that produced soluble hydroxylase were those in which the media was supplemented with Zn<sup>2+</sup>, either in the form of the form of ZnSO<sub>4</sub> or as part of a trace metals solution containing all essential metals.

Because the M9 media supplemented with zinc produced soluble protein, several large-scale expressions and protein purifications were attempted with cells grown in this media employing different concentrations of  $^{57}\text{Fe}$  and Zn (Table 4.3). Tuning the iron to zinc ratio was necessary to provide protein with optimal iron content and specific activity (Table 4.3). At stoichiometric or low iron-to-zinc ratios, the purified protein was characterized by low iron content, presumably because zinc and iron compete for binding to the active site. At high iron to zinc ratios, the purified protein displayed high iron content. Hydroxylase obtained from the pGEM3Z/PHAM $\Delta$ P expression system in this media was therefore used for all of the Mössbauer spectroscopic experiments performed after this system was developed.

*Characterization of PHM.* Purification of the PH regulatory protein, PHM, by Q Sepharose FF ion exchange chromatography revealed two peaks containing the protein of interest (Figure 4.4a). Analysis of these peaks by native gel electrophoresis demonstrated that both contain two distinct PHM protein forms that are not distinguishable by SDS-PAGE. The first peak to elute from the column (peak 1) contained more of a faster-migrating protein form, and the second comprised mainly a more slowly migrating species (Figure 4.4b). Electrospray ionization mass spectrometric analysis of samples from both peaks revealed a single small protein with a mass of 10,348 Da, as expected for PHM with truncation of the N-terminal methionine (data not shown). Separation of the two species was achieved on a small analytical gel filtration column (10 min time scale), but not on a large Sephadex S75 column (12 h time scale), suggesting that these species interconvert on a time-scale that is intermediate to those of the two experiments.

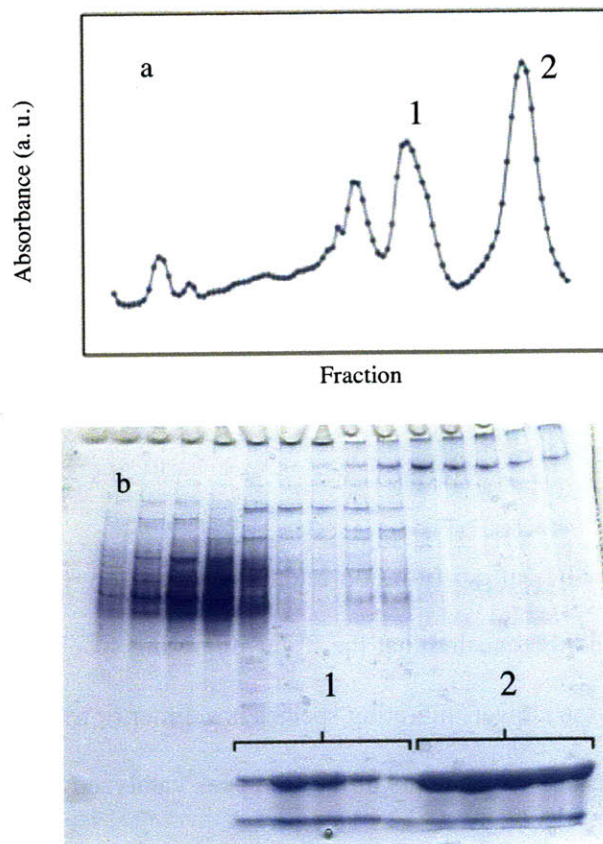


**Figure 4.4.** Representative Q Sepharose FF anion exchange trace for purification of PHM. (a) Trace of eluent monitored at 280 nm displays two major peaks. (b) Native gel analysis of the two peaks show that peak 1 contains more of the faster-migrating PHM form than peak 2 and peak 2 contains more of the slower-migrating PHM form than peak 1.

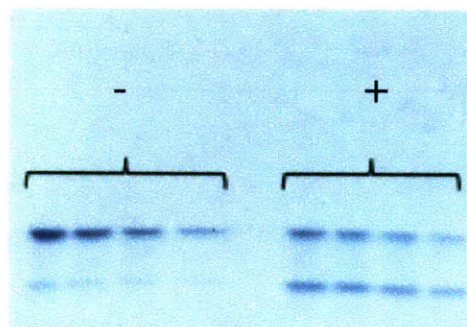


**Figure 4.5.** Representative native gel depicting the two PHM forms before (left) and after (right) thermal refolding.

Comparison of the analytical gel filtration retention times from the two samples with a series of protein standards revealed that the faster-migrating species is a monomer ( $M_r = \sim 13,500$  Da) and that the slower-migrating species is a dimer or trimer ( $M_r = \sim 31,000$  Da) (data not shown). Because the contents of the first peak catalyzed the oxidation of phenol six times more rapidly than the second peak (data not shown), we assign the faster-migrating monomer to active regulatory protein and the slower-migrating oligomer as inactive material.

The existence of two forms of recombinant *Pseudomonas* sp. CF600 phenol hydroxylase regulatory protein DmpM has been previously observed and attributed to dimerization to form an inactive state (51). The DmpM dimer displayed similar behavior to that of the PHM multimer on a gel filtration column. Although the exact nature of the fast and slow-migrating forms of PHM is not yet fully understood, analogy to the Dmp system suggests that the slow-migrating form is an inactive dimer. There is also



precedence for dimerization of regulatory proteins in both the toluene 4-monooxygenase (T4mo) (52) and sMMO (53, 54) systems.

To improve the activity of the PHM dimer, a method for partially denaturing then refolding the protein was developed. This procedure, based on a protocol used for activation of DmpM (51), converted some inactive PHM to active protein, but the resulting solution still contained a significant fraction of inactive material (Figure 4.5). Steady state activity assays revealed that maximal activity was achieved upon addition of 2 to 6 equivalents of PHM per PHH dimer, depending on the protein preparation (Figure 4.6). These numbers probably do not represent the ideal PHH/PHM binding stoichiometry because of the significant amount of inactive protein present in the samples, however. Adding more than 4-6 equivalents of PHM had an inhibitory affect on activity, as noted previously for PHM (37) and for MMOB (18).

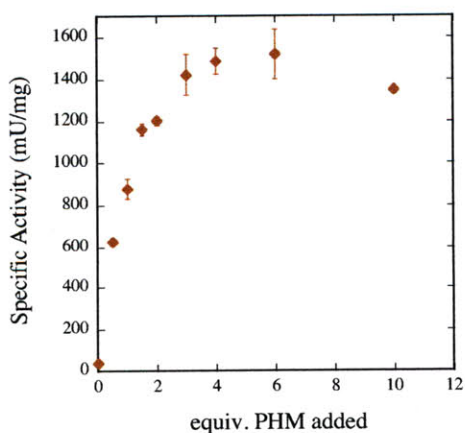


**Figure 4.6.** Dependence of steady state PH activity on equiv of PHM added at 25 °C. Catechol 2,3-dioxygenase coupled assays contained 0.5  $\mu$ M PHH, 0 to 5  $\mu$ M PHM, 1 mM PHP, 1 M NADH, and 1 mM phenol in 500 mL of Tris-HCl, pH 7.5.

*Mössbauer Spectra of Reduced and Oxidized PHH.* The zero-field 4.2 K Mössbauer spectrum of  $^{57}\text{Fe}$ -enriched PHH expressed from pGEM3Z/PHLMNOP and reduced with excess  $\text{Na}_2\text{S}_2\text{O}_4$  in the presence of 2 equiv of PHM fit well to two quadrupole doublets corresponding to 90% of a diiron(II) species,  $\text{PHH}_{\text{red}}$ , and 10% of a diiron(III) cluster (Figure 4.7a). The Mössbauer parameters of these species are provided in Table 4.4. The parameters of  $\text{PHH}_{\text{red}}$  are characteristic of high-spin ( $S = 2$ ) ferrous iron coordinated by oxygen and nitrogen ligands and are similar to those of  $\text{MMOH}_{\text{red}}$  (8, 24) and  $\text{ToMOH}_{\text{red}}$  (48). A similar spectrum was obtained when higher activity  $^{57}\text{Fe}$ -enriched PHH expressed from pGEM3Z/PH $\Delta$ M $\Delta$ P was reduced with excess NADH in the presence of 2 equiv of PHP and 2 equiv of PHM, except that the ratio of the diiron(III) cluster to diiron(II)

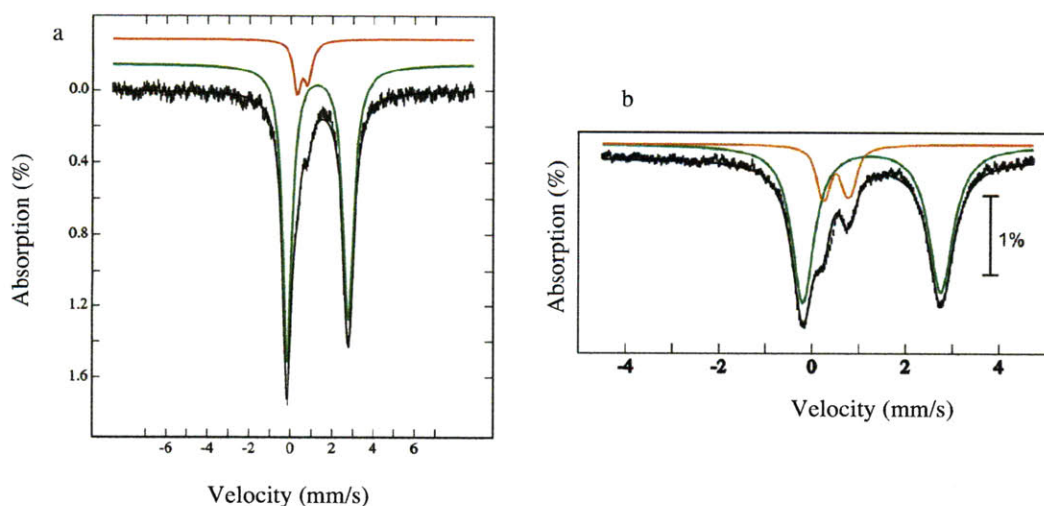


**Figure 4.7.** 4.2 K Mössbauer spectra of  $\text{PHH}_{\text{red}}:2\text{M}$  generated by reduction of  $\text{PHH}_{\text{ox}}:2\text{M}$  with excess  $\text{Na}_2\text{S}_2\text{O}_4$  (a) and with excess NADH in the presence of 2 equiv of natural abundance iron-containing PHP (b). Protein samples were prepared in 25 mM MOPS pH 7.0, 10% glycerol.  $^{57}\text{Fe}$ -enriched PHH was expressed from pGEM3Z/PHLMNOP (a) or pGEM3Z/PH $\Delta$ M $\Delta$ P (b). Data were collected in a 50 mT field applied parallel to the  $\gamma$ -ray beam. Data (black dashes) were fit to two quadrupole doublets (black line) comprising 90% (a) or 83% (b) of the diiron(II)  $\text{PHH}_{\text{red}}$  species (green doublet) and 10% (a) or 17% (b) of a diiron(III) impurity (red or orange doublet, respectively).

PHH<sub>red</sub> was slightly higher (Figure 4.7b). The observation that the diiron(III) form is present when PHH is reduced with its natural reducing agent, NADH, via PHP suggests that is not physiologically relevant and we therefore assign it as an impurity. A similar species was observed in Mossbauer studies of MMOH<sub>red</sub> (8).

The 4.2 K Mössbauer spectrum of as-purified oxidized PHH (PHH<sub>ox</sub>) expressed from pGEM3Z/PHLMNOP in the absence of PHK (Figure 4.8a) required the assignment to two quadrupole doublets corresponding to diiron(III) species to fit the data. The outer doublet, hereafter referred to as cluster form I, having  $\delta = 0.53$  mm/s and  $\Delta E_Q = 1.35$  mm/s, accounted for 25% of the total iron absorption in the sample and the inner doublet, hereafter referred to as cluster form II, with  $\delta = 0.52$  mm/s and  $\Delta E_Q = 0.54$  mm/s,

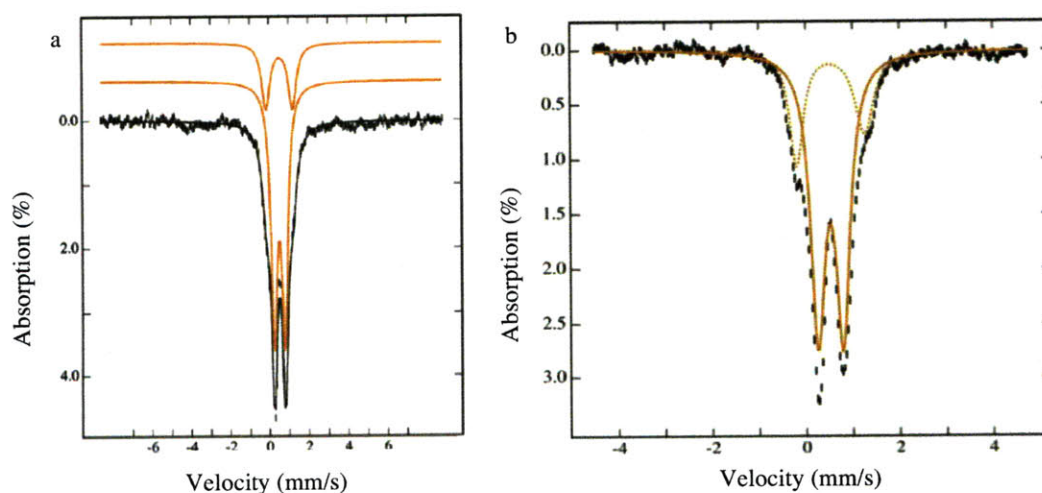


**Figure 4.8.** 4.2 K Mössbauer spectrum of as-purified <sup>57</sup>Fe-enriched PHH<sub>ox</sub>:2M expressed from pGEM3Z/PHLMNOP (a) or pGEM3Z/PHΔMΔP (b). Protein samples were prepared in 25 mM MOPS pH 7.0, 10% glycerol. Data were collected in a 50 mT field applied parallel to the  $\gamma$ -ray beam. Data (black dashes) were fit to two quadrupole doublets (black line) comprising two distinct diiron(III) species (orange doublets).

**Table 4.4.** Mössbauer Parameters of PHH Species<sup>a</sup>

Species	$\delta$ (mm/s)	$\Delta E_Q$ (mm/s)	$\Gamma$ (left) (mm/s)	$\Gamma$ (right) (mm/s)
H <sub>red</sub>	1.32	2.95	0.43	0.57
H <sub>ox</sub> (I)	0.53	1.35	0.49	0.49
H <sub>ox</sub> (II)	0.52	0.54	0.37	0.37
H <sub>peroxo</sub>	0.59	0.63	0.23	0.23
Ferric impurity	0.55	0.51	0.42	0.52

<sup>a</sup>The error associated with each measurement is 0.02 mm/s.

represented 70% of the total iron absorption in the sample (Table 4.4). The remaining 5% of total iron was present as adventitiously bound high-spin iron(III). Cluster forms I and II are attributed to oxo-bridged and hydroxo-bridged diiron(III) units, respectively, by comparison to other well-characterized diiron(III) systems (8, 55-57).

Mössbauer studies of the diiron center of native phenol hydroxylase purified from *Pseudomonas* sp. CF600 also identified two cluster forms of the oxidized hydroxylase that were attributed to oxo- and hydroxo-bridged species (56). The Mössbauer parameters of the two clusters reported for *Pseudomonas* sp. CF600 phenol hydroxylase differ significantly from those measured here for *Pseudomonas* sp. OX1 phenol hydroxylase, however, indicating that these two enzyme systems feature distinct active site compositions. The presence of two oxidized species has also been observed in spectroscopic studies of the diiron center of sMMO (7, 24), stearyl acyl carrier protein (ACP)  $\Delta^9$  desaturase (58), and toluene 4-monooxygenase (20).

The 4.2 K Mössbauer spectrum of as-purified PHH<sub>ox</sub> expressed from pGEM3Z/PHMAP in the presence of PHK (Figure 4.8b) demonstrated that the diiron

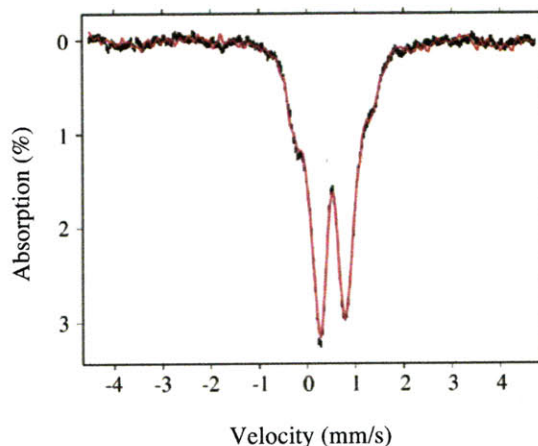


**Figure 4.9.** Overlay of 4.2 K Mössbauer spectra of  $^{57}\text{Fe}$ -enriched  $\text{PHH}_{\text{ox}}:2\text{M}$  prepared in 25 mM MOPS, pH 7.0, 10% glycerol (black) and 25 mM HEPES, pH 8.0, 10% glycerol (pink).  $^{57}\text{Fe}$ -enriched PHH was expressed from the pGEM3Z/PHAMAP plasmid. Data were collected in a 50 mT field applied parallel to the  $\gamma$ -ray beam.

forms are present in the same ratio despite the marked increase in specific activity. We predicted that the oxo- and hydroxo-bridged species might exist in an equilibrium that could be modulated by the external buffer pH if the active site is accessible to buffer components. A comparison of the 4.2 K Mössbauer spectra of  $\text{PHH}_{\text{ox}}:2\text{M}$  prepared in 25 mM MOPS, pH 7.0, and 25 mM HEPES, pH 8.0, indicates that the ratio of cluster forms is independent of external buffer pH (Figure 4.9). These results indicate that (i) the two species are not in direct equilibrium, or that (ii) the largely hydrophobic active site is internally buffered such that external buffer components do not affect the equilibrium between these diiron units.

*Stopped-Flow Optical Spectroscopy:*  $\text{PHH}_{\text{red}}:2\text{M} + \text{O}_2$ . Stopped-flow optical spectroscopy was used to probe the reaction of  $\text{PHH}_{\text{red}}$  with  $\text{O}_2$  in the presence of 2 equiv of PHM. No transient absorption bands were observed between 350 and 750 nm over the

course of 20 min between at 4 and 24 °C, however (data not shown). Similar results were observed for reaction of ToMOH<sub>red</sub> with O<sub>2</sub> in the presence and absence of the regulatory protein ToMOD (48).

*RFQ-Mössbauer Spectroscopy: PHH<sub>red</sub>:2M + O<sub>2</sub>.* The reaction of PHH with O<sub>2</sub> was also probed by Mössbauer spectroscopy. A time course study of the reaction indicates that a transient diiron(III) intermediate forms and then slowly decays (Figure 4.10, blue doublet). To obtain the parameters for this species, we assumed that the spectra collected at early time points did not contain diiron(III) products. The early spectra were then fit with two quadrupole doublets; one representing the diiron(II) starting material and the other corresponding to the diiron(III) intermediate. In these fits, the isomer shift and quadrupole splitting parameters of the diiron(II) starting material were fixed with the values measured for the reduced PHH<sub>red</sub>:2M sample (vide supra), and only the parameters of the diiron(III) transient were allowed to vary. Using this procedure the intermediate was determined to have  $\delta = 0.59$  mm/s and  $\Delta E_Q = 0.63$  mm/s (Table 4.4). These parameters are identical to those reported for the putative peroxodiiron(III) intermediate of ToMOH (14); however, they differ greatly from those measured for other diiron proteins, in which  $\delta > 0.6$  mm/s and  $\Delta E_Q > 1.00$  mm/s.

In analyzing the remaining time points, the percent absorption of diiron(II) starting material was determined using its well-resolved high-energy peak around 3.0 mm/s, and the contribution from this species was then subtracted from the spectra. The resulting spectra were fit using a least-squares method by fixing the parameters of cluster form I, cluster form II, and the diiron(III) transient species at the values measured in control

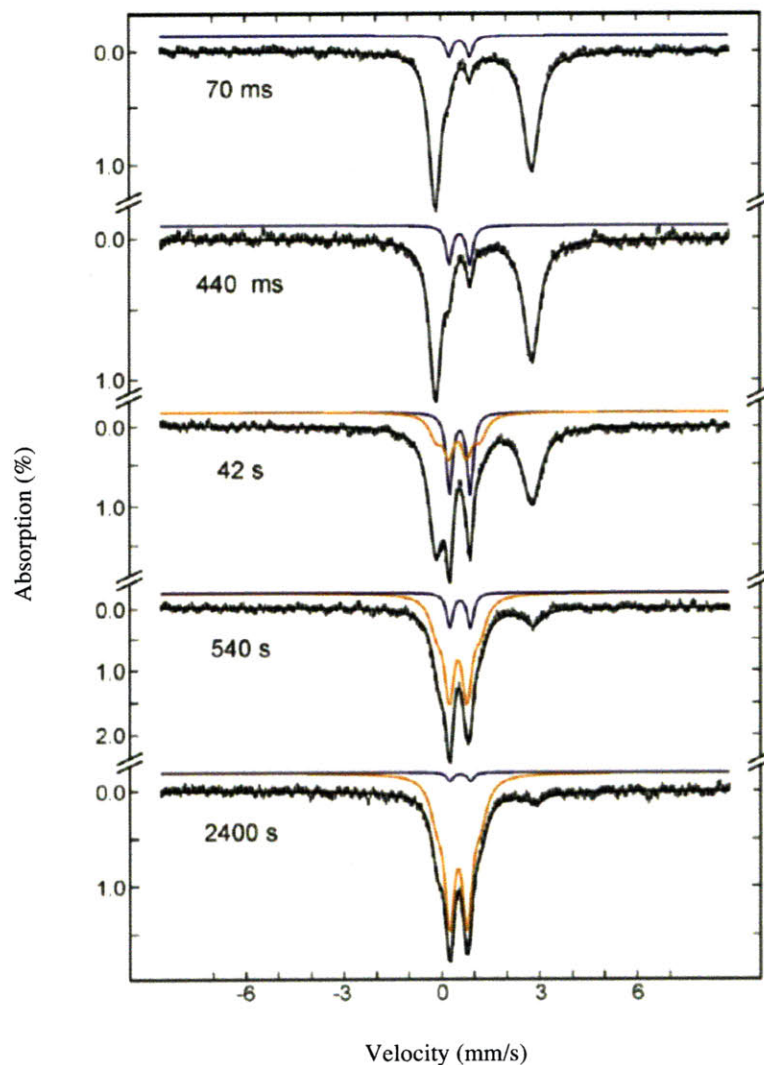
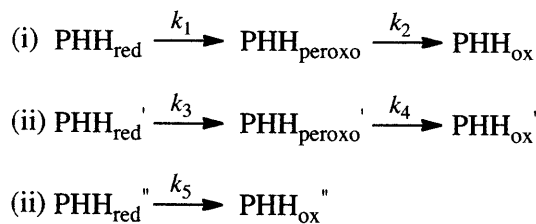


**Figure 4.10.** 4.2 K Mössbauer spectrum of selected RFQ samples quenched at specified time periods during the 4 °C reaction of  $^{57}\text{Fe}$ -enriched  $\text{PHH}_{\text{red}}:2\text{M}$  with  $\text{O}_2$ .  $^{57}\text{Fe}$ -enriched PHH was expressed from the pGEM3Z/PHLMNOP plasmid. Data were collected in a 50 mT field applied parallel to the  $\gamma$ -ray beam. Data (black dashes) were fit (black lines) as described in the text. Quadrupole doublet components corresponding to the diiron(III) intermediate (blue lines) and the sum of the two diiron(III) products (orange lines) are also shown. The parameters and concentration of the diiron(III) impurity identified in the Mössbauer spectrum of  $\text{PHH}_{\text{red}}:2\text{M}$  is assumed to remain constant and its contribution was removed from all data prior to fitting.

experiments but allowing their intensities to vary. In the late time points collected 2400 and 4200 s after reaction initiation, 8% of diiron(II) starting material remains. The spectra are identical, however, indicating that the reaction is complete. A complete set of results from the Mössbauer analyses are presented in Table 4.5.

**Table 4.5.** Percent Mössbauer Absorption of Species Detected in the Reaction of  $\text{PHH}_{\text{red}}:2\text{M}$  with  $\text{O}_2$

Time (s)	$\text{H}_{\text{red}}$ (%)	Diiron(III) Transient (%)	Diiron(III) Product I	Diiron(III) Product II
0	90	0	0	0
0.07	84	6	0	0
0.205	83	7	0	0
0.440	80	10	0	0
1.5	79	11	0	0
6	69	13	5	3
42	48	18	11	14
78	35	20	13	22
200	16	16	20	38
300	13	13	21	43
540	13	10	19	48
1140	10	7	17	56
2400	8	2	20	60
4200	8	2	19	61



**Scheme 4.1.** Three Parallel Processes Model used to Fit Mössbauer Kinetic Data from Reaction of  $\text{PHH}_{\text{red}}:2\text{M}$  with  $\text{O}_2$



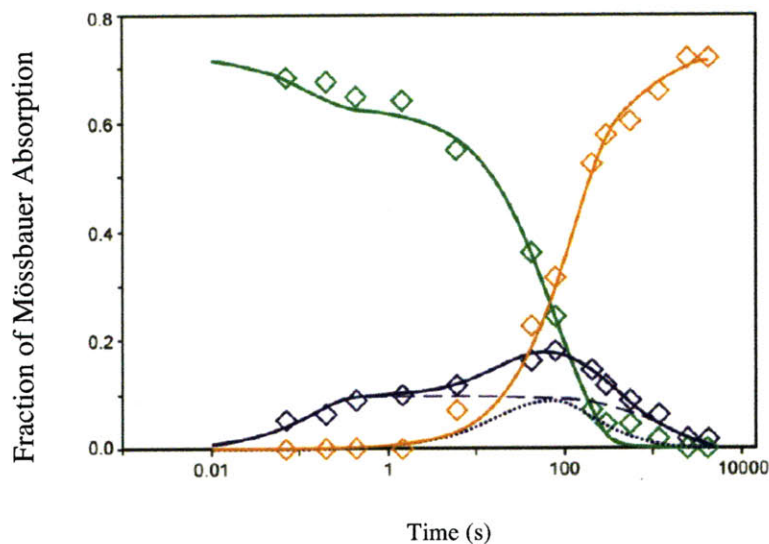
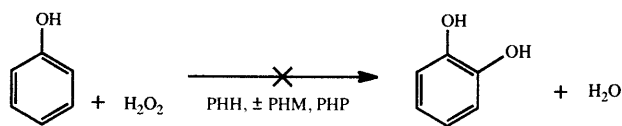


**Figure 4.11.** Speciation plot for reaction of  $\text{PHH}_{\text{red}}:2\text{M}$  with  $\text{O}_2$ . Data depict the fraction of Mössbauer absorption for  $\text{PHH}_{\text{red}}$  (green diamonds), the transient diiron(III) species (blue diamonds), and a sum of the two forms of  $\text{PHH}_{\text{ox}}$  (orange diamonds) as a function of time. The 8% of final un-reacting diiron(II) was not included in calculating the fraction of diiron(II) species. A simulation of the data to the processes shown in Scheme 4.1 is shown in solid lines for  $\text{PHH}_{\text{red}}$  (green), the transient diiron(III) species (blue), and a sum of the two forms of  $\text{PHH}_{\text{ox}}$  (orange). The individual contributions of processes i and ii to the fraction of the diiron(III) intermediate are depicted in dashed and dotted blue lines, respectively.

Several kinetic schemes were considered in modeling the data. The best fit was achieved when the three parallel processes of Scheme 4.1 are employed (Figure 4.10). Parameters obtained from this simulation were  $A_0 = 0.095$  equiv,  $k_1 = 8 \text{ s}^{-1}$ ,  $k_2 = 0.0007 \text{ s}^{-1}$ ,  $A_0' = 0.105$  equiv,  $k_3 = 0.045 \text{ s}^{-1}$ ,  $k_4 = 0.003 \text{ s}^{-1}$ ,  $A_0'' = 0.52$  equiv, and  $k_5 = 0.01 \text{ s}^{-1}$ , where  $A_0$ ,  $A_0'$ , and  $A_0''$  are the fractions of total iron that proceed through pathways i, ii, and iii, and  $k_1$ ,  $k_2$ ,  $k_3$ ,  $k_4$ , and  $k_5$ , are the rate constants describing the processes shown in Scheme 4.1. These fits necessitate that two populations proceed through the diiron(III) intermediate, one with a 180-fold higher rate constant for diiron(III) intermediate formation than the other. This unusual observation could result from disparate  $\text{O}_2$

activation kinetics of cluster forms I and II even though these two sites are indistinguishable by Mössbauer spectroscopy in the reduced enzyme form. Overall, only ~20% of the diiron centers in PHH react with O<sub>2</sub> to generate the diiron(III) intermediate, an observation that might reflect improper assembly of the diiron cluster when this protein is recombinantly expressed in *E. coli* in the absence of PHK. The diiron(III) intermediate is also extremely long-lived; it maximizes at ~90 s after reaction initiation and is still present 540 s later at 4 °C. The peroxodiiron(III) intermediates of stearyl ACP Δ<sup>9</sup>-desaturase (59) and human deoxyhypusine hydroxylase (60) are also unusually long-lived, with half-lives of 26 min and days at room temperature, respectively.

*Attempt to Activate PHH<sub>ox</sub> for Hydrocarbon Oxidation with a Peroxide Shunt.* Attempts to utilize H<sub>2</sub>O<sub>2</sub> instead of O<sub>2</sub>, electrons, and protons, to activate PHH<sub>ox</sub> for oxidation of phenol in the absence or presence of PHM failed to produce hydroxylated products. HPLC analysis of the phenolic contents of reaction mixtures resulting from a 20 min incubation of PHH, 0 or 6 equiv PHM, 2 equiv PHP, and phenol with a 1000-fold excess of H<sub>2</sub>O<sub>2</sub> indicated that no catechol, resorcinol, or hydroquinone were formed and that no phenol substrate was consumed (data not shown). Furthermore, the HPLC peak corresponding to H<sub>2</sub>O<sub>2</sub> was not diminished, suggesting that it is not consumed over the



**Scheme 4.2.** Inability of PH to Access a Peroxide Shunt

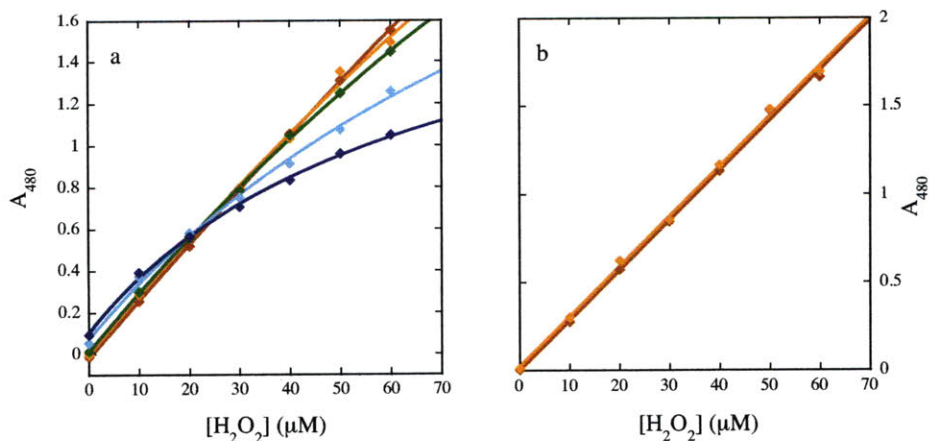


**Figure 4.12.** (a)  $H_2O_2$  standard curves generated in the presence of 0  $\mu M$  (red), 50  $\mu M$  (orange), 100  $\mu M$  (green), 500  $\mu M$  (cyan), and 1 mM (blue) NADH. (b)  $H_2O_2$  standard curves generated in the presence of 0 mM (red) or 200 mM (orange) NADH employing the thermal- and acid-based NADH denaturation procedure described in the text.

course of the incubation period (data not shown). Together, these results indicate that a peroxide shunt is not accessed by PH (Scheme 4.2).

*H<sub>2</sub>O<sub>2</sub> is Generated when PHH<sub>ox</sub> is Activated with Electrons and O<sub>2</sub> in the Absence of Phenol.* Under certain circumstances, some BMM systems generate hydrogen peroxide (15, 18). To determine the mechanism(s) by which  $H_2O_2$  is generated, we measured the ability of different component proteins mixtures to produce and/or consume this molecule. In many of these assays the *E. coli* catalase inhibitor  $NH_2OH$  was added to prevent competing  $H_2O_2$  generation or consumption by trace *E. coli* catalase impurities. Initial attempts to quantify  $H_2O_2$  production by PH employed a method that utilizes the oxidation of an Fe(II) source by hydrogen peroxide followed by complexation of the resulting Fe(III) ion with thiocyanate to form a colored species (45). However, this procedure had to be modified because NADH interferes with formation of the colored

isothiocyanatoiron(III) complex in a complicated, concentration-dependent manner (Figure 4.12a). Therefore, a method was developed to inactivate the reducing agent following reaction quenching but prior to  $\text{H}_2\text{O}_2$  analysis. Although  $\text{H}_2\text{O}_2$  is reasonably stable to heat for short time periods ( $\sim 1$  hr) under acidic conditions, NADH can be inactivated when exposed to low pH and elevated temperatures (61). Accordingly, the quenched reaction mixtures were heated to  $90^\circ\text{C}$  for 15 min and then cooled to room temperature over a period of 45 min before the precipitated protein was removed by centrifugation and the supernatant was assayed for hydrogen peroxide content. Using this method, a hydrogen peroxide standard curve was found to be independent of NADH concentration (Figure 4.12b). This procedure was therefore employed in all  $\text{H}_2\text{O}_2$  detection experiments performed in the presence of NADH.

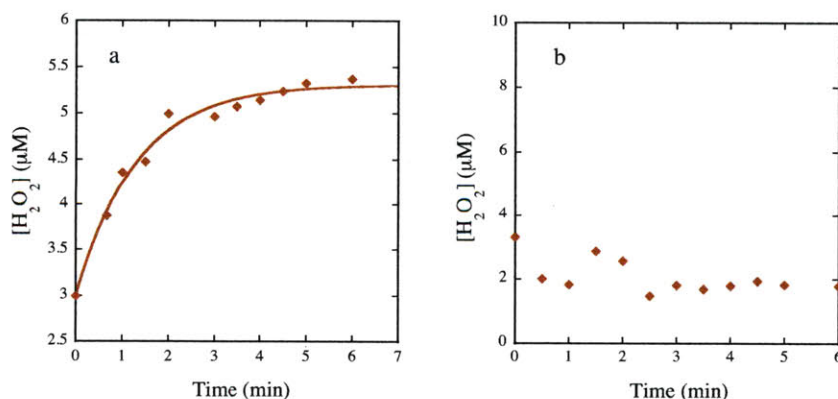
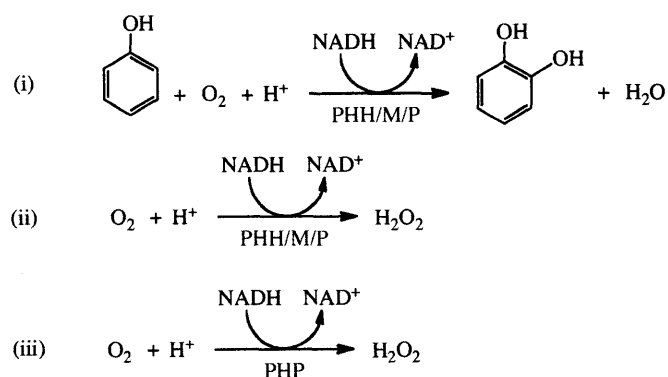


**Figure 4.13.**  $\text{H}_2\text{O}_2$  generation by PH. (a) Representative  $\text{H}_2\text{O}_2$  generation profile (red diamonds) upon addition of  $200\ \mu\text{M}$  NADH to a solution of  $1\ \mu\text{M}$  PHH,  $6\ \mu\text{M}$  PHM,  $2\ \mu\text{M}$  PHP, and  $10\ \mu\text{M}$   $\text{NH}_2\text{OH}$  at  $4^\circ\text{C}$ . Data were fit to the single exponential formation process  $y = A \cdot \exp(-kt) + B$ . Similar reaction profiles were obtained in the absence of  $\text{NH}_2\text{OH}$ . (b) Representative  $\text{H}_2\text{O}_2$  generation profile (red diamonds) upon addition of  $200\ \mu\text{M}$  NADH to a solution of  $1\ \mu\text{M}$  PHH,  $6\ \mu\text{M}$  PHM,  $2\ \mu\text{M}$  PHP, and  $5\ \text{mM}$  phenol at  $4^\circ\text{C}$ . Similar reaction profiles were obtained in the presence of  $\text{NH}_2\text{OH}$ . Reaction solutions were assayed for  $\text{H}_2\text{O}_2$  content as noted in the text.



**Scheme 4.3.** Steady State Product Evolution by PH in the Presence (i) or Absence (ii) of Phenol and by PHP in the Absence of Phenol (iii).

Steady state assays indicated that  $\text{H}_2\text{O}_2$  is evolved from the complete PH system in the absence of phenol but not in its presence when the *E. coli* catalase inhibitor  $\text{NH}_2\text{OH}$  was added to prevent competing  $\text{H}_2\text{O}_2$  generation or consumption by trace catalase impurities (Figure 4.13 and Scheme 4.3). In these assays, the ratio of protein components added were those that yield maximal product formation in steady state titration experiments. Similar results were obtained in the absence of  $\text{NH}_2\text{OH}$ . Importantly,  $\text{NH}_2\text{OH}$  did not inhibit enzyme activity, for steady state assays performed in the presence and absence of this compound yielded identical amounts of catechol at 2 min and 10 min after reaction initiation (data not shown).

The observation that  $\text{H}_2\text{O}_2$  is not generated by PH when phenol is present suggests that electron consumption is fully coupled to hydrocarbon oxidation under these conditions (Figure 4.13b and Scheme 4.3i). The  $\text{H}_2\text{O}_2$  evolution profile from the enzyme system obtained in the absence of phenol displays hyperbolic  $\text{H}_2\text{O}_2$  release behavior with a non-

zero y-intercept (Figure 4.13a). The small amount of apparent  $\text{H}_2\text{O}_2$  present in the assay mixtures at time zero probably results from protein-bound iron(III) that dissociates upon precipitation and binds to thiocyanate in the reaction mixture to produce the red compound detected. Accordingly, the value on the y-intercept approximately corresponds to the iron content of the proteins being assayed (Figure 4.13). A fit of the  $\text{H}_2\text{O}_2$  evolution profile to a single exponential process revealed a first-order rate constant of  $1.8 \text{ min}^{-1}$  (Figure 4.13a, red line). The hyperbolic behavior of the  $\text{H}_2\text{O}_2$  generation curve suggests that PH is inactivated over time, possibly by hydrogen peroxide, as previously reported for phenol hydroxylase from *Pseudomonas* sp. CF600 (56) and ToMO (15).

To examine whether PH is indeed inactivated over the course of the reaction, we treated the enzyme system with NADH for time periods between 1 and 8 min before adding phenol. The resulting mixture was incubated for 20 min and then analyzed for catechol content. Catechol yield decreased as a function of NADH-enzyme incubation time, indicating that time-dependent protein inactivation occurs under the conditions employed in the steady state  $\text{H}_2\text{O}_2$  assays (Figure 4.14). To determine whether the observed enzyme inactivation could be mediated by formation of  $\text{H}_2\text{O}_2$ , the enzyme system was incubated with a 100-fold excess of  $\text{H}_2\text{O}_2$  for 20 min prior to assaying for catechol content. HPLC quantification revealed that the  $\text{H}_2\text{O}_2$ -exposed system generated only 63% of the catechol observed for the untreated enzyme. Together, these results indicate that the hyperbolic nature of the  $\text{H}_2\text{O}_2$  generation curve results from enzyme inactivation by  $\text{H}_2\text{O}_2$ . The mechanism of inactivation probably stems from  $\text{H}_2\text{O}_2$ -mediated free radical damage to the PH proteins.

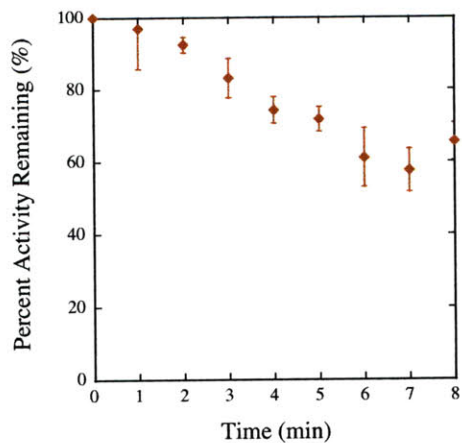


**Figure 4.14.** Percent PH activity remaining as a function of time incubated with NADH. Experiments were carried out as described in the text. Data points represent the average of two trials performed with different batches of protein.

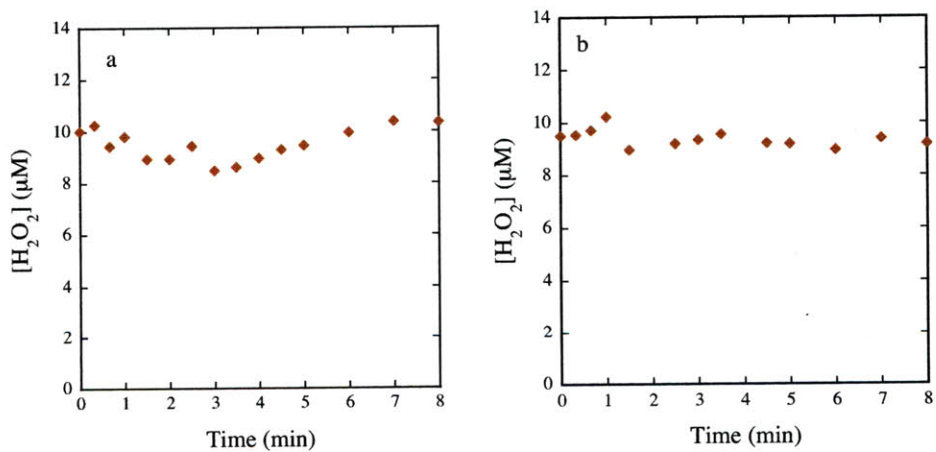


**Figure 4.15.** H<sub>2</sub>O<sub>2</sub> consumption by PH. (a) Representative H<sub>2</sub>O<sub>2</sub> consumption profile upon addition of 10 μM H<sub>2</sub>O<sub>2</sub> to a solution of 1 μM PHH, 6 μM PHM, 2 μM PHP, and 10 μM HNOH at 4 °C. (b) Representative H<sub>2</sub>O<sub>2</sub> consumption profile upon addition of 10 μM H<sub>2</sub>O<sub>2</sub> to a solution of 1 μM PHH, 2 μM PHP, and 10 μM HNOH at 4 °C. Reaction solutions were assayed for H<sub>2</sub>O<sub>2</sub> content as noted in the text.

We also examined the ability of PH to consume  $\text{H}_2\text{O}_2$  in the absence of hydrocarbon substrate. Detection assays employing a 10-fold excess of  $\text{H}_2\text{O}_2$  indicated that no  $\text{H}_2\text{O}_2$  was consumed by the enzyme system over the course of 8 min in the absence (Figure 4.15a) or presence (Figure 4.15b) of PHM when phenol was absent and the *E. coli* catalase inhibitor  $\text{NH}_2\text{OH}$  was added. Similar results were obtained when a 50-fold excess of  $\text{H}_2\text{O}_2$  was employed (data not shown). Given these findings, reports that both ToMOH (15) and toluene 2-monooxygenase (T2MO) from *Burkholderia cepacia* G4 (62) can consume  $\text{H}_2\text{O}_2$  by means of catalase activity are likely to reflect small amounts of catalase protein contaminants rather than hydroxylase activity as a catalase (20).

In the PH system,  $\text{H}_2\text{O}_2$  generation can arise from two possible processes: (i) reductase oxidase activity and/or (ii) release from the hydroxylase diiron center. To characterize better the mechanism of  $\text{H}_2\text{O}_2$  evolution in PH, we examined both possibilities (Figure 4.16). First, we measured the ability of PHP to generate  $\text{H}_2\text{O}_2$ . Indeed, PHP generates  $\text{H}_2\text{O}_2$  in the presence of  $\text{O}_2$  and NADH (Figure 4.16a and Scheme 4.3iii). The reaction is characterized by hyperbolic kinetics, and a fit of the data to an exponential growth model revealed a first-order rate constant  $k$  of  $0.82 \text{ min}^{-1}$ . Under similar conditions, PHP did not consume  $\text{H}_2\text{O}_2$  (Figure 4.17). The measured rate of  $\text{H}_2\text{O}_2$  formation by 2 equivalents of PHP is insufficient to account for the  $\text{H}_2\text{O}_2$  generation profile obtained in the presence of the complete enzyme system (Figure 4.13a). It is therefore likely that the  $\text{H}_2\text{O}_2$  arises instead from PHH or from both PHH and PHP. To distinguish these two possibilities,  $\text{H}_2\text{O}_2$  assays were performed employing a sub-stoichiometric amount (0.1 equivalent) of PHP. At these ratios, electron consumption and product formation are fully coupled (37),



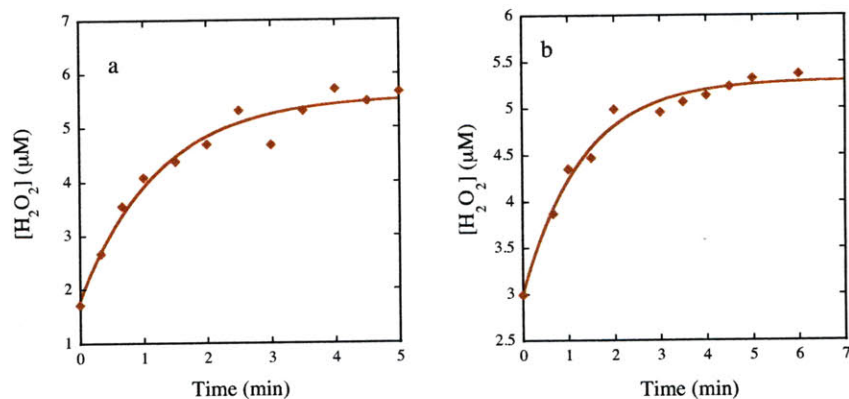


**Figure 4.16.** (a) Representative  $H_2O_2$  generation profile (red diamonds) upon addition of 200  $\mu M$  NADH to 2  $\mu M$  PHP at 4  $^{\circ}C$ . Similar reaction profiles were obtained in the presence of  $NH_2OH$ . (b) Representative  $H_2O_2$  generation profile (red diamonds) upon addition of 200  $\mu M$  NADH to a solution of 1  $\mu M$  PHH, 6  $\mu M$  PHM, 0.1  $\mu M$  PHP, and 10  $\mu M$   $NH_2OH$  at 4  $^{\circ}C$ . Similar reaction profiles were obtained in the absence of  $NH_2OH$ . Reaction solutions were assayed for  $H_2O_2$  content as noted in the text.

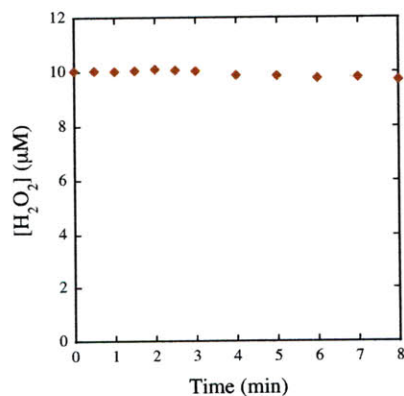


**Figure 4.17.** (a) Representative  $H_2O_2$  consumption profile (red diamonds) upon addition of 10  $\mu M$   $H_2O_2$  to 2  $\mu M$  PHP at 4  $^{\circ}C$ . Reaction solutions were assayed for  $H_2O_2$  content as noted in the text.

and  $\text{H}_2\text{O}_2$  should not be generated from oxidase activity of the reductase. Under these conditions,  $\text{H}_2\text{O}_2$  is released in a hyperbolic fashion with a first-order rate constant  $k$  of  $0.77 \text{ min}^{-1}$  (Figure 4.16b). The rate of  $\text{H}_2\text{O}_2$  formation of a solution of 0.1 equiv of PHP is negligible (data not shown), however, and we therefore attribute the origin of the observed  $\text{H}_2\text{O}_2$  to liberation from the hydroxylase diiron sites. The rate of  $\text{H}_2\text{O}_2$  production under these conditions is also insufficient to account for the  $\text{H}_2\text{O}_2$  generation profile observed in the presence of the complete enzyme system, however (Figure 4.13a). We therefore conclude that  $\text{H}_2\text{O}_2$  arises from *both* PHP oxidase activity and from generation at the hydroxylase diiron centers.

*Single Turnover Assays: Evidence for Half-Sites Reactivity and the Allosteric Influence of PHP.* Experiments in which the amount of product formed by various ratios of the PH protein components in a single enzyme turnover established the importance of the fully constituted system for efficient catalysis (Table 4.6). No catechol was formed when the reduction of PHH was performed with  $\text{Na}_2\text{S}_2\text{O}_4$  in the absence of PHM and PHP. Addition of the regulatory protein PHM to PHH did not enhance product yield (Table 4.6). Addition of the reductase, PHP, to PHH slightly improved the yield, although the amount of catechol formed under these circumstances is too low to be physiologically relevant.

Only the fully coupled system containing the hydroxylase, regulatory protein, and reductase could generate a significant amount of product. Although substrate was present in great excess, only ~50% with respect to protein active site clusters converted to

**Table 4.6.** PH Single Turnover Yields

Reaction Conditions	Reductant	% Catechol Formed/Active Sites
PHH	Na <sub>2</sub> S <sub>2</sub> O <sub>4</sub>	None Detected
PHH:6M:2P	NADH	54 ± 2
PHH:6M:2P	Na <sub>2</sub> S <sub>2</sub> O <sub>4</sub>	54 ± 1
PHH <sub>red</sub> :6M:2P <sub>ox</sub> <sup>a</sup>	Na <sub>2</sub> S <sub>2</sub> O <sub>4</sub>	24 ± 6
PHH:6M	Na <sub>2</sub> S <sub>2</sub> O <sub>4</sub>	None Detected
PHH:2P	Na <sub>2</sub> S <sub>2</sub> O <sub>4</sub>	8 ± 3
PHH:6M:0.1P	NADH	49 ± 3
PHH:0.1P	NADH	None Detected

<sup>a</sup>PHH<sub>red</sub>:2M was pre-reduced with stoichiometric Na<sub>2</sub>S<sub>2</sub>O<sub>4</sub> for 20 min prior to adding PHP.

catechol under these conditions. The amount of product formed was independent of reductase concentration; experiments employing a sub-stoichiometric amount (0.1 equivalent) of PHP also generated half an equivalent of catechol. In these single turnover experiments, product yields lower than the theoretical maximum were not a consequence of the use of an unnatural chemical reducing agent, because experiments employing NADH instead of Na<sub>2</sub>S<sub>2</sub>O<sub>4</sub> also yielded ~50% catechol.

In order to investigate whether the reductase protein exerts regulatory effects on the hydroxylase in a manner that influences the product yield, single turnover experiments were carried out in which a mixture of the hydroxylase and appropriate regulatory protein was reduced with stoichiometric Na<sub>2</sub>S<sub>2</sub>O<sub>4</sub> for 20 min prior to addition of oxidized PHP. Analysis of catechol generated after introduction of dioxygen into the reaction solutions revealed values approximately half of that formed in experiments employing a physiologically relevant reducing agent (~25% per active sites). However, these values

were significantly greater than those obtained by a mixture of  $\text{PHH}_{\text{red}}$  and PHM, suggesting that PHP affects activity of the PHH/PHM complex.

To further examine the influence of PHP on the hydroxylase-regulatory protein complex and to determine whether the reductase directly affects the structure of the diiron active site, we measured the Mössbauer spectra of  $^{57}\text{Fe}$ -enriched  $\text{PHH}_{\text{red}}$  and  $\text{PHH}_{\text{ox}}$  in complex with 2 equiv of PHM and 2 equiv of PHP not enriched in  $^{57}\text{Fe}$ . PHP does not alter the Mössbauer parameters of the reduced (Figure 4.7b) or oxidized (Figure 4.18) hydroxylase. A comparison of the ratio of  $\text{PHH}_{\text{ox}}$  cluster forms I and II in the presence and absence of PHP indicates that a subtle change occurs upon addition of the reductase, however (Figure 4.18). Cluster forms I and II account for 32% and 68% of the total iron

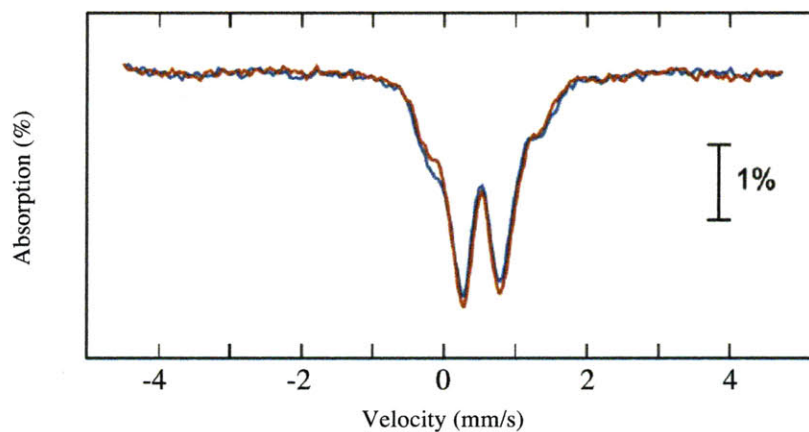


**Figure 4.18.** 4.2 K Mössbauer spectrum of  $^{57}\text{Fe}$ -enriched  $\text{PHH}_{\text{ox}}:2\text{M}$  in the presence (blue line) or absence (pink line) of 2 equiv of natural-abundance iron-containing PHP. Samples were prepared in 25 mM MOPS, pH 7.0.  $^{57}\text{Fe}$ -enriched PHH was expressed from the pGEM3Z/PH $\Delta$ M $\Delta$ P plasmid. Data were collected in a 50 mT field applied parallel to the  $\gamma$ -ray beam.

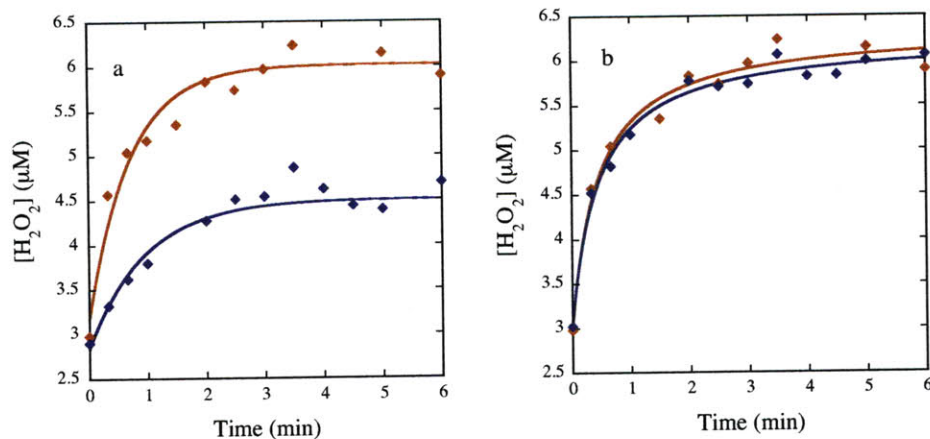


**Figure 4.19.** (a) Representative  $\text{H}_2\text{O}_2$  generation profile upon addition of 200  $\mu\text{M}$  NADH to 1  $\mu\text{M}$  PHH, 6  $\mu\text{M}$  PHM, and 2  $\mu\text{M}$  PHP (red) or 1  $\mu\text{M}$  PHH and 2  $\mu\text{M}$  PHP (blue) at 4  $^\circ\text{C}$ . Similar reaction profiles were obtained in the presence of  $\text{NH}_2\text{OH}$ . Data were collected on the same day with the same batches of protein and can therefore be directly compared. (b) Representative  $\text{H}_2\text{O}_2$  generation profile upon addition of 200  $\mu\text{M}$  NADH to a solution of 1  $\mu\text{M}$  PHH, 6  $\mu\text{M}$  PHM, and 0.1  $\mu\text{M}$  PHP (red) or 1  $\mu\text{M}$  PHH and 0.1  $\mu\text{M}$  PHP (blue) at 4  $^\circ\text{C}$ . Data were collected on the same day with the same batches of protein and can therefore be directly compared. Data were fit (solid lines) as described in the text. Reaction solutions were assayed for  $\text{H}_2\text{O}_2$  content as noted in the text.

in the sample, respectively, when PHP was added, a 25% increase in the amount of the putative oxo-bridged form of the protein. Although the accuracy of this quantitation is low, the fact that the ratio of the cluster forms could be reproduced within one percentage point for several  $^{57}\text{Fe}$ -enriched  $\text{PHH}_{\text{ox}}:2\text{PHM}$  samples prepared with multiple batches of protein expressed from different plasmids assures that the observed difference upon addition of PHP is significant. The data suggest that PHP imparts an allosteric effect on PHH or the PHH/PHM complex that can be transmitted to the active site.

*$\text{H}_2\text{O}_2$  Production in the Absence of the Regulatory Protein.* The effect of PHM on  $\text{H}_2\text{O}_2$  production was examined to provide information about its possible role. These experiments are facilitated by the  $\text{H}_2\text{O}_2$  generation from the hydroxylase active site (vide

supra), which provides a means to evaluate the influence of PHM on O<sub>2</sub> activation. In the absence of the regulatory protein, H<sub>2</sub>O<sub>2</sub> is generated at a slower rate ( $k = 1.0 \text{ min}^{-1}$ ) than in its presence ( $k = 1.8 \text{ min}^{-1}$ ). As a consequence, less H<sub>2</sub>O<sub>2</sub> is formed overall before the enzyme is inactivated (Figure 4.19a). Hydrogen peroxide is not differentially consumed in the presence and absence of PHM, indicating that the difference in H<sub>2</sub>O<sub>2</sub> evolution profiles results from an inherent ability to generate this product and not from the ability of the system to consume it in the absence of the regulatory protein (Figure 4.15). Experiments probing H<sub>2</sub>O<sub>2</sub> production by the PH system employing sub-stoichiometric (0.1 equiv) PHP revealed that the rate of H<sub>2</sub>O<sub>2</sub> production is independent of the regulatory protein (Figure 4.19b).

*NADH Consumption by PH.* Table 4.7 shows the rates of NADH consumption by PH monitored under a variety of conditions. PHH does not consume NADH in the absence of the electron transfer proteins. The rate of NADH consumption is significantly enhanced by the presence of phenol. In experiments employing stoichiometric amounts of reductase, the NADH consumption rate measured in the absence of phenol is retarded when the regulatory protein is not included in the reaction mixtures. However, in experiments employing sub-stoichiometric (0.1 equiv) PHP, the presence of the regulatory protein or of phenol does not affect the rate of NADH consumption. This result indicates that electron transfer, and not O<sub>2</sub> activation or product formation, is rate-determining. These results are consistent with H<sub>2</sub>O<sub>2</sub> evolution assays performed in the presence and absence of PHM at sub-stoichiometric (0.1 equiv) PHP concentrations (Figure 4.19b). Similar trends in the NADH consumption rates were observed at 4 °C (data not shown).

**Table 4.7. PH NADH Consumption Rates<sup>a</sup>**

Reaction Conditions	NADH Consumption Rate ( $\mu\text{M}/\text{min}$ )
PHH	0
PHH:6M:2P	$67.2 \pm 0.7$
PHH:2P	$17.6 \pm 0.2$
PHH:6M:2P:phenol	$180 \pm 7$
2PHP	$4.0 \pm 0.3$
PHH:6M:0.1P	$25.4 \pm 0.8$
PHH:0.1P	$33.0 \pm 0.8$
PHH:6M:0.1P:phenol	$34 \pm 2$
0.1PHP	$0.16 \pm 0.01$

<sup>a</sup>Experiments were performed at 25 °C

## DISCUSSION

The remarkable ability of BMM systems to perform challenging hydrocarbon oxidation reactions in a regioselective manner depends on the coordinated efforts of three or more protein components. Regulation of the dynamic interplay between these proteins is crucial to maintaining effective and sustainable enzyme systems. However, these protein interactions are complicated and the functions of the individual protein components are still not fully understood.

*The Hydroxylase Component of Recombinant Phenol Hydroxylase.* Recombinant PHH expressed in the absence of PHK from the pGEM3Z/PHLMNOP construct displayed a specific activity 5-fold lower than that of *Pseudomonas sp.* CF600 purified from the native organism (56). Consistent with this quantitation, only ~20% of the iron clusters in the protein sample obtained under these conditions proceeded through the O<sub>2</sub> activation pathway, as judged by Mössbauer spectroscopy (Figure 4.11) and single turnover studies (data not shown). These results highlight the difficulty of expressing this protein with the

diiron cofactor properly assembled in *E. coli*, which could result from improper loading of a non-native but functional metal or the lack of small protein factors that are required for correct metal insertion during protein expression. It is possible that the incorrect metal is incorporated into the protein, suggested by a recent study of a Class 1b RNR-R2 demonstrates that this protein can form a functional diiron protein in vitro but is probably composed of a dimanganese cluster in vivo (63). We do not favor this possibility for PHH, however, because the specific activity of iron-containing PHH expressed in *E. coli* in the presence of PHK is similar to that measured for *Pseudomonas sp.* CF600 purified from the native organism (56). The latter protein consists of a dinuclear iron center composed of two cluster forms distinguishable by Mössbauer spectroscopy. Instead, we believe that the lack of appropriate protein components in the expression vector is responsible for the observed low hydroxylase activity of PHH expressed from pGEM3Z/PHLMNOP. Indeed, addition of PHK to the PHH expression vector raised activity to levels that match those of native *Pseudomonas sp.* CF600 phenol hydroxylase and increased single turnover yields to ~50% per diiron clusters, a number that is consistent with the protein being fully active if a half-sites reactivity mechanism is operative.

*Studies of PHK, A Novel Zinc(II) Chaperone in the PH Operon?* Previous biochemical studies identified a PHK homolog from *Pseudomonas sp.* CF600, DmpK, in trafficking and inserting iron into its associated hydroxylase (49). In this system, addition of Fe(II) to inactive hydroxylase activated the enzyme only in the presence of DmpK (49). Such a role seems unlikely here given our results. First, the purified PHH/PHK complex has low iron levels (Table 4.2). In addition, co-expression of PHH with PHK yields high activity



hydroxylase but does not alter the Mössbauer parameters or the ratio of the two diiron(III) cluster forms (Figure 4.8).

To understand better the function of PHK, a BLAST (NCBI) search of the protein sequence was undertaken. The search identified several genes from various BMMs that encode PHK-like proteins, including phenol hydroxylases from multiple bacterial species, a three component toluene/benzene-2-monooxygenase from *Pseudomonas* sp. JS150, a three component toluene *ortho*-monooxygenase from *Burkholderia cepacia*, and a dimethyl sulfide oxidase from *Acinetobacter* sp. st. 20B. A putative PHK-like protein,

PHK	-----ELVLPHEAF	9
phkA	MTRHPVAGPPALGQEDNDAFDPTRRFVVRTGINRRGFVEFEFSVGIPELCELMLPRAAF	60
tomA0	MHKQ-----AALEAEPR--FDPNLRVSVTAINTQGFVQFEFSVGTPELCELMLPVAAF	53
phcK	METS-----TLDLPAC---DLTRRSVRVLQKRANGFVDFEFSVWPELSVELAMTEADF	51
tbmA	MTIQ-----LSQPSNEMPVVDLTRKYVSRIERRTDGLVSFEFAIGWPELSVDLLLPEPAF	55
poxA	MINQ-----SVPLFEATPRYVRVEGRTPEGFVLFASFVADPDLNVELILPEPMF	49
touK	-MTT-----QPETKSFEELTRYIRVRSEPGDKFVEFDFAIALPELVELVLPHEAF	50
dmpK	MTVT-----NTPPTPFDQLTRYIRVRSEPEAKFVEFDFAIHPELVELVLPQDAF	51
dsoA	MIDA-----KQPT---ALVKYIRITGERNAKFVEFDFAIQDPTLVELILPQQAF	47
PHK	EIFCKHNVVHMSNIIRKIDEDMVKWRFG-----EHGKRY-----	45
phkA	EEFCIAQNVVRLTAEGEPMTSRSRQ-----	85
tomA0	EEFCIAQKVTRLDAFGEIVRH-----	74
phcK	EAFQVQKARLL-----	63
tbmA	TAFKERHQVTRLGS-----	69
poxA	EAFCSANHVRFPLPAQAACADSGEDA-----	74
touK	EIFCKHNVVHMSNISAKLTKDMVKWGFG-----EHGKRY-----	86
dmpK	VKFCQHNRVAMDEAMAKAVDDDMVKWRFG-----DVGRRLPKDPG--	92
dsoA	QHFCIEINHVIEMTAEQQAWNDAQEDKWRYGIEPTVLNHRHQHSDQDDQA	96

**Figure 4.20.** Sequence alignment of PHK and related sequences as determined from a BLAST (NCBI Database) search. Residues highlighted in cyan are strictly conserved. Yellow shading denotes conserved charged residues. The protein sequences and accession numbers used for the alignment are as follows. PHK, *Pseudomonas* sp. OX1 (AAO47355); phkA, *Burkholderia kururiensis* KP23 (BAB79279); tomA0, *Burkholderia cepacia* (AAL50370); phcK, *Comamonas testosteroni* R5 (BAA87868); tbmA, *Pseudomonas* sp. st. JS150 (AAA88456); poxA, *Ralstonia eutropha* st. E2 (AAC32452); touK, *Pseudomonas* sp. OX1 (CAC38005); dmpK, *Pseudomonas* sp. CF600 (AAA25939); dsoA, *Acinetobacter* sp. st. 20B (BAA23330).

touK, also resides in the operon encoding toluene/*o*-xylene monooxygenase from *Pseudomonas* sp. OX1. Except for touK, the proteins identified in this search belong to the class of three component phenol hydroxylases (3).

The sequences of these small PHK-like proteins do not offer much information about their functions (Figure 4.20). A sequence alignment reveals that not many amino acid residues are conserved within this protein. Among those that are strictly conserved are a cysteine residue, a glutamate, and a number of hydrophobic amino acids. The cysteine and acid residues might possibly contribute ligands in a metal-binding motif; however, biochemical studies on *Pseudomonas* sp. CF600 DmpK suggest that the purified protein does not bind iron or any other inorganic or organic cofactor exhibiting a distinctive optical signal (49).

PHN	PQLCQVCQIPTIFTEKD-APTMLSHRQIEHEGERYHFCSDGCCDIFK	440
dmpN	PHLCQVCQLPVIFTEPD-DPTKLSLRSLVHEGERYQFCSHGCCDIFK	441
dsoD	PQLCQVCQIPMTFTEMDGPTLFSYRDSIYKDERYHTCSHGCHDIFE	448
tbmD	PMLCTTCQVPMFFTEPG-DATKIAYRESDFGNKYHFCSDHCKHIFD	442
phkD	PMLCQTCQIPMLFTEPG-NAKKLCARESDYLGNNRYHFCSDHCKEIFD	453
phcN	PMLCTTCQIPMGFTEPG-DATKICYRESYEGSKYHFCSDGCKHVFD	443
tomA3	PMLCTTCQIPMIFTEPG-DATKICYRESAYLGDKYHFCSDHCKEIFD	443
poxD	PMLCQTCQIPMVFSEPD-DPTQTCYRESSYHGMKFHFCSDGCKDIFD	439
touA	PTICNMCNLP IAHTPGN--KWNVKDYQLEYEGRLYHFGSEADRWCFO	438

**Figure 4.21.** Sequence alignment of hydroxylase  $\alpha$ -subunit C-terminal domains from the BMM systems compared in Figure 4.20. Residues highlighted in cyan form a putative tetrathiolate cysteine binding motif in the three component aromatic hydroxylating enzymes. Two of these cysteines are conserved in touA, a four component aromatic hydroxylase. The protein sequences and accession numbers used for the alignment are as follows. PHN, *Pseudomonas* sp. OX1 (AAO47358); phkD, *Burkholderia kururiensis* KP23 (BAB79282); tomA3, *Burkholderia cepacia* (AAL50373); phcN, *Comamonas testosteroni* R5 (BAA87871); tbmD, *Pseudomonas* sp. st. JS150 (AAA88459); poxD, *Ralstonia eutropha* st. E2 (AAC32455); touA, *Pseudomonas* sp. OX1 (AAT40431); dmpN, *Pseudomonas* sp. st. CF600 (AAA25942); dsoD, *Acinetobacter* sp. st. 20B (BAA23333).

A sequence alignment of the hydroxylase component  $\alpha$ -subunits corresponding to the BMM systems encoding PHK-like proteins reveals that all but *touA* contain a tetracysteine motif in the C-terminal region (Figure 4.21). Recent crystallographic characterization of the PHH/PHM complex indicates that each of these four cysteine residues contributes one ligand to a tetrathiolate zinc-binding motif, believed to be structural in nature (29). These observations suggest a connection between the occurrence of a PHK-like protein in the BMM operon and the presence of a structural zinc element in the hydroxylase. We therefore envision a mechanism in which PHK binds to un- or misfolded hydroxylase and aids in zinc insertion. The zinc(II) ion provides a structural scaffold around which the protein can further fold into its mature form. This hypothesis is supported by the observation that PHH expressed from pGEM3Z/PHLMNOP in media containing no zinc yields soluble protein, whereas that expressed from pGEM3Z/PHKLMNOP in the absence of zinc forms inclusion bodies (*vide supra*). Additionally, the purified PHH/PHK complex displayed low activity and iron content (Table 4.3), suggesting that PHK only binds to inactive, iron-free hydroxylase. The abundance of conserved hydrophobic amino acids in PHK suggests a role in hydrophobic protein-protein interactions of the kind that occur when a protein is unfolded (Figure 4.20).

Proteins like PHK might bind zinc via their conserved cysteine and glutamate residues and shuttle the metal into the hydroxylase directly, or they might assist in loading zinc by a less direct mechanism. Once properly folded, spontaneous assembly of the diiron cofactor can occur, as noted for other BMM hydroxylases such as ToMOH. Spontaneous assembly of the diiron active site is also supported by the observation that active protein

can be obtained when it is expressed in the absence of PHK, although the activity is low. A role involving zinc insertion was not previously suggested from biochemical studies of *Pseudomonas* sp. CF600 DmpK, but the authors may have overlooked presence of a d<sup>10</sup> zinc ion that would have been undetectable by the spectroscopic methods used in their analyses (49).

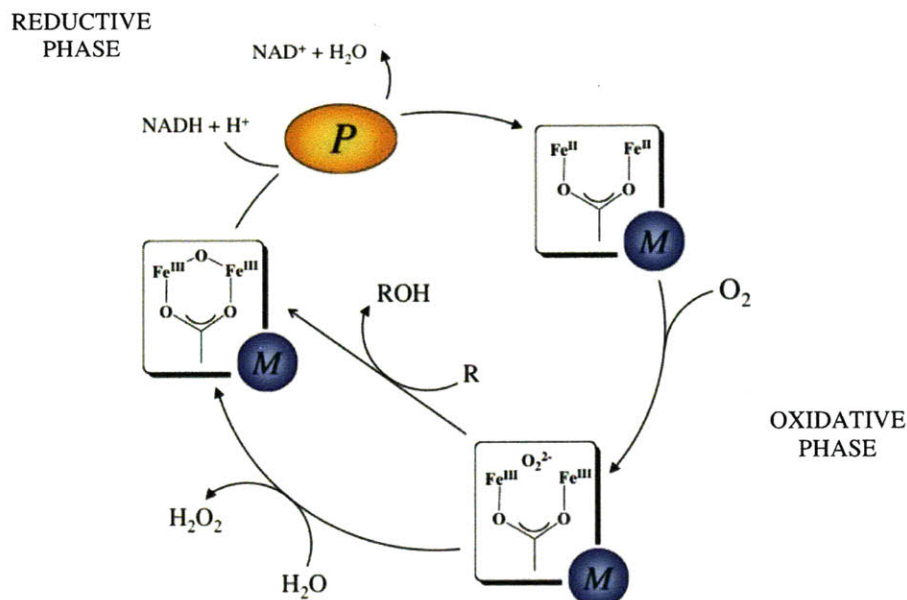
The ToMO system is the only four component alkene/arene monooxygenase that encodes a PHK-like protein, which has two of the four conserved cysteines, but crystallographic analysis of the protein did not reveal the presence of zinc in ToMOH (64). The three component phenol hydroxylases and four component alkene/arene monooxygenases are close evolutionary relatives, presumably formed by a gene duplication event (3, 4). The two cysteine residues in ToMOH may therefore be vestiges of an evolutionary ancestor that contained zinc and evolved into the three component and four component aromatic hydroxylases. Further studies are necessary to determine whether the PHK homolog in ToMO is biochemically and physiologically essential.

*Dioxygen Activation in PH in the Absence of Hydrocarbon Substrate.* BMMs and other members of the family of carboxylate-bridged diiron proteins activate dioxygen to perform substrate oxidation reactions (Chapter 1). Typically, reaction of the reduced diiron(II) form of the enzyme with O<sub>2</sub> generates one or more activated iron-oxygen species. Peroxodiiron(III) intermediates have been characterized in several of these enzymes including sMMOH (7), ToMOH (15), ribonucleotide reductase (RNR) R2 subunit (65), stearoyl ACP Δ<sup>9</sup> desaturase (59), human deoxyhypusine hydroxylase (60), and amine oxidase (AurF) (66). These intermediates are directly responsible for substrate

oxidation in all of the well-characterized diiron systems except for sMMOH and RNR-R2, where they evolve into higher oxidation state intermediates.

Reaction of PHH<sub>ox</sub>:2M with O<sub>2</sub> resulted in the formation of a diiron(III) transient with similar Mossbauer parameters to those of peroxodiiron(III) species of ToMOH (15) and AurF (66). As for the diiron(III) peroxide of ToMO, hereafter referred to as ToMOH<sub>peroxo</sub>, the species characterized in PHH displays no discernable optical bands in the UV-visible region. By analogy to ToMO and from the observation that PHH liberates H<sub>2</sub>O<sub>2</sub> in the absence of hydrocarbon substrate when treated with an electron source in the presence of O<sub>2</sub>, we assign the species as a peroxodiiron(III) unit. The observed spectroscopic differences between this center and peroxodiiron(III) species characterized in most other carboxylate-bridged diiron proteins and model complexes reflect an alternative geometry and/or protonation. Because double-mixing Mössbauer spectroscopic experiments show that the rate of decay of ToMOH<sub>peroxo</sub> is accelerated in the presence of substrate, the peroxodiiron(III) species of PH might similarly be responsible for aromatic hydroxylation. A working model for the PH catalytic cycle based on these considerations is provided in Scheme 4.4, and will form the basis for future work.

Although the peroxodiiron(III) species observed in PH displays similar spectroscopic characteristics to ToMOH<sub>peroxo</sub>, the kinetic parameters that define its formation and decay differ. At 4 °C, ToMOH<sub>peroxo</sub> forms ( $k_{\text{form}} = 26 \text{ s}^{-1}$ ) and decays ( $k_{\text{decay}} = 0.02 \text{ s}^{-1}$ ) with kinetics that afford maximal accumulation 170 ms after reaction initiation (15). The kinetic parameters of the PH peroxodiiron(III) species are much lower, however, such that the intermediate accumulate maximally at ~90 s after reaction initiation (Figure



**Scheme 4.4.** Cartoon Representation of Catalysis by PHH

4.11). Given that the active site structures of PHH (29) and ToMOH (64) are nearly identical and that these enzymes perform similar reactions, these results are surprising. Slow accumulation of the PHH intermediate relative to that of ToMOH might be due to the fact that O<sub>2</sub> activation in the former originates from a partially inactivated diiron cluster form (Figure 4.8). Alternatively, the inherent inertness of the PH intermediate relative to ToMOH<sub>peroxo</sub> may reflect disparate protein forces at the active site. Indeed, ToMOH might have evolved more oxidizing power than PH in order to hydroxylate benzene and toluene rapidly, substrates that are less activated for electrophilic aromatic substitution, which have greater C–H bond strengths than phenol.

The differences in O<sub>2</sub> activation pathways between PH and MMOH are also striking. Mössbauer spectroscopy provided no evidence for a stable, high-valent Q-type

intermediate in PH. The active site structures of PHH (29) and MMOH<sub>mv</sub> (67) are similar, however, providing no insight into why MMOH can generate such a potent, stable oxidant but PHH cannot. Recent quantum mechanical/molecular modeling investigations of MMOH indicate that the protein environment compresses the active site in such a manner to promote progression along the reaction coordinate (68). If the PH protein matrix does not provide similar pressure at the active site, then there might not be enough thermodynamic driving force to generate a high-energy diiron(IV) intermediate in PH. Further studies are necessary to understand why the reaction pathways of PH, MMOH, and other carboxylate-bridged diiron proteins with similar core structures differ.

*H<sub>2</sub>O<sub>2</sub> Generation by PH.* Under appropriate conditions, PH generates H<sub>2</sub>O<sub>2</sub> (Figures 4.13 and 4.16). Catalytic production of H<sub>2</sub>O<sub>2</sub> in this system results from two sources, protonation and liberation from the peroxide intermediate generated at the hydroxylase diiron active site and oxidase activity of the reductase protein. The PH system generates H<sub>2</sub>O<sub>2</sub> when sub-stoichiometric amounts of PHP are employed and the rate of H<sub>2</sub>O<sub>2</sub> formation by the reductase is too slow to account for that formed by the complete system. The putative peroxodiiron(III) intermediate of PHH decays slowly to the diiron(III) product (Figure 4.11) and must liberate its bound peroxide by some, as yet undefined mechanism. Consistent with these findings is the observation that sMMO does not produce H<sub>2</sub>O<sub>2</sub> under steady-state conditions (18). In this system the second peroxodiiron(III) intermediate that accumulates, H<sub>peroxo</sub>, rapidly converts to the di(μ-oxo)diiron(IV) species Q, which can decay acquiring two electrons and two protons to release of H<sub>2</sub>O and form the diiron(III) product (18, 69).

In addition to releasing  $\text{H}_2\text{O}_2$  from the hydroxylase diiron sites, PH generates  $\text{H}_2\text{O}_2$  via oxidase activity of the reductase (Figure 4.16a). Raising the quantity of electron transfer protein in BMMs above the optimal level uncouples electron transfer from substrate oxidation and leads to formation of  $\text{O}_2^-$  and  $\text{H}_2\text{O}_2$  (18, 33).  $\text{O}_2$  activation is slow in PH, because the peroxodiiron(III) intermediate accumulates over  $\sim 90$  s and decays slowly over a period of 900 s at 4 °C. The rate of NADH consumption by the enzyme is continuous and is more rapid than one cycle of  $\text{O}_2$  activation as monitored in such experiments. The excess electrons consumed must therefore be used to produce  $\text{H}_2\text{O}_2$  by PHP oxidase activity. The cellular relevance of this observation is unknown; however, it is possible that the ratio of PHP to PHH employed in our experiments is not physiologically correct, even though the PH activity is highest at the PHP:PHH ratio employed (37). It is estimated that the cellular concentration of MMOR is only 10% of that of MMOH and MMOB in *M. trichosporium* (OB3b) (70). If the PHP:PHH ratio is similar for the PH system of *Pseudomonas* sp. OX1,  $\text{H}_2\text{O}_2$  would not evolve in the cell when aromatic substrates are absent (vide supra).

The ability of BMM hydroxylases to utilize  $\text{H}_2\text{O}_2$  instead of electrons, protons, and molecular oxygen as an oxidant, the so-called ‘peroxide shunt’, has also been documented in the sMMO (71, 72) and T4mo (73) systems. In the former, activation of  $\text{MMOH}_{\text{ox}}$  with  $\text{H}_2\text{O}_2$  results in oxidation of methane and other substrates in the presence or absence of MMOB at a rate comparable to that of  $\text{O}_2$ -mediated turnover. In the latter, the rate of  $\text{H}_2\text{O}_2$ -promoted aromatic hydroxylation is 600-fold slower than the analogous reaction with  $\text{O}_2$  and electrons.<sup>1</sup> The authors of these studies concluded that product

---

<sup>1</sup>It should be noted, however, that no control experiments were performed in these studies to test the ability of  $\text{H}_2\text{O}_2$  to mediate nonenzymatic aromatic hydroxylation reactions.



formation resulted from  $\text{H}_2\text{O}_2$  binding at the active site and forming functional oxygenated iron species. The results presented here reveal that PH cannot participate in a peroxide shunt in the presence or absence of its regulatory protein. Similar results were reported for ToMO (15). It is apparent that  $\text{H}_2\text{O}_2$  and possibly the deprotonated forms of this molecule,  $\text{HO}_2^-$  and  $\text{O}_2^{2-}$ , cannot bind the diiron center to form functional oxidizing species.

*Evidence for Half-Sites Reactivity in PH.* The observations that the complete PH system generates ~50% of product per active sites in single turnover assays (Table 4.6) and that fewer than 50% of the diiron sites proceed through the putative peroxodiiron(III) intermediate in Mössbauer spectroscopic experiments indicate that this protein reacts by a half-sites reactivity mechanism (1). In this model, negative cooperativity between the two active site protomers assures a mechanism in which only one subunit of the dimer activate  $\text{O}_2$  at a time. Such allosteric communication ensures that the other active site is simultaneously engaged in the reductive phase of the catalytic cycle (Scheme 4.4). In support of this mechanism, the crystal structure of the PHH/PHM complex revealed a regulatory protein bound only at one side of the hydroxylase dimer (29). Together, these results suggest that one active site in the dimer proceeds through the catalytic cycle at a time. In contrast, MMOH does not proceed by a half-sites type of mechanism, because 90-100% of product forms per diiron sites in single turnover assays (36).

*PHP Regulates PHH Chemistry.* Single turnover experiments reveal that the electron transfer protein PHP affects  $\text{O}_2$  activation/substrate oxidation steps of catalysis as well as reducing the hydroxylase diiron sites, because the product yield is greatly enhanced by the presence of this protein (Table 4.6). This conclusion is particularly strengthened by

results from single-turnover assays in which addition of oxidized PHP to a pre-reduced mixture of PHH and PHM generated more product than that obtained from the reduced PHH and PHM alone (Table 4.6). Although maximal (~50%, *vide infra*) catechol accumulation does not occur under these conditions, the amount of product formed is significantly greater than that generated in the absence of PHP. Because electron transfer from the reductase to the hydroxylase is not likely to occur under these conditions, the enhancement in product yield must arise solely from allosteric effects. The mechanism(s) by which the electron transfer protein regulates these processes in PH is unknown; however, studies from sMMO suggest that the binding of MMOR induces a long-lived conformational change in MMOH (25, 30, 31) and that MMOR modulates product regioselectivity and impacts catalysis by altering the way in which MMOH interacts with substrates (25). It is therefore possible that the mechanism by which the reductase affects PHH activity involves a conformationally induced substrate gate. In the presence of PHP, PHH would assume a conformational setting in which hydrocarbon substrates can more readily access the active site. In agreement with this notion, recent structural studies of the complex between T4moH and T4moD (28) indicate that hydrocarbon substrate must enter the active site prior to binding of the regulatory protein, before or during reduction of the hydroxylase.

The regulatory roles of the electron-transfer protein has a more marked effect in PH than in sMMO, because single turnover product yields are more significantly affected by the presence of this protein. PHH alone cannot catalytically generate a significant amount of product; however, reduced sMMO hydroxylase, MMOH, produces ~40% propylene oxide per diiron sites in single turnover reactions using propylene as substrate and ~80%

in the presence of the regulatory protein, MMOB (36). MMOR also slightly enhances the product yield in these experiments. Addition of 0.5 equiv of MMOR to a mixture of MMOH and MMOB prior to protein reduction by  $\text{Na}_2\text{S}_2\text{O}_4$  only increases the product yield from ~80% to ~88% (36), a smaller and less significant effect than in PH. The reasons for the differences between PH and sMMO are unknown, but because it is likely that the mechanisms of hydrocarbon substrate ingress differ between these systems (74), conformational changes in the hydroxylase induced by binding of the electron transfer protein could regulate hydrocarbon substrate entry.

*Roles of PHM.* Experiments performed with stoichiometric amounts of PHP indicate that the rates of  $\text{H}_2\text{O}_2$  formation and NADH consumption are both retarded in the absence of the regulatory protein (Figure 4.19 and Table 4.7). The slower rate of  $\text{H}_2\text{O}_2$  formation could arise from no or reduced generation by the hydroxylase and/or from lower oxidase activity of PHP. In sMMO,  $\text{H}_2\text{O}_2$  is produced by MMOR oxidase activity only in the absence of MMOB even though NADH is consumed at a slower rate (18), suggesting that the later scenario is unlikely. PHM-independent  $\text{H}_2\text{O}_2$  evolution from reactions containing PHH and substoichiometric amounts of PHP suggest that this product derives from the hydroxylase, because reductase oxidase activity is negligible under these conditions (Figure 4.19b). Although  $\text{H}_2\text{O}_2$  generated in the absence of the regulatory protein could result entirely from oxidase activity of the reductase, it is therefore more likely that  $\text{H}_2\text{O}_2$  formation by the hydroxylase is retarded rather than inhibited completely.

No or slow evolution of  $\text{H}_2\text{O}_2$  from PHH in the absence of PHM could arise by two processes: (i) a change in the ability to generate active site peroxodiiron(III) intermediates or in the formation kinetics describing this species or (ii) quenching of the

peroxodiiron(III) intermediate by untimely injection of electrons and concomitant reduction to H<sub>2</sub>O. For (i), the intermediate formation rate could be retarded such that it becomes slower than the rate of decay and does not accumulate in sufficient amounts to be detected by spectroscopic measures, as observed in MMOH (35). For (ii), the regulatory protein could function to block electron transfer to the oxygenated intermediates that would effect unproductive four-electron reduction of O<sub>2</sub> to H<sub>2</sub>O. Both (i) and (ii) have been proposed in the literature (28-30, 35, 36). The fact that the NADH consumption rates are retarded in the absence of the regulatory proteins suggests that (i) is more likely; however, the data do not rule out (ii) or a combination of (i) and (ii).

In PH, the rates of H<sub>2</sub>O<sub>2</sub> production and NADH consumption are independent of PHM in experiments employing 0.1 equivalent of PHP (Figure 4.19b and Table 4.7). Under these conditions, the rate of NADH consumption is also independent of phenol, suggesting that electron transfer rather than O<sub>2</sub> activation or substrate oxidation is rate-determining. If the regulatory protein slows the kinetics of O<sub>2</sub>-activation, then the effect might not be observed if the electron-transfer step is slower than these processes. In addition, if electron transfer becomes slower than decay of the peroxodiiron(III) species, then case (ii) would not be operative. Further work is necessary to delineate the mechanism of the observed PHM effects.

## **CONCLUDING REMARKS**

The present data reveal that O<sub>2</sub> is activated by the PH hydroxylase to form a quasi-stable putative peroxodiiron(III) intermediate similar to that formed in ToMOH. Single turnover and steady state analyses show that component interactions are crucial for

efficient catalysis in this system. In addition to its role as an electron transfer agent, the reductase affects the substrate reactivity of the hydroxylase through allosteric considerations. The regulatory protein accelerates  $\text{H}_2\text{O}_2$  evolution and NADH consumption by  $\text{PHH}_{\text{peroxo}}$ , revealing that it alters the kinetics of the enzymatic processes. Further studies could utilize spectroscopic and biochemical methods to distinguish between the mechanisms by which the regulatory protein affects the generation of the hydroxylase peroxodiiron(III) species and to understand better the dynamics of component interactions during the reductive and oxidative phases of the catalytic cycles. Investigating the structural and dynamic features of PHH that cause the  $\text{O}_2$  activation pathway of this enzyme to be different from that of MMOH is also a priority. Inactive forms of recombinant regulatory protein and hydroxylase complicate the PH system, however, and these studies should be undertaken with caution.

#### ACKNOWLEDGMENTS

pGEM3Z/PHKLMNOP, pGEM3Z/PHLMNOP, pGEM3Z/PHAP, and pGEM3Z/PHAMAP, plasmids were kindly supplied by Dr. Viviana Izzo and Prof. Alberto Di Donato (Università di Napoli Federico II, Naples, Italy). pET22b(+)/PHP and pET22b(+)/PHM plasmids were supplied by Prof. Alberto Di Donato. I thank Dr. Viviana Izzo for developing and sharing the expression and purification protocols for PHH (from the pGEM3Z/PHAMAP plasmid), PHM, and PHP and the procedure for PHM thermal reconstitution during her time at MIT. I also thank Dr. Viviana Izzo, Dr. Sunil Naik, and Prof. Boi Hanh Huynh for their significant contributions to the Mössbauer

studies. Last, I thank Ioannis Papayannopoulous at the MIT Biopolymers Facility for performing the ESI-MS experiments.

## REFERENCES

1. Murray, L. J., and Lippard, S. J. (2007) *Acc. Chem. Res.* 40, 466-474.
2. Sazinsky, M. H., and Lippard, S. J. (2006) *Acc. Chem. Res.* 39, 558-566.
3. Leahy, J. G., Batchelor, P. J., and Morcomb, S. M. (2003) *FEMS Microbiology Reviews* 27, 449-479.
4. Notomista, E., Lahm, A., Di Donato, A., and Tramontano, A. (2003) *J. Mol. Evol.* 56, 435-445.
5. Brazeau, B. J., Austin, R. N., Tarr, C., Groves, J. T., and Lipscomb, J. D. (2001) *J. Am. Chem. Soc.* 123, 11831-11837.
6. Tinberg, C., and Lippard, S. J. (2009) *Biochemistry* 48, 12145-12158.
7. Liu, K. E., Valentine, A. M., Qiu, D., Edmondson, D. E., Appelman, E. H., Spiro, T. G., and Lippard, S. J. (1995) *J. Am. Chem. Soc.* 117, 4997-4998.
8. Liu, K. E., Valentine, A. M., Wang, D., Huynh, B. H., Edmondson, D. E., Salifoglou, A., and Lippard, S. J. (1995) *J. Am. Chem. Soc.* 117, 10174-10185.
9. Valentine, A. M., Stahl, S. S., and Lippard, S. J. (1999) *J. Am. Chem. Soc.* 121, 3876-3887.
10. Lee, S.-K., and Lipscomb, J. D. (1999) *Biochemistry* 38, 4423-4432.
11. Lee, S.-K., Fox, B. G., Froland, W. A., Lipscomb, J. D., and Münck, E. (1993) *J. Am. Chem. Soc.* 115, 6450-6451.

12. Lee, S.-K., Nesheim, J. C., and Lipscomb, J. D. (1993) *J. Biol. Chem.* 268, 21569-21577.
13. Liu, K. E., Wang, D., Huynh, B. H., Edmondson, D. E., Salifoglou, A., and Lippard, S. J. (1994) *J. Am. Chem. Soc.* 116, 7465-7466.
14. Murray, L. J., García-Serres, R., Naik, S., Huynh, B. H., and Lippard, S. J. (2006) *J. Am. Chem. Soc.* 128, 7459-7460.
15. Murray, L. J., Naik, S. G., Ortillo, D. O., García-Serres, R., Lee, J. K., Huynh, B. H., and Lippard, S. J. (2007) *J. Am. Chem. Soc.* 129, 14500-14510.
16. Merckx, M., Kopp, D. A., Sazinsky, M. H., Blazyk, J. L., Müller, J., and Lippard, S. J. (2001) *Angew. Chem. Int. Ed.* 40, 2782-2807.
17. Fox, B. G., Liu, Y., Dege, J. E., and Lipscomb, J. D. (1991) *J. Biol. Chem.* 266, 540-550.
18. Gassner, G. T., and Lippard, S. J. (1999) *Biochemistry* 38, 12768-12785.
19. Green, J., and Dalton, H. (1985) *J. Biol. Chem.* 260, 15795-15801.
20. Pikus, J. D., Studts, J. M., Achim, C., Kauffmann, K. E., Münck, E., Steffan, R. J., McClay, K., and Fox, B. G. (1996) *Biochemistry* 35, 9106-9119.
21. Liu, K. E., and Lippard, S. J. (1991) *J. Biol. Chem.* 266, 12836-12839.
22. Paulsen, K. E., Liu, Y., Fox, B. G., Lipscomb, J. D., Münck, E., and Stankovich, M. T. (1994) *Biochemistry* 33, 713-722.
23. DeWitt, J. G., Rosenzweig, A. C., Salifoglou, A., Hedman, B., Lippard, S. J., and Hodgson, K. O. (1995) *Inorg. Chem.* 34, 2505-2515.
24. Fox, B. G., Hendrich, M. P., Surerus, K. K., Andersson, K. K., Froland, W. A., Lipscomb, J. D., and Münck, E. (1993) *J. Am. Chem. Soc.* 115, 3688-3701.

25. Froland, W. A., Anersson, K. K., Lee, S.-K., Liu, Y., and Lipscomb, J. D. (1992) *J. Biol. Chem.* *257*, 17588-17597.
26. Mitić, N., Schwartz, J. K., Brazeau, B. J., Lipscomb, J. D., and Solomon, E. I. (2008) *Biochemistry* *47*, 8386-8397.
27. Pulver, S. C., Froland, W. A., Lipscomb, J. D., and Solomon, E. I. (1997) *J. Am. Chem. Soc.* *119*, 387-395.
28. Bailey, L. J., McCoy, J. G., Phillips Jr., G. N., and Fox, B. G. (2008) *Proc. Natl. Acad. Sci. USA* *105*, 19194-19198.
29. Sazinsky, M. H., Dunten, P. W., McCormick, M. S., Di Donato, A., and Lippard, S. J. (2006) *Pseudomonas* sp. OX1, *Biochemistry* *45*, 15392-15404.
30. Blazyk, J. L., Gassner, G. T., and Lippard, S. J. (2005) *J. Amer. Chem. Soc.* *127*, 17364-17376.
31. Gallagher, S. C., Callaghan, A. J., Zhao, J., Dalton, H., and Trehwella, J. (1999) *Biochemistry* *38*, 6752-6760.
32. Wallar, B. J., and Lipscomb, J. D. (2001) *Biochemistry* *40*, 2220-2233.
33. Mitchell, K. H., Studts, J. M., and Fox, B. G. (2002) *Biochemistry* *41*, 3176-3188.
34. Zheng, H., and Lipscomb, J. D. (2005) *Biochemistry* *45*, 1685-1692.
35. Liu, Y., Nesheim, J. C., Lee, S.-K., and Lipscomb, J. D. (1995) *J. Biol. Chem.* *270*, 24662-24665.
36. Liu, Y., Nesheim, J. C., Paulsen, K. E., Stankovich, M. T., and Lipscomb, J. D. (1997) *Biochemistry* *36*, 5223-5233.
37. Cafaro, V., Izzo, V., Scognamiglio, R., Notomista, E., Capasso, P., Casbarra, A., Pucci, P., and Di Donato, A. (2004) *Appl. Environ. Microbiol.* *70*, 2211-2219.



38. Powlowski, J., and Shingler, V. (1994) *Biodegradation* 5, 219-236.
39. Arenghi, F. L., Berlanda, D., Galli, E., Sello, G., and Barbieri, P. (2001) *Appl. Environ. Microbiol.* 67, 3304-3308.
40. Cafaro, V., Scognamiglio, R., Viggiani, A., Izzo, V., Passaro, I., Notomista, E., Dal Paiz, F., Amoresano, A., Casbarra, A., Pucci, P., and Di Donato, A. (2002) *Eur. J. Biochem.* 269, 5689-5699.
41. Gibbs, C. R. (1976) *Anal. Chem.* 48, 1197-1201.
42. Ravi, N., Bollinger, J. M. J., Huynh, B. H., Stubbe, J., and Edmondson, D. E. (1994) *J. Am. Chem. Soc.* 116, 8007-8014.
43. Kent, T. A. (1998) WMOSS v. 2.5: Mössbauer Spectral Analysis Software, WEB Research Co., WEB Research Co., Minneapolis, MN.
44. Lambeth, D. O., and Palmer, G. (1973) *J. Biol. Chem.* 248, 6095-6103.
45. Hildebrandt, A. G., and Roots, I. (1975) *Arch. Biochem. Biophys.* 171, 385-397.
46. Switala, J., and Loewen, P. C. (2002) *Arch. Biochem. Biophys.* 401, 145-154.
47. Messner, K. R., and Imlay, J. A. (2002) *Methods Enzym.* 349, 354-361.
48. Murray, L. J., García-Serres, R., McCormick, M. S., Davydov, R., Naik, S., Kim, S.-H., Hoffman, B. M., Huynh, B. H., and Lippard, S. J. (2007) *Biochemistry* 46, 14795-14809.
49. Powlowski, J., Sealy, J., Shingler, V., and Cadieux, E. (1997) *J. Biol. Chem.* 272, 945-951.
50. Nordlund, I., Powlowski, J., and Shingler, V. (1990) *J. Bacteriology* 172, 6826-6833.
51. Cadieux, E., and Powlowski, J. (1999) *Biochemistry* 38, 10714-10722.

52. Moe, L. A., McMartin, L. A., and Fox, B. G. (2006) *Biochemistry* 45, 5478-5485.
53. Brandstetter, H., Whittington, D. A., Lippard, S. J., and Frederick, C. A. (1999) *Chem. Biol.* 6, 441-449.
54. Shinohara, Y., Uchiyama, H., Yagi, O., and Kusakabe, I. (1998) *J. Ferment. Bioeng.* 85, 37-42.
55. Bollinger, J. M. J., Tong, W. H., Ravi, N., Huynh, B. H., Edmondson, D. E., and Stubbe, J. (1994) *J. Am. Chem. Soc.* 116, 8015-8023.
56. Cadieux, E., Vrajmasu, V., Achim, C., Powlowski, J., and Münck, E. (2002) *Biochemistry* 41, 10680-10691.
57. Shu, L., Broadwater, J. A., Achim, C., Fox, B. G., and Münck, E. (1998) *J. Biol. Inorg. Chem.* 3, 392-400.
58. Fox, B. G., Shanklin, J., Somerville, C., and Münck, E. (1993) *Proc. Natl. Acad. Sci. USA.* 90, 2486-2490.
59. Broadwater, J. A., Ai, J., Loehr, T. M., Sanders-Loehr, J., and Fox, B. G. (1998) *Biochemistry* 37, 14664-14671.
60. Vu, V. V., Emerson, J. P., Martinho, M., Kim, Y. S., Münck, E., Park, M. H., and Que Jr., L. (2009) *Proc. Natl. Acad. Sci. USA* 106, 14814-14819.
61. Yang, X., and Ma, K. (2005) *Anal. Biochem.* 344, 130-134.
62. Newman, L. M., and Wackett, L. P. (1995) *Biochemistry* 34, 14066-14076.
63. Cotruvo, J. Jr., and Stubbe, J. (2010) *Biochemistry* 49, 1297-1309.
64. Sazinsky, M. H., Bard, J., Di Donato, A., and Lippard, S. J. (2004) *J. Biol. Chem.* 279, 30600-30610.

65. Bollinger, J. M. Jr., Krebs, C., Vicol, A., Chen, S., Ley, B. A., Edmondson, D. E., and Huynh, B. H. (1998) *J. Am. Chem. Soc.* *120*, 1094-1095.
66. Korboukh, V. K., Li, N., Barr, E. W., Bollinger, J. M. J., and Krebs, C. (2009) *J. Am. Chem. Soc.* *131*, 13608-13609.
67. Whittington, D. A., and Lippard, S. J. (2001) *J. Am. Chem. Soc.* *123*, 827-838.
68. Rinaldo, D., Philipp, D. M., Lippard, S. J., and Friesner, R. A. (2007) *J. Am. Chem. Soc.* *129*, 3135-3147.
69. Lund, J., Woodland, M. P., and Dalton, H. (1985) *Eur. J. Biochem.* *147*, 297-305.
70. Fox, B. G., Froland, W. A., Dege, J. E., and Lipscomb, J. D. (1989) *J. Biol. Chem.* *254*, 10023-10033.
71. Andersson, K. K., Froland, W. A., Lee, S.-K., and Lipscomb, J. D. (1991) *New J. Chem.* *15*, 411-415.
72. Jiang, Y., Wilkins, P. C., and Dalton, H. (1993) *Biochim. Biophys. Acta* *1163*, 105-112.
73. Bailey, L. J., and Fox, B. G. (2009) *Biochemistry* *48*, 8932-8939.
74. McCormick, M. S. (2008) Structural Investigations of Hydroxylase Proteins and Complexes in Bacterial Multicomponent Monooxygenase Systems, Ph.D. Thesis (Massachusetts Institute of Technology, Cambridge, MA).

## Chapter 5

### **Characterization of Iron Dinitrosyl Species Formed in the Reaction of Nitric Oxide with a Biological Rieske Center\***

\*All work presented in this chapter was performed in collaboration with Dr. Zachary Tonzetich. <sup>57</sup>Fe-enriched ToMOC<sub>ox</sub> NRVS spectra were collected and analyzed by Dr. Hongxin Wang (Lawrence Berkeley National Labs)

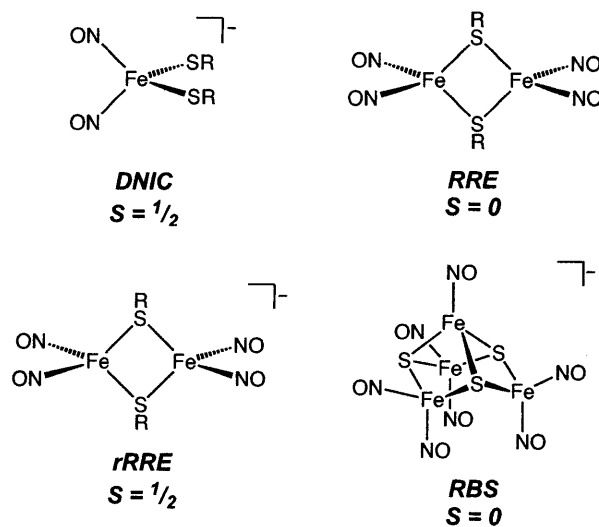
\*Reproduced in part with permission from *J. Am. Chem. Soc.*, submitted for publication

Unpublished Work © 2010 American Chemical Society

## INTRODUCTION

Nitric oxide (NO) participates in a variety of biological processes, serving as a neurotransmitter (1), a transcriptional regulator (2-6), a cytotoxic agent (7, 8) a signaling molecule in the immune response (9), and the endothelium-derived relaxing factor (10, 11). Inside the cell, this small molecule functions primarily by interacting with metal-containing proteins, although its reaction products with O<sub>2</sub> (NO<sub>x</sub>), superoxide (ONOO<sup>-</sup>), and transition metals (NO<sup>+</sup>) can lead to modification of nucleic acids, amino acid side chains, and small amines and thiols (12-14). Among the metal sites targeted by NO are iron-sulfur cluster proteins (15-17). The chemistry of NO at these sites typically results in disassembly of the iron-sulfur core and formation of dinitrosyl iron complexes (DNICs, Scheme 5.1) (18). EPR spectroscopy is usually employed to detect these species in proteins (19) and biological tissue samples (20) because of the characteristic axial  $g_{av} = 2.03$  signal associated with the thiolate-ligated DNIC (21). These species, designated  $\{\text{Fe}(\text{NO})_2\}^9$  in the Enemark-Feltham notation (22), have the general formula  $[\text{Fe}(\text{NO})_2\text{L}_2]^-$ , where L typically represents a sulfur-based ligand such as cysteine residues or mobile thiols such as glutathione (23). DNICs form readily at the [2Fe-2S] and [4Fe-4S] clusters of various proteins (4, 6, 18, 24-27) and have been proposed to elicit a variety of physiological functions including vasodilation (28-30), regulation of enzymatic activity (25, 27), transcription (4, 6), and DNA repair response mechanisms (31, 32) as well as initiation of heat-shock protein synthesis (33). Treatment of tumor cells that do not generate NO with NO-producing murine macrophages led to EPR-detectible DNICs, suggesting a role for these centers in the immune response process (7).

Although the mononuclear DNIC is generally deemed to be the important species in biological systems,  $\{\text{Fe}(\text{NO})_2\}^9$  units can occur as a component of several different compounds (34). Included are the dimeric Roussin's red ester (RRE), the reduced Roussin's red ester (rRRE), and an [4Fe-3S] cluster known as Roussin's black salt (RBS) (Scheme 5.1). Like the DNIC, rRRE species can be detected readily by EPR spectroscopy (35, 36), and have been generated in several instances upon reduction of NO-treated [4Fe-4S] cluster proteins (18, 25). The relevance of iron dinitrosyl species other than the mononuclear DNIC in biological settings is largely unexplored owing to the difficulty of detecting the diamagnetic RRE and RBS species. Using nuclear resonance vibrational spectroscopy (NRVS), we recently showed that Roussin's black salt, rather than a DNIC, is the predominant product formed in the reaction of a D14C mutant [4Fe-4S] ferredoxin



**Scheme 5.1.** Iron Dinitrosyl Species Observed in Biological and Biomimetic Synthetic Systems

from *Pyrococcus furious* with NO (37). In addition, many of the reported products of iron-sulfur cluster protein reactions with NO typically contain EPR-integrated DNIC signals that account for only a fraction of total protein iron despite complete cluster degradation (4, 6, 18, 25). A more insightful spectroscopic method for analyzing of the products of NO reactions with iron-sulfur proteins would enhance our understanding of the potential pathological and physiological properties of the molecule.

Despite the sizeable body of literature describing DNIC formation from cysteine-ligated iron-sulfur clusters, there are currently no reports of formation of iron dinitrosyl species at Rieske centers. Rieske proteins, which harbor [2Fe-2S] clusters ligated by two terminal cysteine and two terminal histidine residues, are common to both prokaryotes and eukaryotes and play important roles in electron transport, mitochondrial respiration, and photosynthesis (38, 39). Because of their similarity to ferredoxins, these proteins are expected to be targeted by NO in vivo. We recently reported that reaction of NO with a synthetic [2Fe-2S] complex featuring an N<sub>2</sub>S<sub>2</sub> ligand scaffold resulted in formation of both *N*-bound and *S*-bound DNICs, suggesting that similar chemistry could occur in Rieske systems (40). The only report to our knowledge of Rieske protein nitrosylation revealed no evidence for DNIC formation (41). The authors of this study employed purified beef heart ubiquinol-cytochrome *c* reductase (QCR) as a model Rieske system and showed that no  $S = \frac{1}{2}$  DNIC species were generated upon reaction with NO gas, although protein activity was reversibly inhibited. The Rieske cluster in QCR is buried within the protein matrix and further shielded from solvent by protein complexation with



**Figure 5.1.** Solution NMR structure of T4moC, a Rieske protein that shares 57% sequence identity with ToMOC. The [2Fe-2S] center including the coordinating histidine and cysteine ligands are depicted as spheres and in ball-and-stick format and are colored by atom type: carbon (gray), nitrogen (blue), sulfur (red), iron (orange). PDB ID code 1SJC.

succinate-ubiquinone reductase, a component used in the assays (41). It is therefore possible that NO could not efficiently access the cluster.

To determine whether DNICs and/or other iron dinitrosyl species can form at biological Rieske centers, in the present study we exposed the Rieske protein, toluene/*o*-xylene monooxygenase component C (ToMOC) from *Pseudomonas* sp. OX1, to NO. This 112-residue protein is an ideal system because it harbors a relatively stable [2Fe-2S] Rieske cluster that we expect to be largely solvent-exposed based on structural characterization of closely related toluene 4-monooxygenase component C (T4moC), which shares 57% sequence identity with ToMOC (42). A solution NMR structure determination of T4moC revealed a Rieske cluster coordinated by two histidine and two cysteine ligands on two loop regions extending from the top of a  $\beta$ -sandwich structure. Although one face of the Rieske cluster is shielded by a small  $\beta$ -sheet, the other is largely solvent-exposed (Figure 5.1). Exogenous NO should be able to reach the [2Fe-2S] center in ToMOC and react to



form iron dinitrosyl species in a manner similar to the chemistry observed with 2Fe-2S ferredoxins. Furthermore, *Pseudomonas* sp. OX1 is known to possess machinery for the metabolism of NO. A description of the reactivity of potential target proteins other than those intended for NO metabolism is therefore relevant to the global management of nitric oxide within the organism (43). Here we demonstrate that iron dinitrosyl species are indeed generated in this chemistry and provide evidence that the major product is not a DNIC species, but rather, the diamagnetic Roussin's red ester (RRE). The implications of these findings with respect to the NO chemistry of other iron sulfur clusters are discussed.

## **MATERIALS AND METHODS**

*General Considerations.* Manipulations requiring anaerobic conditions were conducted in a Vacuum Atmospheres glovebox under an atmosphere of purified N<sub>2</sub>. Buffer solutions were degassed by sparging with N<sub>2</sub> for a minimum of 1 h. ToMOC was expressed in *E. coli* and purified as described elsewhere (44). Protein obtained by this method generally exhibited an A<sub>458</sub>/A<sub>280</sub> ratio ≥ 0.12. The buffer system employed in all experiments was 25 mM potassium phosphate (KP<sub>i</sub>), pH 7.0. *S*-nitroso-*N*-acetyl-D,L-penicillamine (SNAP) and diethylamine NONOate (DEANO) were purchased from Cayman Chemical (Ann Arbor, MI) and used as received. Nitric oxide (99%) was purchased from AirGas and was purified according to a protocol described previously (45). Briefly, NO was passed through an Ascarite column (NaOH fused on silica gel) and then a 6-ft coil filled with silica gel and cooled to -78 °C with a dry ice/acetone bath. NO gas was stored and transferred under an inert atmosphere using a gas storage bulb. <sup>57</sup>Fe metal (95.5%) was

purchased from Cambridge Isotope Laboratories (Andover, MA). All other chemicals were obtained from Aldrich and were used as received. Distilled water was deionized with a Milli-Q filtering system.

*Preparation of  $^{57}\text{Fe}$ -ToMOC.* For incorporation of  $^{57}\text{Fe}$  into ToMOC, BL21(DE3) *E. coli* cells harboring the touC-pET22b(+) plasmid were grown in minimal media consisting of 10 g bactotryptone and 5 g NaCl in 1L ddH<sub>2</sub>O supplemented with 4 g/L casamino acids, 1 mM thiamine hydrochloride, 4 g/L glucose, 100 mg/mL ampicillin, and 50 mM  $^{57}\text{FeCl}_3$ . Solutions of  $^{57}\text{FeCl}_3$  were prepared by dissolving  $^{57}\text{Fe}$  metal in ultrapure concentrated HCl. Cells were grown at 37 °C and induced at an O.D.<sub>600</sub> of 0.7 with 400 μM isopropyl β-D-1-thiogalactopyranoside (IPTG). Following induction, cells were grown at 37 °C for 3 h, collected by centrifugation, and stored at -80 °C until further use.

*ToMOC Reduction.* Na<sub>2</sub>S<sub>2</sub>O<sub>4</sub> was titrated into ToMOC<sub>ox</sub> to determine the number of electrons needed to achieve complete protein reduction. A solution of Na<sub>2</sub>S<sub>2</sub>O<sub>4</sub> in 25 mM KP<sub>i</sub>, pH 7.0, was prepared and its concentration was determined by anaerobic titration into K<sub>3</sub>[Fe(CN)<sub>6</sub>] (46). This solution was then diluted to 937 μM and then anaerobically titrated into 92.6 μM ToMOC<sub>ox</sub> in 5 μL aliquots. Experiments were conducted in a glass tonometer equipped with a titrator and a quartz optical cell. UV-vis spectra were recorded after addition of each aliquot of Na<sub>2</sub>S<sub>2</sub>O<sub>4</sub>.

*General Spectroscopic Measurements.* EPR samples of ToMOC<sub>red</sub> were prepared by incubating ToMOC<sub>ox</sub> with 0.5 equiv of Na<sub>2</sub>S<sub>2</sub>O<sub>4</sub> at room temperature in an anaerobic chamber. Reactions of ToMOC<sub>ox</sub> and ToMOC<sub>red</sub> with DEANO were carried out by incubating the protein with excess (at least 5 equiv) of DEANO for 1 h at room temperature. Mössbauer samples were prepared by incubating  $^{57}\text{Fe}$ -enriched ToMOC<sub>ox</sub>

with 34 equiv of DEANO for 1 h at room temperature. Zero field  $^{57}\text{Fe}$  Mössbauer spectra were recorded at 90 K on an MSI spectrometer (WEB Research Company) with a  $^{57}\text{Co}$  source embedded in a Rh matrix. The isomer shift ( $\delta$ ) values are reported with respect to iron foil ( $\alpha\text{-Fe}$ ). Spectra were folded and simulated using the WMOSS software program (WEB Research Company) (47). UV-vis spectra were measured on a Cary-50 spectrophotometer at 25 °C in a septum-capped quartz cell. X-Band EPR spectra were recorded at 77 K on a Bruker EMX spectrometer equipped with a quartz finger dewar. Spin quantitations were performed by comparison of the doubly integrated signals to those of a 500  $\mu\text{M}$  CuEDTA solution in  $\text{KPi}$ , or a standard of 250  $\mu\text{M}$   $[\text{Fe}(\text{Ar-nacnac})(\text{NO})_2]$  (Ar-nacnac =  $[(2,6\text{-diisopropylphenyl})\text{NC}(\text{Me})_2\text{CH}]$ ) prepared in 2-MeTHF or toluene.

*NRVS Measurements.* Samples of 1.56 mM  $^{57}\text{Fe}$ -enriched  $\text{ToMOC}_{\text{ox}}$  and 1.66 mM  $^{57}\text{Fe}$ -enriched  $\text{ToMOC}_{\text{ox}}$  treated with 10 equiv DEANO were loaded into 3 x 7 x 1 mm<sup>3</sup> (interior dimensions) Lucite sample cells encased in Mylar tape. Samples were frozen in liquid nitrogen and stored at -80 °C for four days prior to shipping. To confirm that the integrity of the DEANO-treated  $^{57}\text{Fe}$ -enriched  $\text{ToMOC}_{\text{ox}}$  sample was maintained over the time between preparation and measurement, the 77 K EPR spectra of small aliquots of the reaction mixture diluted 7.5-fold and used as-is or treated with 14 equiv of  $\text{Na}_2\text{S}_2\text{O}_4$  were recorded concomitantly with the NRVS spectrum.  $^{57}\text{Fe}$  NRVS spectra were measured using published procedures (48, 49) at beamline 9-XU at Spring-8, Japan. Flux were on the order of  $1.2 \times 10^9$  photons/sec in a 0.9 meV bandpass. During data collection the sample was maintained at low temperature using a liquid He cryostat (head temperature < 10 K). Accurate sample temperatures were calculated from the ratio of

anti-Stokes to Stokes intensity by the expression  $S(-E) = S(E)e^{(-E/kT)}$  and were around 80 K. Fluorescence and delayed Fe *K* fluorescence emissions were recorded with an avalanche photodiode array. Spectra were recorded between -30 and 740  $\text{cm}^{-1}$ . The data recorded for the DEANO-treated ToMOC<sub>ox</sub> sample represent the sum of 30 65-min scans. Scans were summed and normalized to the intensity of the incident beam. Partial vibrational density of states (PVDOS) were calculated from the raw NRVs spectra using the PHOENIX Software package (50).

*Stopped-Flow Optical Spectroscopy.* Stopped-flow optical spectroscopic experiments were performed on a Hi-Tech Scientific (Salisbury, UK) SF-61 DX2 instrument. Reactions of 40  $\mu\text{M}$  ToMOC<sub>ox</sub> with DEANO were carried out by rapidly mixing anaerobic solutions of protein with DEANO dissolved in KP<sub>i</sub>. DEANO solutions were allowed to stand at room temperature for at least one half-life, as designated by the manufacturer, to ensure that the monitored kinetics events resulted from the inherent reactivity of the cluster with NO and not from slow release of NO from the NONOate. Data were recorded at 365 and 459 nm using a photomultiplier tube. The temperature for all experiments was maintained at 25 °C using a circulating water bath. Data analyses were performed with Origin v. 6.1 (OriginLab Corporation) software and data fits were evaluated on the basis of the goodness-of-fit  $\chi^2_{\text{red}}$  value, the fit residuals, and the parameter errors. Data collected at 365 and 459 nm were fit simultaneously using fixed rate constant parameters to ensure that the model used in the analysis appropriately described the events occurring at both wavelengths. Data were fit well using the three exponential function  $y = A_1 \exp(-k_{\text{obs1}} * t) + A_2 \exp(-k_{\text{obs2}} * t) + A_3 \exp(-k_{\text{obs3}} * t) + \text{Abs}_{t=\infty}$ , where  $t$  is time,  $A_1$ ,  $A_2$ ,  $A_3$  and are the pre-exponential factors for the three processes,

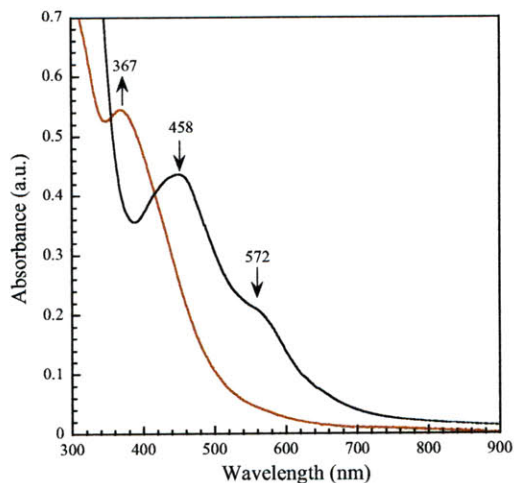


**Figure 5.2.** UV-vis spectra before (black) and after (red) incubation of 57  $\mu\text{M}$  ToMOC<sub>ox</sub> with 20 equiv of DEANO at 25 °C in 25 mM KP<sub>i</sub> buffer, pH 7.0 for 90 min.

$k_{\text{obs}1}$ ,  $k_{\text{obs}2}$ , and  $k_{\text{obs}3}$  are the rate constants for the three processes, and  $\text{Abs}_{t=\infty}$  is the final absorbance value (black lines). Attempts to fit the data to a two exponential function describing two processes yielded poor fit statistics and residual plots.

## RESULTS

*Reactions of ToMOC with NO and NO Donors.* The optical spectrum of ToMOC<sub>ox</sub> exhibits a broad band at 458 nm and a shoulder around 572 nm that are attributed to S-to-Fe(III) charge transfer transitions (Figure 5.2, red spectrum). As Na<sub>2</sub>S<sub>2</sub>O<sub>4</sub> is added, these two peaks become less intense and three new maxima characteristic of reduced ToMOC appear at 380 nm, 420 nm, and 520 nm (44). After addition of 0.56 equiv of Na<sub>2</sub>S<sub>2</sub>O<sub>4</sub>, or 1.12 equiv of electrons, the spectra no longer change with increasing Na<sub>2</sub>S<sub>2</sub>O<sub>4</sub>

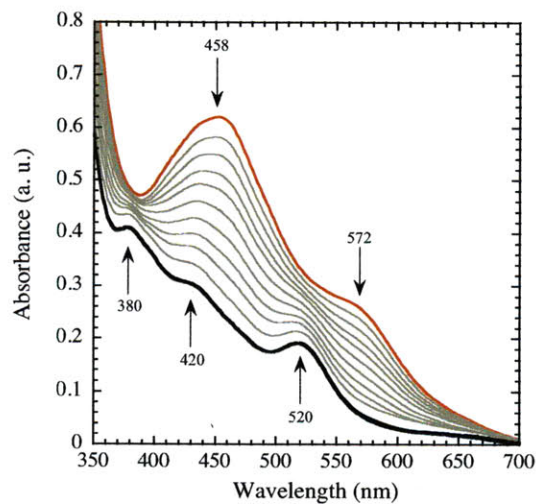


**Figure 5.3.** UV-vis spectra of the anaerobic titration of  $93 \mu\text{M}$  ToMOC<sub>ox</sub> with  $937 \mu\text{M}$  Na<sub>2</sub>S<sub>2</sub>O<sub>4</sub> at  $25 \text{ }^\circ\text{C}$  in  $25 \text{ mM}$  KP<sub>i</sub> buffer, pH 7.0. A solution of Na<sub>2</sub>S<sub>2</sub>O<sub>4</sub> was added to ToMOC<sub>ox</sub> in  $5 \mu\text{L}$  aliquots. Spectra of ToMOC<sub>ox</sub> (red) and ToMOC<sub>ox</sub> titrated with 5, 10, 15, 20, 25, 30, 35, 40, 45, 55, 60, and 65 (black)  $\mu\text{L}$  of Na<sub>2</sub>S<sub>2</sub>O<sub>4</sub> are depicted. The last three spectra overlap, indicating reaction completion.

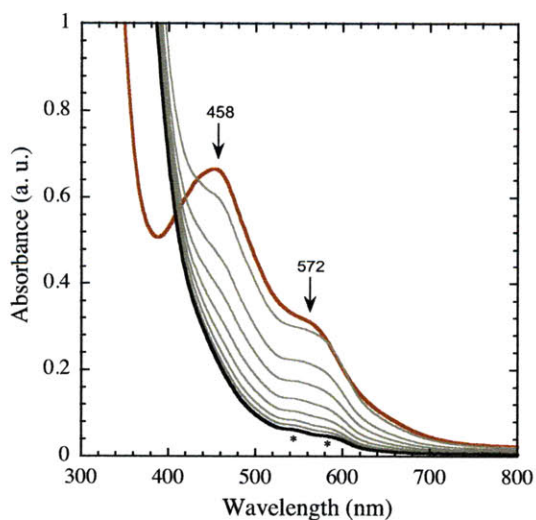


**Figure 5.4.** UV-vis spectral changes associated with the anaerobic reaction of  $91 \mu\text{M}$  ToMOC<sub>ox</sub> with 20 equiv of SNAP at  $25 \text{ }^\circ\text{C}$  in  $25 \text{ mM}$  KP<sub>i</sub> buffer, pH 7.0. Data show the spectra before reaction (red), and at 1 min, 20 min, 40 min, 60 min, 80 min, 100 min, 120 min, and 140 min (black) after reaction initiation. Peaks denoted with an asterisk are due to SNAP.

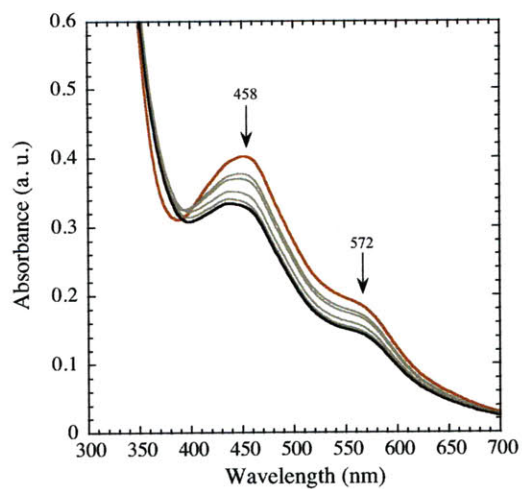


**Figure 5.5.** UV-vis spectral changes associated with the anaerobic reaction of 58  $\mu\text{M}$  ToMOC<sub>ox</sub> with  $\sim 120$  equiv of NO (g) at 25  $^{\circ}\text{C}$  in 25 mM KP<sub>i</sub> buffer, pH 7.0. Data show the spectra before reaction (red), and at 10 min, 25 min, 60 min, 80 min, and 90 min (black) after reaction initiation.

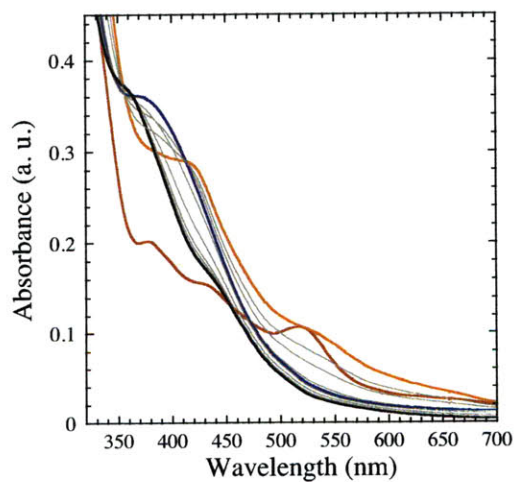


**Figure 5.6.** UV-vis spectral changes associated with the anaerobic reaction of 40  $\mu\text{M}$  ToMOC<sub>red</sub> with 20 equiv of DEANO at 25  $^{\circ}\text{C}$  in 25 mM KP<sub>i</sub> buffer, pH 7.0. Data show the spectra before reaction (red), and at intervals after reaction initiation, including 30 s (orange), 5 min (blue), and 64 min (black). The colored spectra reveal clear isosbestic points observed over the course of the reaction.

concentration, indicating complete reduction of the iron-sulfur cluster (Figure 5.3). These optical features of  $\text{ToMOC}_{\text{ox}}$  and  $\text{ToMOC}_{\text{red}}$  were used as benchmarks to determine whether the various redox states of the cluster react with NO (g) and NO donors such as DEANO and SNAP under anaerobic conditions.

Upon addition of excess DEANO (Figure 5.2), SNAP (Figure 5.3), or NO (g) (Figure 5.4) to an anaerobic solution of  $\text{ToMOC}_{\text{ox}}$ , the charge transfer bands of  $\text{ToMOC}_{\text{ox}}$  bleached, consistent with cluster disassembly. When the reaction was complete, as judged by no further changes in the spectrum, a new optical feature indicative of iron dinitrosyl species appeared at 367 nm (Figure 5.2, red) (51-53). Several crossover points were observed at distinct time points during the course of the reaction of  $\text{ToMOC}_{\text{ox}}$  with DEANO, indicating the presence of multiple intermediate species on the reaction pathway. Anaerobic addition of excess DEANO to  $\text{ToMOC}_{\text{red}}$  yielded a final product with an optical spectrum identical to that resulting from the analogous reaction with  $\text{ToMOC}_{\text{ox}}$ , indicating that the same iron dinitrosyl species forms in both reactions (Figure 5.6). Reaction of  $\text{ToMOC}_{\text{red}}$  with DEANO is more complicated and appears to proceed through a greater number of intermediate species than the reaction with  $\text{ToMOC}_{\text{ox}}$ . It is therefore appears that, although both reactions yield the same product, the mechanism of its formation depends on the redox state of the cluster.

EPR spectroscopy was employed to further characterize the products, hereafter  $\text{ToMOC}_{\text{NO}}$ , of the reactions of  $\text{ToMOC}_{\text{ox}}$  and  $\text{ToMOC}_{\text{red}}$  with NO and NO donors. Whereas  $\text{ToMOC}_{\text{ox}}$  is EPR-silent due to antiferromagnetic coupling between the iron atoms,  $\text{ToMOC}_{\text{red}}$  displays a broad rhombic signal having  $g_x = 2.01$ ,  $g_y = 1.92$ , and  $g_z =$



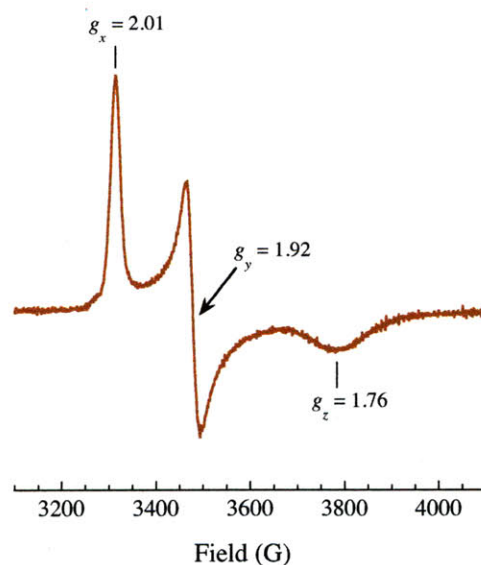


**Figure 5.7.** X-Band EPR spectrum (77 K) of 467  $\mu\text{M}$  ToMOC<sub>red</sub> in 25 mM KP<sub>i</sub>, pH 7.0. Instrument parameters: 9.332 GHz microwave frequency; 0.201 mW microwave power;  $5.02 \times 10^4$  receiver gain; 100.0 kHz modulation frequency; 8.00 G modulation amplitude; 20.480 ms time constant.

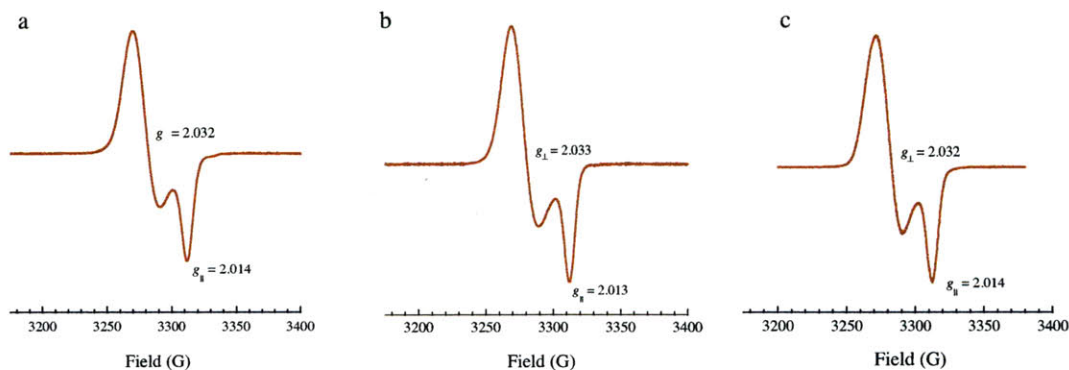


**Figure 5.8.** 77 K X-band EPR spectrum of ToMOC<sub>NO</sub> prepared by incubating 250  $\mu\text{M}$  ToMOC<sub>ox</sub> with 10 equiv of DEANO (a), 20 equiv of SNAP (b), or 100 equiv of NO (g) (c) for 1 h at 25 °C. Instrument parameters: 9.332 GHz microwave frequency; 0.201 mW microwave power;  $5.02 \times 10^3$  receiver gain; 100.0 kHz modulation frequency; 8.00 G modulation amplitude; 40.960 ms time constant.

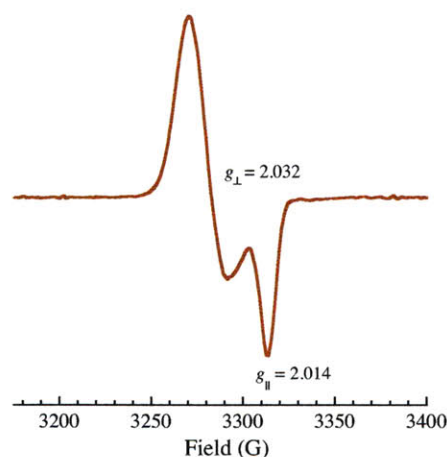


**Figure 5.9.** X-Band EPR spectrum (77 K) of the DNIC species formed from reaction of 250  $\mu\text{M}$  ToMOC<sub>red</sub> with 15 equiv of DEANO after 1 h at 25 °C in 25 mM KP<sub>i</sub>, pH 7.0. Instrument parameters: 9.332 GHz microwave frequency; 0.201 mW microwave power;  $1.00 \times 10^3$  receiver gain; 100.0 kHz modulation frequency; 8.00 G modulation amplitude; 40.960 ms time constant.

1.76 at 77 K (Figure 5.7). The observed spectrum is similar to those of other reduced Rieske centers (54, 55) and consistent with a valence trapped Fe(II)/Fe(III) unit in which the Fe(II) ion is coordinated to histidine residues (54, 56, 57).

Anaerobic treatment of ToMOC<sub>ox</sub> with excess DEANO (Figure 5.8a), SNAP (Figure 5.8b), or NO (g) (Figure 5.8c) for 1 h at 25 °C resulted in an axial  $S = \frac{1}{2}$  EPR signal with  $g_{\perp} = 2.032$  and  $g_{\parallel} = 2.013$  at 77 K. This type of signal is characteristic of a thiolate-bound  $\{\text{Fe}(\text{NO})_2\}^9$  DNIC (23) and suggests the formation of such a species during the reaction. Double integration of the signals from multiple experiments employing DEANO, SNAP, or NO gas indicated that the DNIC is present in at most 20% of the total iron concentration. Treatment of ToMOC<sub>red</sub> with excess DEANO yielded the same EPR signal, which integrated to 7% of the total iron concentration (Figure 5.9). The resulting

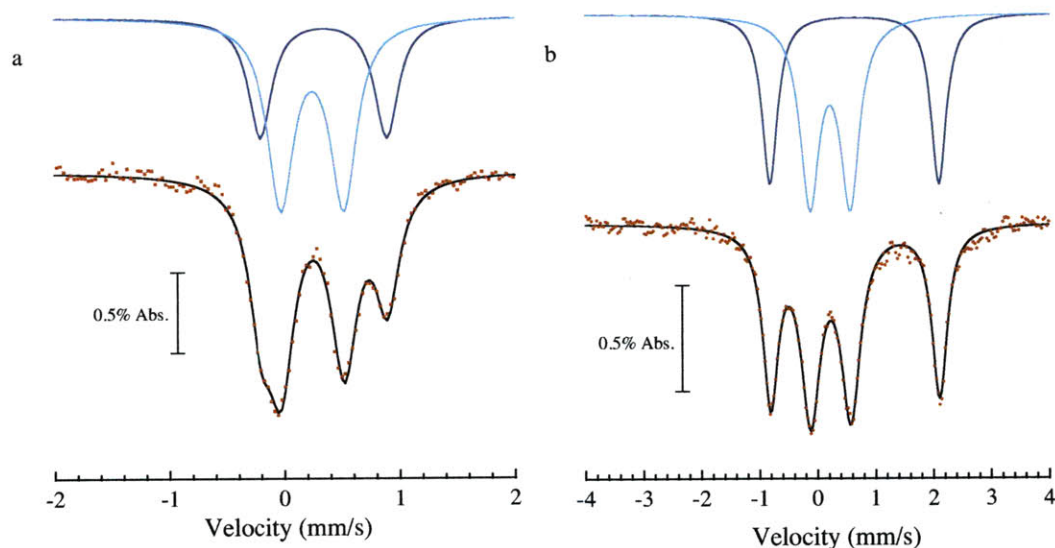


**Figure 5.10.** (a) Zero-field  $^{57}\text{Fe}$  Mössbauer spectrum (90 K) of  $378\ \mu\text{M}$   $^{57}\text{Fe}$ -enriched  $\text{ToMOC}_{\text{ox}}$  in 25 mM  $\text{KP}_i$ , pH 7.0. Data were fit to two quadrupole doublets with  $\delta_1 = 0.34(1)\ \text{mm/s}$ ,  $\Delta E_{\text{Q1}} = 1.10(1)\ \text{mm/s}$ ,  $\Gamma_1 = 0.25(1)\ \text{mm/s}$ ,  $\delta_2 = 0.24(1)\ \text{mm/s}$ ,  $\Delta E_{\text{Q2}} = 0.55(1)\ \text{mm/s}$ ,  $\Gamma_2 = 0.28(1)\ \text{mm/s}$  (black line). Subsites 1 (cyan) and 2 (aqua), shown above the fit, accounted for 42% and 58% of the iron in the sample, respectively. (b) Zero-field  $^{57}\text{Fe}$  Mössbauer spectrum (230 K) of  $966\ \mu\text{M}$   $^{57}\text{Fe}$ -enriched  $\text{ToMOC}_{\text{red}}$  in 25 mM  $\text{KP}_i$ , pH 7.0. Data were fit to two quadrupole doublets with  $\delta_1 = 0.65(1)\ \text{mm/s}$ ,  $\Delta E_{\text{Q1}} = 2.92(1)\ \text{mm/s}$ ,  $\Gamma_1 = 0.32(1)\ \text{mm/s}$ ,  $\delta_2 = 0.23(1)\ \text{mm/s}$ ,  $\Delta E_{\text{Q2}} = 0.69(1)\ \text{mm/s}$ ,  $\Gamma_2 = 0.40(1)\ \text{mm/s}$  (black line). Subsites 1 (cyan) and 2 (aqua), shown above the fit, accounted for 43% and 57% of the iron in the sample, respectively.

spectrum did not show any features indicative of  $\text{ToMOC}_{\text{red}}$ , indicating complete consumption of the original  $\{\text{Fe}_2\text{S}_2\}^{1+}$  cluster.

Zero-field  $^{57}\text{Fe}$  Mössbauer spectroscopy was also employed to study the reactions of  $\text{ToMOC}$  with  $\text{NO}$ . The Mössbauer spectrum of  $\text{ToMOC}_{\text{ox}}$  recorded at 90 K consists of two nested quadrupole doublets of narrow Lorentzian line shape ( $\Gamma = 0.32(2)\ \text{mm/s}$  for subsite 1 and  $0.28(2)$  for subsite 2), which account for all of the iron in the sample (Figure 5.10a). Data analysis using a least-squares fitting algorithm returned the parameters  $\delta = 0.25(2)\ \text{mm/s}$  and  $\Delta E_{\text{Q}} = 0.54(2)\ \text{mm/s}$  for subsite 1 and  $\delta = 0.34(2)\ \text{mm/s}$

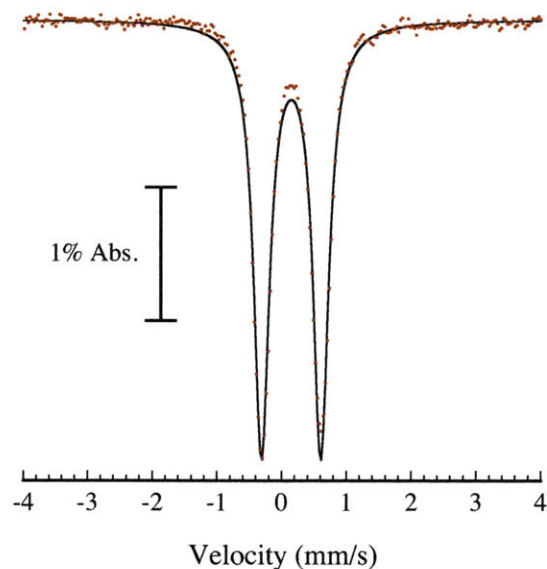


**Figure 5.11.** 77 K Mössbauer spectrum (red points) of the iron dinitrosyl species formed from reaction of 711  $\mu\text{M}$   $^{57}\text{Fe}$ -enriched ToMOC<sub>ox</sub> with 34 equiv DEANO for 1 h at 25 °C in 25 mM KP<sub>i</sub> buffer, pH 7.0. Data were fit to a single quadrupole doublet with  $\delta = 0.15(2)$  mm/s,  $\Delta E_Q = 0.92(2)$  mm/s, and  $\Gamma = 0.29(1)$  mm/s (black line).

and  $\Delta E_Q = 1.11(2)$  mm/s for subsite 2. These values are identical to those of several well-characterized Rieske proteins, including closely related T4moC (54, 55). Tetrahedral iron(III) coordinated by sulfur-based ligands such as thiolate and sulfide typically display isomer shifts between 0.20 and 0.30 mm/s (54) We therefore assign subsite 1 as the cysteine-bound iron atom. Larger isomer shifts are characteristic of mixed histidine/sulfide coordination, and subsite 2 therefore represents the histidine-bound iron atom (54, 55).

The zero-field 230 K  $^{57}\text{Fe}$  Mössbauer spectrum of ToMOC<sub>red</sub> generated by anaerobic incubation of ToMOC<sub>ox</sub> with 0.54 equiv of Na<sub>2</sub>S<sub>2</sub>O<sub>4</sub> contains two quadrupole doublets that account for all of the iron in the sample (Figure 5.10b). At lower temperatures, the

lines broaden appreciably due to magnetic hyperfine interactions and two unresolved envelopes are observed (data not shown). However, at 230 K, the spin relaxation rate is fast and magnetic hyperfine interactions are averaged, leading to two resolved quadrupole doublets (54). Data analysis using a least-squares fitting algorithm revealed that  $\delta = 0.65(2)$  mm/s and  $\Delta E_Q = 2.92(2)$  mm/s for the histidine-bound ferrous site and  $\delta = 0.23(2)$  mm/s and  $\Delta E_Q = 0.69(2)$  mm/s for the cysteine-ligated ferric site. These parameters are again identical to those of several well-characterized Rieske proteins (54, 55). Although the lineshapes of these doublets are narrow enough to obtain a good data fit,  $\Gamma = 0.32(2)$  mm/s for the Fe(II) site and 0.40(2) for the Fe(III) site, the latter doublet is significantly broadened by nuclear relaxation at 230 K (54).

The zero-field 90 K  $^{57}\text{Fe}$  Mössbauer spectrum of  $\text{ToMOC}_{\text{ox}}$  treated with 34 equiv of DEANO displays a single quadrupole doublet with a narrow linewidth,  $\Gamma = 0.29(2)$  mm/s, which accounts for all of the iron in the sample (Figure 5.11). Data analysis using a least-squares fitting algorithm revealed that  $\delta = 0.15(2)$  mm/s and  $\Delta E_Q = 0.92(2)$  mm/s. These parameters are strongly indicative of iron dinitrosyl species, although its exact nature cannot be definitively assigned because the Mössbauer parameters of various iron

**Table 5.1.** Comparison of Mössbauer Parameters for ToMOC-Derived and Synthetic Iron Dinitrosyl Species

Compound	$\delta$ (mm/s)	$\Delta E_Q$ (mm/s)	$\Gamma$ (mm/s)
$(\text{Et}_4\text{N})[\text{Fe}(\text{NO})_2(\text{SPh})_2]^{\text{a}}$ (DNIC)	0.17(2)	0.68(2)	0.26(2)
$[\text{Fe}_2(\mu\text{-SPh})_2(\text{NO})_4]^{\text{a}}$ (RRE)	0.15(2)	0.97(2)	0.29(2)
$(\text{Et}_4\text{N})[\text{Fe}_4(\mu_3\text{-S})_3(\text{NO})_7]^{\text{a}}$ (RBS)	0.15(2)	0.81(2)	0.32(2)
$(\text{Et}_4\text{N})[\text{Fe}_2(\mu\text{-SPh})_2(\text{NO})_4]^{\text{a}}$ (rRRE)	0.23(2)	0.35(2)	0.30(2)
$\text{ToMOC}_{\text{ox}} + \text{DEANO}$	0.15(2)	0.92(2)	0.29(2)
$(\text{ToMOC}_{\text{ox}} + \text{DEANO})_{\text{red}}$	0.15(2)	0.83(2)	0.31(2)

<sup>a</sup> Data from (37).

dinitrosyls are similar (Table 5.1) (37). The presence of a single quadrupole doublet indicates that both iron atoms of the [2Fe-2S] cluster are converted to an iron dinitrosyl species. In light of the results from the EPR quantitations (vide supra), these Mössbauer spectroscopic experiments demonstrate that dinitrosyl iron species other than the DNIC must account for most of the iron in these reaction products.

To gain further insight into the nature of the iron dinitrosyl species in ToMOC<sub>NO</sub>, we employed <sup>57</sup>Fe nuclear resonance vibrational spectroscopy (NRVS). The NRVS spectrum of <sup>57</sup>Fe-enriched ToMOC<sub>ox</sub> contains four well-resolved peaks in the region between 300 and 450 cm<sup>-1</sup> and a weaker signal near 280 cm<sup>-1</sup> (Figure 5.12, red). The four most intense peaks, located at 332, 361, 410, and 425 cm<sup>-1</sup>, are very similar in energy and relative intensity to the asymmetric and symmetric Fe–S vibrational modes observed in the NRVS spectra of [2Fe-2S] ferredoxins from *Rhodobacter capsulatus* and *Aquifex aeolicus* (58). Moreover, these peaks also correspond well to those assigned as Fe-S normal modes in resonance Raman spectra of the related T4moC protein (59). The

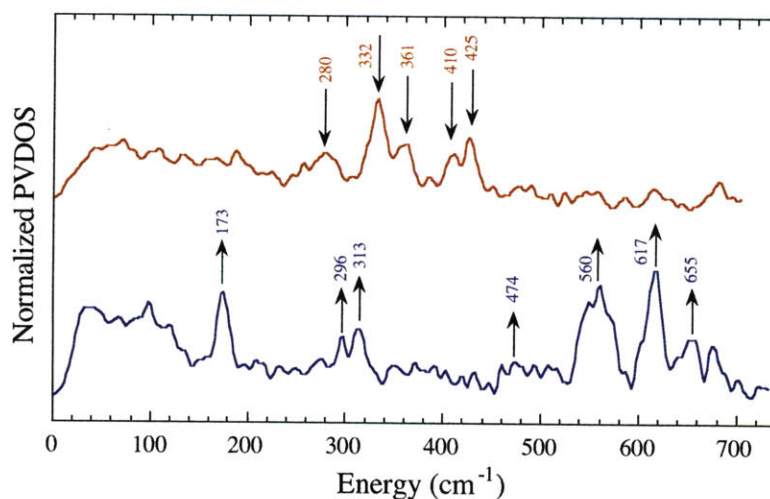


**Figure 5.12.** <sup>57</sup>Fe partial vibrational density of states (PVDOS) NRVS spectra of 1.56 mM <sup>57</sup>Fe-enriched ToMOC<sub>ox</sub> (red) and 1.66 mM <sup>57</sup>Fe-enriched ToMOC<sub>ox</sub> treated with 10 equiv of DEANO for 1 h at 25 °C in 25 mM KP<sub>i</sub> buffer, pH 7.0 (blue).

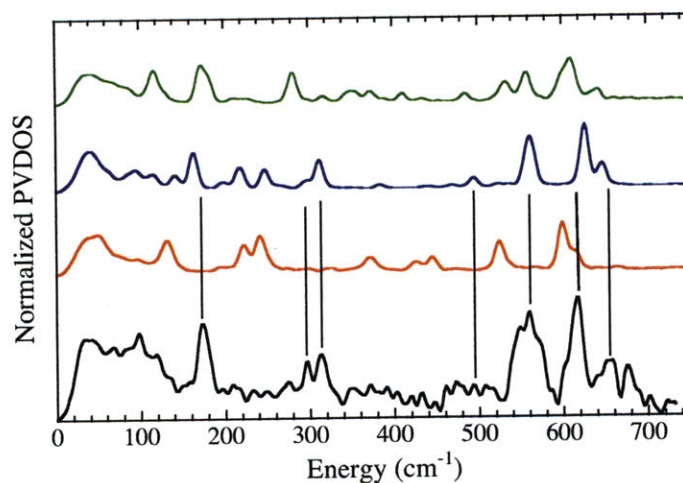


**Figure 5.13.** Normalized  $^{57}\text{Fe}$  partial vibrational density of states (PVDOS) for 1.66 mM  $^{57}\text{Fe}$ -enriched  $\text{ToMOC}_{\text{ox}}$  treated with 10 equiv of DEANO for 1 h at 25 °C in 25 mM  $\text{KP}_i$  buffer, pH 7.0 (black) compared to those of  $(\text{Et}_4\text{N})[\text{Fe}(\text{NO})_2(\text{SPh})_2]$  (DNIC; red),  $[\text{Fe}_2(\mu\text{-SPh})_2(\text{NO})_4]$  (RRE; blue), and  $(\text{Et}_4\text{N})[\text{Fe}_4(\mu\text{-S})_3(\text{NO})_7]$  (RBS; green). Data for the model compounds are taken from (37).

weaker absorbance at  $\sim 280\text{ cm}^{-1}$  is probably due to a mode involving the terminal ligands (His or Cys), although the large degree of coupling between these modes and those of the Fe–S core precludes direct assignment of the peak.

Upon treatment of  $^{57}\text{Fe}$ -enriched  $\text{ToMOC}_{\text{ox}}$  with DEANO, the Fe–S modes disappear and three distinct new peaks are observed in the high-energy region between 500 and 700  $\text{cm}^{-1}$  (Figure 5.12, blue). These peaks, located at  $\sim 560$ , 617, and 655  $\text{cm}^{-1}$ , are attributed to normal vibrational modes involving the nitrosyl ligands, which arise from a bend and asymmetric and symmetric stretches of the N–Fe–N atoms of the  $\{\text{Fe}(\text{NO})_2\}^9$  unit (37, 60). Comparisons of these peak intensities and energies to those of several previously characterized iron dinitrosyl synthetic compounds, including synthetic models of DNIC,  $((\text{Et}_4\text{N})[\text{Fe}(\text{NO})_2(\text{SPh})_2])$ , RRE,  $([\text{Fe}_2(\mu\text{-SPh})_2(\text{NO})_4])$ , and RBS,  $((\text{Et}_4\text{N})[\text{Fe}_4(\mu\text{-S})_3(\text{NO})_7])$  species (37) indicate that NRVS spectrum of the reaction product most closely matches

that of a RRE (Figure 5.13) . The spectral features do not overlap significantly with those of a DNIC model compound, further stressing that the paramagnetic, mononuclear DNIC is not the major iron dinitrosyl species formed in this chemistry.

*Reduction of the Iron Dinitrosyl Species formed in the Reaction of ToMOC with NO.*

The reaction of the  $\text{ToMOC}_{\text{NO}}$  with an electron donor,  $\text{Na}_2\text{S}_2\text{O}_4$ , was also investigated. We reasoned reduction of diamagnetic ( $S = 0$ ), EPR-silent nitrosyl species formed in the reaction might yield an open shell product with a demonstrable paramagnetic resonance spectrum. Upon anaerobic addition of stoichiometric or excess sodium dithionite to  $\text{ToMOC}_{\text{NO}}$ , the solution immediately turned from pale yellow to bright green and two new optical features at 640 and 960 nm appeared, which we attribute to the one-electron reduced Roussin's red ester species (Figure 5.14, red) (35-37). For reactions performed

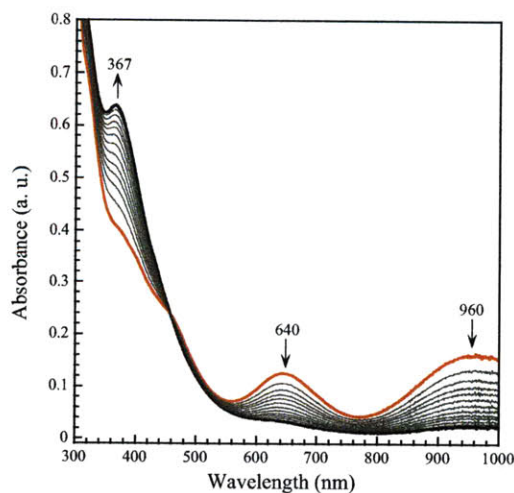


**Figure 5.14.** UV-vis spectral changes associated with the decay of reduced iron dinitrosyl species formed by addition of 2 equiv of  $\text{Na}_2\text{S}_2\text{O}_4$  to a mixture of  $79 \mu\text{M ToMOC}_{\text{ox}}$  and DEANO at  $25 \text{ }^\circ\text{C}$  in  $25 \text{ mM KP}_i$  buffer, pH 7.0. Data show the spectra 2 min after addition of reductant (red) and at various intervals until reaction completion after 80 min (black).



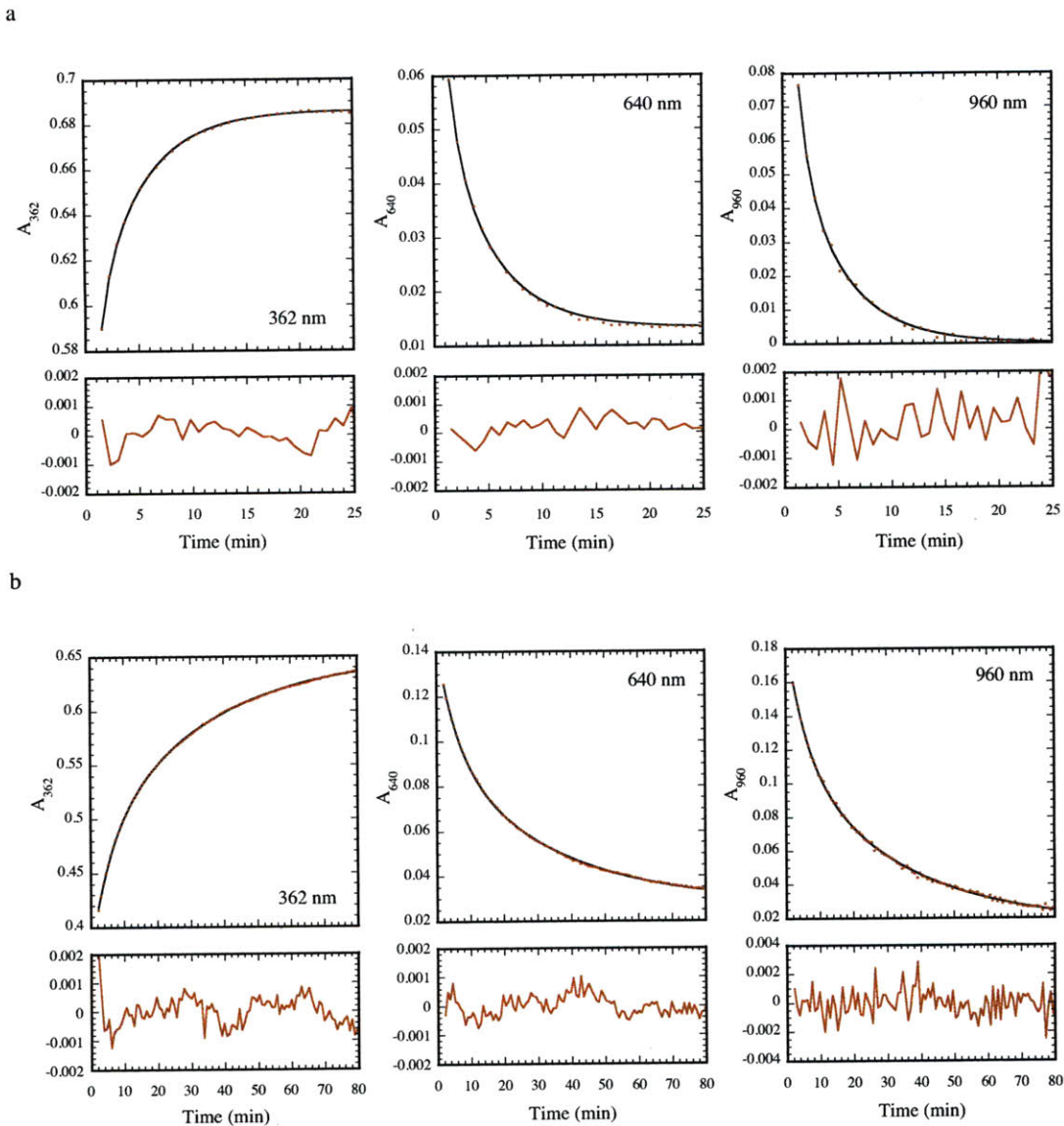


**Figure 5.15.** (a) Anaerobic decay kinetics (red points) of the rRRE formed the DNIC species generated from reaction of  $80 \mu\text{M ToMOC}_{\text{ox}}$  with 10 equiv DEANO for 1 h at  $25 \text{ }^\circ\text{C}$  with 0.5 equiv of  $\text{Na}_2\text{S}_2\text{O}_4$ . (b) Anaerobic decay kinetics (red points) of the product of (a) treated a second time with 0.5 equiv of  $\text{Na}_2\text{S}_2\text{O}_4$ . All data were fit using the two exponential function  $y = A_1 \exp(-k_{\text{obs1}} * t) + A_2 \exp(-k_{\text{obs2}} * t) + \text{Abs}_{\text{res}}$ , where  $t$  is time,  $A_1$  and  $A_2$  are the pre-exponential factors for the two processes,  $k_{\text{obs1}}$  and  $k_{\text{obs2}}$  are the rate constants for the two processes, and  $\text{Abs}_{\text{res}}$  is the final absorbance value (black lines). Attempts to fit the data to a one exponential function describing a single process yielded poor fit statistics and residual plots (not shown). Data were fit at 362 nm, 640 nm, and 960 nm simultaneously using shared rate constant parameters. Residual plots are shown in the bottom panels of (a) and (b). For (a),  $k_{\text{obs1}} = 1.10 \text{ min}^{-1}$  and  $k_{\text{obs2}} = 0.23 \text{ min}^{-1}$ . For (b),  $k_{\text{obs1}} = 0.17 \text{ min}^{-1}$  and  $k_{\text{obs2}} = 0.031 \text{ min}^{-1}$ .

with excess reducing agent (4 equiv of electrons), these optical features bleached over the course of 90 min and the initial ToMOC<sub>NO</sub> spectrum, having  $\lambda_{\text{max}} = 367$  nm, reappeared (Figure 5.14, black spectrum), indicating reversible formation of the RRE. Similar results were obtained upon addition of 1 electron to the DEANO-treated ToMOC<sub>ox</sub> sample, although the rRRE species decayed more rapidly in this instance. For the latter case, addition of a second electron to the reaction mixture after decay of the rRRE spectrum regenerated the green rRRE species, but the decay process was an order of magnitude slower than after the first electron addition (Figure 5.15). The nature of the oxidant and mechanism of decay of the rRRE species are unknown at this time, but may be correspond to reduction of adjacent protein residues such as cystines. Because ToMOC has six highly flexible cysteine residues, we propose that oxidation of the rRRE may be affected by nearby disulfide bonds. Upon utilization of these oxidants, the decay process would become much slower.

The 77 K EPR spectrum of reduced ToMOC<sub>NO</sub> displays an axial signal with  $g_{\perp} = 2.011$  and  $g_{\parallel} = 1.971$  (Figure 5.16). As with the optical features, these values are characteristic of the rRRE (35-37). A small peak at  $g = 2.04$  attributed to the original DNIC signal is also present, indicating that this species was not totally eliminated by treatment with Na<sub>2</sub>S<sub>2</sub>O<sub>4</sub>. Spin quantitation of the rRRE signal indicates that the new peak accounts for 70% of the total iron concentration. The 90 K zero-field Mössbauer spectrum of a sample of the ToMOC<sub>NO</sub> treated with 1 equiv of Na<sub>2</sub>S<sub>2</sub>O<sub>4</sub> displays a single quadrupole doublet with  $\delta = 0.15(2)$  mm/s,  $\Delta E_{\text{Q}} = 0.83(2)$  mm/s, and  $\Gamma = 0.31(2)$  mm/s (Figure 5.17). These parameters demonstrate that the integrity of the dinitrosyl iron is preserved upon

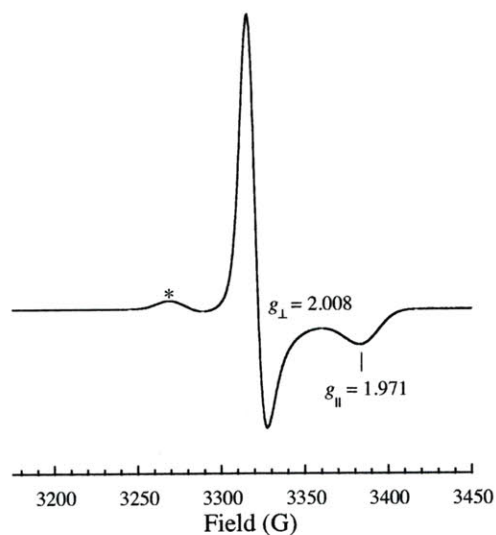


**Figure 5.16.** 77 K X-band EPR spectrum of ToMOC<sub>NO</sub> prepared by incubating 250  $\mu$ M ToMOC<sub>ox</sub> with 10 equiv DEANO for 1 h at 25 °C and then treated with 1 equiv of Na<sub>2</sub>S<sub>2</sub>O<sub>4</sub>; asterisk denotes a small amount of signal from a DNIC. Instrument parameters: 9.332 GHz microwave frequency; 0.201 mW microwave power;  $1.00 \times 10^3$  receiver gain; 100.0 kHz modulation frequency; 8.00 G modulation amplitude; 40.960 ms time constant.

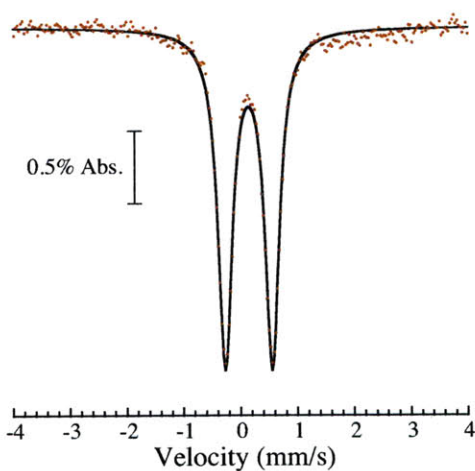


**Figure 5.17.** Zero-field <sup>57</sup>Fe Mössbauer spectrum (90 K) of the DNIC species formed by incubation of 700  $\mu$ M <sup>57</sup>Fe-enriched ToMOC<sub>ox</sub> with 34 equiv DEANO for 1 h at 25 C followed by treatment with 1 equiv Na<sub>2</sub>S<sub>2</sub>O<sub>4</sub>. Reactions were performed in 25 mM KP<sub>i</sub>, pH 7.0. Data were fit to a single quadrupole doublet with  $\delta = 0.15(2)$  mm/s,  $\Delta E_Q = 0.83(2)$  mm/s, and  $\Gamma = 0.31(2)$  mm/s (black line).

reduction, because only one quadrupole doublet is observed. Given the similarity in isomer shift and quadrupole coupling parameters between the RRE and rRRE (37) and the propensity for the latter to oxidize, Mössbauer data for reduced ToMOC<sub>NO</sub> cannot be used to definitely assign this species (Table 5.1).

*Kinetics of ToMOC Iron Dinitrosyl Formation.* Using stopped-flow kinetic techniques, changes in the optical bands at 459 and 365 nm were followed over the course of ~40 min under pseudo-first order conditions (> 10 fold excess of DEANO) after mixing ToMOC<sub>ox</sub> and DEANO. These bands, which correspond to the iron-sulfur cluster (459 nm) and the dinitrosyl iron species (365 nm), provide a means to examine both cluster degradation and iron dinitrosyl formation (Figure 5.18). Data from the two wavelengths, fit simultaneously to kinetic models, were best described by a three exponential process characterized by three distinct kinetic rate constants. Variation of the DEANO concentration resulted in a change in all three rate constants, revealing that each is NO-dependent (Table 5.2). A linear relationship between  $k_{\text{obs}}$  and [DEANO] was observed for concentrations below 2 mM. Above 2 mM the concentration of NO in aqueous solution saturates (61), and the observed rate constants level off with increasing [DEANO] (Figure 5.19). Decay of the band at 459 nm was associated with all three processes, indicating that cluster decomposition is not complete until the final kinetic phase (Figure 5.18a). In contrast, the band at 365 nm was associated only with the slowest phase of the process, indicating that formation of the iron dinitrosyl species with  $\lambda_{\text{max}}$  at this wavelength corresponds only to the final phase of reaction (Figure 5.18b).

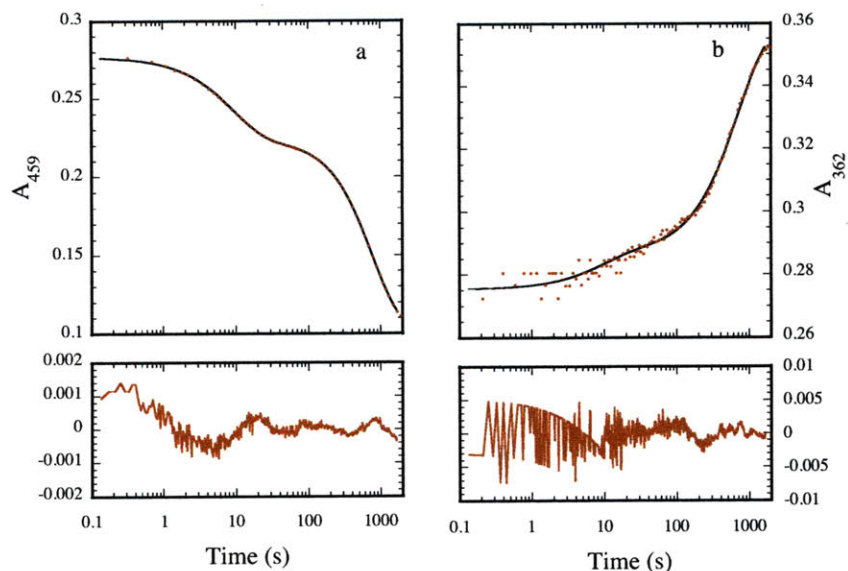


**Figure 5.18.** Representative stopped-flow absorbance profiles (red points) for the reaction of 40  $\mu\text{M}$  ToMOC<sub>ox</sub> with 150 equiv DEANO in 25 mM KP<sub>i</sub> buffer, pH 7.0, at 25 °C at 362 nm (a) and 459 nm (b). Data were analyzed as described in the text. Residual plots are shown in the bottom panels of (a) and (b).

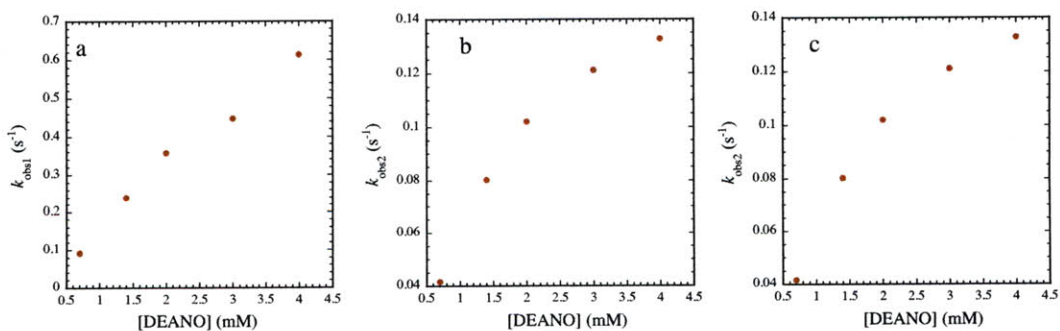


**Figure 5.19.** Plots of  $k_{\text{obs}}$  versus [DEANO] for the reaction of ToMOC<sub>ox</sub> with DEANO at 25 °C in 25 mM KP<sub>i</sub>, pH 7.0.

**Table 5.2.** Dependence of Rate Constants  $k_{\text{obs1}}$ ,  $k_{\text{obs2}}$ , and  $k_{\text{obs3}}$  for the Reaction of ToMOC<sub>ox</sub> with DEANO on [DEANO]

[DEANO] (mM)	$k_{\text{obs1}}$ (s <sup>-1</sup> )	$k_{\text{obs2}}$ (s <sup>-1</sup> )	$k_{\text{obs3}}$ (s <sup>-1</sup> )
0.7	0.092	0.042	0.00038
1.4	0.24	0.080	0.00080
2.0	0.36	0.10	0.00079
3.0	0.45	0.12	0.0013
4.0	0.61	0.13	0.0015

## DISCUSSION

Reactions of nitric oxide with cysteine-coordinated iron-sulfur clusters have been extensively investigated due to their importance in physiological signal transduction and NO-mediated pathology. DNIC products of these reactions have been proposed to regulate variety of biological processes. The working hypothesis that mononuclear DNICs are the major species responsible for the biological effects of biological iron nitrosyls has been called into question as more complete characterization of the reaction products has been achieved. The present results contribute to this paradigm shift.

*Characterization of RRE as the Primary Product in the Reaction of the Rieske Protein ToMOC with NO.* The results of UV-visible, EPR, <sup>57</sup>Fe-Mössbauer, and <sup>57</sup>Fe-NRVS spectroscopic experiments conclusively reveal [2Fe-2S] cluster degradation and formation of iron dinitrosyl species upon treatment of ToMOC<sub>ox</sub> with NO, providing the first evidence that iron dinitrosyls can form at biological Rieske centers. Although EPR spectroscopy has been used historically as the primary tool to identify DNICs, a major limitation of this method is that  $S = 0$  EPR-inactive species are not detected if formed, including RRE and RBS. The various spectroscopic methods employed here prove that

iron dinitrosyl species form in 100% yield from the reaction of  $\text{ToMOC}_{\text{ox}}$  with NO. Integration of the observed DNIC EPR signal clearly shows that this species is not the predominant reaction product. Rather, the RRE appears to be the major product, as judged by Mössbauer and NRVS spectroscopy. Further evidence for RRE as the major species is provided by experiments in which  $\text{ToMOC}_{\text{NO}}$  was treated with  $\text{Na}_2\text{S}_2\text{O}_4$ . The reaction generated optical and EPR signatures that are distinctive for a rRRE, the formation of which most likely results from reduction of the corresponding RRE (35-37). This experiment thus provides indirect evidence that  $\text{ToMOC}_{\text{NO}}$  is a RRE species.

Spectral features similar to those observed here have previously been attributed to the reduction of a  $\{\text{Fe}(\text{NO})_2\}^9$  DNIC (termed a “ $d^7$  DNIC”) to generate a “ $d^9$  DNIC” (18, 25). Recent work has shown, however, that the  $d^9$  DNIC is in fact a rRRE (35, 36). The agreement between the spectroscopic properties of the observed species with synthetic rRRE complexes of known structure suggests that these features arise from a red ester species rather than a reduced mononuclear DNIC.

Integration of the rRRE EPR signal from several experiments indicates that it forms in yields as high as 70%, implying that the RRE forms in comparable levels. The remaining ~30% of iron not accounted for by either the DNIC or the rRRE signal could be an EPR silent species, such as a histidine-ligated  $\{\text{Fe}(\text{NO})_2\}^{10}$  DNIC, or the iron-sulfur nitrosyl cluster, Roussin’s black salt (RBS, Scheme 5.1).

*Nature of DNIC Species Formed in the Reaction of ToMOC with NO.* The Rieske-type ferredoxin offers the possibility that a DNIC might form at either or both of the cysteine- and histidine-ligated iron atoms. Although biological DNICs typically feature cysteine thiolate ligation, there is also evidence for DNICs with O/N coordination in proteins.

Exposure of the [3Fe-4S] form of mitochondrial aconitase to NO resulted in DNIC formation and migration of the resulting  $\{\text{Fe}(\text{NO})_2\}^9$  species to a histidine residue, presumably to form a mixed cysteine/histidine unit (25). Histidine- and carboxylate-coordinated DNICs have also been observed in the reaction of NO with mammalian ferritins (62). Treatment of bovine serum albumin with  $[\text{Fe}(\text{NO})_2(\text{L-cysteine})_2]$  resulted in transfer of the DNIC to surface histidine residues on the protein (63). We recently reported that a synthetic model of a Rieske cluster reacts with NO to form both sulfur- and nitrogen-ligated DNIC species, although the nitrogen-based ligand used in these studies was anionic and better able to stabilize DNICs than neutral histidine residues (40). The present EPR data indicate that only cysteine-bound DNIC species form in the reaction of ToMOC with NO. There is no evidence for histidine-bound DNICs, which are distinguishable from cysteine-bound DNICs by their EPR parameters (25). The possibility that the  $\{\text{Fe}(\text{NO})_2\}^{10}$  unit formed upon treatment of  $\text{ToMOC}_{\text{NO}}$  with dithionite is transferred to the histidine ligands cannot be ruled out, given the precedence for stabilization of such a DNIC redox state by imidazole ligands (64).

*Mechanism of Formation of Iron Dinitrosyl Species.* One aspect of biological iron-sulfur NO chemistry that remains ill-defined is the mechanism by which the iron-sulfur clusters transform into iron dinitrosyl species. Some insight is provided by synthetic biomimetic chemistry involving simple homoleptic iron thiolates. Studies with these compounds demonstrated the intermediacy of a mononitrosyl iron complex (MNIC) along the pathway from  $[\text{Fe}(\text{SR})_4]^{2-/1-}$  to DNIC (65, 66). Analogous reactions with synthetic [2Fe-2S] and [4Fe-4S] clusters also yield DNICs but no intermediates have yet been identified (67, 68). Previous work from our laboratory with a synthetic analog of a



Rieske cluster revealed that both *N*-bound and *S*-bound DNICs are produced upon reaction with NO (40). This reactivity is analogous to that described for purely thiolate-bound [2Fe-2S] clusters and suggests a generality in the reactivity of the {Fe<sub>2</sub>S<sub>2</sub>}<sup>2+</sup> core toward nitric oxide.

In contrast to results with the synthetic Rieske cluster, we find here no evidence for formation of histidine-bound DNICs with ToMOC. Moreover, formation of cysteine-bound DNICs accounts for only a small fraction of the total nitrosylated iron, with most of the iron converting to the dinuclear RRE (*vide supra*). Investigation of the kinetics of the reaction indicates that several intermediate species are produced during disassembly of the iron-sulfur cluster. The kinetic data are best fit by a three-exponential process, with each rate constant depending on DEANO concentration. We cannot at this time assign specific structures to these discrete intermediates along the pathway from [2Fe-2S] cluster to RRE, although it is likely that at least one of these intermediates corresponds to mononitrosyl iron species.

*Implications for Other Iron-Sulfur Systems.* Previous reports have associated the biological consequences of NO reactivity with [2Fe-2S] and [4Fe-4S] clusters with the formation of mononuclear DNIC species. Such DNICs are probably the focus of such investigations due to their ease of detection by EPR spectroscopy. However, spin quantitation of the DNIC EPR signal in such reactions typically reveal that < 10% of the initial iron sites form DNICs even though complete cluster degradation occurs (4, 6, 25, 40, 69). Evidence from some of these earlier investigations implies that other types of iron dinitrosyl species might be formed during these reactions. A study probing the reaction of NO with FNR, a [4Fe-4S] transcription factor, estimated that < 20% of the

iron originating from the [4Fe-4S] cluster formed a DNIC. The authors suggested RRE to be the major product, present in 80% yield, although there was no direct evidence for this species (70). rRREs have previously been shown to result from chemical reduction of the products of iron-sulfur cluster nitrosylation (18, 25). Our results provide clear evidence that a RRE species is the major product formed in the reaction of the ToMOC Rieske center with NO. Given that treatment of cysteine-coordinated iron-sulfur clusters proceeds with relatively little DNIC formation but complete cluster degradation, it is likely that the major products of reaction are also Roussin's red ester species and that iron dinitrosyl species other than the mononuclear DNIC are principally responsible for the observed *in vitro* and *in vivo* effects of iron-sulfur cluster nitrosylation.

## **CONCLUDING REMARKS**

In this study we examined the reactivity of a prototypical Rieske protein with nitric oxide. Our results indicate that Rieske proteins can react with NO and that dinuclear dinitrosyl iron species (RREs) are the predominant products formed. In light of these findings, we suggest that the dinuclear RRE, not the mononuclear DNIC, could be responsible for many of the observed pathological and physiological consequences of iron-sulfur cluster nitrosylation. Further studies on a variety of different iron-sulfur proteins are necessary to test this hypothesis and explore its generality.

## **ACKNOWLEDGEMENTS**

I thank Dr. Zachary Tonzetich for co-authoring this work. Mr. Loi Do (MIT), Dr. Hongxin Wang (Lawrence Berkeley National Labs), and Dr. Yoshitaka Yoda (SPRING-8) assisted with  $^{57}\text{Fe}$ -enriched ToMOC<sub>NO</sub> NRVS data collection. I thank Dr. Hongxin Wang

for teaching me how to analyze NRVS data and Dr. Hongxin Wang and Prof. Stephen Cramer for helpful discussions. Dr. Hongxin Wang collected and analyzed <sup>57</sup>Fe-enriched ToMOC<sub>ox</sub> NRVS data at the Advanced Photon Source (Argonne National Labs).

## REFERENCES

1. Prast, H., and Philippu, A. (2001) *Prog. Neurobiol.* 64, 51-68.
2. D'Autréaux, B., Touati, D., Bersch, B., Latour, J.-M., and Michaud-Soret, I. (2002) *Proc. Natl. Acad. Sci. U.S.A.* 99, 16619-16624.
3. D'Autréaux, B., Tucker, N. P., Dixon, R., and Spiro, S. (2005) *Nature* 437, 769-772.
4. Ding, H., and Demple, B. (2000) *Proc. Natl. Acad. Sci. U.S.A.* 97, 5146-5150.
5. Strube, K., de Vries, S., and Cramm, R. (2007) *J. Biol. Chem.* 282, 20292-20300.
6. Yukl, E. T., Elbaz, M. A., Nakano, M. M., and Moënné-Loccoz, P. (2008) *Biochemistry* 47, 13084-13092.
7. Drapier, J. C., Pellat, C., and Henry, Y. (1991) *J. Biol. Chem.* 266, 10162-10167.
8. Lancaster, J. R., and Hibbs, J. B. (1990) *Proc. Natl. Acad. Sci. U.S.A.* 87, 1223-1227.
9. Bogdan, C. (2001) *Nat. Immunol.* 2, 907-916.
10. Ignarro, L. J., Buga, G. M., Wood, K. S., Byrns, R. E., and Chaudhuri, G. (1987) *Proc. Natl. Acad. Sci. U.S.A.* 84, 9265-9269.
11. Derbyshire, E. R., and Marletta, M. A. (2009) Biochemistry of Soluble Guanylate Cyclase, in *cGMP: Generators, Effectors and Therapeutic Implications*, pp 17-31.

12. Bosworth, C. A., Toledo, J. C., Jr., Zmijewski, J. W., Li, Q., and Lancaster, J. R., Jr. (2009) *Proc. Natl. Acad. Sci. U.S.A.* 106, 4671-4676.
13. Radi, R. (1996) *Chem. Res. Toxicol.* 9, 828-835.
14. Stamler, J. S. (1994) *Cell* 78, 931-936.
15. Ren, B., Zhang, N., Yang, J., and Ding, H. (2008) *Mol. Microbiol.* 70, 953-964.
16. Asanuma, K., Iijima, K., Ara, N., Koike, T., Yoshitake, J., Ohara, S., Shimosegawa, T., and Yoshimura, T. (2007) *Nitric Oxide* 16, 395-402.
17. Reddy, D., Lancaster, J. R., Jr., and Cornforth, D. P. (1983) *Science* 221, 769-770.
18. Foster, M. W., and Cowan, J. A. (1999) *J. Am. Chem. Soc.* 121, 4093-4100.
19. Woolum, J. C., Tiezzi, E., and Commoner, B. (1968) *Biochim. Biophys. Acta, Protein Struct.* 160, 311-320.
20. Commoner, B., and Ternberg, J. L. (1961) *Proc. Natl. Acad. Sci. U.S.A.* 47, 1374-1384.
21. Vanin, A. F., Serezhenkov, V. A., Mikoyan, V. D., and Genkin, M. V. (1998) *Nitric Oxide* 2, 224-234.
22. Enemark, J. H., and Feltham, R. D. (1974) *Coord. Chem. Rev.* 13, 339-406.
23. Butler, A. R., and Megson, I. L. (2002) *Chem. Rev.* 102, 1155-1165.
24. Duan, X., Yang, J., Ren, B., Tan, G., and Ding, H. (2009) *Biochem. J.* 417, 783-789.
25. Kennedy, M. C., Antholine, W. E., and Beinert, H. (1997) *J. Biol. Chem.* 272, 20340-20347.
26. Rogers, P. A., Eide, L., Klungland, A., and Ding, H. (2003) *DNA Repair* 2, 809-817.

27. Sellers, V. M., Johnson, M. K., and Dailey, H. A. (1996) *Biochemistry* 35, 2699-2704.
28. Vanin, A. F., Stukan, R. A., and Manukhina, E. B. (1996) *Biochim. Biophys. Acta, Protein Struct. Mol. Enzymol.* 1295, 5-12.
29. Vedernikov, Y. P., Mordvintcev, P. I., Malenkova, I. V., and Vanin, A. F. (1992) *Eur. J. Pharmacol.* 211, 313-317.
30. Vanin, A. F. (2009) *Nitric Oxide* 21, 1-13.
31. Lobysheva, I. I., Stupakova, M. V., Mikoyan, V. D., Vasilieva, S. V., and Vanin, A. F. (1999) *FEBS Lett.* 454, 177-180.
32. Stupakova, M. V., Lobysheva, I. I., Mikoyan, V. D., Vanin, A. F., and Vasilieva, S. V. (2000) *Biochemistry (Moscow)* 65, 690-695.
33. Wiegant, F. A. C., Malyshev, I. Y., Kleschyov, A. L., van Faassen, E., and Vanin, A. F. (1999) *FEBS Lett.* 455, 179-182.
34. Butler, A. R., Glidewell, C., and Li, M.-H. (1988) *Adv. Inorg. Chem.* 32, 335-393.
35. Lu, T.-T., Tsou, C.-C., Huang, H.-W., Hsu, I.-J., Chen, J.-M., Kuo, T.-S., Wang, Y., and Liaw, W.-F. (2008) *Inorg. Chem.* 47, 6040-6050.
36. Tsou, C.-C., Lu, T.-T., and Liaw, W.-F. (2007) *J. Am. Chem. Soc.* 129, 12626-12627.
37. Tonzetich, Z. J., Wang, H., Mitra, D., Tinberg, C. E., Do, L. H., Jenney, F. E., Adams, M. W. W., Cramer, S. P., and Lippard, S. J. (2010) *J. Am. Chem. Soc.* 132, 6914-6916.
38. Lippard, S. J., and Berg, J. M. (1994) *Principles of Bioinorganic Chemistry*, University Science Books, Mill Valley, CA.

39. Beinert, H., Holm, R. H., and Münck, E. (1997) *Science* 277, 653-659.
40. Tonzetich, Z. J., Do, L. H., and Lippard, S. J. (2009) *J. Am. Chem. Soc.* 131, 7964-7965.
41. Welter, R., Yu, L., and Yu, C.-A. (1996) *Arch. Biochem. Biophys.* 331, 9-14.
42. Skjeldal, L., Peterson, F., Doreleijers, J., Moe, L., Pikus, J., Westler, W., Markley, J., Volkman, B., and Fox, B. (2004) *J. Biol. Inorg. Chem.* 9, 945-953.
43. Cladera, A. M., Sepúlveda-Torres, L. d. C., Valens-Vadell, M., Meyer, J.-M., Lalucat, J., and García-Valdés, E. (2006) *Syst. Appl. Microbiol.* 29, 422-430.
44. Cafaro, V., Scognamiglio, R., Viggiani, A., Izzo, V., Passaro, I., Notomista, E., Piaz, F. D., Amoresano, A., Casbarra, A., Pucci, P., and Di Donato, A. (2002) *Eur. J. Biochem.* 269, 5689-5699.
45. Lorković, I. M., and Ford, P. C. (2000) *Inorg. Chem.* 39, 632-633.
46. Lambeth, D. O., and Palmer, G. (1973) *J. Biol. Chem.* 248, 6095-6103.
47. Kent, T. A. (1998) *WMOSS v. 2.5: Mössbauer Spectral Analysis Software*, WEB Research Co., WEB Research Co., Minneapolis, MN.
48. Smith, M. C., Xiao, Y., Wang, H., George, S. J., Coucouvanis, D., Koutmos, M., Sturhahn, W., Alp, E. E., Zhao, J., and Cramer, S. P. (2005) *Inorg. Chem.* 44, 5562-5570.
49. Xiao, Y., Fisher, K., Smith, M. C., Newton, W. E., Case, D. A., George, S. J., Wang, H., Sturhahn, W., Alp, E. E., Zhao, J., Yoda, Y., and Cramer, S. P. (2006) *J. Am. Chem. Soc.* 128, 7608-7612.
50. Sturhahn, W. (2000) *Hyperfine Interact.* 125, 149-172.

51. Costanzo, S., Menage, S., Purrello, R., Bonomo, R. P., and Fontecave, M. (2001) *Inorg. Chim. Acta* 318, 1-7.
52. D'Autréaux, B., Horner, O., Oddou, J. L., Jeandey, C., Gambarelli, S., Berthomieu, C., Latour, J.-M., and Michaud-Soret, I. (2004) *J. Am. Chem. Soc.* 126, 6005-6016.
53. Lobysheva, I. I., Serezhenkov, V. A., Stucan, R. A., Bowman, M. K., and Vanin, A. F. (1997) *Biochemistry (Moscow)* 62, 801-808.
54. Fee, J. A., Findling, K. L., Yoshida, T., Hille, R., Tarr, G. E., Hearshen, D. O., Dunham, W. R., Day, E. P., Kent, T. A., and Münck, E. (1984) *J. Biol. Chem.* 259, 124-133.
55. Pikus, J. D., Studts, J. M., Achim, C., Kauffmann, K. E., Munck, E., Steffan, R. J., McClay, K., and Fox, B. G. (1996) *Biochemistry* 35, 9106-9119.
56. Ballmann, J., Albers, A., Demeshko, S., Dechert, S., Bill, E., Bothe, E., Ryde, U., and Meyer, F. (2008) *Angew. Chem. Int. Ed.* 47, 9537-9541.
57. Bertrand, P., Guigliarelli, B., Gayda, J. P., Beardwood, P., and Gibson, J. F. (1985) *Biochim. Biophys. Acta, Protein Struct. Mol. Enzymol.* 831, 261-266.
58. Xiao, Y., Tan, M.-L., Ichiye, T., Wang, H., Guo, Y., Smith, M. C., Meyer, J., Sturhahn, W., Alp, E. E., Zhao, J., Yoda, Y., and Cramer, S. P. (2008) *Biochemistry* 47, 6612-6627.
59. Rotsaert, F., Pikus, J., Fox, B., Markley, J., and Sanders-Loehr, J. (2003) *J. Biol. Inorg. Chem.* 8, 318-326.
60. Dai, R. J., and Ke, S. C. (2007) *J. Phys. Chem. B* 111, 2335-2346.
61. Armor, J. N. (1974) *J. Chem. Eng. Data* 19, 82-84.

62. Lee, M., Arosio, P., Cozzi, A., and Chasteen, N. D. (1994) *Biochemistry* 33, 3679-3687.
63. Boese, M., Mordvintcev, P. I., Vanin, A. F., Busse, R., and Mülsch, A. (1995) *J. Biol. Chem.* 270, 29244-29249.
64. Reginato, N., McCrory, C. T. C., Pervitsky, D., and Li, L. (1999) *J. Am. Chem. Soc.* 121, 10217-10218.
65. Lu, T.-T., Chiou, S.-J., Chen, C.-Y., and Liaw, W.-F. (2006) *Inorg. Chem.* 45, 8799-8806.
66. Harrop, T. C., Song, D., and Lippard, S. J. (2006) *J. Am. Chem. Soc.* 128, 3528-3529.
67. Harrop, T. C., Tonzetich, Z. J., Reisner, E., and Lippard, S. J. (2008) *J. Am. Chem. Soc.* 130, 15602-15610.
68. Tsai, F.-T., Chiou, S.-J., Tsai, M.-C., Tsai, M.-L., Huang, H.-W., Chiang, M.-H., and Liaw, W.-F. (2005) *Inorg. Chem.* 44, 5872-5881.
69. Foster, M. W., Liu, L., Zeng, M., Hess, D. T., and Stamler, J. S. (2009) *Biochemistry* 48, 792-799.
70. Cruz-Ramos, H., Crack, J., Wu, G., Hughes, M. N., Scott, C., Thomson, A. J., Green, J., and Poole, R. K. (2002) *EMBO J.* 21, 3235-3244.



## **Appendix A**

### **Preliminary Characterization of $^{57}\text{Fe}$ -enriched $\text{MMOH}_{\text{ox}}$ and $\text{MMOH}_{\text{Q}}$ by Nuclear Vibrational Resonance Spectroscopy**

## INTRODUCTION

Soluble methane monooxygenase (sMMO) converts methane to methanol at ambient temperatures and pressures (1). This reaction occurs at a carboxylate-bridged diiron center housed within a hydroxylase protein (MMOH). Several oxygenated iron intermediates generated during reaction of the reduced diiron(II) form of MMOH with O<sub>2</sub> have been identified kinetically and spectroscopically, including the peroxodiiron(III) species P\* and H<sub>peroxo</sub> as well the diiron(IV) unit Q (2-6). The latter intermediate is directly responsible for methane hydroxylation (2, 4-6).

Characterization of *M. trichosporium* OB3b Q by EXAFS spectroscopy revealed a di( $\mu$ -oxo)diiron(IV) 'diamond core' with an Fe-Fe distance of 2.46 Å and Fe-O bond lengths of 1.77 Å and 2.05 Å at each iron atom (7). A head-to-tail dimer of Fe<sup>IV</sup>=O units structure was proposed (Figure 1.4) The inability of the sole di( $\mu$ -oxo)diiron(IV) model complex (8) (Table 1.2) and all high-level calculations (9-12) to reproduce the short Fe-Fe distance measured by EXAFS underscores the need for further structural characterization of this intermediate, however. The reactivity patterns of several model complexes suggest that terminal Fe(IV)=O oxidants may be more effective for C-H bond cleavage than those featuring a Fe-O-Fe unit and therefore also question the proposed structure of Q, as discussed in detail in Chapter 1 (8, 13, 14).

Synchrotron-based nuclear resonance vibrational spectroscopy (NRVS) is a recently developed, powerful technique that probes selectively the vibrations of Mössbauer active nuclei such as <sup>57</sup>Fe (15, 16). Unlike infrared and raman spectroscopy, this technique is not subject to optical selection rules and therefore all vibrational modes involving iron motion are observed. NRVS has been applied to heme proteins and model complexes

(15), heme nitrosyls (17-19), iron sulfur proteins (20), non-heme iron dinitrosyls (21), nitrogenase (22, 23), and mononuclear  $\text{Fe}^{\text{IV}}=\text{O}$  (24) and  $\text{Fe}(\text{V})$  nitrido (25) compounds. In order to evaluate whether this technique could be used to characterize structural features of non-heme diiron centers, including intermediates  $\text{H}_{\text{peroxo}}$  and Q, we recorded the spectra of  $^{57}\text{Fe}$ -enriched  $\text{MMOH}_{\text{ox}}$  and Q. The results are described here.

## MATERIALS AND METHODS

*Sample Preparation.*  $^{57}\text{Fe}$ -enriched MMOH was obtained from *M. capsulatus* (Bath) grown on medium supplemented with  $\sim 62 \mu\text{M}$   $\text{Na}^{57}\text{FeEDTA}$  as the sole source of iron (5).  $\text{Na}^{57}\text{FeEDTA}$  was prepared from  $^{57}\text{Fe}$  metal (95% enriched, Cambridge Isotope Labs) as described previously (5). Protein was purified using established methods (26) except that the iron source added to the buffers was a solution of  $^{57}\text{FeCl}_3$  prepared by dissolving  $^{57}\text{Fe}$  metal in ultrapure, concentrated HCl.  $^{57}\text{Fe}$  was added to a final concentration of  $100 \mu\text{M}$ . Protein obtained using this method had an iron content  $4.0 \pm 0.1$  of iron/dimer (27) and a specific activity  $240 \pm 38$  mU/mg of for propylene oxidation at  $45^\circ\text{C}$  (6). MMOB and MMOR were expressed recombinantly in *E. coli* and purified as described previously (28, 29).

NRVS samples were prepared with  $^{57}\text{Fe}$ -enriched MMOH. Freeze-quench studies were performed on an Update Instruments rapid freeze-quench apparatus as outlined elsewhere (30). A solution of  $766 \mu\text{M}$   $\text{MMOH}_{\text{red}}$  and 2 equiv of MMOB, prepared as noted previously (26) was mixed rapidly with an equal volume of  $\text{O}_2$ -saturated potassium phosphate ( $\text{KP}_i$ ) buffer, pH 7.0, at  $34.5^\circ\text{C}$ . The protein mixture was quenched in liquid

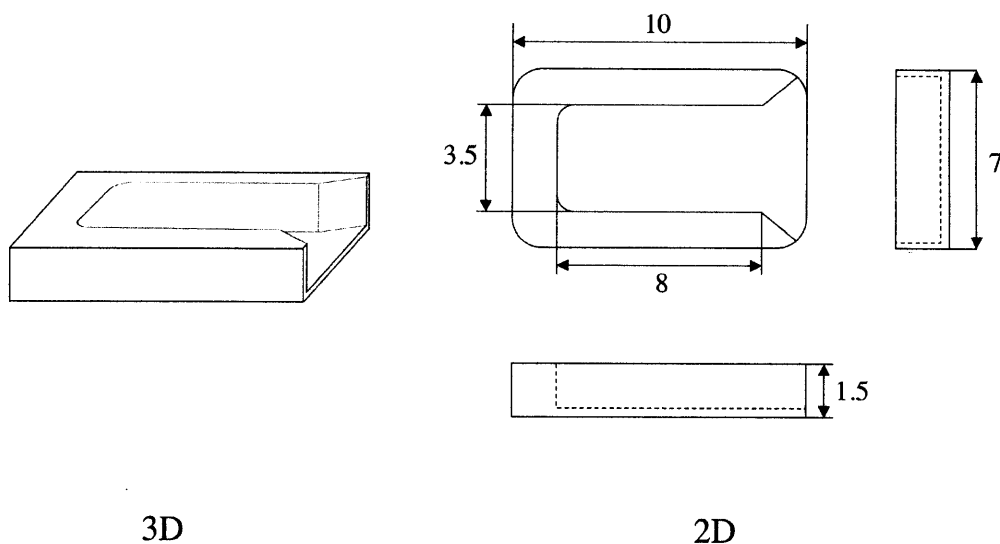


**Figure A.1.** Specifications of designed Lucite RFQ NRVS sample cells. Measurements are given in mm.

nitrogen 53 ms after reaction initiation. Under these conditions, the active iron in the sample is expected to be  $\sim 98\%$  Q (see Chapter 2). The quenched reaction frozen solution was packed under liquid nitrogen into a custom-made Lucite cell and encased in Mylar tape that was prepared at the MIT central machine shop (Figure A.1). A sample of 1.50 mM  $^{57}\text{Fe}$ -enriched  $\text{MMOH}_{\text{ox}}:2\text{B}$  was loaded into a  $3 \times 7 \times 1 \text{ mm}^3$  (interior dimensions) Lucite sample cell and encased in Mylar tape. Samples were frozen in liquid nitrogen and stored at  $-80 \text{ }^\circ\text{C}$  for four days prior to shipping.

*NRVS Measurements.*  $^{57}\text{Fe}$  NRVS spectra were recorded using published procedures at beamline 9-XU at SPring-8, Japan (20, 22, 31). Fluxes were on the order of  $1.2 \times 10^9$  photons/sec in a 0.9 meV bandpass. During data collection the sample was maintained at low temperature using a liquid He cryostat (head temperature  $< 10 \text{ K}$ ). Accurate sample

temperature values were calculated from the ratio of anti-Stokes to Stokes intensity by the expression  $S(-E) = S(E)e^{(-E/kT)}$  and were around 95 K. Fluorescence and delayed Fe *K* fluorescence emissions were recorded with an avalanche photodiode array. Spectra were recorded between -30 and 740  $\text{cm}^{-1}$  for  $\text{MMOH}_{\text{ox}}:2\text{B}$  and -30 and 870  $\text{cm}^{-1}$  for Q. The data recorded for the  $\text{MMOH}_{\text{ox}}:2\text{B}$  and Q samples represent the sum of 65 and nine 65-min scans, respectively. Scans were summed and normalized to the intensity of the incident beam. Partial vibrational density of states (PVDOS) were calculated from the raw NRVS spectra using the PHOENIX Software package.

## RESULTS AND DISCUSSION

NRVS spectroscopy is a powerful technique that can be used to structurally characterize materials, compounds, and proteins containing  $^{57}\text{Fe}$  (15). The NRVS spectrum of a frozen solution of 1.5 mM  $^{57}\text{Fe}$ -enriched  $\text{MMOH}_{\text{ox}}:2\text{B}$  revealed a very limited number of identifiable peaks, even after continuous data collection for ~3 days (Figure A.2, red spectrum). Attempts to concentrate the protein further for spectral enhancement were unsuccessful. The low energy region of the spectrum is a large envelope from 50–300  $\text{cm}^{-1}$  with distinct features at 199 and 263  $\text{cm}^{-1}$ , assigned as metal-ligand vibrational modes arising from protein side chains (32, 33). A high-energy peak at 677  $\text{cm}^{-1}$  is also apparent, particularly when error analyses were performed (data not shown). This feature is unassigned but may result from vibrational modes involving solvent-derived ligands. Two hydroxide bridges and one terminal water molecule coordinate the diiron center of  $\text{MMOH}_{\text{ox}}$  (1).  $\text{Di}(\mu\text{-hydroxo})\text{diiron(III)}$  species typically

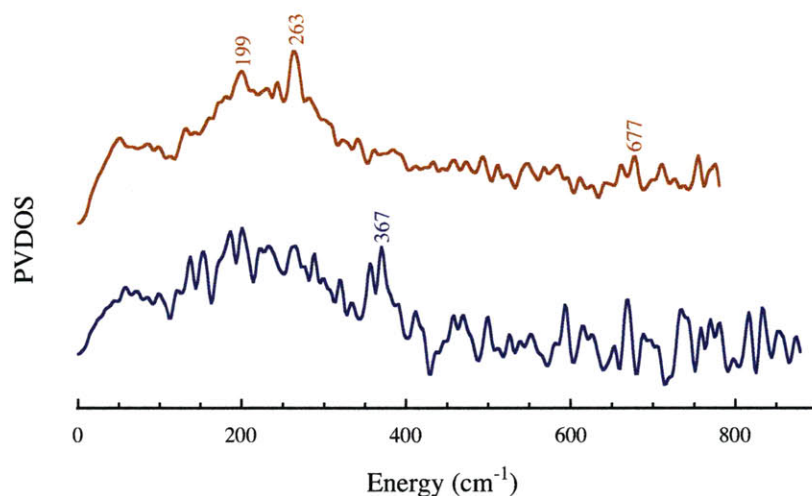


**Figure A.2.**  $^{57}\text{Fe}$  partial vibrational density of states (PVDOS) NRVS spectra of 1.5 mM  $^{57}\text{Fe}$ -enriched  $\text{MMOH}_{\text{ox}}:2\text{B}$  (red) and Q (blue) prepared by quenching a mixture of  $^{57}\text{Fe}$ -enriched 766  $\mu\text{M}$   $\text{MMOH}_{\text{red}}:2\text{B}$  and  $\text{O}_2$  53 ms after reaction initiation at 34.5 °C.

display  $\text{Fe}(\text{OH})_2\text{Fe}$  deformation modes around  $\sim 900\text{ cm}^{-1}$ , beyond the experimental range investigated (33). Alternatively, the symmetric and asymmetric stretches of  $\text{Fe}(\text{III})\text{--O--Fe}(\text{III})$  units occur between 380 and 540  $\text{cm}^{-1}$  and 725 and 885  $\text{cm}^{-1}$ , respectively (33). The observed peak is unlikely to arise from an  $\text{Fe}(\text{III})\text{--OH}_2$  vibration, which is expected to be lower in energy than the identified peak (33).

The NRVS spectrum of a sample of  $^{57}\text{Fe}$ -enriched intermediate Q prepared by RFQ methodology was also recorded (Figure A.2, blue spectrum). The high energy NRVS region is of particular interest because the peaks located in this area are diagnostic of bridged or terminal  $\text{Fe}(\text{IV})$  oxo species. The only available  $\{\text{Fe}_2(\mu\text{-O})_2\}^{4+}$  model complex displays a core deformation mode around 660–700  $\text{cm}^{-1}$  (8). Terminal  $\text{Fe}^{\text{IV}}=\text{O}$  units have higher energy  $\text{Fe--O}$  stretches around 820–830  $\text{cm}^{-1}$ , however (24). Unfortunately, the

spectrum of Q was too noisy to resolve any real features, despite the high protein concentration employed. Resolution in the high-energy region of interest was particularly poor, because the NRVS signal drops off as a function of synchrotron beam energy. It is not possible to prepare higher concentration samples because of limitations enforced by the maximum protein and O<sub>2</sub> concentrations obtainable (34).

### **CONCLUDING REMARKS AND FUTURE DIRECTIONS**

Although NRVS is a powerful technique to study iron-containing proteins and complexes, it cannot be used with the current technology to definitively characterize MMOH<sub>ox</sub>:2B and intermediate Q, mainly because of limitations in sample preparation. Brighter synchrotron sources are required to glean NRVS structural information about this system. Other techniques, such as resonance Raman spectroscopy, may aid in structural characterization.

### **ACKNOWLEDGEMENTS**

I thank Prof. JoAnne Stubbe for allowing me to use her RFQ instrument and Dr. Rachel Behan for assisting me with rapid-freeze quench procedures. Mr. Loi Do (MIT), Dr. Hongxin Wang (Lawrence Berkeley National Labs), and Dr. Yoshitaka Yoda (SPring-8) assisted with data collection. I thank Dr. Hongxin Wang for teaching me how to analyze NRVS data and Dr. Hongxin Wang and Prof. Stephen Cramer for helpful discussions.

## REFERENCES

1. Merkx, M., Kopp, D. A., Sazinsky, M. H., Blazyk, J. L., Müller, J., and Lippard, S. J. (2001) *Angew. Chem. Int. Ed.* 40, 2782-2807.
2. Brazeau, B. J., and Lipscomb, J. D. (2000) *Biochemistry* 39, 13503-13515.
3. Lee, S.-K., Fox, B. G., Froland, W. A., Lipscomb, J. D., and Münck, E. (1993) *J. Am. Chem. Soc.* 115, 6450-6451.
4. Lee, S.-K., Nesheim, J. C., and Lipscomb, J. D. (1993) *J. Biol. Chem.* 268, 21569-21577.
5. Liu, K. E., Valentine, A. M., Wang, D., Huynh, B. H., Edmondson, D. E., Salifoglou, A., and Lippard, S. J. (1995) *J. Am. Chem. Soc.* 117, 10174-10185.
6. Valentine, A. M., Stahl, S. S., and Lippard, S. J. (1999) *J. Am. Chem. Soc.* 121, 3876-3887.
7. Shu, L., Nesheim, J. C., Kauffmann, K., Münck, E., Lipscomb, J. D., and Que, L. J. (1997) *Science* 275, 515-518.
8. Xue, G., Wang, D., De Hont, R., Fiedler, A. T., Shan, X., Münck, E., and Que Jr., L. (2007) *Proc. Natl. Acad. Sci. USA* 104, 52.
9. Gherman, B. F., Baik, M.-H., Lippard, S. J., and Friesner, R. A. (2004) *J. Am. Chem. Soc.* 126, 2978-2990.
10. Han, W.-G., and Noodleman, L. (2008) *Inorg. Chim. Acta* 361, 973-986.
11. Rinaldo, D., Philipp, D. M., Lippard, S. J., and Friesner, R. A. (2007) *J. Am. Chem. Soc.* 129, 3135-3147.
12. Siegbahn, P. E. M. (2001) *J. Biol. Inorg. Chem.* 6, 27-45.



13. Rowe, G. T., Rybak-Akimova, E. V., and Caradonna, J. P. (2007) *Inorg. Chem.* 46, 10594-10606.
14. Xue, G., De Hont, R., Münck, E., and Que Jr., L. (2010) *Nat. Chem.* 2, 400-405.
15. Scheidt, W. R., Durbin, S. M., and Sage, J. T. (2005) *J. Inorg. Biochem.* 99, 60-71.
16. Sturhahn, W. (2004) *J. Phys.: Condens. Matter* 16, S497-S530.
17. Paulat, F., Berto, T. C., DeBeer George, S., Goodrich, L., Praneeth, V. K., Sulok, C. D., and Lehnert, N. (2008) *Inorg. Chem.* 47, 11449-11451.
18. Lehnert, N., Galinato, M. G., Paulat, F., Richter-Addo, G. B., Sturhahn, W., Xu, N., and Zhao, J. (2010) *Inorg. Chem.* 49, 4122-4148.
19. Zeng, W., Silvernail, N. J., Wharton, D. C., Georgiev, G. Y., Leu, B. M., Scheidt, W. R., Zhao, J., Sturhahn, W., Alp, E. E., and Sage, J. T. (2005) *J. Am. Chem. Soc.* 127, 11200-11201.
20. Xiao, Y., Tan, M.-L., Ichiye, T., Wang, H., Guo, Y., Smith, M. C., Meyer, J., Sturhahn, W., Alp, E. E., Zhao, J., Yoda, Y., and Cramer, S. P. (2008) *Biochemistry* 47, 6612-6627.
21. Tonzetich, Z. J., Wang, H., Mitra, D., Tinberg, C. E., Do, L. H., Jenney, F. E., Adams, M. W. W., Cramer, S. P., and Lippard, S. J. (2010) *J. Am. Chem. Soc.* 132, 6914-6916.
22. Xiao, Y., Fisher, K., Smith, M. C., Newton, W. E., Case, D. A., George, S. J., Wang, H., Sturhahn, W., Alp, E. E., Zhao, J., Yoda, Y., and Cramer, S. P. (2006) *J. Am. Chem. Soc.* 128, 7608-7612.

23. George, S. J., Igarashi, R. Y., Xiao, Y., Hernandez, J. A., Demuez, M., Zhao, D., Yoda, Y., Ludden, P. W., Rubio, L. M., and Cramer, S. P. (2008) *J. Am. Chem. Soc.* *130*, 5673-5680.
24. Bell III, C. B., Wong, S. D., Xiao, Y., Klinker, E. J., Tenderholt, A. L., Smith, M. C., Rohde, J.-U., Jr., L. Q., Cramer, S. P., and Solomon, E. I. (2008) *Angew. Chem. Int. Ed.* *47*, 9071-9074.
25. Petrenko, T., DeBeer George, S., Aliaga-Alcalde, N., Bill, E., Mienert, B., Xiao, Y., Guo, Y., Sturhahn, W., Cramer, S. P., Wieghardt, K., and Neese, F. (2007) *J. Am. Chem. Soc.* *129*, 11053-11060.
26. Tinberg, C., and Lippard, S. J. (2009) *Biochemistry* *48*, 12145-12158.
27. Gibbs, C. R. (1976) *Anal. Chem.* *48*, 1197-1201.
28. Coufal, D. E., Blazyk, J. L., Whittington, D. A., Wu, W. W., Rosenzweig, A. C., and Lippard, S. J. (2000) *Euro. J. Biochem.* *267*, 2174-2185.
29. Kopp, D. A., Gassner, G. T., Blazyk, J. L., and Lippard, S. J. (2001) *Biochemistry* *40*, 14932-14941.
30. Ravi, N., Bollinger, J. M. J., Huynh, B. H., Stubbe, J., and Edmondson, D. E. (1994) *J. Am. Chem. Soc.* *116*, 8007-8014.
31. Smith, M. C., Xiao, Y., Wang, H., George, S. J., Coucouvanis, D., Koutmos, M., Sturhahn, W., Alp, E. E., Zhao, J., and Cramer, S. P. (2005) *Inorg. Chem.* *44*, 5562-5570.
32. Cramer, S. P. (2010). Personal Communication.
33. Kurtz, D. M. J. (1990) *Chem. Rev.* *90*, 585-606.
34. Wilhelm, E., Battino, R., and Wilcock, R. J. (1977) *Chem. Rev.* *77*, 219-262.

## **BIOGRAPHICAL NOTE**

Christine E. Tinberg was born on October 31, 1982 in Evanston, Illinois to parents Elaine M. and Richard W. Tinberg. She was raised in Winnetka, Illinois, with one younger brother, Richard J. Tinberg. She graduated from New Trier High School in 2001 and matriculated to Northwestern University, where she received her Bachelor of Arts in Chemistry in 2005. During her undergraduate studies she worked in the laboratory of Professor Amy C. Rosenzweig investigating the copper chelator Methanobactin. In 2005 Christine began graduate work in biological chemistry at the Massachusetts Institute of Technology (MIT). During her time at MIT she participated in the NIGMS/MIT Interdepartmental Biotechnology Training Grant and spent the summer of 2008 interning at the Novartis Institutes for BioMedical Research. Christine enjoys athletics, cooking, painting, and reading.

## Christine E. Tinberg

### Education

Ph.D. Biological Chemistry                      Massachusetts Institute of Technology, Cambridge MA  
2005-2010    Advisor: Stephen J. Lippard

B.A. Chemistry                                      Northwestern University, Evanston IL  
2001-2005    Advisor: Amy C. Rosenzweig

### Honors

2007-2010      NIGMS/MIT Interdepartmental Biotechnology Training Grant Fellow  
2006              MIT Chemistry Department Teaching Award  
2004-2005      Northwestern University Undergraduate Research Fellowship

### Publications

Tonzetich, Z. J.; Wang, H.; Mitra, D.; Tinberg, C. E.; Do, L. H.; Jenney, F. E.; Adams, M. W. W.; Cramer, S. P.; Lippard, S. J. Identification of Protein-Bound Dinitrosyl Complexes by Nuclear Resonance Vibrational Spectroscopy. *J. Am. Chem. Soc.* **2010**, *132*, 6914-6916.

Tinberg, C. E.; Lippard, S. J. Revisiting the Mechanism of Dioxygen Activation in Soluble Methane Monooxygenase from *M. capsulatus* (Bath): Evidence for a Multi-Step, Proton-Dependent Reaction Pathway. *Biochemistry*, **2009**, *48*, 12145-12158.

Hakemian, A. S.; Tinberg, C. E.; Kondapalli, K. C.; Telser, J.; Hoffman, B. M.; Stemmler, T. L.; Rosenzweig, A. C. The Copper Chelator Methanobactin from *Methylosinus trichosporium* OB3b Binds Copper(I). *J. Am. Chem. Soc.* **2005**, *127*, 17142-17143.

### Presentations

C. E. Tinberg and S. J. Lippard. Dioxygen Activation in Methane Monooxygenase. Poster Presentation. NIGMS/MIT Annual Biotechnology Training Grant Seminar (Dedham, MA: May 1, 2010).

C. E. Tinberg and S. J. Lippard. Investigating Dioxygen Activation in Methane Monooxygenase. Selected Speaker. MIT Biological Chemistry Seminar Series (Cambridge, MA: Mar. 8, 2010).

C. E. Tinberg and S. J. Lippard. Dioxygen Activation in Methane Monooxygenase. Poster Presentation. Metals in Biology Gordon Research Conference (Ventura, CA: Jan. 31-Feb. 5, 2010).

C. E. Tinberg and S. J. Lippard. Dioxygen Activation in Methane Monooxygenase. Poster Presentation. Bioinorganic Gordon Research Seminar (Ventura, CA: Feb. 4-7, 2010).

C. E. Tinberg and S. J. Lippard. Mechanistic Studies of Soluble Methane Monooxygenase. Selected Speaker. NIGMS/MIT Annual Biotechnology Training Grant Seminar (Dedham, MA: Apr. 11, 2009)

C. E. Tinberg, V. Izzo, R. García-Serres, S. G. Naik, B. H. Huynh, and S. J. Lippard. Dioxygen Activation and Component Interactions in *Pseudomonas sp.* OX1 Phenol Hydroxylase. Poster Presentation. NIGMS/MIT Annual Biotechnology Training Grant Seminar (Dedham, MA: April 2008).

A. S. Hakemian, C. E. Tinberg, J. Telser, B. M. Hoffman, T. L. Stemmler, and A. C. Rosenzweig. Characterization of Methanobactin from *Methylococcus capsulatus* (Bath) and *Methylosinus trichosporium* OB3b. Poster Presentation. 12<sup>th</sup> International Conference of Biological Inorganic Chemistry (Ann Arbor, MI: July 31- Aug. 5, 2005).